



**University of
Nottingham**
UK | CHINA | MALAYSIA

Surface Ion and Electron Regulation Strategies for Rechargeable Lithium Metal Batteries

A thesis submitted to be University of Nottingham for the degree of
Doctor of Philosophy, July 2023.

Qiang Guo

20219120

Supervised by

Di Hu

Zhaoping Liu

Xufeng Zhou

George Zheng Chen

Signature Qiang GUO

Date 08052023

Abstract

With the growing popularity of portable electronic devices and electric vehicles, conventional lithium ion batteries (LIBs) are facing challenges from increasing demands for higher energy density. Instead, lithium metal (LM) has been historically and widely recognised as the most promising negative electrode (negatrode) material owing to its low density (0.53 g cm^{-3}), high theoretical specific capacity (3860 mAh g^{-1}), and lowest (most negative) redox potential (-3.04 V vs. the standard hydrogen electrode). Thus, the lithium metal negative electrode (LMNE) is widely regarded as a crucial part in next-generation energy storage devices such as lithium metal rechargeable batteries (LMRBs). However, uncontrolled dendrite growth can result in infinite volume expansion, sharp capacity degradation, and dangerous short circuit, restricting the application of LMRBs. The non-uniform lithium ion (Li^+) flow on the surface of the negatrode and the non-uniform distribution of electrons on the surface of the conventional current collector (e.g., Cu) are two key factors that lead to the non-uniformity of lithium (Li) deposition. Thus, this thesis provides new strategies based on the above two crucial factors to alleviate Li dendrites' formation. The work is summarised below.

(1) The surface of the LM is frequently observed to exhibit a non-uniform distribution of Li^+ flux in LMRBs. Although nitrogen-containing (N-containing) functional groups in carbon materials are reported to be effective in homogenizing the Li^+ flux, the effective interaction distance between Li^+ and N-containing groups is relatively small (down to the nanometre scale) according to the Debye length law. Thus, it is necessary to carefully design the microstructure of N-containing carbon materials to make the most of their roles in regulating the Li^+ flux. In Chapter 3, porous carbon nitride microspheres (PCNMs) with abundant nanopores have been synthesised and utilised to

fabricate a uniform lithiophilic coating layer having pores of both the nano- and micrometre scales on the Cu/Li foil. Physically, the three-dimensional (3D) porous framework is favourable for accommodating volume expansion and guiding Li growth. Chemically, this coating layer can render a suitable interaction distance to effectively homogenise Li^+ flux and contribute to establishing a robust and stable solid electrolyte interphase (SEI) layer with Li-F, Li-N, and Li-O-rich contents based on the Debye length law. Such a physical and chemical synergistic regulation strategy using PCNMs can lead to dendrite-free Li plating, resulting in a low nucleation overpotential and stable Li plating/stripping performance in both Li||Cu and Li||Li symmetric cells. Meanwhile, a full cell using the PCNM-coated Li delivered high capacity retention of ~80% after 200 cycles at 1 C and achieved remarkable rate capability. The high-areal-capacity pouch cell retained ~73% of the initial capacity after 150 cycles at 0.2 C.

(2) Although the PCNMs with abundant nanopores can homogenise the Li^+ flow effectively, it is still difficult to avoid the direct contact between Li and electrolyte during the cycling. Therefore, Chapter 4 reports a method in which a Li-F-rich layer was built in advance on the surface of the Li foil@PCNM electrode as an artificial SEI to reduce the direct contact with the electrolyte. Dimethylacetamide (DMAC) was used as a solvent to promote the self-driven chemical reaction between polyvinylidene fluoride (PVDF) and Li. This facilitated reaction may be attributed to the distinctive solvation structure formed by DMAC with PVDF and moderate structural stability toward LM. The corrosion of Li by different solvents was tested, and X-ray photoelectron spectroscopy (XPS) was applied on the surface of LM treated with different solvents to analyse the effect of solvents on the surface composition of Li. In addition, the effectiveness of the coating material in achieving dendrite-free Li deposits and suppressing the volume expansion of LMRBs (*in-situ* swelling testing) was investigated. Finally, excellent electrochemical performances of symmetric cells and full cells using modified Li were achieved.

(3) In Chapter 3 and Chapter 4, LMRBs, where pre-placement of LMNE as the main Li resource delivers reversible electrochemical plating/stripping, are promising electrochemical energy storage devices. However, the pre-placement of LMNE will hurt the specific energy of the battery and scientific evaluation of materials, and result in concerns regarding manufacturing costs and safety. The issues mentioned above can be avoided in lithium metal rechargeable batteries with a lithium-metal-free negatrod (LMFRBs). Nevertheless, uncontrolled formation of polymorphous Li deposits, e.g., whiskers, mosses, or dendrites in LMFRBs may result partly from non-uniform interfacial current distribution and internal stress release in the upward direction above the surface of a conventional current collector (e.g., Cu foil). If it occurs in a lithium-metal-free negatrod, rapid performance degradation or serious safety problems may be anticipated. The 3D carbon nanotubes (CNTs) skeleton has been proven to effectively reduce the current density on individual CNTs and eliminate the internal accumulation of stress. However, remarkable electrolyte decomposition, inherent Li source consumption due to repeated SEI formation, and Li^+ intercalation in CNTs limit the application of the 3D CNTs skeleton. Thus, it is necessary to avoid the side effects of the 3D CNTs skeleton and retain uniform interfacial current distribution and stress mitigation. In Chapter 5, the CNTs network with a soft functional polymer PVDF is reported to form a relatively dense coating layer on the Cu foil. This is expected to shield the contact between the internal surface of the 3D CNTs and the electrolyte. Simultaneously, the Li-F-rich SEI resulting from the partial reduction of PVDF by the deposited Li and the soft nature of the coating layer release the accumulated internal stress in the parallel direction to the current collector surface. As a result, Li deposition without mosses and whiskers has been achieved, leading to improve reversibility of Li deposition and dissolution and stability of the cycling performance of LMFRBs.

(4) Although CNT/PVDF composite coating layer on Cu foil can achieve dendrite-free

Li deposition, the entire composite current collector is still physically heavy. In addition, Cu is still chemically inappropriate for LMFRBs. Physically light carbon-based current collectors (CBCCs) may offer sufficiently high conductivity and a strong resistance toward corrosion by oxygen or electrolyte. They can also be engineered to possess suitable macro-, micro- and nanostructures that can assist the more uniform current distribution and hence replace the Cu foil as a preferable deposition substrate. However, there are potential limitations in the application of CBCCs in LMFRBs. For example, the large surface area of CBCC (e.g., CNTs) can induce higher consumption of the limited Li source (e.g., SEI). Also, lithiation or electrolyte penetration may lead to mechanical strength reduction. It is anticipated that fragile SEI may result from the lithiophobicity of CBCCs. Last but not least, welding between carbon and metal can be problematic. In Chapter 6, a novel method is described for the preparation of free-standing graphene/PVDF composite current collectors via the coating and etching process. Highly conductive graphene sheets are tightly stacked to reduce the electrochemically reactive surface area and suppress the lithiation behaviour. PVDF not only facilitates the formation of the sturdy free-standing film but also hinders the Li⁺ insertion and electrolyte penetration to reinforce the mechanical strength of the CBCCs. Meanwhile, the Li-F-rich SEI derived from the partial reduction of PVDF by the deposited Li can considerably reduce the formation of fragile SEI. Also, the newly-formed SEI can further minimise the electrolyte decomposition owing to PVDF's low Fermi level suppressing electron transfer to the electrolyte. It is also reported that Cu tabs can be bonded firmly to the CBCCs with acceptable resistance via etching, promising practical application. Therefore, basic requirements of the current collector, such as high conductivity, sufficient mechanical strength, viable tab welding, and improved Li deposition and dissolution behaviour in half and full cells have been satisfactorily achieved using this free-standing CBCC. The assembled pouch cell has achieved a remarkable 80% capacity retention after ~50 cycles at 0.1 C.

Key words: Lithium Metal Negative Electrode, Porous Carbon Nitride Microspheres, Carbon Nanotubes, Polyvinylidene Fluoride, Graphene.

Acknowledgements

After about three years of academic training, I have gained a lot not only in research skills but also in confidence and critical thinking. On this occasion, I would like to take this opportunity to appreciate many people who offered tremendous help in my research, life, and study.

I would like to express my sincere thanks to my main supervisor-Prof. Zhaoping Liu who provided the perfect experimental conditions and academic/life guidance in CNITECH. I was deeply touched by Prof. Zhaoping Liu's passion for pursuing academics and entrepreneurship. Then I would like to express my deep thanks to my second supervisor-Prof. Xufeng Zhou, who was vital to my research progress during my Ph.D. at CNITECH. He provided a free academic environment to allow me to explore unknown areas independently. His critical comments/rigorous logical thinking have greatly enlightened me in advancing my research and mode of thinking. I would like to thank my main supervisor- Associate Professor Di Hu, who provided lots of suggestions for my papers, thesis, and viva and supported huge help in my CSC scholarship application at UNNC. I would like to appreciate the assistance provided by my lead supervisor-Prof. George Zheng Chen, who supported lots of academic help in advancing my research at UNUK or CNITECH. He guided me to look at scientific issues from a higher perspective and often encouraged me to focus on the basic knowledge of electrochemistry. Finally, I also want to thank my internal assessor-Associate Professor Binjie Hu, who provided valuable suggestions in my papers and presentations.

I greatly thank the discussion, guidance, and companionship supported by my research mates and scholars such as Dr. Wei Deng, Dr. Xueyan Xu, Ning Dong, Zhepu Shi, Fei

Zhao, Zibo Zhang, Wen Chen, Xue Yin, Bangyi He, Zhiyuan Hu, Jianhua Liang, Sasa Zhang, Shengjie Xia, Zhenyuan Liu, Daojie Dong, Yanan Yu, Shuhui Wang, Yimei Li, Jin Wang, Yong Wu, Danfeng Ying, Aihua Cao, et al. in CNITECH and Dr. Li Guan, Peiying Fan, Yuhan Zhang, Dr. Ming Li and Dr. Han Wang et al. in UNUK as well as Mingchan Ma in UNNC. Without your contributions to my research, my academic progress is unlikely to go smoothly.

I also thank the Doctoral Training Partnership Programme from the University of Nottingham Ningbo, China and Ningbo Institute of Materials Technology & Engineering, Chinese Academy of Sciences. I appreciate the Chinese Scholarship Fund provided by the China scholarship council to study in the U. K.

Last, I will thank my beloved parents, relatives, and friends for your intimate companionship and huge support. I will show the thanks to myself. Thanks to my persistence and hard work during the Ph.D. period, I can smoothly finish my research.

Content

Abstract	I
Acknowledgements	VI
List of Tables	XII
List of Figures	XIII
Abbreviations	XXX
Dissemination Section	XXXIII
Chapter1 Introduction	1
1.1. Research background	1
1.2. Brief introduction of Li-metal-based batteries	7
1.2.1. Advantages of Li metal.....	7
1.2.2. Different Li-metal-based batteries.....	9
1.3. Problems of Li metal negative electrodes	13
1.3.1. Li dendrite growth.....	13
1.3.2. High activity of metallic Li.....	20
1.3.3. Volume expansion of Li metal negative electrodes.....	20
1.3.4. Practical challenges of Li metal negative electrodes.....	22
1.4. Factors affecting the interface stability of Li metal negative electrodes	23
1.4.1. Current density.....	23
1.4.2. Distribution of Li ⁺ flux.....	25
1.4.3. SEI properties.....	27
1.4.4. Pressure.....	31
1.4.5. Working temperature.....	31
1.4.6. Positive electrodes.....	33
1.5. Current modification strategies on Li metal negative electrodes	33
1.5.1. 3D current collectors.....	33

1.5.2. Lithiophilic decoration.....	35
1.5.3. Electrolyte design	41
1.5.4. Artificial SEI.....	47
1.5.5. Others.....	52
1.6. Thesis structure.....	54
Chapter2 Methodology and Techniques.....	59
2.1. Materials preparation.....	59
2.1.1. Experimental reagents and consumables	59
2.1.2. Electrodes preparation	60
2.2. Electrochemical Measurements	61
2.3. Material structure characterisations.....	61
2.4. Ionic conductivity tests	62
2.5. <i>In-situ</i> swelling tests during charging/discharging	63
2.6. Simulation methods	64
Chapter3 Porous Carbon Nitride Microsphere Layer with Nano- Channel-Based Physical and Chemical Synergic Regulation for Dendrite-Free Lithium Plating.....	65
3.1. Introduction.....	65
3.2. Experimental section	68
3.2.1. Materials preparation	68
3.2.2. Electrodes preparation	69
3.2.3. Electrochemical Measurements	69
3.3. Results and discussion	72
3.3.1. Materials characterisations	72
3.3.2. Morphology of Li plating	81
3.3.3. SEI characterisations.....	86
3.3.4. Electrochemical performances of half cells.....	89

3.3.5. Li ions regulation by g-C ₃ N ₄ materials.....	97
3.4.6. Electrochemical performances of full cells.....	101
3.4. Conclusions.....	104
Chapter4 Solvent Modification of Porous-Carbon-Nitride- Microsphere-based Coating Slurry on Lithium Metal Negative Electrode for Improved Lithium Deposition/Dissolution.....	105
4.1. Introduction.....	105
4.2. Experimental section	108
4.2.1. Electrodes preparation	108
4.2.2. Electrochemical Measurements	108
4.3. Results and discussion	111
4.3.1. Materials characterisations.....	111
4.3.2. Morphology of Li plating.....	117
4.3.3. Volume expansion tests	118
4.3.4. Electrochemical performances of half cells.....	119
4.3.5. Electrochemical performances of full cells.....	124
4.4. Conclusions.....	128
Chapter5 CNT/PVDF Composite Coating Layer on Cu with a Synergy of Uniform Current Distribution and Stress Releasing for Improving Reversible Li Plating/Stripping.....	129
5.1. Introduction.....	129
5.2. Experimental section	134
5.2.1. Electrodes preparation	134
5.2.2. Electrochemical Measurements	135
5.3. Results and discussion	137
5.3.1. Materials characterisations.....	137
5.3.2. Initial SEI characterisations	145

5.3.3. Morphology of Li plating	149
5.3.4. Half-cell electrochemical performances of CNT-based electrodes	159
5.3.5. Full-cell electrochemical performances of CNT-based electrodes	169
5.4. Conclusions.....	171
Chapter6 Free-standing and Low-Density Composite of Graphene and PVDF as Promoting Current Collector for Reversible Lithium Deposition	172
6.1. Introduction.....	172
6.2. Experimental section	176
6.2.1. Electrodes preparation	176
6.2.2. Electrochemical Measurements	177
6.3. Results and discussion	180
6.3.1. Physical characterisations of Graphene-based current collectors.....	180
6.3.2. The adaptability of Graphene-based electrodes to cell operating conditions	188
6.3.3. SEI and Li deposit characterisations.....	193
6.3.4. Electrochemical performances of Graphene-based electrodes of half and full cells.....	202
6.3.5. Failure analysis of Graphene-based electrodes.....	215
6.4. Conclusions.....	222
Chapter7 Conclusions and Prospect.....	223
7.1. Conclusions.....	223
7.2. Prospect.....	225
Reference	228
Biography	247

List of Tables

Table 1.1. Lithiophilic difference between metal oxide/metal and Lewis-base site. ..	39
Table 2.1. Experimental reagents and consumables.....	59
Table 3.1. Atomic concentration and mass concentration of C and N elements in PCNM determined by TEM and XPS.	73
Table 3.2. Specific surface area and pore volume of BCN, SCN, and PCNM.	76
Table 3.3. Fitting resistance data of the galvanostatic plating/stripping in symmetrical cells using Li@PCNM or bare Li foil with an areal capacity of 1.0 mAh cm ⁻² at 2.0 mA cm ⁻²	96
Table 3.4-1. Fitting resistance data of the BCN/SCN/PCNM&LiTFSI@Cu.....	97
Table 3.4-2. Fitting resistance data of the BCN/SCN/PCNM&LiTFSI@Cu.....	97
Table 4.1. Fitting resistance data of the galvanostatic plating/stripping in symmetrical cells using bare Li foil or Li@PCNM-DMAC with an areal capacity of 1.0 mAh cm ⁻² at 3.0 mA cm ⁻²	122
Table 5.1. Specific surface area, pore volume, and pore size of CNT-X/1 (X = 0, 0.5, 2.5 and 5) and PVDF.....	139
Table 5.2. Fitting resistance data of fresh CNT-based electrodes with different PVDF contents (CNT-X/1 (X = 0, 0.5, 2.5, 5, and 7.5)) in Li Cu coin half cell.	154
Table 5.3. Fitting resistance data of galvanostatic plating/stripping in symmetrical cells using CNT-5/1 or Cu foil with an areal capacity of 1.0 mAh cm ⁻² at 1 mA cm ⁻²	165
Table 6.1. Pouch cell details assembled with Gra-5/1 and high areal capacity LR-114 positrodes (~ 6 mAh cm ⁻²).....	214
Table 6.2. Fitting resistance data of the galvanostatic plating/stripping in symmetrical cells using Gra-5/1 or Cu foil with an areal capacity of 1.0 mAh cm ⁻² at 2 mA cm ⁻²	218

List of Figures

Figure 1.1. Schematic diagram of energy conversion, storage, and utilisation in various forms. ¹⁷	2
Figure 1.2. Comparison of different types of rechargeable batteries in terms of energy density and specific energy. ¹⁸	3
Figure 1.3. The history of Li batteries. ²⁵	5
Figure 1.4. Potential versus capacity in terms of the positive and negative materials for the next generation of rechargeable Li batteries. ¹⁸	6
Figure 1.5. Schematic of a traditional LIB. ²⁸	7
Figure 1.6. Comparison of the standard reduction potential versus the charge density or specific charge capacity for different metal and graphite negative electrodes in the LIB. ³¹ ..	8
Figure 1.7. Comparison of the practical specific energy (pink) and energy densities (blue) regarding petrol (gasoline) and Li-based rechargeable batteries, including LIBs, conventional LMRBs, Li-S, and Li-air batteries. ³⁵	9
Figure 1.8. Schematic illustration of Li-O ₂ cells operating in non-aqueous and aqueous electrolytes. ⁴¹	10
Figure 1.9. Schematic illustration of Li-S cells operating in organic electrolyte. ⁴¹ ...	11
Figure 1.10. The proposed device structure of LM-based supercapattery. The left is LM and the right is activated carbon. ⁴⁴	11
Figure 1.11. Schematic illustration of the Li stripping/plating process. ³⁵	13
Figure 1.12. Schematic diagram of metal in thermal evaporation deposition and electrochemical deposition. ⁵⁹	15
Figure 1.13. Five regimes of behaviour and growth pattern during the initial stages of heterogeneous nucleation. ⁶³	16
Figure 1.14. (a) Scheme of a battery and (b) profile of ion concentrations and electrostatic potential, which result from the numerical simulation in the hypothetical	

case of uniform deposition. C_c : concentration of cations; C_a : concentration of anions; C_0 : initial concentration; V : potential; V_0 : initial potential; L : cell distance. ⁶⁶	17
Figure 1.15. Stress model of Li deposition and dissolution ⁶⁸	19
Figure 1.16. Schematic illustration of volume expansion in the LMNE. ⁷⁵	21
Figure 1.17. Challenges that LMRBs face from lab research to industrial production. ⁷⁷	22
Figure 1.18. Schematic illustration of anions and Li^+ flow model (White balls are Li ions and blue balls are anions).	24
Figure 1.19. Non-uniform distribution of Li^+ flux in the horizontal or vertical direction to the current collector surface.	26
Figure 1.20. Schematic illustration of (a) SEI formation condition in a liquid electrolyte; ⁸⁶ (b) Mosaic SEI structure in the top view; ⁸⁷ (c) Dual-layer SEI structure in the cross-section view. ³⁴	28
Figure 1.21. Li deposition/dissolution behaviour difference between mosaic and layered SEI. ⁹²	30
Figure 1.22. Schematic diagram of deposition morphology and SEI structure of LM at different temperatures. ¹⁰⁰	32
Figure 1.23. (a) Schematic demonstration of the fabrication of 3D Li-F-Li-Cu 3D composite LMNE. ¹¹⁶ (b) Schematic demonstration of the Li plating and stripping process on carbon nanotube sponges. ¹¹⁷	34
Figure 1.24. (a) Nucleation overpotential during Li deposition on various substrates with certain solubility and negligible solubility. ⁶⁵ (b) Schematic illustration of Li plating/stripping on Cu@Cu foam and Au/Cu@Cu foam. ¹¹⁹ (c) Fabrication of carbon fibre-based composite Li negatrode. ¹²⁰	36
Figure 1.25. Schematic illustration of Lewis-base site and Li^+ interaction.	38
Figure 1.26. Schematic illustration of the lithiophilic difference in metal oxide/metal, e.g., ZnO/Zn, and Lewis-base site, e.g., R-N.	39
Figure 1.27. Graphitic carbon nitride with two different structures of (a) s-triazine and	

(b) tri-s-triazine. ¹³⁹ (c) Schematic illustration of Li deposition on the 3D g-C ₃ N ₄ /G/g-C ₃ N ₄ electrode. ¹⁴⁰	40
Figure 1.28. (a) Model of SEI generated from the FEC-containing electrolyte; (b) schematic of diffusion fields at deposited Li from FEC-containing electrolyte. ⁷³	43
Figure 1.29. (a) Different Li ⁺ solvate species in dilute and concentrated electrolytes. Schematic demonstration of the electrolyte reduction mechanism at the electrode/electrolyte interface in (b) dilute and (c) concentrated electrolytes. ¹⁴⁸	44
Figure 1.30. Exhibition of Li deposition process based on the self-healing electrostatic shield mechanism. ⁷²	46
Figure 1.31. Examples of literature on inorganic protective layers. (a) Schematic illustrations of the function of the unprotected and alloy/LiCl-protected Li foil. ¹⁶⁹ (b) Schematic diagrams of the Li deposit on the bare Cu foil and the modified Cu foil with a hollow carbon nanosphere layer. ¹⁷⁰ (c) SEM characterisation of electrochemically plated Li. Schematics and SEM characterisation of electrochemical Li deposit on bare Cu, h-BN/Cu, LiF/Cu, and LiF/h-BN/Cu. ¹⁷¹ (d) Schematic illustrations of LM growth on and underneath the unprotected and lithiophilic protective (C ₃ N ₄) Cu foil. ¹⁷²	49
Figure 1.32. (a) Schematic demonstration of layer-by-layer Li deposition and preferential diffusion pathways for Li ⁺ . ¹⁷⁴ (b) Schematic diagrams of the Li deposit on the bare Cu and Cu foil coated with PDMS film. ¹⁷⁶ (c) Schematic diagrams illustrating the integration of dynamic flowability, fast single-ion conduction, and electrolyte-blocking property into a single matrix, the dynamic single-ion-conductive network. ¹⁷⁷	51
Figure 1.33. (a) Schematic illustration of Li nucleation and growth mechanism under high and low temperatures. ¹⁸¹ (b) SEM images of Li microstructures generated under different external applied pressures. ¹⁸² (c) SEM images of electrodeposited Li under direct current and pulse plating conditions. ¹⁸³ (d) Schematic illustration showing the effects of magnetic field on Li ⁺ deposition process. ¹⁸⁴	54
Figure 2.1. Diagram showing electrode preparation process.....	60

Figure 2.2. Diagram showing components of coin cell and pouch cell.	61
Figure 2.3. <i>In-situ</i> swelling test cell.	63
Figure 3.1. (a) SEM image and (b) TEM image of PCNM. (c) SEM image and (d) TEM image of SCN. (e) SEM image and (f) TEM image of BCN (The blue dashed circle is the pores of PCNM).	72
Figure 3.2. (a) C 1s and (b) N 1s XPS spectra of PCNM.	73
Figure 3.3. (a) X-ray diffraction patterns of BCN (light blue short dashed dot), SCN (dark blue short dot), and PCNM (red line) and (b) SAED pattern of PCNM (The red dashed circle is the diffraction ring corresponding to (002) face of PCNMs; 5 1/nm is the reciprocal space scale, and it represents that the length of the scale bar is 1/5 nm).	74
Figure 3.4. FT-IR spectra of BCN (light blue short dashed dot), SCN (dark blue short dot), and PCNM (red line).	75
Figure 3.5. (a) Nitrogen adsorption and desorption isotherms and (b) the pore size distribution data of BCN (light blue line), SCN (dark blue line), and PCNM (red line).	76
Figure 3.6. (a) Top-view and (b) cross-section view SEM images of Cu@PCNM. The inset of (a) shows the optical photograph of Cu@PCNM. (c) Top-view and (d) cross-section view SEM images of Cu@SCN. The inset of (c) is the optical photograph of Cu@SCN. (e) Top-view and (f) cross-section view SEM images of Cu@BCN. The inset of (e) is the optical photograph of Cu@BCN (The red dashed circle represents the pores of Cu@BCN).	78
Figure 3.7. (a) Top-view and (b) cross-section view SEM images of Cu@PCNM. EDS mapping of the cross-section of the PCNM coating layer on Cu for (c) SEM image, (d) F, (e) C, and (f) N element.	79
Figure 3.8. Contact angles of electrolyte toward (a) bare Cu foil and (b) Cu@PCNM. Contact angles of water toward (c) bare Cu foil and (d) Cu@PCNM.	80
Figure 3.9. Diagrams showing the morphology of electrodeposited Li on (a) bare Cu	

foil, (b) Cu@SCN, (c) Cu@BCN and (d), and (e) Li plating process on Cu@PCNM; (f) Schematic diagram of PCNMs in regulating Li ion flux (The red dashed line is the interaction force between Li ion and electric field/PCNM and the blue solid line is real Li ion movement route).81

Figure 3.10. (a) SEM image of bare Cu foil. (b) Cross-section view and (c) top-view SEM images of Cu foil after plating Li with 5.0 mAh cm⁻². (d) SEM image of Cu@SCN. (e) Cross-section view and (f) top-view SEM images of Cu@SCN after plating Li with 5.0 mAh cm⁻². (g) SEM image of Cu@BCN. (h) Cross-section view and (i) top-view SEM images of Cu@BCN after plating Li with 5.0 mAh cm⁻². (j) SEM image of Cu@PCNM. (k) Cross-section view and (l) top-view SEM images of Cu@PCNM after plating Li with 5.0 mAh cm⁻². The regions marked with light blue, light red, and light yellow colours correspond with plated Li, Cu foil, and g-C₃N₄ coatings, respectively. The current density is 1 mA cm⁻².82

Figure 3.11. Morphology evolution of the Cu@PCNM electrode during Li plating with capacities from 0.5 to 15 mAh cm⁻². (a) Discharge curve of the Cu@PCNM electrode. Cross-section view SEM images of the Cu@PCNM electrode after plating with (b) 0.5 mAh cm⁻², (c) 1 mAh cm⁻², (d) 2.5 mAh cm⁻², (e) 5 mAh cm⁻², (f) 10 mAh cm⁻² and (g) 15 mAh cm⁻² of Li. The current density is 1 mA cm⁻².84

Figure 3.12. Comparison of morphology evolution during Li plating/stripping on (a-d) Cu@PCNM and (e-h) bare Cu foil with different deposition and stripping capacities. (a) and (e) are top-view SEM images, and others are cross-section view SEM images.85

Figure 3.13. Cross-sectional FIB-SEM images of (a) Cu@PCNM and (b) bare Cu with plating 15 mAh cm⁻² at 1 mA cm⁻². EDS mapping regarding the local FIB-SEM image of Li@Cu@PCNM for (c) SEM image, (d) N, and (e) C element distribution. Light green districts in (b) represent the thick SEI layer.86

Figure 3.14. XPS Full spectra of the surface of deposited LM on (a) bare Cu foil and (b) Cu@PCNM. (c, d) F 1s, (e, f) N 1s, (g, h) O 1s and (i, j) C 1s and (k, l) S 2p XPS

spectra of the surface of plated Li on Cu foil coated with (d, f, h, j and l) and without PCNM (c, e, g, i and k).87

Figure 3.15. (a) CE Comparison of Li plating on/stripping on bare Cu foil electrode and Cu foil coated with SCN, BCN, and PCNM with an areal capacity of 1.0 mAh cm^{-2} at 2.0 mA cm^{-2} . (b) Comparison of CE of Li plating on/stripping over Cu foil coated with and without PCNM with 1.0 mAh cm^{-2} at 1.0 mA cm^{-2} and 0.5 mA cm^{-2} , and with 5 mAh cm^{-2} and 10 mAh cm^{-2} at 0.5 mA cm^{-2}89

Figure 3.16. Comparison of (a) potential profiles, (b) magnified potential profiles within the plating time range of 0-2 h, and (c) nucleation overpotential of Li plating on/stripping from bare Cu foil electrode and Cu foil coated with SCN, BCN, and PCNM with an areal capacity of 1.0 mAh cm^{-2} at 2.0 mA cm^{-2} . (d) Comparison of Li plating/stripping potential profiles on Cu foil coated with and without PCNM at different current densities ranging from 0.5 to 3 mA cm^{-2} with an areal capacity of 1 mAh cm^{-2}90

Figure 3.17. The EIS of (a) bare Cu foil electrode and (b) Cu@PCNM before cycling and after 50 and 150 cycles.93

Figure 3.18. (a, c, e, and g) Top view and (b, d, f, h) cross-section view SEM images of Cu@PCNM and bare Cu after (a-d) 30 cycles and (e-h) 60 cycles with an areal capacity of 2 mAh cm^{-2} at 1.0 mA cm^{-2} . The regions marked with light green colour correspond with PCNM coatings and “dead Li” respectively.93

Figure 3.19. The galvanostatic plating/stripping profiles of Li||Li symmetrical cells with an areal capacity of (a) 1.0 mAh cm^{-2} at 2.0 mA cm^{-2} , (b) 1.0 mAh cm^{-2} at 4.0 mA cm^{-2} and (c) 3.0 mAh cm^{-2} at 1.0 mA cm^{-2} using Li foil@PCNM, and bare Li foil electrodes.94

Figure 3.20. The EIS of the bare Li foil and Li foil@PCNM (a) before cycling and after (b) 50 and (c) 150 cycles with an areal capacity of 1.0 mAh cm^{-2} at 2.0 mA cm^{-2} . (d) applied fitting resistance model: R1: R_0 (Ohmic resistance); R2: R_{SEI} (Migration resistance of Li^+ through the SEI); R3: R_{ct} (Charge transfer resistance); Wo1: Warburg

(Li ⁺ diffusion resistance); CPE1/CPE2: Constant phase element (Conventional double-layer and passivation film capacitance).....	96
Figure 3.21. (a) Temperature-dependent ionic conductivity plots and (b) corresponding activation energy of Cu@SCN, Cu@BCN, and Cu@PCNM.	97
Figure 3.22. <i>In-situ</i> Raman spectra of (a) bare Cu foil and (b) Cu@PCNM; (c) Summary of intensity evolution of Raman peaks of electrolytes in the cells using Cu foil coated with and without PCNM in charging process at 1mA cm ⁻²	99
Figure 3.23. Performances of Li foil@PCNM in coin full cells and pouch cells. (a) Rate capability and (d) cycling performance of Li foil@PCNM and bare Li foil paired with high areal capacity LFP positrodes (~2mAh cm ⁻²). Voltage profiles of (b) Li foil@PCNM LFP full cell and (c) bare Li foil LFP full cell from 0.2C to 2C. Voltage profiles of (e) Li foil@PCNM LFP full cell and (f) bare Li foil LFP full cell at the 5 th , the 55 th , and the 105 th cycle. (g) Cycling performance and (h) <i>in-situ</i> discharge internal resistance profiles of Li foil@PCNM and bare Li foil paired with high areal capacity NCM 811 positrodes (~3.75 mAh/cm ²). (i) Voltage profiles of Li foil@PCNM NCM 811 pouch cell and bare Li foil NCM 811 pouch cells from the 5 th to the 125 th cycle.	101
Figure 4.1. Diagrams showing the mechanism of electrodeposited Li on Li@PCNM-DMAC and self-driven chemical reaction between Li and PVDF.	108
Figure 4.2. Digital photographs showing the time-dependent corrosion behaviour between LM and DMF, NMP, and DMAC.	111
Figure 4.3. (a) Uniform and stable PVDF solution and (b) coating slurry (PVDF+PCNMs) using DMF, NMP, and DMAC, respectively.	112
Figure 4.4. (a) F 1s XPS spectra and (b) optical photos of Li foil coated with PVDF solution using NMP as a solvent. (c) F 1s XPS spectra and (d) optical photos of Li foil coated with PVDF solution using DMAC as a solvent.	112
Figure 4.5. Comparison of optical photos of Li@PCNM using (a) DMF, (b) NMP, and (c) DMAC as solvents.....	113

Figure 4.6. (a) The top-view and (b) cross-section view SEM images of Li@PCNM-DMAC. (c) The top-view and (d) cross-section view high-magnification SEM images of Li@PCNM-DMAC. The inset of (d) is an SEM image of the bare Li. 116

Figure 4.7. (a) Cross-section view and (b) top-view SEM images of bare Li foil after plating with 3.0 mAh cm⁻² of Li. (c) Cross-section view and (d) top-view SEM images of Li@PCNM-DMAC after plating with 3.0 mAh cm⁻² of Li. The current density is 0.5 mA cm⁻²..... 117

Figure 4.8. *In-situ* swelling dimension of (a) bare-Li-foil-based and (b) Li@PCNM-DMAC-based cells paired with high areal capacity NCM811 positrodes (~4 mAh cm⁻²) during charging and discharging. (c) Comparison of the maximum swelling dimension of (a) bare-Li-foil-based and (b) Li@PCNM-DMAC-based full cells within 4 cycles. 118

Figure 4.9. (a) The galvanostatic plating/stripping profiles of Li||Li symmetrical cells with an areal capacity of 1.0 mAh cm⁻² at 1.0 mA cm⁻² using Li@PCNM-NMP, Li@PCNM-DMF, Li@PCNM-DMAC, and bare Li foil. Magnified potential profiles within the plating/stripping time range of (b) 190-200h and (c) 360-370h. 119

Figure 4.10. The galvanostatic plating/stripping profiles of Li||Li symmetrical cells with an areal capacity of 1.0 mAh cm⁻² at (a) 2.0 mA cm⁻² and (b) 3.0 mA cm⁻² using Li@PCNM-DMAC and bare Li foil..... 121

Figure 4.11. Comparison of nucleation overpotential of Li plating on bare Li foil and Li@PCNM-DMAC with an areal capacity of 1.0 mAh cm⁻² at 0.5 mA cm⁻². 121

Figure 4.12. The EIS of the bare (a) Li foil and (b) Li@PCNM-DMAC after 50 cycles, 100 cycles, and 150 cycles with an areal capacity of 1.0 mAh cm⁻² at 3.0 mA cm⁻². (c) Applied fitting resistance model: R1: R₀ (Ohmic resistance); R2: R_{SEI} (Migration resistance of Li⁺ through the SEI); R3: R_{ct} (Charge transfer resistance); Wo1: Warburg (Li⁺ diffusion resistance); CPE1/CPE2: Constant phase element (Conventional double-layer and passivation film capacitance). 122

Figure 4.13. (a) Long-term cycling performance of Li@PCNM-NMP, Li@PCNM-

DMAC, and bare Li foil paired with LFP positrodes ($\sim 1.7 \text{mAh cm}^{-2}$) in coin full cell. Voltage profiles of (b) Li@PCNM-DMAC||LFP and (c) bare Li||LFP full cell at the 150th, 300th, 450th and 600th cycle. (d) The rate capability of Li@PCNM-DMAC and bare Li foil paired with LFP positrodes ($\sim 2 \text{mAh cm}^{-2}$). Voltage profiles of (e) Li@PCNM-DMAC||LFP and (f) bare Li||LFP full cell from 0.1C to 3C. 124

Figure 4.14. (a) Long-term cycling performance of Li@PCNM-DMAC and bare Li foil electrodes paired with high areal capacity NCM 811 positrodes ($\sim 4 \text{mAh cm}^{-2}$) in coin full cells. Voltage profiles of (b) Li@PCNM-DMAC||NCM 811 and (c) bare Li||NCM 811 full cell at the 20th, 40th, 60th, and 80th cycle. 126

Figure 4.15. (a) Long-term cycling performance and (b) *in-situ* discharge internal resistance profiles of Li@PCNM-DMAC and bare Li foil electrodes paired with high areal capacity NCM 811 positrodes ($\sim 4 \text{mAh cm}^{-2}$) in pouch cell. Voltage profiles of (c) bare Li foil||NCM 811 and (d) Li@PCNM-DMAC||NCM 811 pouch cells from the 4th to the 275th cycle. 127

Figure 5.1. Schematic diagrams showing the morphology of electrodeposited Li on bare Cu foil and CNT-5/1. Red area: high current strength; yellow area: low current strength; orange area: medium current strength. 134

Figure 5.2. (a) High-magnification TEM and (b) selected area electron diffraction (SAED) pattern of CNTs. (The yellow dashed circle is the diffraction ring corresponding to (002) face of multi-wall CNTs; 10 1/nm is the reciprocal space scale, and it represents that the length of the scale bar is $1/10 \text{ nm}$). 137

Figure 5.3. (a) X-ray diffraction pattern and (b) Raman spectrum of CNTs. 137

Figure 5.4. (a) Top-view and (b) cross-section view SEM images of CNT-5/1. (c) High-magnification SEM image of the cross-section view of CNT-5/1. (d) Top-view SEM image of CNT-0/1. 138

Figure 5.5. (a) Nitrogen adsorption and desorption isotherms and (b) the pore size distribution data of CNT-0/1 (yellow line) and CNT-5/1 (red line). 139

Figure 5.6. XPS result of CNT-5/1. (a) full spectrum, (b) C 1s, (c) F 1s and (d) O 1s.

.....	140
Figure 5.7. EDS mapping for (a) SEM image and (b) C, (c) F, and (d) O elements on the surface of CNT-5/1.....	141
Figure 5.8. Surficial morphology, surface current distribution, and DMT modulus over (a), (b), and (c) bare Cu, (d), (e) and (f) CNT-0/1, and (g), (h) and (i) CNT-5/1 through AFM characterisation.....	142
Figure 5.9. (a) Surface current distribution and (b) morphology of the bare Cu after being washed by HCl.	142
Figure 5.10. Contact angles of Li toward (a) bare Cu foil, (b) CNT-0/1, and (c) CNT-5/1 at 350°C.....	144
Figure 5.11. EIS evolution with discharging from 2V to -0.25V at 0.1 mV·s ⁻¹ over (a) bare Cu, (b) CNT-0/1, and (c) CNT-5/1.....	146
Figure 5.12. XPS spectra of the F 1s of plated Li (1 mAh cm ⁻² at 0.5 mA cm ⁻²) on (a) bare Cu, (b) CNT-0/1, and (c) CNT-5/1.....	147
Figure 5.13. The EIS of (a) fresh bare Cu foil and (b) fresh CNT-5/1 under different temperatures ranging from -10°C to 40°C.....	148
Figure 5.14. Li deposition morphology with capacities from 0.2 to 3 mAh cm ⁻² on the bare Cu, CNT-0/1, and CNT-5/1. Top-view SEM images of the bare Cu, CNT-0/1, and CNT-5/1 electrode after plating with (a), (d), and (g) 0.2 mAh cm ⁻² , (b), (e), and (h) 1 mAh cm ⁻² and (c), (f) and (i) 3 mAh cm ⁻² of Li (The blue dashed line represents the boundary between the spliced LM particles). The current density is 0.5 mA cm ⁻² . ..	149
Figure 5.15. Top-view SEM images of electrodeposited Li with 3.0 mAh cm ⁻² at 0.5 mA cm ⁻² on (a) Cu and (b) CNT-5/1.....	150
Figure 5.16. Cross-section view (a) bare Cu with related EDS mapping of (b) F, (c) C, and (d) Cu, and cross-section view of (e) CNT-5/1 with related EDS mapping of (f) F, (g) C and (h) Cu after Li plating with an areal capacity of 3 mAh cm ⁻²	152
Figure 5.17. Top-view SEM images of fresh CNT-based electrodes with different PVDF contents (CNT-X/1 (X = 0, 0.5, 2.5, 5 and 7.5)) (upper), and Li plated electrodes	

with 1 mAh cm ⁻² at 0.5 mA cm ⁻² (down).....	153
Figure 5.18. (a) EIS of the fresh CNT-based electrodes added with different PVDF contents (CNT-X/1 (X = 0, 0.5, 2.5, 5, and 7.5)). (b) applied fitting resistance model: R1:R0 (Ohmic resistance); R2: R _{ct} (Charge transfer resistance); CPE1: Constant phase element (Conventional double-layer and passivation film capacitance); Wo1: Warburg (Li ⁺ diffusion resistance).....	154
Figure 5.19. t/t _{max} -I/I _(max) ² plots of the (a) fresh CNT-5/1 and (b) fresh bare Cu foil under different voltages (-0.2V, -0.3V, and -0.5V).	155
Figure 5.20. Lithiation capacity (>0V) of the CNT-X/1 (X = 0, 0.5, 2.5, 5, and 7.5) at (a) 0.5 mA cm ⁻² and (b) 2 mA cm ⁻²	156
Figure 5.21. The electrical resistance of CNT-X/1 (X = 0, 0.5, 2.5, 5, and 7.5).....	156
Figure 5.22. Optical photographs of Cu foil with half coated with CNT-5/1 (a) before and (b) after Li plating. SEM images of electroplated Li on (c) bare Cu and (d) CNT-5/1 coated Cu.	157
Figure 5.23. Top-view SEM images of fresh CNT-based electrodes added with (a) PEO, (b) PAN, and (c) PVDF. (d) comparison of CE of Li plating on/stripping from the above electrodes with a capacity of 1 mAh cm ⁻² at 2 mA cm ⁻²	158
Figure 5.24. Comparison of CE of Li plating on/stripping with a capacity of (a) 1 mAh cm ⁻² and (b) 3 mAh cm ⁻² at 0.5 mA cm ⁻² over bare Cu, CNT-0/1, and CNT-5/1. (c) CE of Li plating on/stripping from Cu coated with CNTs and PVDF with mass ratio (PVDF/CNTs) from 0 to 7.5 with a capacity of 1 mAh cm ⁻² at 2 mA cm ⁻²	159
Figure 5.25. Comparison of CE of Li plating on/stripping over bare Cu foil, CNT-0/1 and CNT-5/1 with 1.0 mAh cm ⁻² at (a) 1 mA cm ⁻² , (b) 2 mA cm ⁻² and (c) 3 mA cm ⁻²	160
Figure 5.26. (a) Top-view and (b) cross-sectional view SEM images of Cu coated with PVDF only (Cu@PVDF). (c) Top-view SEM image of Li plated Cu@PVDF with a capacity of 1 mAh cm ⁻² at 0.5 mA cm ⁻² . (d) EIS of the fresh Cu@PVDF electrode. (e) CE of Li plating on/stripping from bare Cu, Cu@PVDF, and CNT-5/1 with a capacity	

of 1.0 mAh cm ⁻² at 2.0 mA cm ⁻²	162
Figure 5.27. (a) Comparison of potential profiles of Li plating on/stripping from bare Cu, CNT-0/1, and CNT-5/1 with a capacity of 1 mAh cm ⁻² at (a) 0.5 mA cm ⁻² , (b) 1 mA cm ⁻² , (c) 2 mA cm ⁻² and (d) 3 mA cm ⁻²	163
Figure 5.28. Cycling performance of Li@Bare Cu and Li@CNT-5/1 at 1mA cm ⁻² with 1mAh cm ⁻² . Li is pre-deposited on bare Cu and CNT-5/1 with 5 mAh cm ⁻² to fabricate Li@Bare Cu and Li@CNT-5/1, respectively.	163
Figure 5.29. Potential profiles at the 4 th cycle of Li plating/stripping with an areal capacity of 1 mAh cm ⁻² at 2 mA cm ⁻² on (a) bare Cu, (b) CNT-0/1, and (c) CNT-5/1.	164
Figure 5.30. EIS of (a) bare Cu and (b) CNT-5/1 after 10, 30, and 50 cycles with an areal capacity of 1 mAh cm ⁻² at 1 mA cm ⁻² . (c) applied fitting resistance model: R1:R0 (Ohmic resistance); R2: R _{SEI} (Migration resistance of Li ⁺ through the SEI); R3: R _{ct} (Charge transfer resistance); CPE1/CPE2: Constant phase element (Conventional double-layer and passivation film capacitance).....	165
Figure 5.31. F 1s, C 1s, and O 1s XPS spectra of (a, b), (c, d), and (e, f) bare Cu and (g, h), (i, j), and (k, l) CNT-5/1 electrodes with 30 cycles of Li plating/stripping with a capacity of 1 mAh cm ⁻² at 1 mA cm ⁻² before (a, c, e, g, i, and k) and after the 30s of etching (b, d, f, h, j, and l).....	166
Figure 5.32. Top-view SEM images of (a) CNT-5/1 and (b) bare Cu after 30 cycles of Li plating/stripping with an areal capacity of 1.0 mAh cm ⁻² at 1.0 mA cm ⁻²	167
Figure 5.33. The summary diagram of the relationship between cycling performance, resistance, surface area, and CNT contents. Dots are original data, and solid lines are rough-fitting curves.....	168
Figure 5.34. (a) Cycling performance of bare Cu and CNT-5/1 paired with high areal capacity LiFePO ₄ positrodes (~1.7 mAh cm ⁻²) in the ether-based electrolyte. (b) Cycling performance of bare Cu and CNT-5/1 paired with high areal capacity NCM811 positrodes (~2 mAh cm ⁻² and ~4 mAh cm ⁻²) in the esters-based electrolyte.....	169

Figure 5.35. (a) Cycling performance of bare Cu, CNT-0/1, CNT-5/1, and CNT-5/1 with pre-activation capacity of 2 mAh cm ⁻² at 0.5 mA cm ⁻² for 2 cycles paired with LiFePO ₄ positrodes (~1.7 mAh cm ⁻²) in the ethers-based electrolyte. (b) Cycling performance of bare Ni foil and Ni foam paired with LiFePO ₄ positrodes (~1.7 mAh cm ⁻²) in the esters-based electrolyte.	170
Figure 6.1. (a) Schematic illustration showing the preparation process of free-standing Gra-5/1. Schematic diagrams showing the morphology of electrodeposited Li and “dead Li” after cycling on (b) bare Cu foil and (c) Gra-5-1.....	176
Figure 6.2. (a) Raman spectra and (b) X-ray diffraction pattern of graphene powders.	180
Figure 6.3. (a) Top-view of normal-magnification and (b) High-magnification SEM images of Gra-5/1. (c) FIB cross-section view of normal-magnification and (d) High-magnification SEM images of Gra-5/1. (e) Top-view and (f) cross-section view of SEM image of Gra-0/1.....	181
Figure 6.4. Optical photographs showing the appearance and weight of bare Cu (left) and Gra-5/1 (right).....	181
Figure 6.5. (a) XPS spectra of the F 1s over the fresh Gra-5/1. EDS mapping of the (b) cross-section view for (c) C, (d) F, and (e) Cu element of Gra-5/1.	183
Figure 6.6. (a) Specific tensile strength and (b) specific shear strength of Cu, Gra-5/1, and graphite paper. The inset photograph of (a) shows the flexibility of the Gra-5/1.	184
Figure 6.7. DMT modulus over (a) bare Cu, (b) Gra-0/1, and (c) Gra-5/1 through AFM characterisation.	184
Figure 6.8. TGA and relevant derivative curves of the Gra-5/1.	185
Figure 6.9. Resistance of Gra-X/1-Cu (X = 0, 1, 5, and 10), Gra- 5/1, and bare Cu foil.	186
Figure 6.10. (a) Contact resistance between different current collectors and metallic tabs using different connecting methods. The inset optical photographs show the	

appearance of different samples. (b) Optical photograph showing the tabs welded on the Gra-5/1 in a practical pouch cell. 186

Figure 6.11. Contact angles of electrolyte toward (a) Cu foil and (b) Gra-5/1. 188

Figure 6.12. Cross-section views SEM images of (a), (b) Gra-5/1, (c), (d) graphene paper and (e), (f) carbon nanotube film before soaking and after soaking in the electrolyte solution for 15h, respectively. 189

Figure 6.13. (a) Potential profiles of Li plating on the 2D current collector: bare Cu foil, Gra-0/1-Cu, Gra-5/1-Cu, Gra-5/1, and the graphene paper at 0.5 mA cm^{-2} . (b) Potential profiles of Li plating on the 3D current collector: carbon cloth and carbon nanotube film with an areal capacity of 3.5 mAh cm^{-2} at 0.5 mA cm^{-2} 190

Figure 6.14. Optical photograph of (i) the carbon cloth, (ii) carbon nanotube film, (iii) graphene paper, and (iv) Gra-5/1 after (a) 20 cycles of direct deposition/dissolution and (b) 30 cycles with Li foil covering on the upper surface at 0.5 mA cm^{-2} with a capacity of 3.5 mAh cm^{-2} 191

Figure 6.15. The optical photograph shows the flexibility of Gra-5/1 after 100 cycles of deposition/dissolution in a full pouch cell. 191

Figure 6.16. Potential profiles showing the capacity difference in comparison of galvanic corrosion before and after standing for 100h over the bare Cu and Gra-5/1 with plating Li at $0.01 \text{ mA cm}^{-2}/0.5 \text{ mA cm}^{-2}$ and stripping Li at 0.01 mA cm^{-2} 192

Figure 6.17. (a) Simulation result of Fermi energy level over Li, graphene, PVDF, and Cu. (b) Mechanism of lower Fermi level in suppressing electron transfer to the electrolyte on the Cu and Gra-5/1. 193

Figure 6.18. EIS evolution with discharging from 2V to -0.25V at $0.1 \text{ mV}\cdot\text{s}^{-1}$ over (a) bare Cu, (b) Gra-0/1-Cu, and (c) Gra -5/1-Cu. 195

Figure 6.19. XPS spectra of the F 1s of plated 1 mAh cm^{-2} Li at 0.5 mA cm^{-2} on (a) bare Cu, (b) Gra-0/1-Cu, and (c) Gra-5/1-Cu. 196

Figure 6.20. Top-view and cross-section view SEM images and corresponding EDS mapping for C, O, F, and Cu elements of (a, b, e) bare Cu, and (c, d, f) Gra-5/1-Cu with

a plating areal capacity of 3 mAh cm⁻². The current density is 0.5 mA cm⁻². 197

Figure 6.21. LM deposition morphology evolution with capacities from 0.2 to 1 mAh cm⁻² on the bare Cu and Gra-based electrodes. Top-view SEM images of the (a) bare Cu, (b) Gra-0/1-Cu, and (c) Gra-5/1-Cu electrode after plating with 0.2 mAh cm⁻², 0.6 mAh cm⁻² and 1.0 mAh cm⁻² of Li. The current density is 0.5 mA cm⁻². 199

Figure 6.22. $t/t_{\max}-I/I_{(\max)}^2$ plots of the fresh bare Cu, fresh Gra-0/1-Cu, and fresh Gra-5/1-Cu. 200

Figure 6.23. Comparison of CE of Li plating on/stripping with the capacity of 1 mAh cm⁻² at (a) 1 mA cm⁻² and (b) 2 mA cm⁻² and with the capacity of (c) 3 mAh cm⁻² at 1 mA cm⁻² over bare Cu, Gra-0/1-Cu, and Gra-5/1-Cu under ester-based electrolyte. 202

Figure 6.24. Comparison of Li plating/stripping potential profiles on Cu foil and Gra-5/1-Cu at different current densities ranging from 0.5 to 3 mA cm⁻² with 1 mAh cm⁻². 203

Figure 6.25. (a) Top-view SEM images, (b) EIS, and (c) related CE of Li plating on/stripping with the capacity of 1 mAh cm⁻² at 2 mA cm⁻² over fresh Gra-X/1-Cu (X = 0, 1, 5, and 10). 204

Figure 6.26. Comparison of CE of Li plating on/stripping with 1 mAh cm⁻² at 1 mA cm⁻² over (a) bare Cu, Gra-0/1-Cu, Gra-5/1-Cu, and Cu foil washed with HCl and (b) over Gra-5/1-Cu and Gra-5/1-PAN-Cu. (c) Cycling performance of pouch cell assembled with Cu foil, Gra-0/1-Cu, Gra-5/1-Cu, and Gra-5/1-PAN-Cu current collectors and high areal capacity NCM 811 positrodes (~ 4 mAh cm⁻²). 206

Figure 6.27. (a) Cycling performance of LM-free coin full cell assembled with bare Cu, Gra-0/1-Cu, Gra-5/1-Cu, and CNT-5/1 with an areal capacity of ~2 mAh cm⁻². (b) Cycling performance of full cells assembled with bare Cu, Gra-0/1-Cu, and Gra-5/1-Cu with an areal capacity of ~4 mAh cm⁻². (c) The rate capability of full cells assembled with bare Cu and Gra-5/1-Cu from 0.1 C to 2 C with an areal capacity of ~ 4 mAh cm⁻². 207

Figure 6.28. Optical photograph of the fresh (a) graphite paper, (b) graphene paper, and

(c) expanded graphite paper. (d) Comparison of CE of Li plating on/stripping with 1 mAh cm⁻² at 2 mA cm⁻² over the Gra-5/1, graphite paper, graphene paper, and expanded graphite paper. (e) Cycling performance of coin full cell assembled with Gra-5/1, graphite paper, graphene paper, and expanded graphite paper current collectors and high areal capacity NCM 811 positrodes (~ 4 mAh cm⁻²).208

Figure 6.29. (a) Cycling performance and *in-situ* (b) discharge and (c) charge internal resistance profiles of pouch cells assembled with bare Cu, Gra-0/1-Cu, Gra-5/1-Cu, and Gra-5/1 and high areal capacity NCM 811 positrodes (~ 4 mAh cm⁻²).209

Figure 6.30. Optical photograph of (a) large-scale production of Gra-5/1 and (b) related pouch cell scale electrode (47 mm × 57mm). (c) Optical photograph of graphite paper in pouch cell. Optical photograph of welding condition over the (d) Gra-5/1 and graphite paper using (e) Cu sticker and (f) silver paste.211

Figure 6.31. (a) *in-situ* charge and discharge internal resistance profiles and (b) cycling performance of pouch cell assembled with Gra-5/1 and graphite paper current collectors using silver and Cu sticker for the welding process and high areal capacity NCM 811 positrodes (~ 4 mAh cm⁻²).211

Figure 6.32. The discharge capacity and Charge and discharge energy profiles of a pouch cell assembled with Gra-5/1 and high areal capacity NCM 811 positrodes (~ 4 mAh cm⁻²) using the modified (a) and (b) rich electrolyte (E/C: ~12μl mAh⁻¹) and (c) lean electrolyte (E/C: ~6μl mAh⁻¹); (d) Optical photo of the pouch cell.212

Figure 6.33. Optical photographs of the (a) front and (b) back surface of Gra-5/1 current collector (64 mm × 74 mm) used in pouch cells. (c) The mass of the naked pouch cell without packaging, and (d) the thickness, (e) appearance, and (f) the voltage profile for the first 3 cycles of the pouch cell assembled with Gra-5/1 and high areal capacity LR-114 positrodes (~ 6 mAh cm⁻²).213

Figure 6.34. (a) CE of Li plating on/stripping with 1 mAh cm⁻² at 1/0.1 mA cm⁻² over Cu foil and Gra-5/1 under lean electrolyte conditions (~20 μL). Top-view SEM images of (b) bare Cu and (c) Gra-5/1 after 30 cycles with 1 mAh cm⁻² at 2 mA cm⁻². Inset (b)

and (c) shows the optical photograph of cycled Cu and Gra-5/1.....215

Figure 6.35. (a) The optical photographs of bare Cu and Gra-5/1, and top-view SEM images of the (b) bare Cu and (c) Gra-5/1 after 100 cycles in pouch cells.217

Figure 6.36. EIS of (a) the bare Cu and (b) Gra-5/1 after 10, 30, and 50 cycles with an areal capacity of 1 mAh cm⁻² at 2 mA cm⁻². (c) applied fitting resistance model: R1:R0 (Ohmic resistance); R2: R_{SEI} (Migration resistance of Li⁺ through the SEI); Wo1: Warburg (Li⁺ diffusion resistance); CPE1/CPE2: Constant phase element (Conventional double-layer and passivation film capacitance).....218

Figure 6.37. XPS full spectrum at various depths of Li plating on/stripping with 1 mAh cm⁻² at 2 mA cm⁻² over the (a), (b) bare Cu, and (c), (d) Gra-5/1 after 50 cycles.....219

Figure 6.38. XPS spectra at different etching depths (0s and 30s) of the (a) F 1s, (b) C 1s, (c) O 1s, and (d) Li 1s of Li plating/stripping with 1 mAh cm⁻² at 2 mA cm⁻² over the bare Cu and Gra-5/1 after 50 cycles. (e) Illustration of the SEI compositions on the bare Cu (top) and Gra-5/1 (down).220

Abbreviations

1D	One-Dimensional
2D	Two-Dimensional
3D	Three-Dimensional
AFM	Atomic Force Microscope
BCN	Bulk Carbon Nitride
BET	Brunauer–Emmett–Teller
BJH	Barrett–Joyner–Halenda
CBCCs	Carbon-based Current Collectors
CE	Coulombic Efficiency
CMC	Carboxymethyl Cellulose
CNTs	Carbon Nanotubes
CV	Cyclic Voltammetry or Cyclic Voltammogram
DEC	Diethyl carbonate
DMAC	Dimethylacetamide
DMC	Dimethyl Carbonate
DME	Dimethoxyethane
DMF	N, N-Dimethylformamide
DMM	Dimethoxymethane
DMSO	Dimethyl Sulfoxide
DOL	1,3-Dioxolane
EC	Ethylene Carbonate
EDS	Energy-Dispersive Spectroscopy
EDL	Electric Double Layer
EES	Electrochemical energy storage
EIS	Electrochemical Impedance Spectroscopy

FEC	Fluoroethylene Carbonate
FIB	Focused Ion Beam
FTIR	Fourier Transform Infrared
h-BN	Hexagonal Boron Nitride
HCE	High-Concentration Electrolyte
LFP/LiFePO ₄	Lithium Iron Phosphate
LHCE	Local High-concentration Electrolyte
Li ₂ O ₂	Lithium Peroxide
Li ₂ O	Lithium Oxide
Li ₃ N	Lithium Nitride
Li ₃ PO ₄	Lithium Orthophosphate
Li ₂ S	Lithium Sulfide
LIBs	Lithium Ion Batteries
LiClO ₄	Lithium Perchlorate
Li ₂ CO ₃	Lithium Carbonate
LiCoO ₂	Lithium Cobaltate
LiDFOB	Lithium Difluoro(oxalato)borate
LiF	Lithium Fluoride
LiFSI	Lithium Bis(fluorosulfonyl)imide
LiMn ₂ O ₄	Lithium Manganate
LiNiO ₂	Lithium Nickelate
Li-O ₂	Lithium-Air/Oxygen
LiOH	Lithium Hydroxide
LiPF ₆	Lithium Hexafluorophosphate
Li-S	Lithium-Sulfur
Li ⁺	Lithium Ion
LiTFSI	Lithium Bis(trifluoromethanesulphonyl)imide
LM	Lithium Metal

LMFRBs	Lithium Metal Rechargeable Batteries with lithium-metal-Free negatode
LMRBs	Lithium Metal Rechargeable Batteries
LMNEs	Lithium Metal Negative Electrodes
NCM	$\text{LiNi}_{1-x-y}\text{Co}_x\text{Mn}_y\text{O}_2$
NCM 811	$\text{LiNi}_{0.8}\text{Co}_{0.1}\text{Mn}_{0.1}\text{O}_2$
negatodes	negative electrodes
NMP	N-methyl-2-pyrrolidone
PAN	Polyacrylonitrile
PCNMs	Porous Carbon Nitride Microspheres
PDMS	Poly(dimethylsiloxane)
PEO	Polyethylene Oxide
PMMA	Poly(methyl methacrylate)
positodes	positive electrodes
PVDF	Poly(vinylidene difluoride)
SAED	Selected Area Electron Diffraction
SBR	Styrene Butadiene Rubber
SCN	Sheet Carbon Nitride
SEI	Solid Electrolyte Interphase
SEM	Scanning Electron Microscope
SSEs	Solid-State Electrolytes
SWCNTs	Single-Walled Carbon Nanotubes
TEM	Transmission Electron Microscope
TGA	Thermogravimetric Analysis
TiS ₂	Titanium Sulfide
TTE	1,1,2,2-Tetrafluoroethyl-2,2,3,3-Tetrafluoropropylether
XPS	X-ray Photoelectron Spectroscopy
XRD	X-ray Diffraction
ZnO	Zinc Oxide

Dissemination Section

The main content of this thesis comes from the author's formal **publications 1, 2, and 3**. The partial contents of **chapter 1 and Abstract** are mainly based on **Publication 1, 2, and 3**. The experiment sections of **chapter 2** mainly come from the experiment sections of **Publication 1, 2, and 3**. The contents of **chapter 3** are mainly based on **Publication 1**. The contents of **chapter 5** mainly come from **Publication 2**. The contents of **chapter 6** mainly come from **Publication 3**, which has been submitted for publication. The contents of **chapter 7** are mainly based on **Publications 1, 2, and 3**.

1. **Q. Guo**, W. Deng, S. Xia, Z. Zhang, F. Zhao, B. Hu, S. Zhang, X. Zhou, G. Chen, Z. Liu, Nano-channel-based physical and chemical synergic regulation for dendrite-free lithium plating. *Nano Research* **2021**, 14 (10), 3585-3597.

2. **Q. Guo**, Y. Yu, S. Xia, C. Shen, D. Hu, W. Deng, D. Dong, X. Zhou, G. Chen, Z. Liu, CNT/PVDF Composite Coating Layer on Cu with a Synergy of Uniform Current Distribution and Stress Releasing for Improving Reversible Li Plating/Stripping. *ACS Applied Materials & Interfaces* **2022**, 14 (40), 46043-46055.

3. **Q. Guo**, S. Wang, Y. Li, J. Wang, Y. Wu, Y. Yu, S. Xia, D. Hu, B. Hu, Z. Ye, X. Zhou, G. Chen, Z. Liu, Free-standing and Low-Density Composite of Graphene and PVDF as Promoting Current Collector for Reversible Lithium Deposition. *Advanced Functional Materials*. **2023**. (submitted to the journal)

Chapter1

Introduction

This chapter reports the background and purpose of this thesis. Also, this chapter introduces a lot of literature reviews including the importance of developing Li metal negatrodes, issues, influential factors, and the current research progress.

1.1. Research background

Energy has always been the basis for the survival and development of human society. The history of energy exploration and utilisation is also the history of human social civilisation. The earliest human use of energy began with learning to use fire. Fire was first used for various purposes of living, including burning, cooking, heating, and lighting which enable people to move at night and fight with animals. The emergence and improvement of the internal combustion engine during the industrial revolution promoted the utilisation of fossil energy into a new era. Currently, fossil energy, represented by coal, oil, and natural gas, is still the leading force in the whole energy supply structure. However, fossil energy is non-renewable naturally in the short term and its reserve is limited in the earth's crust, which makes the exploitation increasingly challenging to meet human needs. In addition, sulfur (S), nitrogen (N), carbon, and other elements in fossil fuels will release harmful substances such as carbon dioxide, carbon monoxide, nitrogen oxides, sulfur dioxide, and soot when burned.¹⁻³ Therefore, in the face of the depletion of fossil fuels and climate change, the development strategy of energy has gradually shifted to the utilisation of green and renewable clean energy, such as wind energy,⁴⁻⁶ solar energy,⁷⁻⁹ tidal energy,¹⁰⁻¹² and geothermal energy (Fig.

1.1).¹³⁻¹⁵ However, due to geographical environment, weather, and other factors, these forms of clean and renewable energy show various levels of instability and intermittence. Therefore, energy storage technology is essential to use all forms of renewable energy in a more convenient, stable, and economical way. Electrochemical energy storage (EES) is one of the most important energy storage technologies. An EES device is a converter between chemical energy and electric energy, as shown in Fig. 1.1. It possesses the advantages of convenient use, low environmental pollution, and no geographical restrictions. At the same time, it is not limited by the Carnot cycle¹⁶ in energy conversion. Thus, it has high conversion efficiency, specific energy, and specific power.

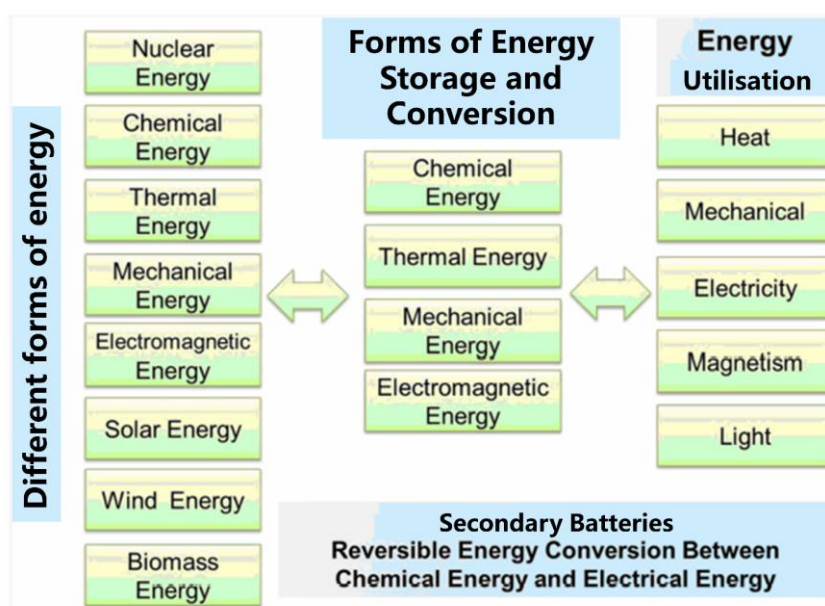


Figure 1.1. Schematic diagram of energy conversion, storage, and utilisation in various forms.¹⁷

Since the advent of lead-acid batteries in the 18th century, several major batteries have been developed, such as cadmium nickel, nickel-hydrogen, and lithium ion batteries (LIBs). Larger capacity, higher power, lower pollution, longer lifetime, and better safety are the main trend of battery technology development. Fig. 1.2 compares the energy

densities of several types of batteries. It can be seen that compared with lead-acid, cadmium nickel, and nickel-hydrogen batteries, LIBs have obvious advantages in both energy density and specific energy. These advantages make LIBs the winner in competition with other EES devices and the choice for use in portable electronic products such as mobile phones, laptops, digital cameras, and mobile DVDs.

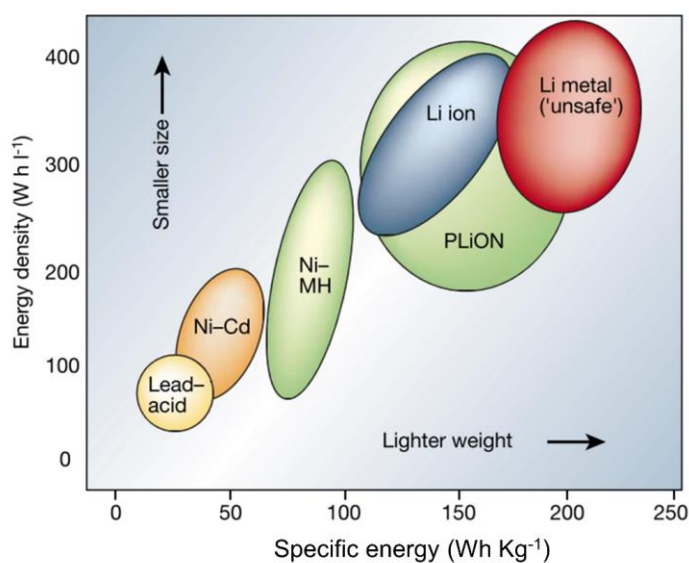


Figure 1.2. Comparison of different types of rechargeable batteries in terms of energy density and specific energy.¹⁸

So far, Li batteries have gone through about 100 years, as shown in Fig. 1.3. The development of Li batteries can be traced back to the 1950s. At that time, primary Li batteries were invented with lithium metal (LM) as the negative electrode (negatrod) and metal oxide or other solid and liquid oxidants as the positive electrode (positrod). Due to their large specific capacity, high voltage, and small volume, they were widely used in small equipment such as electronic watches, alarms, calculators, and cardiac pacemakers.¹⁹ In 1976, Whittingham et al.²⁰ inadvertently found that lithium ion (Li⁺) can be intercalated in layered titanium sulfide (TiS₂). Due to structural retention, this reaction occurs quickly and highly reversibly at room temperatures. Then, lithium metal rechargeable batteries (LMRBs) were successfully assembled with metallic Li as the

negatrod and TiS_2 as the positrod in an electrolyte of lithium perchlorate (LiClO_4) dissolved in a mixture of dimethoxyethane and tetrahydrofuran (30:70 in volume). TiS_2 was also the best intercalation compound available at that time, depending on its highly favourable layered structure. But in the subsequent application, it was found that uneven Li deposition would be caused. Then Li dendrites would be formed in lithium metal negative electrode (LMNE) during each discharge-recharge cycle due to the instability of the interface between electrode and electrolyte, resulting in serious explosion hazards.¹⁸ Later, they replaced the LMNE with Li-Al alloy. Still, unfortunately, Li-Al alloy only survived a limited number of cycles due to the severe volume changes during cycling,¹⁸ and finally, the commercialisation of TiS_2 -based LMRB failed. Later, with a deepening understanding of intercalation compounds, Goodenough et al.^{21, 22} proposed the families of Li-containing layered oxide—lithium cobaltate (LiCoO_2) in the early 1980s. The dendrite problem is well resolved, and the safety is improved due to changing the existence form of Li from the metallic to the ionic state. Around ten years later, in 1990, the Japanese Corporation-Sony successfully prepared the first commercial LIB with LiCoO_2 as the positrod and graphite-structured carbon material as the negatrod. This LIB production was commercialised successfully in 1991.²³ This battery overcomes Li's high activity and solves the dendrites' problem. At the same time, it has the advantages of high output voltage, high specific energy, and good stability. In 1997, Goodenough et al.²⁴ reported lithium iron phosphate (LiFePO_4) positrod materials with an olivine structure. This type of positrod material is safer than the traditional LiCoO_2 positrod materials, and its raw materials are widely available and inexpensive.

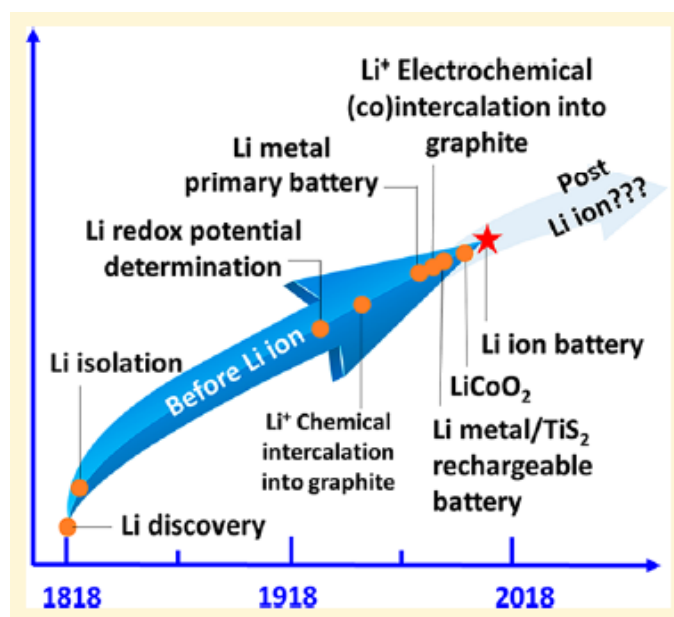


Figure 1.3. The history of Li batteries.²⁵

Li batteries mainly comprise positive materials, electrolytes, separators, and negative materials. As shown in Fig. 1.4, the positive materials are mainly Li-containing transition metal layered compounds, such as LiCoO_2 , LiFePO_4 , lithium manganate (LiMn_2O_4), lithium nickelate (LiNiO_2), nickel cobalt manganese transition metal layered ternary oxide ($\text{LiNi}_{1-x-y}\text{Co}_x\text{Mn}_y\text{O}_2$).^{26, 27} The negative materials mainly include graphite-based carbon materials, silicon-based materials, tin-based materials, transition metal oxide materials, lithium titanate, etc.²⁷ The separators are mostly polyolefin materials, such as polyethylene or polypropylene single-layer microporous membranes and polyethylene/polypropylene multi-layer composite microporous membranes. Electrolytes are generally composed of Li salts and organic solvents.²⁷ Currently, two main electrolytes are most widely used: ether-based electrolytes and ester-based electrolytes. The ether-based electrolyte is generally composed of lithium bis(trifluoromethanesulfonyl)imide (LiTFSI), lithium bis(fluorosulfonyl)imide (LiFSI) as Li salts and one or more of dimethoxyethane (DME), 1,3-dioxolane (DOL), and dimethoxymethane (DMM) as solvents.²⁷ Ester-based electrolytes are mostly composed of lithium hexafluorophosphate (LiPF_6) as Li salts and one or more of ethylene carbonate (EC), dimethyl carbonate (DMC), and diethyl carbonate (DEC) as

solvents.²⁷

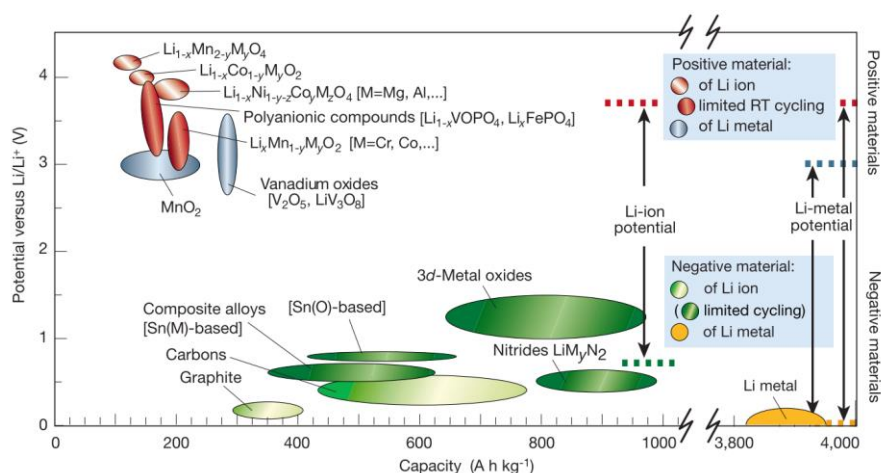


Figure 1.4. Potential versus capacity in terms of the positrode and negatrode materials for the next generation of rechargeable Li batteries.¹⁸

Fig. 1.5 shows the working principle of a typical LIB. The cell comprises layered transition metal compounds (LiMO_2) as the positrode, graphite as the negatrode, and aluminium foil and copper foil as the positrode and negatrode current collectors to connect with the external circuit, respectively. During charging, the Li^+ is deintercalated from the positrode and passes through the electrolyte and the separator. Finally, Li^+ is reduced after obtaining electrons and inserted into the negatrode to form Li_xC_6 ($x \leq 1$). During discharge, Li^+ is de-intercalated from the graphite negatrode and moves back into the electrolyte, migrates to the positrode and then inserts into the layered structure of the positrode. The electrochemical reactions during the whole charging and discharging process are presented as follows:²⁷

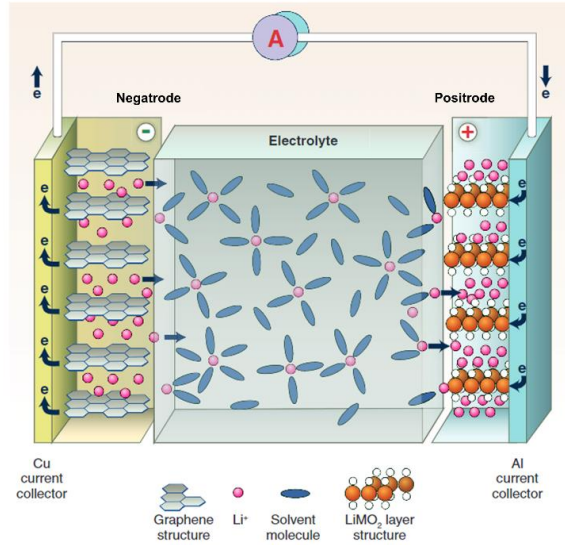
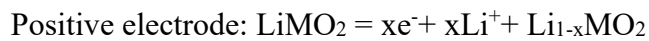
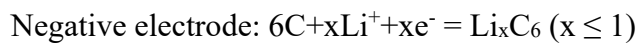
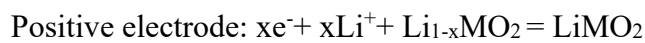


Figure 1.5. Schematic of a traditional LIB.²⁸

Charging:



Discharging:



1.2. Brief introduction of Li-metal-based batteries

1.2.1. Advantages of Li metal

LIBs have been dominant in the past decade. However, with the explosive development of modern science and technology, the requirements of energy storage devices with higher mass and specific energy gradually increase, and the traditional LIB device cannot meet its target requirements. As we all know, the specific energy of a Li battery

is directly determined by the capacity and redox potential of positive and negative electrode materials. The cost of negative electrode materials is comparatively low, and its modification is the more efficient and economical way to improve the specific energy of batteries. In addition, the capacity of negative electrode materials can be primarily affected by the Li storage form.²⁹ For example, graphite shows a typical intercalating chemical reaction. Since Li^+ can intercalate into graphite to form the LiC_6 structure at most, the theoretical capacity of graphite is low, only 372 mAh g^{-1} .³⁰ Currently, the LIB with graphite as a negative electrode material is difficult to meet the growing demand for the specific energy of electric vehicles and smart grids. Therefore, people have extensively researched the new negative electrode materials of rechargeable Li-based batteries to make batteries with a higher specific energy.

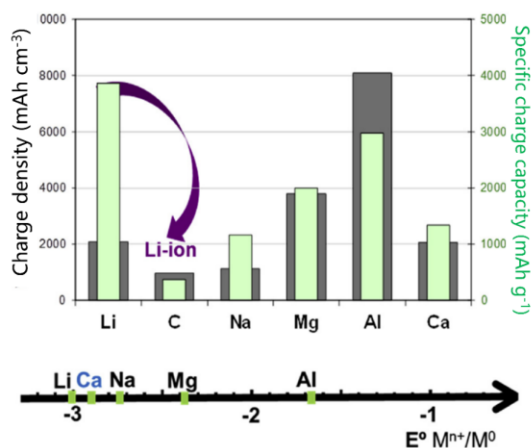


Figure 1.6. Comparison of the standard reduction potential versus the charge density or specific charge capacity for different metal and graphite negative electrodes in the LIB.³¹

LM is an ideal negative electrode material in Li-based batteries. Among the available negative electrode materials, such as silicon-based materials³² and transition metal oxides,³³ LMNE has been recognised as the “Holy Grail” because of its rather high theoretical specific capacity (3860 mAh g^{-1} in Fig. 1.6), low density (0.59 g cm^{-3}) and the lowest electrochemical potential (-3.04 V vs. the standard hydrogen electrode).^{34, 35} As early as the 1970s, LMNEs have been applied in the Li-based battery. However, it was

eventually replaced with safer LIBs owing to the serious safety hazards.¹⁹ With the rise of new Li-based batteries such as the lithium-sulfur (Li-S) battery, lithium-air/oxygen (Li-air/Li-O₂) battery, and solid-state battery, and the continuous development of modern characterisation technologies, LMNE has returned to arouse the interest of researchers all over the world.

1.2.2. Different Li-metal-based batteries

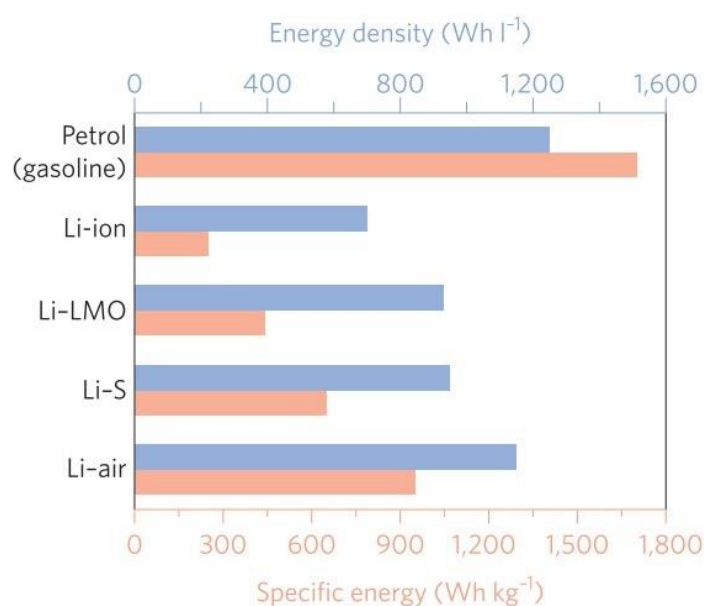


Figure 1.7. Comparison of the practical specific energy (pink) and energy densities (blue) regarding petrol (gasoline) and Li-based rechargeable batteries, including LIBs, conventional LMRBs, Li-S, and Li-air batteries.³⁵

LM-based batteries are usually classified into Li-S battery,³⁶⁻³⁸ Li-air/Li-O₂ battery,³⁹⁻⁴¹ LM-based supercapattery,⁴²⁻⁴⁴ and conventional LMRB paired with the Li-containing positrode and so on, depending on the positrode materials. Compared with the most popular commercial LIBs based on graphite negatropdes, the new battery based on LMNEs, such as Li-S battery and Li-air/Li-O₂ battery, can easily reach incredible specific energy of > 400 Wh kg⁻¹ (Fig. 1.7). Such high specific energy means that an electric vehicle can travel more than 500 kilometres, which can be comparable to or even better than fuel vehicles in the future market.

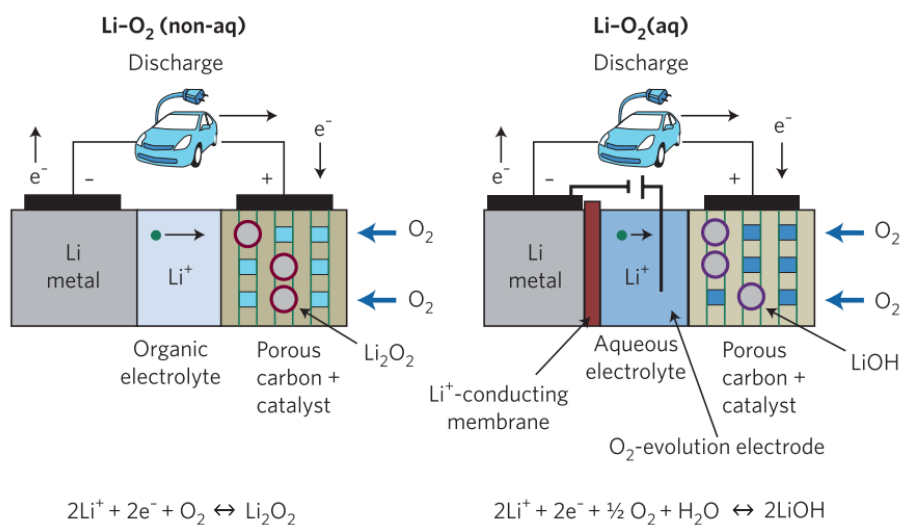


Figure 1.8. Schematic illustration of Li–O₂ cells operating in non-aqueous and aqueous electrolytes.⁴¹

The Li-air battery is based on the Li-O₂ electrochemical couple (conversion reaction). According to Fig. 1.8, the Li is oxidised during discharge, releasing Li⁺ into the electrolyte. At the positive electrode, O₂ from the atmosphere enters the porous positive electrode, dissolves in the organic electrolyte, and is reduced at the electrode surface to form lithium peroxide composition (Li₂O₂) with theoretical specific energy of 3623 Wh kg⁻¹ or lithium oxide (Li₂O) with theoretical specific energy of 5204 Wh kg⁻¹.⁴⁰ Fig. 1.8 shows that aqueous electrolytes can involve the formation of discharge product (LiOH) at the positive electrode. Although the theoretical specific energy of Li-air/Li-O₂ battery is as high as 11680 Wh kg⁻¹,⁴¹ which is almost equivalent to the specific energy of gasoline (~13000 Wh kg⁻¹),⁴⁰ there are many technical challenges from key materials, including electrolytes, LMNEs, positive electrodes, and catalysts to battery design and assembly. It isn't easy to realise practical applications in the short term.^{45, 46}

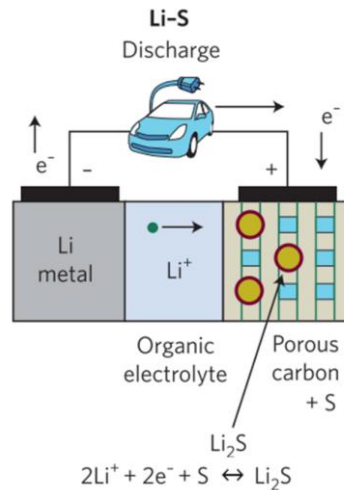


Figure 1.9. Schematic illustration of Li-S cells operating in organic electrolyte.⁴¹

Similarly, Li-S batteries are based on the conversion reaction of Li^+ with S. Fig. 1.9 illustrates the operation principle of Li-S cells. S is reduced at the positive electrode on discharge to form lithium sulfide (Li_2S) with dissolved Li^+ . Li-S cells perform many attractive features, such as the natural abundance, low cost, and high theoretical specific energy of 2567 Wh kg^{-1} .⁴¹ However, Li-S batteries also have their limitations during battery operation, such as the large volume change in the positive electrode, limited rate capability due to poor conductivity of S, and the shuttle of polysulfides leading to the fast capacity fading, which greatly affects the battery's electrochemical performance.^{47,}

48

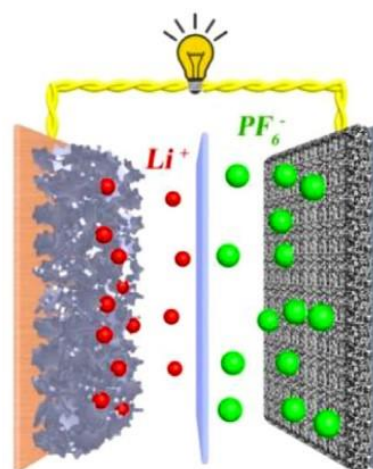


Figure 1.10. The proposed device structure of LM-based supercapattery. The left is LM

and the right is activated carbon.⁴⁴

LM-based supercapattery (sometimes it is called capacitor battery) is a leading-edge energy storage device with high specific energy close to LIBs and high specific power or longer charge-discharge durability close to electrochemical capacitors.^{49, 50} The introduction of the LMNE can give rise to extending the working voltage window and avoid hydrogen evolution reaction in the aqueous electrolyte⁵⁰ owing to the lowest redox potential, further increasing the specific energy of the supercapattery. It is also reported that kinetics discrepancy between the positrode and LMNEs can be efficiently eliminated.⁴⁴ As shown in Fig. 1.10, in this LM-based supercapattery, the LMNE undergoes Li plating/stripping during the charging and discharging process. At the same time, the anion will involve the adsorption/desorption process at the positrode. However, the relevant research has not started for a long time and the relevant mechanism is still unknown. Furthermore, further attention should be paid to optimizing capacitor positrodes, electrolytes, and their unique practical application.

LMRBs assembled with Li-containing positrodes and LMNEs are a more practical choice. Compared with S and air positrodes, the research on intercalation-type Li-containing positrode materials is comparatively mature, with more stable electrochemical performance and high voltage window in constructing LMRBs. Even if only the LMNE is used instead of the traditional graphite negatrode, pairing with transition metal oxide positrodes (such as $\text{LiNi}_{1-x-y}\text{Co}_x\text{Mn}_y\text{O}_2$ (NCM) or Li-rich layered oxides⁵¹), the battery still can show specific energy of $> 400 \text{ Wh kg}^{-1}$ (Fig. 1.7). Furthermore, the current development of solid-state batteries is in full swing.⁵² Solid-state batteries with high specific energy and high safety assembled with LM as the negatrode and transition metal oxide as the positrode are super common in future battery design. It is believed that the above novel LM-based batteries have their research value and features. Their research may be carried out toward more targeted application scenarios. Therefore, it seems to be an inevitable choice to commercially

employ LMRBs composed of Li-containing positrodes and LM negatrodes as a high specific energy battery in the future.

However, LMNEs face severe dendrite growth problems during charging, leading to short circuits and even fires. During the discharge process, the uneven dissolution of Li dendrites easily generates “dead Li”, which can significantly reduce the battery capacity. In addition, since LM has the lowest redox potential, it's chemical and electrochemical reactivity is super high, which means that it will undergo continuous side reactions with almost all liquid electrolytes at the interface, resulting in an unstable solid electrolyte interphase (SEI). This side-effect not only consumes the battery capacity but also further exacerbates the growth of Li dendrites. Li deposition and dissolution will cause a large volume change.

Meanwhile, due to the non-uniform deposition/dissolution process of Li on the surface of metallic Li, the volume change of the LM is more obvious during cycling, making it difficult to use in practical devices. For the Li-S or Li-O battery system, the LMNE also suffers from serious corrosion problems.⁵³ The above problems lead to short cycle life and poor safety performance in LMRBs.

1.3. Problems of Li metal negative electrodes

The intrinsic mechanism and the decoupling of multivariate problems caused by LMNEs during cycling are clarified below.

1.3.1. Li dendrite growth

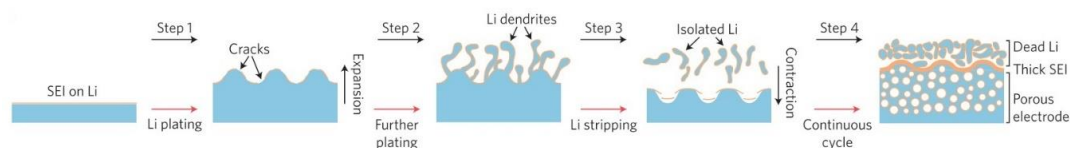


Figure 1.11. Schematic illustration of the Li stripping/plating process.³⁵

The growth of Li dendrites is the main problem limiting the practical application of LMRBs. Metal dendrites are very common in the metal deposition process.⁵⁴⁻⁵⁶ Similar to Zn and Cu metals,⁵⁷ the Li^+ in the electrolyte obtain electrons during the charging process and are deposited on the surface of the negatode, forming needle-like or whisker-like protrusions, as illustrated in Fig. 1.11. The needle-like protrusions can puncture the SEI, exposing fresh Li to the electrolyte. As the reaction continues, the formed bulge will have a higher current density due to the higher curvature, which is more likely to attract Li^+ to further deposit on the same spots, eventually evolving into Li dendrites.⁵⁸ The scary thing is that the dendrites are likely to pierce the separator and cause a short circuit in the battery. Sometimes, the battery suffers from thermal runaway or even explosion. In addition to serious safety issues, battery capacity decay, battery polarisation, battery volume swelling, negatode pulverisation, and electrolyte consumption can all be attributed to the formation of Li dendrites. During the discharge process, the uneven dissolution of dendrites often makes the LM encapsulated with SEI, which is isolated from electrons, forming the so-called “dead Li”. Due to the electronic insulation of “dead Li”, it easily loses its electrochemical reactivity, resulting in low coulombic efficiency (CE) and rapid capacity decay in the battery. At the same time, the savage growth of Li dendrites will also easily increase the surface area of the LMNE, causing the electrolyte and active Li to be continuously consumed owing to the generation of SEI. It is noted that the volume expansion caused by porous Li dendrites should not be ignored. In addition, during cycling, the upper part of the negatode becomes loose and porous, allowing the penetration of the electrolyte. Then, the active Li and “dead Li” phases show rapid inward movement, resulting in irreversible corrosion of the negatode. As it increases, the diffusion path and internal impedance of the battery continue to increase, eventually leading to severe battery polarisation.

The origin of dendritic Li deposition. LM is a crystalline material with a body-centred cubic structure. In 2015, Kramer et al.⁵⁹ found that lithium, sodium, tin, and other

metals will appear to dendrite growth during the thermal evaporation deposition process, indicating that the non-uniform deposition of these metals is intrinsic. Through electron microscopy and *in-situ* optical microscopy observations, they found that LM growth is based on the mechanism of atom insertion into the lattice upon both the thermal evaporation deposition and electrodeposition, as illustrated in Fig. 1.12. Therefore, they believe that ion transport and electrochemical processes may not be the fundamental reasons for the growth of dendrites. Still, the diffusion barriers and crystallisation of LM (surface formation energies) are essential factors affecting the growth of Li dendrites.

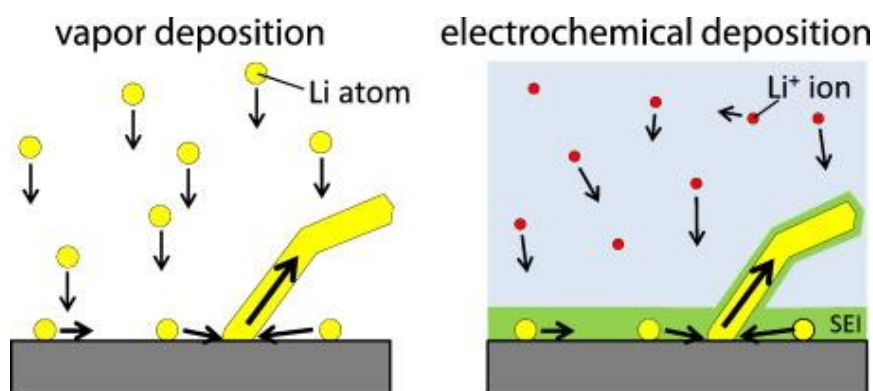


Figure 1.12. Schematic diagram of metal in thermal evaporation deposition and electrochemical deposition.⁵⁹

It is reported that LM is thermodynamically and kinetically easy to grow in dendritic morphology, while magnesium (Mg) is preferable to grow in dendrite-free morphology. The thermodynamic difference in the electrochemical deposition is one reason for Li forming dendritic morphology easily. Ling et al.⁶⁰ reported that due to the stronger Mg–Mg bond strength resulting from DFT calculation, Mg has a higher free energy difference between high-dimensional and low-dimensional phases than Li. Thus, relative to Li, Mg is preferable to deposit in high-dimensional (such as three-dimensional (3D) and two-dimensional (2D)) structures owing to the larger surface energy rather than one-dimensional (1D) dendritic whiskers. The lower diffusion

energy barrier for Mg may be another reason from a kinetic aspect. Through DFT calculations, Jäckle et al.⁶¹ revealed that the self-diffusion ability determines the different electrodeposition behaviours of Li, sodium (Na), and Mg in 2014. In the 2D surface and 3D space diffusion, hexagonal close-packed Mg has a lower self-diffusion energy barrier (0.02 eV), while body-centred cubic Li and Na have higher energy barriers (0.14 eV and 0.16 eV, respectively). Therefore, during the early nucleation stage, Li and sodium tend to grow in island form rather than deposit as thin films (dendrite-free morphology) like magnesium.⁶² Larger surface formation energies and lower diffusion barriers are essential factors that contribute to the dendrites-free Li growth.

Heterogeneous Nucleation Model. The Li nucleation process occurs in each cycle. The initial nucleation condition is critical in the subsequent Li deposition. Three models are proposed to show Li depositing behaviour in the initial nucleation stages.

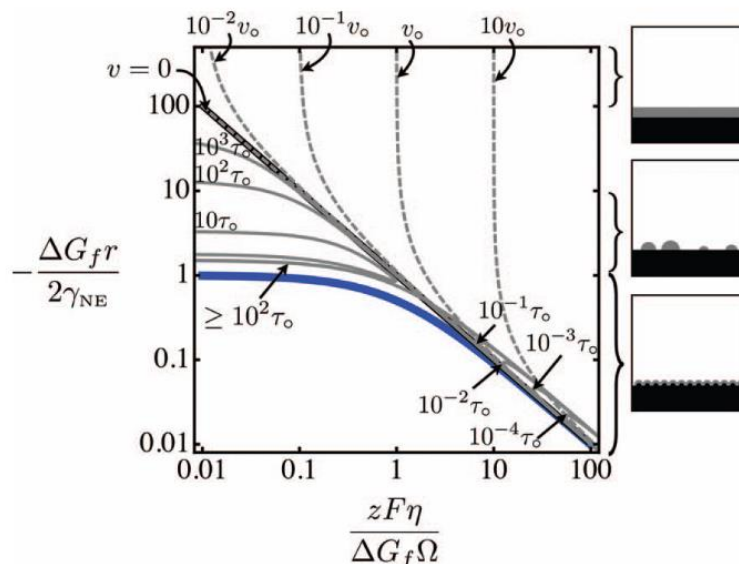


Figure 1.13. Five regimes of behaviour and growth pattern during the initial stages of heterogeneous nucleation.⁶³

In the initial nucleation process, Li^+ can deposit on the surface of the current collector

after obtaining electrons, which is considered the heterogeneous nucleation behaviour. The heterogeneous nucleation process is thermodynamically and kinetically demonstrated by Ely et al.⁶³ via numerical simulation. The complicated heterogeneous nucleation behaviour is clearly illustrated by five regimes, as shown in Fig. 1.13: a nucleation suppression regime, a long incubation time regime, a short incubation time regime, an early growth regime, and a late growth regime.^{34, 63} Embryos are thermodynamically unstable and are inclined to re-dissolve in the electrolyte in the nucleation suppression regime. In the long incubation time regime, embryos are thermodynamically stable. Then, embryos continue growing under favourable conditions after electric and ionic fluctuations. When exceeding a critical overpotential, embryos with narrow size are facilitated favourably in a short incubation regime. Finally, Li with a size of critical kinetic radius nucleates and grows quickly with overpotential enhancement. In the early and later growth regimes, kinetically and thermodynamically stable Li nuclei sequentially grow to approach the same terminal size. Only when the Li nucleus has been established steadily does the growth rate keep constant until the final form.^{34, 64} It is also proved that the difficulty of Li heterogeneous nucleation is largely based on the current collector material property, demonstrating a preferable heterogeneous nucleating model. Some studies showed that the nucleation overpotential of Li on the surface of Cu foil is about 40 mV, while there is no obvious nucleation overpotential on silver (Ag), gold (Au), and Mg metal surfaces.⁶⁵ Thus, It is possible to induce Li deposition intentionally by the substrate materials design.

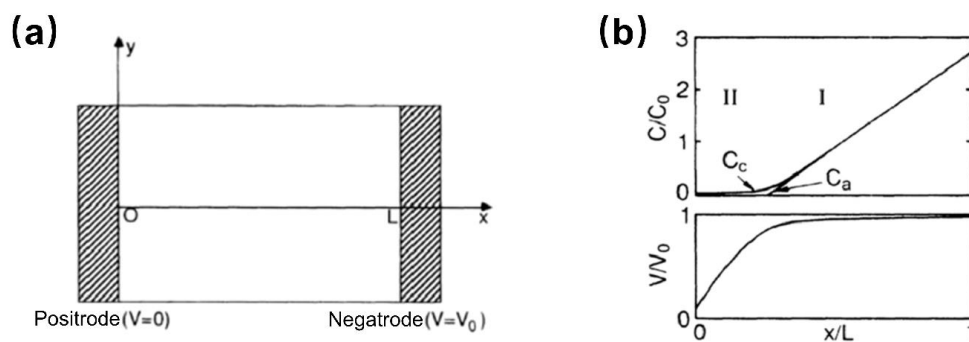


Figure 1.14. (a) Scheme of a battery and (b) profile of ion concentrations and

electrostatic potential, which result from the numerical simulation in the hypothetical case of uniform deposition. C_c : concentration of cations; C_a : concentration of anions; C_0 : initial concentration; V : potential; V_0 : initial potential; L : cell distance.⁶⁶

Space-Charge Model. Chazalviel proposed the space-charge theory⁶⁶ to describe the Li dendrite nucleation. The anions concentration decreases near the electrode surface during Li deposition at high rates in the dilute electrolyte. Then, anion depletion in the vicinity of the electrode surface leads to a super large space charge and an electric field near the electrode/electrolyte interfaces, resulting in a ramified Li deposit growth.⁶⁷ To illustrate the nucleation of Li dendrite induced by space charge, Chazalviel showed the distribution of electrostatic potential and ion concentrations in a dilute electrolyte by the thin rectangular symmetrical cell, as presented in Fig. 1.14a. Region I representing the quasi-neutral region and region II delegating the space-charge region are defined respectively in the battery (Fig. 1.14b). Region I refers to the bulk electrolyte, occupying a larger portion of the battery, where Li^+ transfer is dominated by diffusion. Region II occupies only a small region near the electrode surface, where ion transfer is controlled by electric field migration with a potential significantly smaller than 0V (negative potential). Then, the space charge $Z_c e C_c$ will be retained to drive the ramified growth of Li electrodeposits at a high rate in the dilute salt solution. Space charges are often observed in non-aqueous liquid electrolytes. Increasing the cation conductivity/transfer number or immobilizing anions can alleviate space-charge-induced dendritic Li growth.

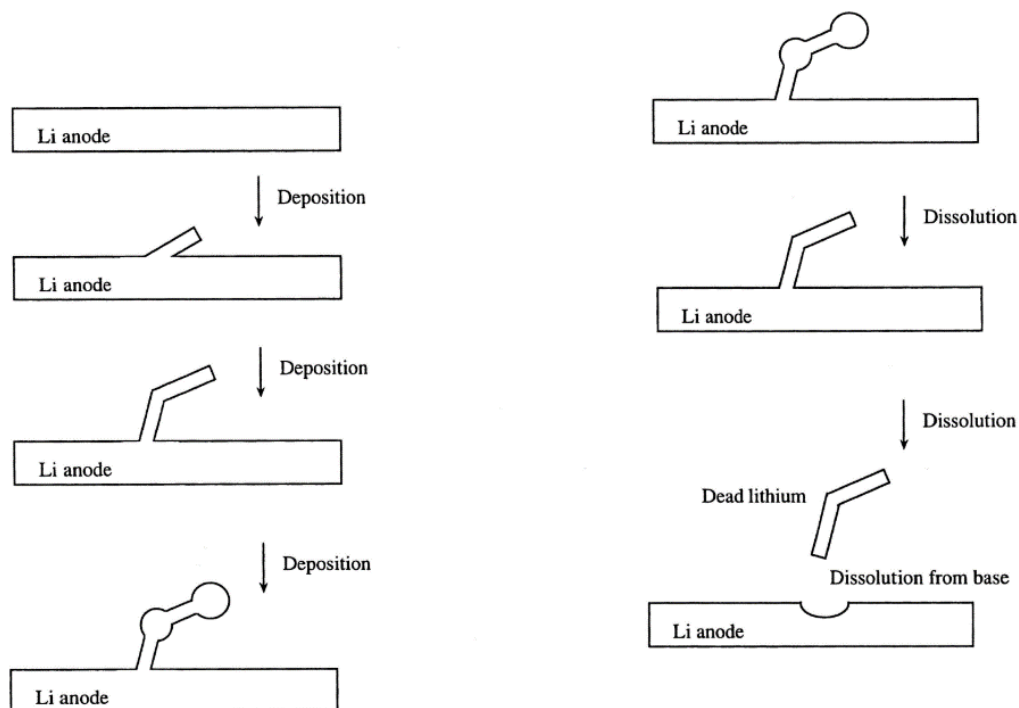


Figure 1.15. Stress model of Li deposition and dissolution⁶⁸

Stress and Plastic Deformation Model. The deposition/dissolution model can also be considered a stress model (SEI model) (Fig. 1.15). Yamaki et al.⁶⁸ hypothesised that there is an ionically conductive and electronically insulating protective layer on the surface of the LMNE and that the preferential Li deposition sites are located in the protective film with higher Li^+ conductivity. This uneven deposition will generate internal stress in the metallic Li under the protective film, causing Li diffusion creep. Since the creep of metallic Li is limited, the protective layer may be damaged, and internal stress will be released. Li will grow out of the cracked protective layer in the form of whiskers and gradually grow. Then, “dead Li” is formed in uneven dissolution. Based on this model, it is shown that a “hard film” with a surface tension greater than 0.2 N m could inhibit the growth of Li dendrites.⁶² This work also provides a good reference for the subsequent surface protection of LMNEs.

Monroe and Newman further extended the surface tension model to consider the effects of elasticity, viscous friction, and applied pressure comprehensively, discussed the

effects of these factors on the exchange current density and electrochemical potential on rough interfaces, and proposed that elastomers with high shear modulus, such as cross-linked polymer electrolytes, can effectively suppress dendrite growth. Therefore, to effectively inhibit dendrite growth, the elastic modulus of the separator needs to be three or more orders of magnitude higher than that of general polymer electrolytes. In addition, through theoretical calculation and fitting process, they believe that the top growth rate of Li dendrites is directly related to the current density.^{62, 69}

1.3.2. High activity of metallic Li

Li is the most reductive metal among all metal elements, and its outer electrons are very easy to lose to form Li^+ , which leads to high reactivity and thermodynamic instability.⁷⁰ Firstly, the storage and use of LM can involve severe safety issues. Alternatively, LMRBs with LM-free negative electrode may be more advantageous. Furthermore, almost all electrolytes, including solid-state electrolytes, will decompose when in contact with LM, forming various reduction products.⁷¹ For example, liquid electrolytes containing additives,⁷² solvents,⁷³ and Li salts⁷⁴ can be decomposed, polymerised, or adsorbed on the surface of metallic Li to form SEI films with an important influence on the deposition/dissolution of Li. Thus, component modification in the electrolyte is an important way to improve SEI film.

1.3.3. Volume expansion of Li metal negative electrodes

The huge volume change during deposition/stripping is another problem for LMNEs. Its variation is more severe than the alloy-type negative electrode, such as lithium-silicon. Such a large volume change means that, even if the electrochemical process is reversible, the mechanical stress generated by the reaction process can damage the electrode, resulting in the degradation of cycling performance. In addition, the volume increase will also accelerate LM's reaction with the electrolyte, further consuming the active Li and the electrolyte.

The volume change of metallic Li from dissolution to deposition is shown in Fig. 1.16. The volume expansion of metallic Li can be attributed to intrinsic Li deposition and the porosities of LMNEs. During the dissolution process, Li atoms lose electrons, migrate out of the SEI, and dissolve into the electrolyte (I). During the deposition process, the solvent molecules of the solvated Li^+ on the electrolyte/SEI interface are extracted, and naked Li^+ is deposited on the surface, becoming part of the metal lattice and forming a uniform coating (II). This volume change is assigned to the intrinsic Li deposition volume change. However, only when the SEI remains intact can this occur.

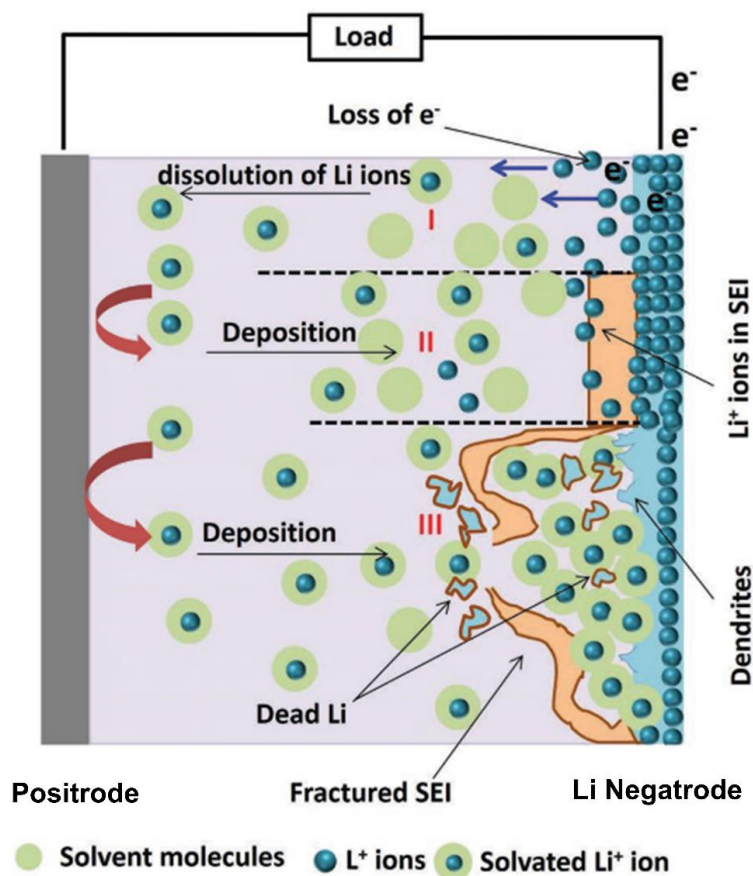


Figure 1.16. Schematic illustration of volume expansion in the LMNE.⁷⁵

In most cases, the SEI is ruptured. Thus, solvated Li^+ easily passes through the cracks on the SEI and deposits directly on the metal surface in an irregular form, leading to

the formation of Li dendrites, “dead Li”, and larger volume expansion (III) due to the large porosities. When the volume expands, the electrolyte molecules will immediately react with the freshly deposited Li on the negatrode surface to form a new SEI layer, providing a channel for the entry of solvated Li^+ . This process is repeated and continued until the electrolyte is consumed.⁷⁶

1.3.4. Practical challenges of Li metal negative electrodes

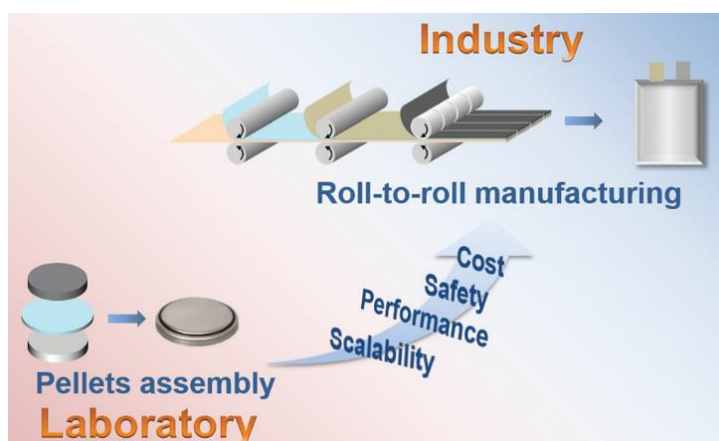


Figure 1.17. Challenges that LMRBs face from lab research to industrial production.⁷⁷

Besides the above-mentioned scientific issues in electrochemistry, attention should be paid to other key technical issues in the practical application of LMNEs. An important factor for LMNEs is their resistance to air and moisture, which are highly demanding for product storage and processing but receive little attention. When exposed to ambient air or moisture, LM is immediately eroded, forming a thick passivation layer consisting mainly of LiOH , Li_2CO_3 , and Li_3N . These reactions limit the processing of Li in expensive dry-room or argon-filled glove boxes and hinder the development of high-energy-density LMRBs. Li reacts more vigorously when in direct contact with H_2O , releasing a lot of heat and gas (H_2) within seconds. If LMRBs experience packaging leakage or mechanical abuse, and water happens to penetrate the damaged packaging, serious safety hazards such as burning or even an explosion can occur. Therefore, solving the atmospheric sensitivity of LM is of great significance for commercializing

LMRBs with reasonable processing costs and improved safety (Fig. 1.17).²⁷ Except for the limitations of the production environment, the production cost of LM is inversely proportional to its thickness. It means that if the pretty thin LMNE is used to achieve the higher specific energy, the cost will be greatly increased. Lastly, many strategies for modifying LMNEs have emerged recently, and attention should also be paid to the overall mass and capacity density of modified LMNEs. If the modification method introduces too high mass, the specific energy advantage of LMRBs will be lost.

1.4. Factors affecting the interface stability of Li metal negative electrodes

1.4.1. Current density

High or nonuniform current density on the current collector would cause the initial nonuniform nucleation density. The adverse effect of high current density has been demonstrated by the Chazalviel space charge model.⁶⁶ Compared to other prevailing models, the Chazalviel space charge model is one of the most popular models describing the Li nucleation and early Li dendrite growth stages.⁷⁰ In dilute solutions, the locations of the concentration of anions and Li^+ that decline to zero are near and at the negative electrode surface at high current rates, respectively (Fig. 1.18).⁷⁰

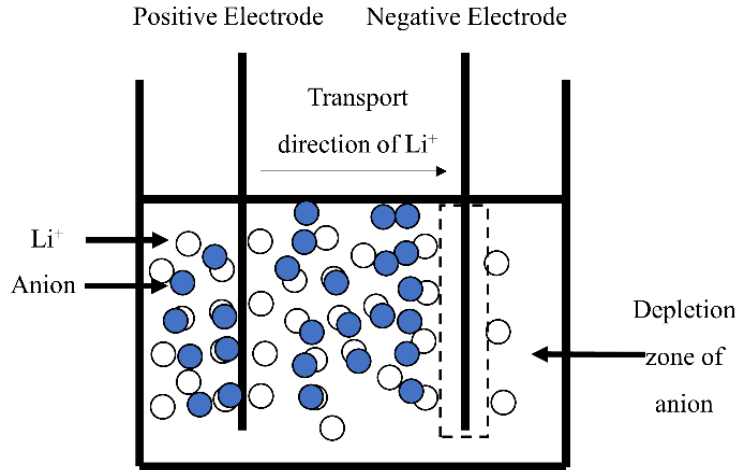


Figure 1.18. Schematic illustration of anions and Li^+ flow model (White balls are Li^+ ions and blue balls are anions).

Also, it is proved that concentration gradient⁷⁸ change of anions and Li^+ in electrolyte significantly depends on the current rate.⁷⁰ (Follow Rosso and co-workers' simulation work^{79, 80} as equation (1.1)).

$$\frac{\partial c}{\partial x}(x) = \frac{J\mu_a}{eD(\mu_a + \mu_{\text{Li}^+})} \quad (1.1)$$

where J represents the effective current density; D represents the ambipolar diffusion coefficient; e is the electronic charge; μ_a and μ_{Li^+} are the numbers of anion and Li^+ mobilities. According to equation (1.1), two diverse behaviours can be predicted depending on the interelectrode distance L , the initial concentration C_0 , the diffusion coefficient D , and the effective current density J . If $dC/dx < 2C_0/L$, the ionic concentration distribution at the negative electrode delivers a steady state with a constant concentration gradient potential value. The electrodeposits show a smooth morphology in this case. If $dC/dx > 2C_0/L$, high ionic concentration variation (ionic concentration ≈ 0) derived from high effective current density will make potential eventually diverge at a time τ , which is called the "Sand's time", as expressed in equation (1.2), where J stands for the effective electrode current density; D is the ambipolar diffusion coefficient; e represents the electronic charge; C_0 is the initial concentration, and t_a represents the transference numbers of anions. A certain relationship between equations (1.1) and (1.2)

can be found in equation (1.3), where t_a and t_{Li^+} represent the percentage of transference numbers of anions and Li^+ , respectively.⁷⁰

$$\tau = \pi D \left(\frac{c_0 e}{2J t_a} \right)^2 \quad (1.2)$$

$$t_a = 1 - t_{Li^+} = \frac{\mu_a}{\mu_a + \mu_{Li^+}} \quad (1.3)$$

The structure and morphology of the metal deposits can be dramatically affected by the ionic distribution near the negatrode.⁷⁹ Based on the Chazalviel space charge model, an employed current density would give rise to different ion concentration gradient behaviours: low effective current density creates a minimal and stable ionic concentration gradient and no Li dendrites. In contrast, highly effective current density leads to ionic concentration in the vicinity of the negatrode dropping to zero and the nucleus formation of Li dendrites at Sand's time (equation (1.2)).⁸¹ Thus, anion depletion in the vicinity of the electrode results in a large space charge and the electric field between the electrode and electrolyte, causing a ramified growth of Li electrodeposits. It is noted that if the effective current density can be decreased, the starting time of dendrite nucleation will be dramatically prolonged due to the inverse proportion relationship⁸² between J and τ . Thus, the low current density in the current collector greatly alleviates Li dendrite formation, especially at the initial nucleation stage.

1.4.2. Distribution of Li^+ flux

The distribution of Li^+ flux plays a decisive role in forming Li dendrites because of the apparent uneven distribution of Li^+ flux density, such as non-uniformity in the horizontal or vertical direction (Fig. 1.19) to the negatrode interface being one of the significant reasons for the dendrite formation. The definition of the distribution of the Li^+ flux and influences affecting the distribution of Li^+ flux will be clarified.

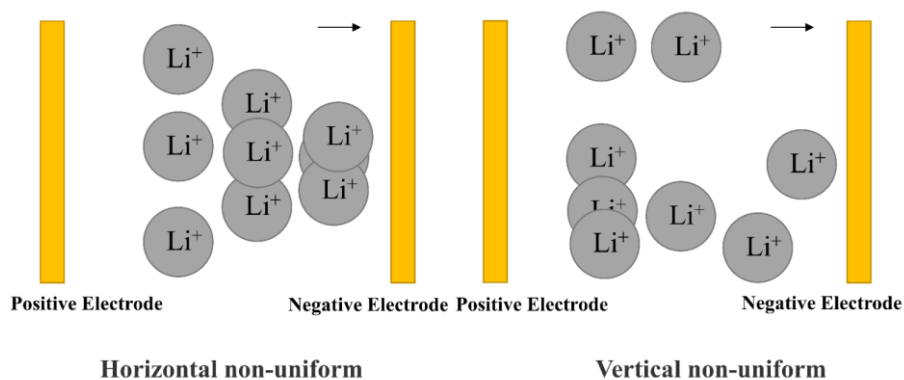


Figure 1.19. Non-uniform distribution of Li⁺ flux in the horizontal or vertical direction to the current collector surface.

The uneven distribution of Li⁺ flux at the electrode interface usually means that, in the horizontal or vertical direction to the electrode interface, the number of Li⁺ per unit area that reaches the negative electrode or can participate in the reaction at the negative electrode is inconsistent at the same time interval (Fig. 1.19). This can lead to rapid localized Li deposition, leading to the formation of dendrites. The factors affecting the Li⁺ flow's uniform distribution include the Li⁺ mass transfer process in the electrolyte, the current density on the electrode surface, and the uniformity of the SEI on the LM surface.

Mass transfer process. The electrode reaction consists of at least two continuous processes for Li electrodeposition. One is that the Li⁺ in the solution is transferred from the bulk electrolyte to the electrode surface through liquid phase mass transfer, which is called the liquid phase mass transfer step. The second is that the Li⁺ transported to the electrode surface is reduced by electrons on the electrode surface, which is called the electron exchange step. Usually, the electron exchange step is much faster than the liquid phase mass transfer process. Therefore, the proceeding speed of the whole electrode reaction is determined by the liquid phase mass transfer. In the actual electrochemical system, the liquid phase mass transfer mode on the electrode surface is a kind of convective diffusion. That is to say, the convection participates in the liquid phase mass transfer process on the electrode surface to a certain extent. The mass

transfer speed and flow rate of convection in different parts of the static electrode surface are not the same, which leads to different amounts of Li^+ being transmitted to different parts of the electrode surface per unit of time and results in the uneven flow of Li^+ .

Current density. Due to the difference in the microscopic topography of the electrode surface, the current density and reaction speed also varies in different regions. Usually, the areas with a smaller curvature radius or sharper and thinner areas are more likely to attract electrons and cause a larger current density. The deposition rate is faster at the places with high current density, and prominent Li growth is exhibited. Once this happens, the mass transfer flow of Li^+ reaching the protruding point will be further increased (on one hand, this is due to the shortening of the transmission distance; on the other hand, the mass transfer changes from a 2D to a 3D way), leading to the more serious uneven deposition. In addition, in the real pouch cell, the polarisation potentials at different distances from the tabs are different due to the inconsistency of the distance between the positrodes and negatrodes. This will also lead to the uneven distribution of the current density on the surface of the negatrode, causing the unevenness of Li^+ distribution.

Electrode surface SEI. Due to the high activity of LM, it is easy to react with the electrolyte to form an SEI film. In the electrochemical process, the composition and thickness of the SEI film will be highly affected by many factors. It is easy to have non-uniform SEI. Therefore, the flux of Li^+ passing through the SEI will also show non-uniform characteristics.

1.4.3. SEI properties

Solid Electrolyte Interphase. Theoretically, any available electrolyte can be reduced by metallic Li due to the strongly negative electrochemical potential of Li^+/Li . The SEI formed by the reaction of LM and electrolyte was discovered firstly by Dey in 1970⁸³

and named SEI by Peled in 1979.⁸⁴ To be of interest, the formation of SEI can be regarded as the passivation process which makes metallic Li not too reactive to exist under such a reductive environment and enlarge the voltage window to 4V and above. SEI's composition, structure, diffusion, and mechanical properties are closely related to the Li deposition morphology.⁸⁵ Especially, the uniformity of composition and structure in the SEI will directly affect the Li^+ flux, thus affecting the Li deposition/dissolution and stability of the electrolyte/electrode interface.

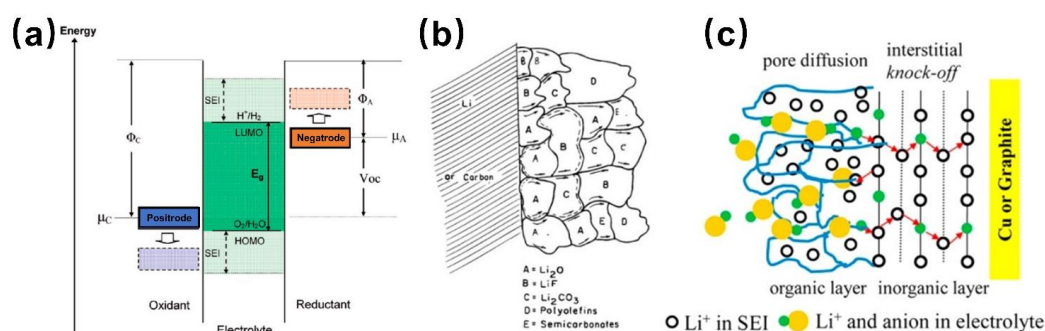


Figure 1.20. Schematic illustration of (a) SEI formation condition in a liquid electrolyte;⁸⁶ (b) Mosaic SEI structure in the top view;⁸⁷ (c) Dual-layer SEI structure in the cross-section view.³⁴

Composition property. Fig. 1.20a shows that the electron in LM intends to be transferred to the unoccupied orbital of the electrolyte whose electrochemical potential is lower than metallic Li, leading to the intrinsic reduction reactions of the electrolyte. It is widely accepted that the mosaic model with the inhomogeneous surface is described as the main SEI structure model, as shown in Fig. 1.20b. Accordingly, the component of SEI strongly depends on the composition of the electrolyte, thus whose reasonable modification determines the nature of SEI films.⁸⁸⁻⁹¹ In addition, SEI film with a dual-layer structure (Fig. 1.20c) consists of an inner layer labelled as the inorganic layer with species of low oxidation states such as Li_2O , Li_3N , LiF , LiOH , and Li_2CO_3 and an outer layer named as the organic layer with species of higher oxidation

states, such as ROCO_2Li , ROLi , and RCOO_2Li (R is an organic group related to the solvent). A possible mechanism illustrated that organic components are established by solvent, and inorganic components originated from the reactions between the salt and organic component.³⁴

Structure property. SEI structure will largely determine the Li deposition/dissolution behaviour. Cui et al.⁹² explored the effect of composition distribution on the structural stability of SEI by cryo-electron microscopy (Fig. 1.21). Mosaic and layered structures are generally recognised as two structural models of SEI. The fluctuation of the grain distribution (e.g., Li_2O , Li_2CO_3) is the key to distinguishing mosaic SEI from layered SEI, and SEI with different structures can significantly affect the Li deposition/dissolution behaviour. It is easy to form a mosaic-structured SEI in the traditional carbonate electrolyte. The nano-inorganic particles in the SEI layer are unevenly distributed, which will cause the metal to preferentially escape from the area with higher inorganic content, resulting in the collapse of the SEI structure. An inactive “dead Li” zone is formed, which in turn deteriorates the cycle stability of the battery. By adding 10 vol% FEC to the electrolyte, the SEI layer was transformed from a mosaic structure to a layered structure. The organic and inorganic components of the layered SEI are distributed more uniformly, and the Li^+ conduction rates of each area are equivalent. Thus, the Li dissolution can be more uniform, and the structure of the SEI layer can be well maintained. The SEI layer with a more uniform structure and composition can significantly reduce the LM loss during cycling and improve the battery’s cycling life. Therefore, the uniformity of the SEI structure and composition energy also significantly affects the performance of the LMRB.

Diffusion property. SEI can provide an essential path, especially when Li^+ gets desolvated and reduced to migrate through the electrode. It turns out that the diffusion behaviour of Li^+ in SEI can dramatically affect the morphology of Li deposition. The

high ionic conductivity of SEI is expected to induce the dendrite-free Li deposition morphology. Additionally, achieving an SEI with a lower activation energy barrier is more important to allow solvated Li^+ to transport freely.⁹³

Mechanical property. SEI with superior mechanical properties ($\sim 10^9$ Pa)⁹⁴ can alleviate its repeated breakdown and reparation, partly suppressing dendrite growth and achieving an efficient and safe battery system.⁹⁵ Thus, the artificial film with a high Young's modulus coated on the surface of LM, like Li_2CO_3 ⁹⁶ or Li_3PO_4 ⁹⁷ film, is much more rewarding to research. However, there is a competition between Young's modulus and adhesion, materials with high Young's modulus generally do not have good adhesion, and when the modulus exceeds a few MPa, the adhesion is greatly reduced. Therefore, if the SEI layer is a simple solid with a modulus of 6 GPa, it is difficult to adhere to the electrode surface, and poor adhesion will increase the interfacial impedance of the negatrode. Therefore, it is necessary to make comprehensive consideration to enhance the mechanical strength of the SEI layer.

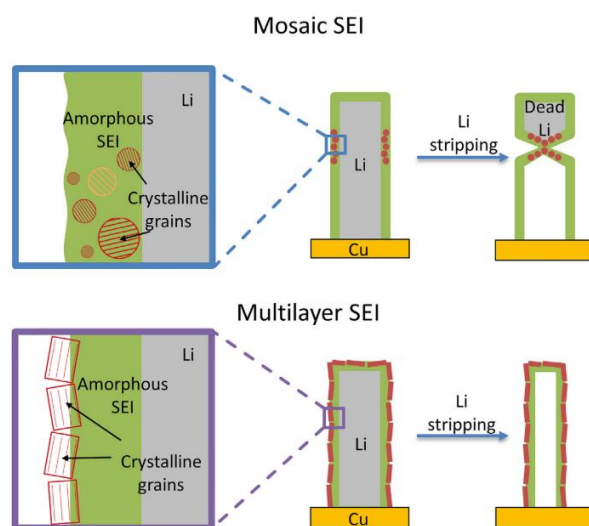


Figure 1.21. Li deposition/dissolution behaviour difference between mosaic and layered SEI.⁹²

1.4.4. Pressure

Due to the malleable nature of LM, a mechanically strong and confined structure can suppress Li dendrites' growth. Therefore, pressure as an important external influence will play an essential role in determining the morphology and cycling behaviour of the LMNE.

In 2018, Yin et al.⁹⁸ investigated the effect of applied external pressure on the electrochemical deposition of Li. A highly porous, wire-like Li growth can be found without pressure. In contrast, a much more compact Li deposit can be formed when applying pressure to the batteries during cycling. Meanwhile, improved Li deposition/dissolution behaviour in the pressed cells achieves a 5% higher CE (~90%) and more than 5-fold longer cycling life than those with no pressure.

Three years later, Zhang et al.⁹⁹ revealed the mechanism of external pressure on Li dendrites, which was quantified by a mechano-electrochemical phase field model. It is outlined that external pressure on a pouch cell can inhibit the progress of electroplating reactions, which decreases the rate performance of cells. Furthermore, external pressure on a pouch cell can shape the morphology of Li dendrites to be smooth and dense but cause mechanical instability. More specifically, there is a threshold level below which external pressure cannot work and above which external pressure linearly improves the performance of LMNE until the saturation stage is reached. Thus, applying external pressure on the LMRBs should be considered for practical application to improve their electrochemical performance.

1.4.5. Working temperature

The diffusion and migration of Li^+ and the electrochemical reaction at the electrode/electrolyte interface are affected by the working temperature, and the properties of the SEI layer are closely related to the interface reaction kinetics, so the

working temperature will greatly change the properties of the SEI layer.

McDowell et al.¹⁰⁰ investigated the morphology changes and the properties of SEI during Li deposition/dissolution at different temperatures (-80 to 20 °C) by cryo-electron microscopy. As the temperature decreases, the size of the deposited Li particles on the current collector becomes smaller. Moreover, compared with the SEI layer formed at -40 °C, the SEI formed at 20 °C is thicker, chemically, and structurally different and has a higher C and lower O content (Fig. 1.22). SEI formed at 20 °C mainly contain Li_2O and Li_2CO_3 microcrystals, while Li-F microcrystals are predominant in the SEI formed at 40 °C.

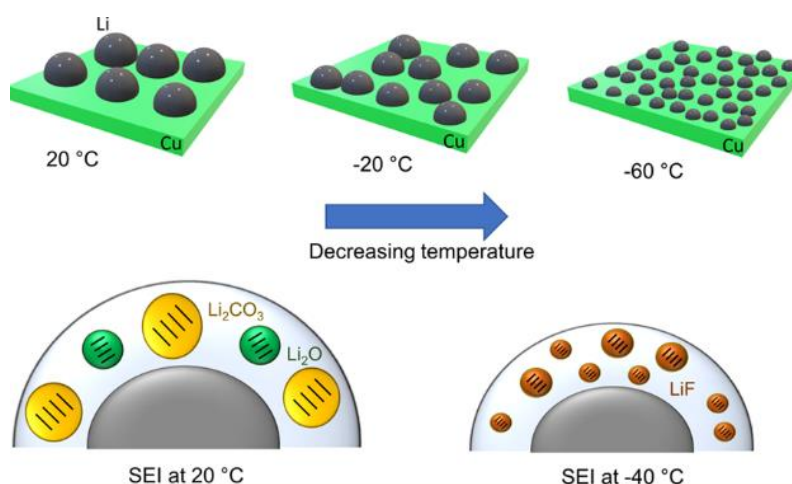


Figure 1.22. Schematic diagram of deposition morphology and SEI structure of LM at different temperatures.¹⁰⁰

Prof. Cui's team¹⁰¹ further studied the discrepancies in the nanostructure of SEI formed at 20 °C and 60 °C through cryo-electron microscopy. The mechanical property of the SEI containing amorphous polymers formed at 20 °C was worse and was more prone to fracture during cycling. This amorphous SEI has a limited passivation effect on the LMNE, which makes the SEI layer continuously broken and reformed during the repeated deposition/dissolution process, thereby reducing the interfacial stability of the LMNE. A thicker and more ordered SEI layer is formed on the surface of the LMNE

because of the higher reaction kinetics at 60 °C. This SEI consists of an inner layer of an amorphous polymer matrix and a layer of large grains of Li₂O, thus effectively passivating the metallic Li surface and maintaining mechanical stability during cycling.¹⁰² The above results show that the working temperature can change the structure and composition of the SEI layer by affecting the diffusion, migration, and interfacial kinetic properties of Li⁺, thereby affecting the interfacial stability and electrochemical performance.

1.4.6. Positive electrodes

At present, researchers pay less attention to the influence of positive materials on the interface of LMNEs. But during the practical operation of the pouch cell, if unstable positive materials such as NCM are selected, partial positive materials will be dissolved in the electrolyte. They will be deposited on the surface of the LMNE during the charging process. This unexpected side effect will affect the interface stability of the LMNE and even seriously cause the perforation behaviour of the LMNE. Therefore, relatively stable positive materials are also important for the long-term cycling of LMRBs.

1.5. Current modification strategies on Li metal negative electrodes

In the past few decades, the rapid development of materials detection and characterisation methods has enabled researchers to understand LMNE's performance deeply. To improve the stability of LMNE, many modification strategies in manipulating the surficial distribution of electrons and ions have been developed.

1.5.1. 3D current collectors

Current density is one of the key factors affecting Li deposition morphology, structure and composition of the SEI layer, and Li dendrite growth via manipulating the surface

distribution of electrons. Seong et al.¹⁰³ systematically investigated the effect of deposition amount and current density on the surface morphology of LM. High current density and high deposition capacity can lead to severe dendrite growth. The dendrite formation can be effectively suppressed when the current density and deposition capacity is relatively small. To reduce the effective current density in local areas without changing the macroscopic current density, it is persuasive to replace the 2D current collector with a porous 3D current collector. Furthermore, manipulating the nano architecture of the LMNE materials and minimizing LMNE dimension variation by stable hosts, skeleton structures, or 3D current collectors can undoubtedly accommodate Li deposition.¹⁰⁴⁻¹⁰⁹ 3D current collectors mainly consist of carbon-based 3D current collectors such as carbon nanotube,¹¹⁰ carbon fibre,¹¹¹ or graphene¹¹² and metal-based 3D current collectors such as Ni foam, Cu foam,^{113, 114} or stainless steel mesh.¹¹⁵ Usually, 3D metal-based current collectors are highly convenient and effective in reducing current density and accommodating LM volume change owing to their perfect electric conductivity and excellent mechanical properties. Qin et al.¹¹⁶ fabricated porous 3D Cu scaffolds using a powder metallurgic strategy and infused the 3D scaffolds with molten Li, followed by forming a Li-F layer to produce excellent 3D LMNE (Fig. 1.23a). It is found that the porous structure can effectively lower the local current density and alleviate the formation of dendrites, resulting in significantly improved rate capability and cycling stability.

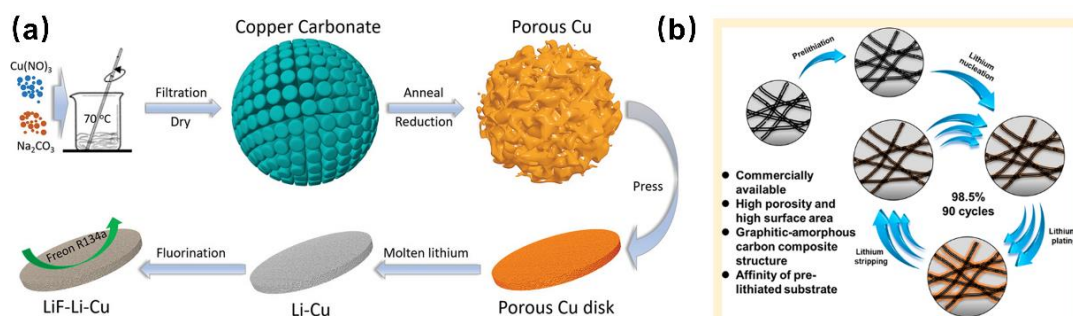


Figure 1.23. (a) Schematic demonstration of the fabrication of 3D Li-F-Li-Cu 3D composite LMNE.¹¹⁶ (b) Schematic demonstration of the Li plating and stripping process on carbon nanotube sponges.¹¹⁷

Carbon-based current collectors (CBCCs) have outstanding physicochemical stability, excellent conductivity, and diversified morphologies. More importantly, compared with metal-based current collectors, carbon-based material possesses a much smaller density ($<3 \text{ mg cm}^{-3}$), which won't adversely affect specific energy.¹¹⁷ Thus, they are ideal materials for developing LMRBs with a high specific energy. Yang et al.¹¹⁸ applied commercial carbon nanotubes (CNTs) sponges as 3D CBCCs for dendrite-free Li deposition to promote the CE and cycling stability of LMRBs. The high specific surface area of CNTs enhances the density of Li nucleation sites, ensuring uniform Li deposition. At the same time, the "pre-lithiation" process increases the affinity of porous CNTs for deposited Li. Meanwhile, high CE and cycling stability are achieved during Li deposition/dissolution on the CNTs sponges owing to the robust structure of the graphitic amorphous carbon composite in the ether-based electrolyte.

3D graphitised carbon can accommodate Li deposition depending on its porous structure and store Li by combining intercalation and electrodeposition mechanism. For instance, Guo et al.¹¹⁷ employed graphitised carbon fibre electrodes as 3D current collectors to store large amounts of Li through intercalation and electrodeposition reactions, as shown in Fig. 1.23b. The obtained negative electrode can deliver areal capacities up to 8 mAh cm^{-2} and does not exhibit apparent dendrite formation. Moreover, enlarged surface area and porous framework of graphitised carbon fibre electrodes can effectively reduce local current densities and mitigate high volume changes during cycling, resulting in low voltage hysteresis, high CE, and long lifetime.

1.5.2. Lithiophilic decoration

The core of lithiophilic modification is to achieve a more uniform Li^+ flow or to reduce the nucleation barrier of Li so that the nucleation density is increased and deposited Li is smoother. Cui et al.⁶⁵ developed rational nucleation grids on various substrates and measured the rational nucleation potentials on Au, Ag, Zn, Mg, Al, Pt, Si, Sn, C, Cu,

and Ni. They found that the nucleation overpotential was minimal on Au, as shown in Fig. 1.24a. Li can selectively deposit on Au with smoother morphology and larger nucleation density. Based on these findings, Xu et al.¹¹⁹ coated Au on a porous Cu to form a 3D current collector with excellent conductivity, high porosity, large specific surface, and superior lithiophilicity. Au can effectively improve the poor affinity between the Cu array and Li and enable uniform Li nucleation (Fig. 1.24b). The fast Li^+ transport channels through the Au/Cu array can be provided via the formation of Li–Au alloy, finally leading to the homogeneous Li deposit. As a result, a high CE of over 96% and a long and stable cycling lifetime of over 970 h were achieved.

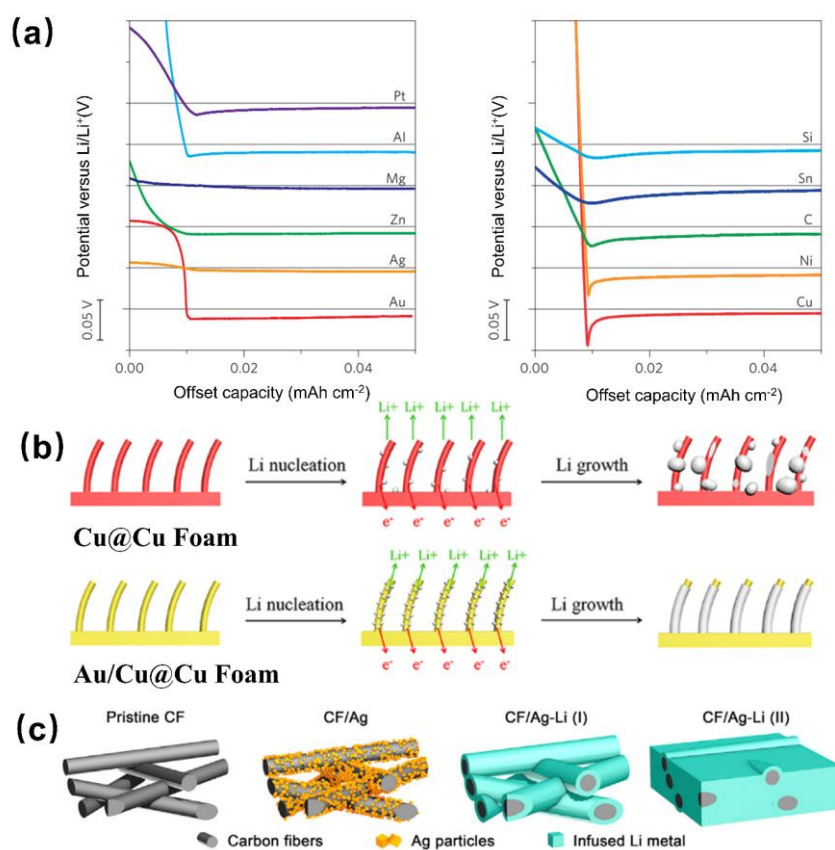


Figure 1.24. (a) Nucleation overpotential during Li deposition on various substrates with certain solubility and negligible solubility.⁶⁵ (b) Schematic illustration of Li plating/stripping on Cu@Cu foam and Au/Cu@Cu foam.¹¹⁹ (c) Fabrication of carbon fibre-based composite Li negatros.¹²⁰

Carbon-based material such as graphene or CNT is the prior choice due to its outstanding physicochemical stability, high Young's modulus, remarkable electrical conductivity, and large specific surface area. However, the practical application of carbon-based material is further hindered due to the lack of lithophilic properties. Thus, introducing a host with strong interaction with Li/Li⁺ can deliver a regulator of nucleation density and Li⁺ diffusion to improve the affinity of 3D CBCCs with LM. The introduction of lithophilic sites in carbon-based materials currently includes coupling with lithophilic materials¹⁰⁶ and introducing defect sites.^{121, 122} For coupling lithophilic materials, metal oxide or metal such as ZnO, Au, and Ag^{106, 123, 124} nanoparticles are easy to couple with lithiophobic CBCCs to accomplish the lithophilic process via alloying with Li. For instance, Cui et al.⁶⁵ designed a dense hollow carbon shell with a 3D structure encapsulating Au nanoparticles. Li can selectively deposit on the inside of a hollow carbon sphere with smooth morphology, mitigating the formation of Li dendrites. The results show that the cell can run more than 300 cycles at 0.5 mA cm⁻² with a CE of 98%. Zhang et al.¹²⁰ proposed a coral-like Ag-coated carbon fibre-based composite LMNE by infusing Li (Fig. 1.24c). Molten Li can be easily injected into the carbon fibre framework due to the lithophilic property of Ag toward Li. It is proved that dendrite-free morphologies and extraordinary electrochemical performance were obtained in LiFePO₄-based and sulfur-based LMRBs. The introduction of defects is to dope heterogeneous atoms such as N, B, and O atoms into the C₆ ring and break up the original electronegativity balance to enhance its affinity to positively charged ions (Li ions) called Lewis-base and acid interaction, as illustrated in Fig. 1.25,¹²⁵ finally achieving preferred nucleation behaviour.

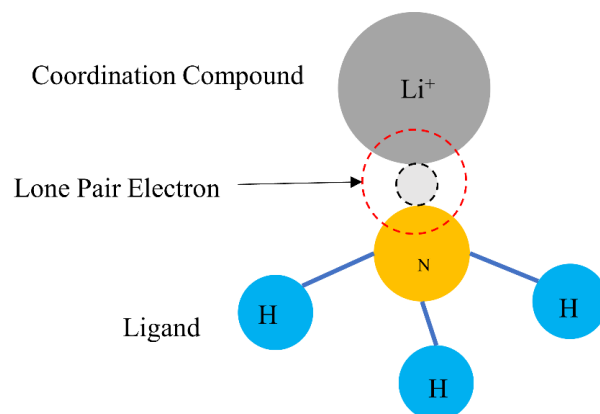


Figure 1.25. Schematic illustration of Lewis-base site and Li⁺ interaction.

Two methods perform highly different interaction mechanisms with Li, which makes them possess different application prospects in LMRBs. Schematic illustration (Fig. 1.26) and Table 1.1 are given to understand the lithiophilic mechanism difference toward Li in metal oxide/metal, e.g., ZnO/Zn, and Lewis-base site, e.g., R-N. Compared with metal, metal oxide involved in a redox reaction with Li will be first reduced to the pure metal before alloying with Li, which will consume more Li and increase irreversible Li. Furthermore, metal oxide/metal intends to interact with the Li atom, while the Lewis-base site is inclined to interact with the Li⁺. More importantly, the Li atom usually moves on the interface of the alloy-coated electrode to achieve uniform deposition, limiting Li mobility and increasing the possibility of side reaction with the electrolyte. In contrast, there are few restrictions on the mobility of Li⁺, which renders advantages in controlling interfacial distribution/migration of Li⁺ and Li⁺ diffusion flux in the bulk electrolyte. Meanwhile, no side reaction with electrolytes can be found.

Thus, coupling with lithiophilic metal materials can increase the complexity of the LMNE. More importantly, it can destroy the high specific energy of LMRBs. So, Lewis-base sites in carbon-based materials as lithiophilic sites exhibit superior potential value.

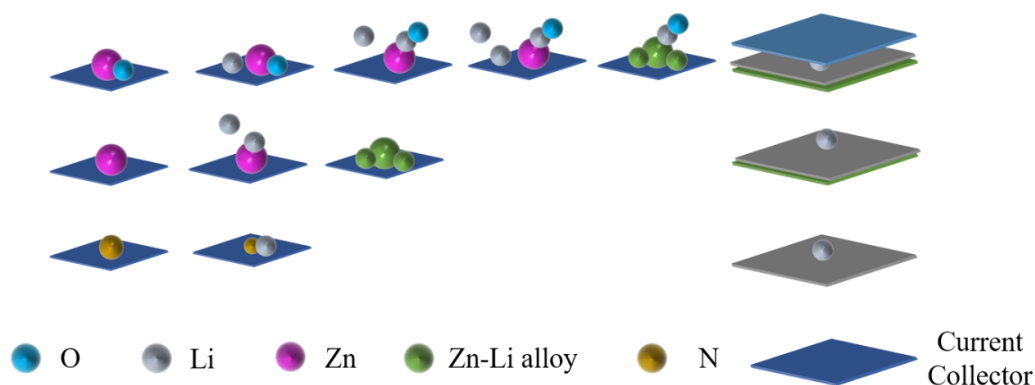


Figure 1.26. Schematic illustration of the lithiophilic difference in metal oxide/metal, e.g., ZnO/Zn, and Lewis-base site, e.g., R-N.

Table 1.1. Lithiophilic difference between metal oxide/metal and Lewis-base site.

Property	Metal/Metal oxide	Lewis-base site
Mechanism	Forming alloy	Adsorbing lithium ions
Mobility	Low (Interface)	High (Bulk+Interface)
Utilisation	Low	High
Stability	Side reaction with Li atom	No side reaction with ions
Reversibility	Low (reaction)	High (absorbing effect)
Density	High	Low (Thin & light)

It is reported that compared to the other electronegativity element, e.g., F, Br, Cl, S, and so on, N, B, and O are much more appropriate to act as Lewis-base sites in carbon-based materials.¹²⁶⁻¹²⁸ Nevertheless, current preparation methods to produce N/B/O-doped carbon-based materials usually involve a complicated fabrication process¹²⁵ with a relatively low yield and a small amount of introduced heterogeneous atoms.¹²⁹ Also, the pristine stable structure of the C₆ ring will be affected greatly due to the substitution of heterogeneous atoms. Thus, it is imperative to search for novel materials with a

uniform Lewis-base-rich site arrangement and a simple fabrication process. Graphitic carbon nitride (g-C₃N₄), which is regarded as a Lewis-base-rich semiconductor material, is commonly applied in the photocatalytic area relying on a narrow bandgap (~2.7eV) as shown in Fig. 1.27a-b.¹³⁰⁻¹³² It can be considered a natural lithiophilic material owing to its high N content of 57 at%.

Moreover, g-C₃N₄ possesses highly stable physical and chemical properties, and different morphologies can be achieved by direct thermal polymerisation via introducing templates.^{133, 134} Lewis-base sites derived from higher electronegativity N atoms can not only ease the non-uniform Li⁺ diffusion flux (Fig. 1.25) by strong interaction between the Lewis-base site and Lewis-acid site (Li ion) but also renders/induces more Li⁺ nucleation sites after coupling with the conductor (Fig. 1.27c).^{125, 135-138} Moreover, the N element can enhance the wettability of the material toward electrolyte.¹³⁷ Thus, it works reversely compared with a pure carbon material in terms of electric conductivity and lithiophilic properties.

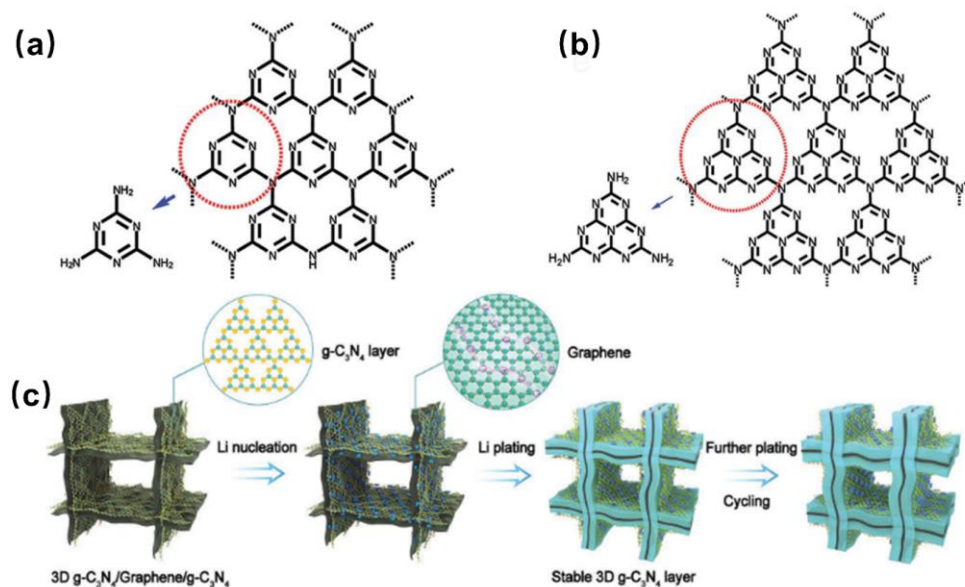


Figure 1.27. Graphitic carbon nitride with two different structures of (a) s-triazine and (b) tri-s-triazine.¹³⁹ (c) Schematic illustration of Li deposition on the 3D g-C₃N₄/G/g-

C₃N₄ electrode.¹⁴⁰

As a typical lithiophilic host to regulate the diffusion and deposition of Li⁺, g-C₃N₄ received much attention from researchers. Yang et al.¹³⁶ coated a 3D current collector with g-C₃N₄ to facilitate the uniform deposition of Li and suppress the formation of dendrites. Notably, the formation of a micro-electric field derived from tri-s-triazine units of g-C₃N₄ can induce numerous Li nuclei during the initial nucleation stage, which is proved by both density functional theory calculations and experimental studies. Moreover, the 3D structure of the current collector can accommodate volume expansion and stabilise the SEI layer during repeated Li plating/stripping. The remarkable electrochemical performance of this novel 3D current collector can be achieved. Gong et al.¹⁴⁰ fabricated a 3D current collector with insulator–metal–insulator sandwiched nanosheets (g-C₃N₄/graphene/g-C₃N₄) to guide uniform Li plating/stripping in the van der Waals gap between the graphene and the g-C₃N₄ (Fig. 1.27c). Li deposition on the surface of g-C₃N₄ can be suppressed because of its insulating nature. Thus, direct contact of the electrolyte with the LM is avoided. The g-C₃N₄ can be regarded as a high-performance 3D artificial SEI owing to its uniform lithiophilic sites and nanopore channels enabling homogeneous Li plating between the graphene and the g-C₃N₄. The results showed that g-C₃N₄-layer-modified 3D LMNE could support long-term Li deposition with high CE and stable cycling even under high positrode loading, limited Li excess, and lean electrolyte conditions,

1.5.3. Electrolyte design

Optimizing electrolyte components (especially additives or Li salts for SEI stabilisation) is an effective way to reinforce SEI formation and prevent dendrite propagation on the LMNE.^{74, 141-146}

Solvent. There are two types of electrolytes commonly used in LMRBs: carbonate-

based electrolytes whose solvents are EC, DMC, DEC, or PC, and ether-based electrolytes whose solvents are DME or DOL. Carbonate electrolytes have a wide electrochemical window but poor compatibility with LM, resulting in an unstable SEI layer and leading to the growth of dendritic deposition. Ether-based electrolytes have good compatibility with LM, especially DOL. They will decompose on the surface of LM to form a highly elastic passive polymer film, which effectively inhibits the growth of Li dendrites. However, the lower electrochemical window (<4.0 V) seriously hinders the practical application of ether electrolytes.¹⁴⁷ Since the SEI is a surface passivation layer formed by the reaction between the metal anode and the electrolyte at the solid-liquid interface, the properties of the SEI are closely related to the composition of the electrolyte. Compatible electrolytes are very important for stabilizing the LM interface. Functional additives such as fluoroethylene carbonate (FEC) and fluorinated ethers can decompose during discharge and promote stable SEI formation. Compared with non-fluorinated solvents with only high oxidative stability or good compatibility, fluorinated solvents can improve the electrolyte's oxidative stability and increase the Li-F content in the SEI layer, thereby enhancing the LMNE interface stability. Lucht et al.⁷³ investigated the mechanism for the performance enhancement of LMNEs by FEC (Fig. 1.28). Electrolytes containing FEC can effectively improve the electrochemical performance of LM symmetrical cells and LiFePO_4 -based full cells. It is demonstrated that the SEI generated from FEC-containing electrolytes is similar to the SEI generated from the baseline electrolyte. Yet, the corresponding Coulombic efficiencies are dramatically different after the initial plating. Electron microscopy results showed that FEC in the electrolyte could facilitate the formation of a unique SEI containing nanostructured Li-F particles on the plated LMNE and improve cycling performance.

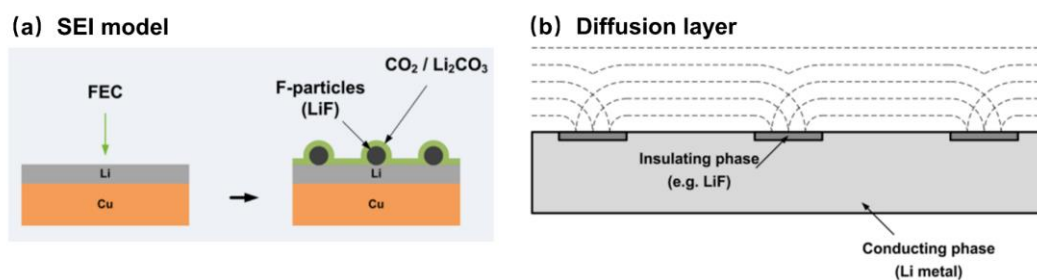


Figure 1.28. (a) Model of SEI generated from the FEC-containing electrolyte; (b) schematic of diffusion fields at deposited Li from FEC-containing electrolyte.⁷³

Lithium Salts. Anionic groups coupled with Li^+ often participate in the construction of SEI during Li deposition. Thus, SEI's composition, structure, and mechanical properties are highly affected by the types of Li salts. Rochelle Weber added dual-salt LiDFOB/ LiBF_4 in a liquid electrolyte, resulting in 80% capacity remaining after 90 charge-discharge cycles. This electrolyte additive enabled smooth dendrite-free Li morphology composed of densely packed columns even after 50 charge-discharge cycles.⁷⁴

In addition to researching new Li salts, increasing the concentration of Li salts in the electrolyte is also a promising method. The solvation induced by high concentrations of Li salts can impart special properties to the electrolyte. As shown in Fig. 1.29, the increasing concentration of Li salt reduces the content of free solvent, allowing more organic molecules and anions to coordinate with Li^+ , increasing the contact ion pair (one anion coordinated with one Li^+) and the content of aggregated clusters (where one anion coordinates with multiple Li^+).¹⁴⁸ This solvated structure can endow the electrolyte with new functions: (1) Improving the balance between ion and anion to prevent the loss of ionic strength and the appearance of Sand's singularity; (2) Reducing the LUMO energy level of the anion to increase the content of inorganic substances in the SEI and improve the stability of the LM interface; (3) The “salt-in-solvent” structure of the high-concentration electrolyte that improves the stability of the electrolyte and inhibits the electrolyte in oxidative decomposition at high voltage while reducing

solvent volatilisation and improving ionic conductivity.¹⁰² Zhang et al.¹⁴⁹ reported that high-rate LMNE cycling can be achieved with high Coulombic efficiencies (up to 99.1%) using a high-concentration electrolyte (HCE) consisting of ether solvents and LiFSI without generating dendrite growth. Using 4M LiFSI in 1,2-dimethoxyethane as the electrolyte, the LM symmetrical batteries can be cycled more than 6000 times at 10mA cm^{-2} , and the Li||Cu half cells can be cycled at 4mA cm^{-2} for more than 1000 cycles with the average CE of 98.4%.

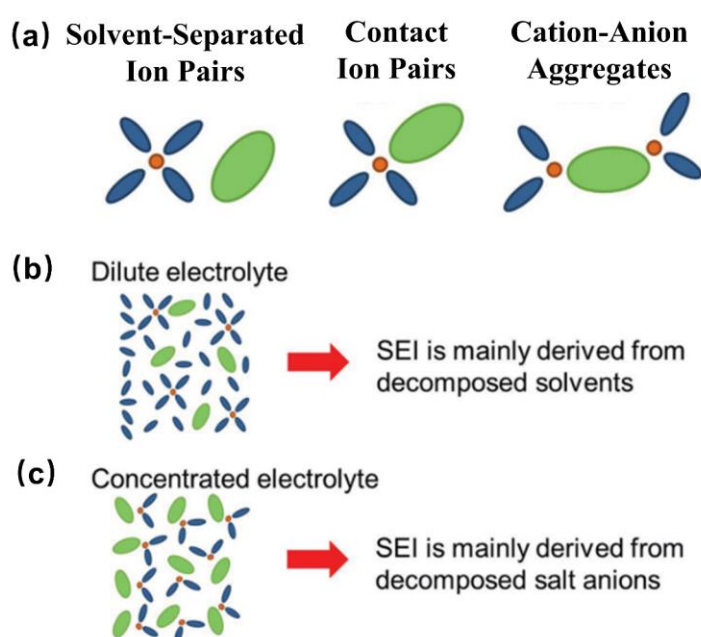


Figure 1.29. (a) Different Li^+ solvate species in dilute and concentrated electrolytes. Schematic demonstration of the electrolyte reduction mechanism at the electrode/electrolyte interface in (b) dilute and (c) concentrated electrolytes.¹⁴⁸

Although HCE provides a suitable route to address the problems associated with Li dendrites, excess Li salts can cause significant reductions in ionic conductivity, increased viscosity, poor wettability, and high costs. Studies have shown that these problems can be alleviated by adding co-solvents to the HCEs.¹⁵⁰ The co-solvent should be immiscible with the salt but miscible with the solvent and used as a diluent to form

a local high-concentration electrolyte (LHCE). Zhang et al.¹⁵⁰ revealed that a novel LHCE (HCE; 1.2 M LiFSI in a mixture of dimethyl carbonate/bis(2,2,2trifluoroethyl) ether (1:2 by mol)) enabled dendrite-free cycling of LMNE with high CE (99.5%) and excellent capacity retention (>80% after 700 cycles) of Li||LiNi_{1/3}Mn_{1/3}Co_{1/3}O₂ batteries. Li deposition experiments have shown that compared to the porous structure of deposited Li formed by conventional electrolytes or HCE, LHCE electrolyte is able to make the deposited Li smoother and form larger nodule-like Li particles.

Additive. Compared with adjusting the main components of commonly used electrolytes, incorporating very small amounts of additives may significantly alter the interfacial properties of electrodes, resulting in robust SEI films to stabilise LMNEs and promote uniform Li deposit. Based on this principle, various additives have been designed, such as FEC,¹⁵¹ vinylene carbonate,¹⁵² succinic anhydride,¹⁵³ methyl viologen,¹⁵⁴ thiourea,¹⁵⁵ LiNO₃,¹⁵⁶ and colloidal silica.¹⁵⁷

In contrast, some additives do not react with Li or the electrolyte during cycling. Zhang et al.⁷² added 0.05 M CsPF₆ to 1 M LiPF₆/PC, and a homogeneous and dendrite-free Li deposit was observed. It is found that caesium cations show an effective reduction potential below the standard reduction potential of Li⁺ at low concentrations. Caesium cations can form a positively charged electrostatic shield (self-healing electrostatic shield shown in Fig. 1.30) around the initial tip of the bumps without consumption and deposition of the caesium. Thus, dense, uniform ultrathin SEI (~1nm) is formed in the electrolyte containing Cesium cations. Besides Cs⁺, K⁺, and alkali metal ions, ions with potential close to the reduction of Li⁺ in small doses can also play a role through the self-healing electrostatic shielding mechanism.¹⁵⁸

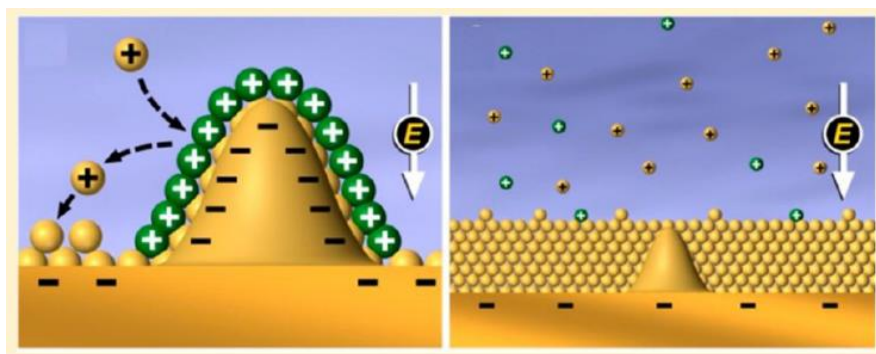


Figure 1.30. Exhibition of Li deposition process based on the self-healing electrostatic shield mechanism.⁷²

Solid state electrolyte. Modifying liquid electrolytes by employing solid-state electrolytes (SSEs) is another feasible strategy to suppress Li dendrites. SSE has high mechanical strength and Li^+ transfer number and avoids safety issues such as leakage, poor chemical stability, and flammability in liquid electrolytes. In addition, it eliminates the shuttle effect of soluble species (polysulfides or O_2).

SSEs in LMRBs mainly consist of two categories of materials: inorganic solid-state electrolytes and polymer solid-state electrolytes. Inorganic solid electrolytes contain many inorganic oxides and non-oxides with amorphous or crystalline structures, roughly divided into three categories: oxide electrolytes, sulfide electrolytes, and halide electrolytes.^{52, 159} Although the research on inorganic solid electrolytes has made significant progress, there are still problems with low ionic conductivity and high interfacial impedance. In addition, the interfacial properties between electrolytes and electrodes are another key factor affecting the performance of inorganic solid electrolytes.¹⁶⁰ The polymer as a solid matrix is used in polymer solid-state electrolytes, and thus, it has higher flexibility, better processability, and compatibility with LM. To date, diverse polymers, including polyethylene oxide (PEO),¹⁶¹ polyacrylonitrile (PAN),¹⁶² polyethylene carbonate,¹⁶³ polypropylene carbonate,¹⁶⁴ and so on, have been developed as polymer solid-state electrolytes.

Among them, PEO-based polymer solid-state electrolytes are the most widely used. However, it still confronts low ionic conductivities and poor mechanical and electrochemical stability, limiting their practical application.¹⁶⁵ Yang et al.¹⁶⁶ fabricated high-shear modulus solid electrolytes (including inorganic, polymer, and hybrid) to suppress dendrite penetration.^{166, 167} A solid polymer electrolyte comprised of PEO, g-C₃N₄, and LiClO₄ was fabricated by a facile solution blending method. This solid polymer electrolyte presents excellent ionic conductivity of $1.76 \times 10^{-5} \text{ S cm}^{-1}$ at 25°C, enhanced Li⁺ transference number (t_{Li^+}), and stable electrochemical window. The full cell paired with LiFePO₄ showed a high initial discharge capacity of 161.2 mAh g⁻¹ and superior cycle stability with a capacity retention ratio of 81% after 200 cycles at 1C at 80 °C. While pristine PEO-LiClO₄ only performs a low initial discharge capacity of 132 mAh g⁻¹ and a capacity retention ratio of 63% after 200 cycles.¹⁶⁶ It is worth noting that g-C₃N₄ plays a crucial role in high-performance solid composite polymer electrolytes, which improves the electrochemical stability of PEO-based solid polymer electrolytes and forms pathways for Li⁺ diffusion.¹⁶⁶

1.5.4. Artificial SEI

It is also an effective strategy to build an interfacial protective layer with uniform Li⁺ flux on the surface of LM, inhibiting the growth of Li dendrites and isolating the direct contact of the electrolyte toward LM. As an artificial SEI, this protective layer should have good mechanical properties, chemical stability, and tunable composition and structure. The artificial SEI layer that completely covers the surface of the LM can isolate the direct contact between the LM and the electrolyte, thereby avoiding the corrosion of the LM by the electrolyte. Benefiting from the development of technology, artificial SEI layers have been widely used in LM interface modification. According to material types, artificial SEI layers can be divided into the inorganic, organic polymer, and inorganic/organic hybrid protective layers.

Inorganic protective layers. Jing et al.¹⁶⁸ constructed a porous Al₂O₃ layer on the surface of LM as a protective layer in Li-S batteries by spin coating. The obtained Al₂O₃ layer can not only suppress the formation of dendrites to stabilise the LM/electrolyte interface but also prevent soluble polysulfides from contacting metallic Li to suppress their side reactions. Halides have good electrical insulation properties and are easy to prepare, and they can also be used as the material of the surface protective layer. Liang et al.¹⁶⁹ synthesised Li-rich composite alloy/LiCl films (e.g., LiZn/LiCl) *in-situ* on LM by directly reducing the metal chlorides with LM at room temperature (Fig. 1.31a). Alloy can provide a conduit for fast Li⁺ migration. Meanwhile, LiCl can work as an insulating surface component preventing the reduction of the Li⁺ on the surface of LM.

Carbon materials are also commonly used to protect LMNEs. As an artificial interface layer, Cui et al.¹⁷⁰ constructed a 3D interconnected hollow carbon nanosphere protective layer on the Cu current collector surface (Fig. 1.31b). The tetrahedral-bonded evaporated carbon lacks long-range order, resulting in a highly insulating surface. In contrast, the bulk electrical conductivity is as high as 7.5 S/m.¹⁰² Therefore, metallic Li is deposited under the hollow carbon nanosphere coating layer. Moreover, the graphite layer helps to form a stable SEI on top of the amorphous carbon nanospheres, preventing the penetration of solvent molecules. Protected by the hollow carbon layer, the LMNE can be stably cycled with high CE.¹⁰²

2D materials are also excellent for constructing artificial SEI layers due to their unique planar structures. 2D hexagonal boron nitride (h-BN) with excellent chemical stability, mechanical strength, and flexibility can be used as an artificial SEI layer to provide excellent interfacial protection for LMNE. During the Li deposition, Li⁺ passes through the point-line defects of the h-BN layer and deposits underneath, thereby avoiding the formation of mossy or dendritic Li and improving the cycling stability.¹⁰² Defects can significantly impact 2D materials by enhancing the chemical activity of defects. Thus,

2D materials can be selectively functionalised through chemical reactions to tune their physicochemical properties. LiF is selectively deposited on the point-line defects of h-BN by Xie et al.¹⁷¹ via chemical vapour deposition, resulting in the preparation of chemically and mechanically stable LiF/h-BN hybrid films (Fig. 1.31c). When this hybrid film is used as a Li-metal interfacial layer, the formation of Li dendrites can be effectively suppressed.¹⁰² Jeon et al.¹⁷² coated the g-C₃N₄ powder as the Li⁺ affinity centre on the Cu/LM foil. The confirmation of the nitrogen changed from pyridinic to graphitic in the presence of Li⁺, which verifies the coordination of Li⁺ to the pyridinic nitrogen (Fig. 1.31d). What's more, the movement of coordinated Li⁺ was facilitated by a site-to-site hopping mechanism. The electrically non-conductive nature of g-C₃N₄ allows Li to be plated with a dendrite-free deposit between the g-C₃N₄ layer and the Cu (or the LM).

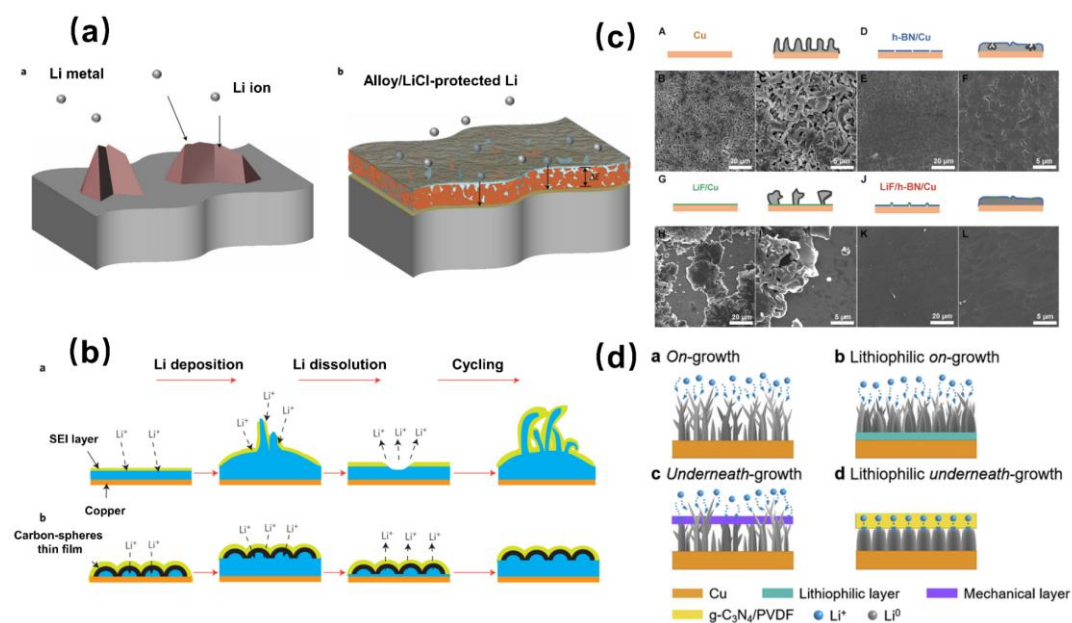


Figure 1.31. Examples of literature on inorganic protective layers. (a) Schematic illustrations of the function of the unprotected and alloy/LiCl-protected Li foil.¹⁶⁹ (b) Schematic diagrams of the Li deposit on the bare Cu foil and the modified Cu foil with a hollow carbon nanosphere layer.¹⁷⁰ (c) SEM characterisation of electrochemically plated Li. Schematics and SEM characterisation of electrochemical Li deposit on bare Cu, h-BN/Cu, LiF/Cu, and LiF/h-BN/Cu.¹⁷¹ (d) Schematic illustrations of LM growth

on and underneath the unprotected and lithiophilic protective (C_3N_4) Cu foil.¹⁷²

Organic protective layers. Due to their high flexibility and viscosity, organic polymers are an ideal artificial SEI layer. Its flexibility adapts to the volume change during the Li deposition/stripping, thus effectively stabilizing the LM interface. Diverse polymers such as Nafion,¹⁷³ poly(vinylidene difluoride) (PVDF),¹⁷⁴ polyallylamine hydrochloride,¹⁷⁵ and poly(dimethylsiloxane) (PDMS)¹⁷⁶ have been applied in the artificial SEI construction. Luo et al.¹⁷⁴ fabricated the Cu/Li coated with β -PVDF, which has a rather high polarity dielectric constant (Fig. 1.32a). The author found that the alignment of F atoms in the β -PVDF may play a critical role in raising the interaction between the electronegative C-F functional groups and Li, which facilitates the formation of dendrite-free Li deposits.

Although PDMS is widely used in microfluidic fields because of its process convenience and chemical inertness, regular PDMS film is not a Li^+ conductor compared with PVDF. Thus, Zhu et al.¹⁷⁶ employed acid treatment to intentionally create nanopores in the PDMS film to provide pathways for Li^+ transport (Fig. 1.32b). The flexibility of the PDMS film enables it to adapt to the volume change of metallic Li without cracking. However, unfortunately, the organic solvent can still migrate to the lower part of the PDMS layer through the nanopores, and side reactions will occur with the LM, resulting in the degradation of the battery performance. Bao et al.¹⁷⁷ focused on the electrolyte penetration issue and fabricated the dynamic single-ion-conductive network as a multifunctional (dynamic flowability, fast single-ion conduction, and electrolyte-blocking property) artificial SEI on LM (Fig. 1.32c). It is found that a multifunctional artificial SEI can simultaneously impede electrolyte penetration, alleviate the side reactions between LM and electrolyte, maintain low interfacial impedance, and allow homogenous Li deposition.

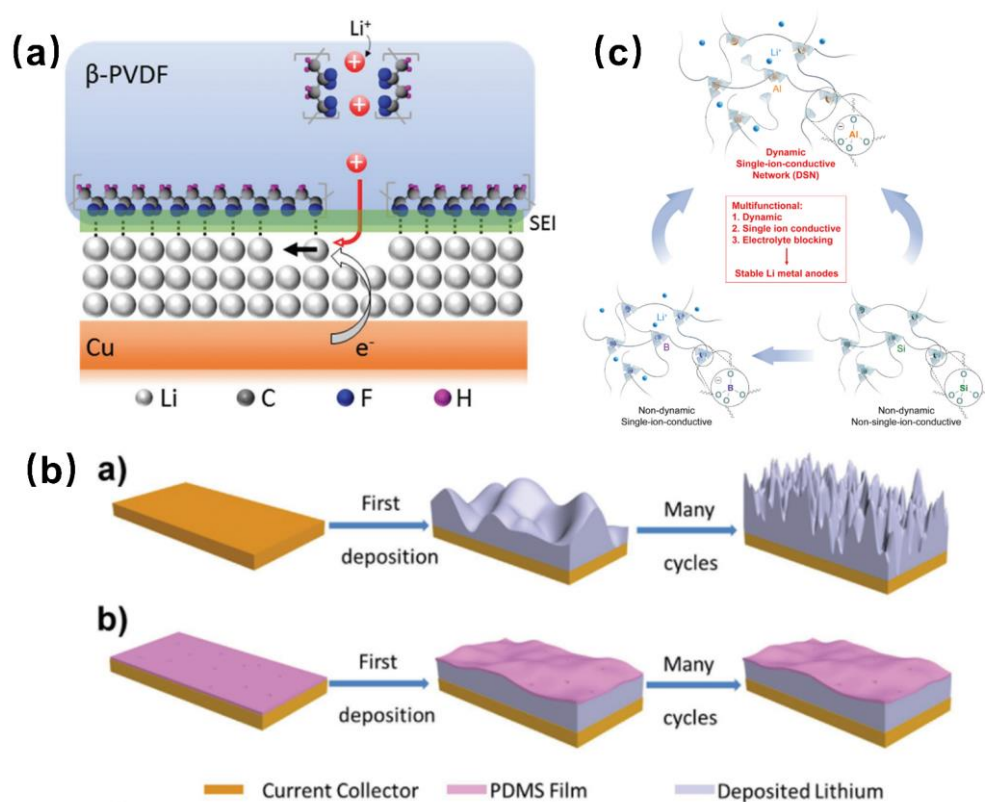


Figure 1.32. (a) Schematic demonstration of layer-by-layer Li deposition and preferential diffusion pathways for Li^+ .¹⁷⁴ (b) Schematic diagrams of the Li deposit on the bare Cu and Cu foil coated with PDMS film.¹⁷⁶ (c) Schematic diagrams illustrating the integration of dynamic flowability, fast single-ion conduction, and electrolyte-blocking property into a single matrix, the dynamic single-ion-conductive network.¹⁷⁷

Inorganic/organic hybrid protective layers. Although the artificial layer based on inorganic materials has excellent mechanical properties, its flexibility and viscosity are poor, reducing the contact with LM and increasing interface impedance. However, the mechanical properties of conventional polymer films are usually not ideal. Therefore, combining the high mechanical strength of inorganic materials and the flexibility and viscosity of organic materials to obtain an inorganic/organic composite artificial SEI layer has gradually attracted the wide attention of researchers.¹⁷⁸

This interfacial layer can inhibit Li dendrite growth while sustaining ionic flux, which is attributed to the nanoscaled pores formed among the nanoparticles. Cui et al.¹⁷⁸

reported a nanoporous, flexible, and electrochemically stable coating of silica@poly(methyl methacrylate) (SiO₂@ PMMA) core-shell nanospheres as an artificial layer on LM. The composite layer has both the high mechanical strength of SiO₂ and the flexibility of PMMA, which can effectively alleviate the volume expansion of LM and inhibit the growth of dendrites. Moreover, as a shell layer, PMMA can prevent the reaction between metallic Li and SiO₂ nanospheres, thus improving the long-cycle stability of the LM.¹⁰²

Therefore, the ideal artificial SEI should meet the following points as much as possible. (1) Artificial SEI having the appropriate Young's modulus and flexibility can inhibit Li dendrite formation and adapt to the volume expansion of LM (2) Artificial SEI has high-speed and uniform channels for conducting Li⁺. (3) Artificial SEI layer can prevent electrolyte penetration.¹⁷⁹

1.5.5. Others

In addition to optimizing the LMNE via the internal materials modification of the battery, various external strategies such as temperature^{180, 181} and pressure control,¹⁸² pulse plating technology,¹⁸³ magnetic field regulation,¹⁸⁴ etc., are employed. The above strategies can change the formation of the SEI, and improve Li deposition or Li⁺ distribution, finally inhibiting Li dendrites' growth.

As a key physical parameter, the temperature has an important influence on the formation of SEI and the viscosity of the electrolyte. Wang et al.¹⁸¹ studied the relationship between temperature, Li nucleation, and Li growth behaviour. As shown in Fig. 1.33a, increasing the temperature from -20°C to 60°C increases the nucleation size of Li and decreases the nucleation density. Still, the morphology of Li deposition becomes flatter and smoother. It is concluded that enhanced lithiophilicity and Li⁺ diffusion coefficient in electrolytes at high temperatures are important factors contributing to the formation of dendrite-free Li.

Pressure is another critical physical parameter that significantly affects Li deposition. Electrodeposition of Li mainly contains two modes:¹⁸⁵ root growth and surface growth mode. Typically, Li is deposited in a root-growing model and forms Li dendrites. After many cycles, the metallic Li will become loose and porous and then react with the electrolyte to form a large amount of “dead Li”. Extensive flocculent Li dendrite growth was observed in unstressed glass tube cells.^{62, 186} Chang et al.¹⁸² showed that additional pressure could effectively improve the density of the deposited Li compared with no extra pressure (Fig. 1.33b). Applying a certain stack pressure can make the LM avoid the root growth mode to inhibit Li dendrites and improve the cycle efficiency.

According to the Chazalviel model of Li dendrite growth, the inhomogeneous diffusion of anions and cations plays a decisive effect on the initial time of Li dendrite growth. Researchers try to apply pulse plating technology to tune the distribution and diffusion of ions inside the battery. Whittingham et al.¹⁸³ investigated the effects of pulse plating on the cycling efficiency of Li electrodeposition and deposit morphology with SEM. Compared with direct current electrodeposition, pulse-plating waveforms with short and widely spaced pulses improve Li deposition morphology and cycling efficiency under diffusion-controlled conditions (Fig. 1.33c).

The application of an external magnetic field can significantly disturb the reaction system, thereby reducing the concentration gradient of Li^+ and inhibiting the growth of dendrites. It is reported that the Li^+ suffering from Lorentz force due to the electromagnetic fields is put into spiral motion, which can cause a magnetohydrodynamics effect. Because the magnetic field and the distorted electric field are not parallel, the Li^+ will be affected by the Lorentz force and change the direction of movement. This motion of Li^+ will lead to the perturbation of electrolytes, which promotes the uniform distribution of Li^+ in the electric double layer (EDL) on the electrode surface. Lu et al.¹⁸⁴ employed the external magnetic field in a cycling

battery. Owing to the magnetohydrodynamics effect, mass transfer and uniform distribution of Li^+ can be promoted to suppress the dendrite growth and achieve a uniform and compact Li deposition, as shown in Fig. 1.33d.

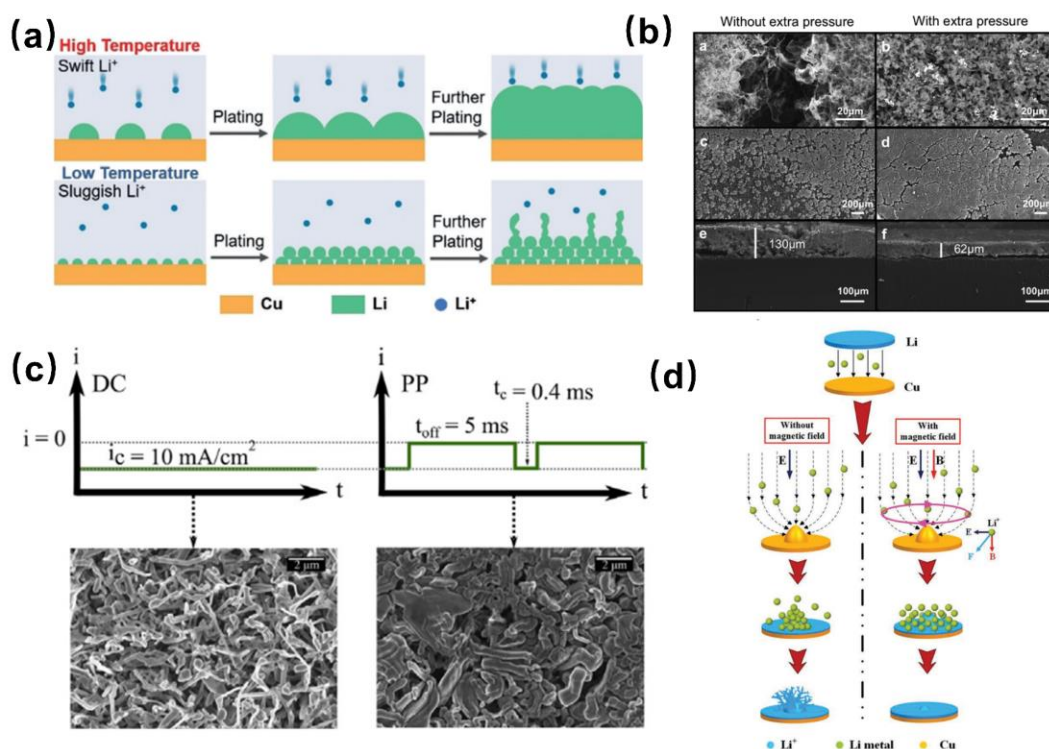


Figure 1.33. (a) Schematic illustration of Li nucleation and growth mechanism under high and low temperatures.¹⁸¹ (b) SEM images of Li microstructures generated under different external applied pressures.¹⁸² (c) SEM images of electrodeposited Li under direct current and pulse plating conditions.¹⁸³ (d) Schematic illustration showing the effects of magnetic field on Li^+ deposition process.¹⁸⁴

1.6. Thesis structure

The essence of lithium metal rechargeable batteries (LMRBs) is the repeated deposition and dissolution process of Li. Non-uniform Li deposition can result in infinite volume expansion, sharp capacity degradation, and dangerous short circuit, restricting the practical application of LMRBs. Based on the above introduction and discussion, the non-uniform Li^+ flow on the surface of the negative electrode and the non-uniform distribution

of electrons on the surface of the conventional current collector (e.g., Cu) are two key factors that lead to the non-uniformity of the Li deposition. For LMRBs, the LM is constantly immersed in the electrolyte. Due to its high electrochemical activity, it reacts more easily with the electrolyte to generate SEI that has certain insulation properties and uneven product distribution. This further amplifies the unevenness of the Li^+ concentration during diffusion and deposition, leading to uneven LM deposition. Therefore, the non-uniform distribution of Li^+ flux in LMRBs constitutes a significant underlying factor contributing to the formation of Li dendrites. N-containing functional groups can effectively interact with Li^+ , finally homogenizing Li^+ flow. Carbon nitride is the ideal material to regulate Li^+ flow in LMRBs. Thus, the purpose of the research of Chapter 3 in this thesis is to improve further the ability of homogenizing Li^+ on the surface of LMNE via pore structure regulation of carbon nitride. Chapter 4 aims to enhance the cycling performance of LMRBs modified with carbon nitride by replacing the suitable solvent to facilitate the formation of a Li-F-rich SEI. Lithium metal rechargeable batteries with a lithium-metal-free negative (LMFRBs) are another type of LMRBs and show a similar working principle as LMRBs. It can further enhance the specific energy of LMRBs and reduce manufacturing costs and safety risks. For LMFRBs, the current collector is directly exposed to the electrolyte. Li^+ migrating from the positive electrode directly deposits onto the current collector, inducing hetero-nucleation behaviour. As a result, the physical and chemical characteristics of the current collector, such as uneven distribution of current density, have a significant impact on LM deposition. Hence, constructing a current collector with uniform current distribution and a chemically stable interface is a pivotal strategy for mitigating the formation of Li dendrite. However, conventional current collectors such as Cu foil cannot provide even current distribution. They are easily eroded by air to form a non-conductive inert layer. Carbon materials such as CNTs or graphene have excellent electrical conductivity and perfect anti-corrosion capability, which can guide uniform Li deposition via reasonable design. Thus, the research in Chapter 5 aims to construct uniform current distribution by CNTs on Cu foil while eliminating their side reactions during Li deposition in

LMFRBs. The research in Chapter 6 aims to directly replace Cu foil by fabricating a free-standing graphene-based current collector with low density and high applicability. The details are listed below:

Chapter 3. Although carbon nitride materials can interact with Li^+ and homogenise the Li^+ flow, according to the Debye length law, the effective interaction distance of Lewis-acid & base usually needs to be at the nanometre scale. Therefore, in Chapter 3, we reported a new method to alleviate Li dendrites by porous carbon nitride microspheres (PCNMs) materials with abundant nanopores coated on Cu/Li foils. The hierarchical pores formed by the coating layer can accommodate LM's volume growth and fully homogenise the Li^+ flow. We characterise the Li deposition process in different carbon nitride materials to analyse the effect of physical space on Li deposition. In addition, the kinetics of Li^+ were evaluated on different carbon nitride materials to analyse the strength of their interaction force. The electrochemical properties of the LMNE before and after modification were investigated by symmetric cell and full cell tests.

Chapter 4. Although PCNMs materials with abundant nanopores can effectively homogenise Li^+ flow, it is still difficult to avoid the direct contact between LM and electrolyte during the cycling. Therefore, in Chapter 4, we report a method in which a Li-F-rich layer was built in advance on the surface of the Li foil@PCNM electrode to reduce the direct contact between the electrolyte and LM. A suitable solvent (DMAC) is chosen to promote the self-driven chemical reaction between PVDF and LM. We tested the corrosion of LM toward different solvents and carried out XPS characterisation to analyse the effect of different solvents on the surface composition of LM. In addition, the effectiveness of the coating material in achieving dendrite-free Li deposition and suppressing the volume expansion of LMRBs (*in-situ* swelling testing) was investigated. Finally, the electrochemical performance of symmetric half cells and full cells using modified LM prepared by different solvents was tested.

Chapter 5. Although the CNT-derived 3D current collectors can effectively uniformise the current density and homogenise the Li^+ flow, the large specific surface area and high Li intercalation capacity of carbon materials often cause negative effects such as electrolyte decomposition and the rise of irreversible Li during cycling. In Chapter 5, the CNTs network with a soft functional polymer PVDF is reported to form a relatively dense coating layer that can retain a uniform current density on Cu foil. It does not only effectively modify/protect the Cu foil but also shields the contact between the electrolyte and bulk CNTs to reduce side reactions. Simultaneously, the Li-F-rich SEI resulting from the partial reduction of PVDF by the deposited Li and the soft nature of the coating layer release the accumulation of internal stress in the horizontal direction to the current collector surface, resulting in mosses/whisker-free Li deposition. We characterise the SEI and Li deposition evolution to analyse the effect of surface coating on the SEI and morphology of Li deposition. The electrochemical performance of current collectors of surface coatings with different CNT contents and different kinds of polymers was studied, and half-cell and full-cell performance tests were carried out.

Chapter 6. Although CNT/PVDF composite coating layer on Cu foil can achieve dendrite-free Li deposition, the entire composite current collector is still physically heavy. Meanwhile, Cu is still chemically inappropriate for LMFRBs. Physically light carbon-based current collectors (CBCCs) with high conductivity, strong resistance toward corrosion by air or electrolyte, and more uniform current distribution can replace the Cu foil as a preferable deposition substrate. However, large-surface-area-induced (e.g., CNTs) consumption of limited Li (e.g., SEI), lithiation or electrolyte penetration-induced mechanical strength reduction, lithiophobicity-induced fragile SEI, and welding problems largely limit the application of CBCCs in LMFRBs. Therefore, in Chapter 6, a novel method for the preparation of the free-standing graphene/PVDF composite current collector with Cu tab is described. The PVDF effectively solves the problems of weak mechanical properties of carbon materials and unstable surface SEI. In addition, the tab welding process can be realised through ingenious etching

operations in the as-prepared CBCCs. We demonstrate the feasibility of this CBCC as a current collector for LMFRBs by testing the resistance, swelling, Li intercalation, and mechanical strength after cycling. The formation mechanism and process of SEI on the surface of this current collector are also characterised to demonstrate that PVDF can effectively promote the generation of excellent SEI. The morphology of Li deposition was characterised to prove the advantage of Li deposition. Finally, we also tested the electrochemical performance of half cells and full cells and carried out the failure analysis of the cells with CBCCs and Cu foil.

Chapter2

Methodology and Techniques

This chapter introduces the relevant methodology and techniques of this thesis. Also, this chapter describes materials preparation, cell assembly and different materials structure characterisations technology.

2.1. Materials preparation

2.1.1. Experimental reagents and consumables

Table 2.1. Experimental reagents and consumables.

Reagents	Specifications	Manufacturer
melamine	Pur. \geq 99.0%	Aladdin
cyanuric acid	Pur. \geq 99.0%	Aladdin
dimethyl sulfoxide (DMSO)	Pur. \geq 99.0%	Aladdin
Lithium iron phosphate (LiFePO₄/LFP)	—	Shenzhen BTR New Energy Materials Inc.
N-methyl-2-pyrrolidone (NMP)	Pur. \geq 99.0%	Sinopharm
LiNi_{0.8}Co_{0.1}Mn_{0.1}O₂ (NCM 811)	—	Ningbo Ronbay Lithium Battery Material Co., Ltd.
polyvinylidene fluoride (PVDF)	MW:1,000,000	Solef
multi-walled carbon nanotubes (CNTs)	Wt 4.3% (solvent: NMP)	Jiangsu Cnano Technology Co., Ltd.
single walled carbon nanotubes (SWCNTs)	Wt 0.4% (solvent:NMP)	OCSiAl
Super P	—	TIMCAL

Graphene powder	—	Ningbo Moxi Technology Co., Ltd.
Polyacrylonitrile (PAN)	MW:150,000	Aladdin
Polyethene oxide (PEO)	MW:2,000,000	Aladdin
N, N-Dimethylformamide (DMF)	Pur. ≥ 99.0%	Aladdin
Dimethylacetamide (DMAC)	Pur. ≥ 99.0%	Aladdin
carboxymethyl cellulose (CMC)	Pur. ≥ 99.0%	Cpkelco
styrene butadiene rubber (SBR)	Pur. ≥ 99.0%	JSR
Iron(III) chloride (FeCl₃)	Pur. ≥ 99.0%	Aladdin
Li_{1.14}Ni_{0.13}Co_{0.13}Mn_{0.54}O₂ (LR-NCM 114)	—	Ningbo Fuli Battery Material Co., Ltd.

2.1.2. Electrodes preparation

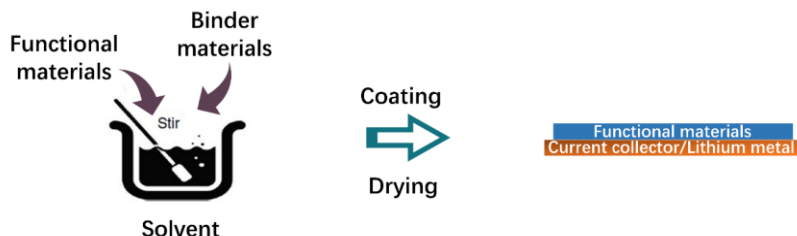


Figure 2.1. Diagram showing electrode preparation process.

Functional materials such as PCNMs or CNTs are mixed with binder materials in the solvent, followed by a coating and drying process as shown in Fig. 2.1. The final electrode can be obtained. Relevant modified LMNE and current collector preparation details have been put in the experimental section of each chapter.

Fabrication of LFP, NCM 811 and LR-NCM 114 positrodes. LFP slurry was prepared by mixing LFP powders, Super P, and PVDF in NMP in a mass ratio of 8:1:1 and coated on Al foil. The as-obtained LFP electrode was punched into disks with a

diameter of 14 mm as the positrode. The areal capacity of the LFP positrode was ~ 2 mAh cm⁻². NCM 811 slurry was prepared by mixing Ni-rich oxides, Super P, SWCNTs, CNTs, and PVDF in NMP with a weight ratio of 97.80:0.40:0.02:0.28:1.50 and coated on Al foil. The as-obtained NCM 811 electrode was punched into a disk of 14 mm in diameter as the positrode in the coin full cell or was tailored in 43 mm \times 53 mm as the positrode in pouch cells. The areal capacity of the NCM 811 positrode was ~ 2 mAh cm⁻² or ~ 3.75 mAh cm⁻². LR-NCM 114 slurry was prepared by mixing Li-rich oxides, Super P, and PVDF in NMP with a weight ratio of 96:2:2 and coated on Al foil. The as-obtained LR-NCM 114 electrodes were tailored to 62 mm \times 72 mm as the positrode in LR-NCM-114-based pouch cells. The areal capacity of the LR-NCM 114 positrode was ~ 6 mAh cm⁻².

2.2. Electrochemical Measurements

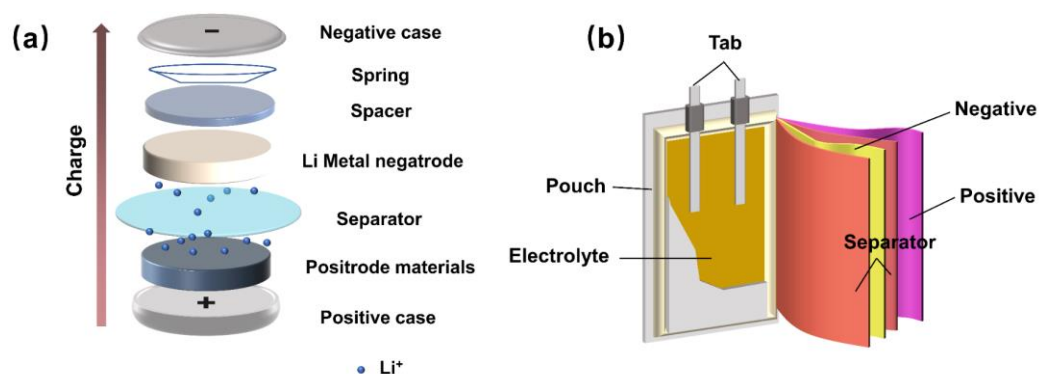


Figure 2.2. Diagram showing components of coin cell and pouch cell.

The required components of the coin cell and pouch cell are displayed respectively in Fig. 2.2. Relevant half/full/pouch cell preparation details have been put in the experimental section of each chapter.

2.3. Material structure characterisations

The microstructure of samples was recorded by a Hitachi S-4800 field emission

scanning electron microscope (SEM). X-ray diffraction (XRD) patterns were performed using an AXS D8 Advance diffractometer (Cu K α radiation; receiving slit, 0.2 mm; scintillation counter; 40 mA, 40 kV) from Bruker Inc. The Fourier transform infrared (FTIR) spectrophotometer (Thermo-Fisher, Nicolet 6700) was used to characterise the chemical structure. The measurements of X-ray photoelectron spectroscopy (XPS) (Axis Ultra DLD) were conducted using Al K α monochromatic beam (1486.6 eV) and C 1 s peak (284.8 eV) to calibrate. High-resolution transmission electron microscope (TEM) images were obtained by transmission electron microscopy (TEM, FEI Tecnai F20) operating at 200 kV. The Li||Cu coin half cell in a sealed quartz cuvette was measured for the *in-situ* Raman analysis. The Renishaw in Via Reflex micro-Raman was equipped with an exciting laser of 785 nm. A focused ion beam (FIB) (Helios-G4-CX) was carried out to reveal the intrinsic cross-section view of samples. Surface tension/dynamic contact angle (DCAT21) was measured to show electrolyte wettability toward the samples. N₂ adsorption-desorption measurements (Micromeritics ASAP 2020 analyser) were conducted at 77 K. Atomic Force Microscope (AFM) using Dimension ICON was used to obtain the physical property of electrodes. The samples' mechanical property was recorded using a 1KN materials testing machine (Zwick/Roell Z1.0). Thermogravimetric analysis (TGA) was employed using a thermogravimetric analyser (TGA209F1) by sealing the samples in a stainless-steel crucible in an air atmosphere. The heating rate was 10°C min⁻¹.

2.4. Ionic conductivity tests

The as-prepared BCN, SCN, or PCNM powders were mixed with PVDF and LiTFSI in NMP (as solvent) with the 1:1:1 mass ratio of BCN, SCN, or PCNM to PVDF to LiTFSI. After stirring for 10 h, the slurry with a thickness of 200 μ m was cast on a Cu foil and vacuum-dried at 80°C for 6 h. The as-obtained BCN, SCN, PCNM, and LiTFSI@Cu were punched into disks with a diameter of 19 mm as the working electrode. The steel disc with a diameter of 14 mm was used as the counter electrode.

The EIS of the cell is tested at various temperatures. The ionic conductivity was calculated following equation (2.2) below:

$$\sigma = \frac{L}{R \cdot S} \quad (2.2)$$

where σ stands for ionic conductivity, L is the solid-state electrolyte thickness, R is the resistance, and S is the contact area of the steel disc.

2.5. *In-situ* swelling tests during charging/discharging



Figure 2.3. *In-situ* swelling test cell.

The as-prepared 14 mm discs of bare Li foil or Li@PCNM-DMAC and NCM 811 were employed as the negatropes and positropes, respectively. The areal capacity of the NCM 811 positrode was $\sim 4 \text{ mAh cm}^{-2}$. The areal loading of the bare Li foil or Li@PCNM-DMAC negatrode was 20 mAh cm^{-2} . Celgard 2500 was used as the separator ($25 \mu\text{m}$). The electrolyte of $225 \mu\text{L}$ 1 M LiPF_6 in EC/DMC=1:1 by volume with 2 wt% FEC was employed herein in an *In-situ* swelling test cell (Fig. 2.3). The cell was shelved for 8 h before testing. The above cells were galvanostatically charged up to 4.3 V and then galvanostatically discharged to 2.6 V at 0.25C for 3 cycles before 0.1C for 1 cycle for the activation procedure. There is no extra applied pressure in the swelling test cell

during charging/discharging. Initial volume swelling data is corrected to 0. As cell cycling, real-time volume swelling data is recorded as the volume change of the battery.

2.6. Simulation methods

The hexagonal primitive cell was used to model pristine graphene. The linear cell was used to model pristine (PVDF) $-(C_2H_2F_2)_n-$ ($n=3$). A $1 \times 1 \times 1$ k-point mesh, including the G-centre, was used to sample the Brillouin zones. The first-principles calculations are performed by density functional theory (DFT) using the Vienna ab initio Simulation Package (VASP) code.^{187, 188} The exchange and correlation functionals are implemented by the generalised gradient approximation (GGA) of the Perdew-Burke-Ernzerhof functional.¹⁸⁹ The thickness of the vacuum layer over 15 \AA is set to avoid interactions between adjacent layers. Structures are fully relaxed until the force converged on each atom is less than 10^{-2} eV/\AA , and the energy criteria is set to 10^{-6} eV . In all calculations, the plane-wave cut-off energy is set to 450 eV .

Chapter3

Porous Carbon Nitride Microsphere Layer with Nano-Channel- Based Physical and Chemical Synergic Regulation for Dendrite- Free Lithium Plating

This chapter reports the fabrication of the novel Li negatrod with a uniform lithiophilic coating layer having hybrid pores with both nanometre and micrometre scales. Porous carbon nitride microspheres (PCNMs) not only provide the physical 3D porous framework to absorb volume changes and guide Li growth but also render suitable chemical interaction distance to effectively homogenize the lithium ion flux. Such a physical-chemical synergic regulation strategy can improve Li plating/stripping cycling performance.

3.1. Introduction

As we talked about in Chapter 1, LM has been widely denoted as the most promising negatrod material in Li-based batteries. Nevertheless, the practical application of LMRBs has been impeded mainly by physical/chemical problems of the LMNE. Infinite volume expansion of the LMNE is a non-negligible issue, which is much more severe than graphite ($\approx 10\%$) and silicon ($\approx 400\%$) negatrod materials.^{105, 170} Meanwhile, Li tends to deposit in dendritic morphology in completely open spaces without any physical constraint.¹⁹⁰ Moreover, uneven Li^+ flow may result from inconsistent SEI layer or surface defects at the electrode/electrolyte interface, leading to localized Li^+ concentration and preferential Li growth on tips or protrusions.

Over the past decades, researchers have developed different strategies, including constructing artificial protective SEI layers,^{169, 191-195} electrolytes optimisation (e.g., adding functional salts¹⁴¹⁻¹⁴³), and current collector modification^{65, 107, 109, 110, 118, 138, 196} to achieve confined growth of Li or reduce parasitic reactions. Recently, 3D scaffold decoration on LMNE was reported as a viable alternative to physically guide the confined growth of Li and efficiently suppress the volume expansion.^{109, 190, 194, 197, 198} In addition, depending on their non-conducting or weak-conducting properties, 3D scaffolds easily could avoid the top deposition that usually occurs in traditional 3D current collectors. Meanwhile, scaffolds with abundant polar functional groups were confirmed to regulate Li⁺ diffusion toward uniform Li deposition chemically.^{109, 197}

Nitrogen doping of carbon materials (e.g., N-doped graphene¹²⁵) is a typical way to provide polar functional groups (e.g., pyridinic nitrogen and pyrrolic nitrogen) for 3D scaffolds, which can interact strongly with Li⁺ and enhance the lithiophilicity to alleviate inhomogeneous Li⁺ flux.¹³⁵ g-C₃N₄ with an ultra-high N content of up to 57 at% was recently demonstrated to show remarkable affinity toward Li⁺ by forming transient Li-N bonds, which could powerfully facilitate deposition kinetics at the vicinity of the negatodes.^{137, 138, 199-201} For instance, 3D Ni foam coated with g-C₃N₄ sheets could guide Li deposition by adjusting the interfacial micro-electric field owing to the affinity of N-containing functional groups with Li⁺.¹³⁶ In addition, ultrahigh shear modulus up to ~21.6 GPa within g-C₃N₄ could help suppress the dendrite proliferation during cycling.²⁰² Therefore, Lewis-acid and base-interaction-induced lithiophilic properties and excellent mechanical strength intrinsically endow g-C₃N₄ with promising applications in stabilizing Li deposition.

However, a fundamental issue on the effective interaction distance between Li⁺ and N-containing functional groups has not yet been fully resolved in the past and ongoing studies.^{109, 190} It is well known that the Li⁺ fluid behaviour in 3D scaffolds is significantly determined by the size of the fluid channel. In macroscopic fluids, the role

of the EDL is often neglected because of the large size of the fluid channel. However, when the fluid channel size shrinks to the nanometre scale, the EDL plays an important role in regulating Li^+ flux.¹⁹⁷ Meanwhile, based on the Debye length law, as shown in equation (3.1),²⁰³ large pores can hardly provide rational space to launch efficient interaction between electronegative atoms and Li^+ .

$$L_D = \left(\frac{\sum_i n_{\infty i} e^2 z_i^2}{\varepsilon_{rs} \varepsilon_0 k T} \right)^{-1/2} \quad (3.1)$$

where L_D is the Debye length, $n_{\infty i}$ the ionic concentration, e the electron charge (1.6×10^{-19} C), z_i the ion valence, ε_{rs} the dielectric constant of the solution, ε_0 the dielectric constant of vacuum (8.85×10^{-12} F m⁻¹), k the boltzmann constant (1.38×10^{-23} J K⁻¹), and T the temperature. The Debye length reflects an important characteristic of the charge shielding effect. In our system, the N in PCNM is regarded as an electron-rich element (Lewis-base), while Li^+ is positively charged (Lewis-acid). Due to the law of Lewis-base and Lewis-acid interaction, N-containing groups are always surrounded by Li^+ , but their electric field can only act within a certain distance. Accordingly, the Debye length that reflects the range of electrostatic forces to interact with Li^+ in the electrolyte is possibly distributed at the nanometre scale. Beyond this distance, N-containing groups will be shielded from the electrical field of the surrounding opposite particles. Only when the distance between N-containing groups and Li^+ is less than the Debye length is there indeed effective interaction between them. Thus, channel widths in a 3D scaffold should be limited to the nanometre scale to regulate Li^+ flux effectively.

Based on the Debye length and excellent lithiophilic properties of g-C₃N₄, we have developed porous carbon nitride microspheres (PCNMs), which contain abundant nanometre pores as structural units of a 3D scaffold. When coating PCNMs on Cu or Li foils, the nano-pores inside PCNMs can effectively homogenise the Li^+ distribution to promote homogeneous Li^+ deposition and construct a robust SEI through the chemical interaction between Li^+ and g-C₃N₄, while the interparticle micro-pores can provide enough space to accommodate and guide Li growth and physically relieve volume expansion. This physical and chemical synergic regulation strategy contributes

to improved Li deposition/dissolution, resulting in stable cycling performance of the LM cells.

3.2. Experimental section

3.2.1. Materials preparation

Synthesis of bulk graphitic carbon nitride powder (BCN). 10 g of melamine was placed in a covered crucible. The crucible was heated at a rate of $2^{\circ}\text{C}\cdot\text{min}^{-1}$ to 550°C and held at 550°C in an argon atmosphere for 4 h. Stiff yellow g- C_3N_4 monolith was acquired after cooling to room temperature, which was then ground in a mortar to form g- C_3N_4 powders.

Synthesis of sheet carbon nitride (SCN). 5 g of melamine was dispersed in 30 mL of deionised water under continuous stirring for 30 min. Then the mixture was transferred into a 70 mL Teflon-lined stainless-steel autoclave and heated at 200°C for 12 h. After cooling, the precipitates were centrifuged and washed repeatedly with deionised water and ethanol and dried at 80°C for 12h, followed by calcination in a covered crucible at 550°C for 4 h with a heating rate of $2^{\circ}\text{C}\cdot\text{min}^{-1}$ under argon to obtain yellow g- C_3N_4 nanosheets.

Synthesis of porous carbon nitride microspheres (PCNM).^{204, 205} 7.92 mmol of melamine was dissolved in 40 mL of DMSO, and equimolar cyanuric acid was dissolved in 20 mL of DMSO. The two solutions were separately heated to 60°C and then mixed by stirring for 15 min. The mixture was filtered, washed 2 times with ethanol and deionised water, respectively, and then dried at 80°C . Finally, the white powders were calcined at 550°C for 4 h with a heating rate of $2^{\circ}\text{C}\cdot\text{min}^{-1}$ under argon to obtain yellow g- C_3N_4 powders.

3.2.2. Electrodes preparation

Fabrication of Cu@BCN, Cu@SCN, and Cu@PCNM. The as-prepared BCN, SCN, and PCNM powders were each mixed with PVDF in NMP with a 1:1 mass ratio of BCN, SCN, or PCNM to PVDF. After stirring for 10 h, PCNM slurry was quickly cast on 100 μm thick Li foil with a thickness of 200 μm in the ultra-dry clean room (Dew point: below -45°C , cleanliness level: 100,000) at room temperature followed by vacuum-dried at 80°C for 6 h. The total loading density on Cu foil was $\sim 1 \text{ mg cm}^{-2}$. The as-obtained Cu@BCN, Cu@SCN, and Cu@PCNM were each punched into a disk of 14 mm in diameter as the working electrode.

Fabrication of Li foil@PCNM. The as-prepared PCNM powders were mixed with PVDF in NMP with a 1:1 mass ratio of PCNM to PVDF. After stirring for 10 h, PCNM slurry was quickly cast on 100 μm thick Li foil with a thickness of 200 μm in the ultra-dry clean room (Dew point: below -45°C , cleanliness level: 100,000) at room temperature followed by vacuum-dried at 80°C for 6h. The as-obtained Li foil@PCNM were punched into 14 mm circular or 47 mm \times 57 mm rectangular discs, respectively, as the negatrode.

3.2.3. Electrochemical Measurements

Two-electrode coin half cells (Li vs. Bare Cu, Cu@BCN, Cu@SCN, and Cu@PCNM). Standard CR2032 coin-type cells were assembled in an Ar-filled glove box with O_2 and H_2O content below 1 ppm. For the Li||Cu coin half cell, a 0.5 mm thick Li disc of 16.0 mm in diameter was employed as both the counter and reference electrode. The as-prepared 14 mm discs of bare Cu foil, Cu@BCN, Cu@SCN, and Cu@PCNM were employed as the working electrode. The Celgard 2500 polypropylene membrane was used as the separator (25 μm). 1 M LiTFSI in DOL/DME (V/V = 1:1) with 2.0 wt% LiNO_3 additive was employed as the electrolyte in each cell. The electrolyte of 75 μL is added to the coin cell. All coin cells were shelved for 8 h before

testing. The galvanostatic performances were conducted at 25 °C using the Land CT 2100A system (Jinnuo Wuhan Corp, China). Li was plated galvanostatically with capacities of 1 to 10 mAh cm⁻² on the bare Cu foil, Cu@BCN, Cu@SCN, and Cu@PCNM and then stripped galvanostatically by a cut-off potential of 0.5 V vs. Li/Li⁺ at different current densities. Cyclic voltammetry (CV) and electrochemical impedance spectroscopy (EIS) were measured by an electrochemical workstation (Solartron 1470E) using CR2032-type coin cells. The frequency range was chosen between 1 MHz and 0.01 Hz.

Two-electrode coin half cells (Bare Li foil vs. Bare Li foil and Li foil@PCNM vs. Li foil@PCNM). Standard CR2032 coin-type cells were assembled in an Ar-filled glove box with O₂ and H₂O content below 1 ppm. For Li||Li symmetrical coin cells, two identical 14 mm discs of bare Li foil or Li foil@PCNM were assembled into symmetrical coin cells with polypropylene (Celgard 2500) as the separator. 1 M LiTFSI in DOL/DME (V/V = 1:1) with 2.0 wt% LiNO₃ additive was employed as the electrolyte in each cell. The electrolyte of 75 μL is added to the coin cell. All coin cells were shelved for 8 h before testing. Li was plated galvanostatically with capacities of 1 to 3 mAh cm⁻² on the bare Li foil and Li foil@PCNM and then stripped galvanostatically with the same capacities of 1 to 3 mAh cm⁻² at different current densities (1-4 mA cm⁻²).

Two-electrode coin full cells (LFP vs. Bare Li foil or LFP vs. Li foil@PCNM). The as-prepared 14 mm discs of bare Li foil or Li foil@PCNM and LFP were employed as the negatodes and positrodes, respectively. The areal loading of the LFP positrode was 12 mg cm⁻², corresponding to an areal capacity of ~2 mAh cm⁻². The areal loading of the bare Li foil or Li foil@PCNM negatode was 20 mAh cm⁻². Celgard 2500 was used as the separator (25 μm). The electrolyte used herein was 1 M LiPF₆ in a mixed solution of EC and DMC (volume ratio of 3:7). Electrolyte injection is fixed at 75 μL in each coin cell. All coin cells were shelved for 8 h before testing. The LFP-based full cells

were galvanostatically charged up to 4 V and then galvanostatically discharged to 2.0 V at various rates from 0.5 to 2 C. Cycling performances of the cells were tested by charging at 0.5 C and discharging at 1 C within the voltage range from 2 to 4 V.

Pouch cells (NCM 811 vs. Bare Li foil or NCM 811 vs. Li foil@PCNM. As-prepared bare Li foil or Li foil@PCNM with a size of 47 mm × 57 mm was employed as the negative electrode (20 mAh cm⁻²). As-prepared NCM 811 electrodes with a size of 43 mm × 53 mm were applied as the positive electrode. Single-side areal loading of the positive electrode was ~20 mg cm⁻², corresponding to the areal capacity of ~3.75 mAh cm⁻². Celgard 2500 was used as the separator (25 μm). Pouch cells are fabricated within ~30 min in the ultra-dry clean room (Dew point: below -45 °C, cleanliness level: 100,000) at room temperature. The electrolyte with 1 M LiPF₆ in EC/DMC=1:1 by volume with 2 wt% FEC was used (6 g Ah⁻¹). After injecting the electrolyte, full cells were at least stored for two days to achieve full infiltration of electrolytes into pores of separators and positive electrodes. The NCM 811-based pouch cells were galvanostatically charged up to 4.3 V and then galvanostatically discharged to 2.6 V at 0.2 C. N/P ratio (Negative capacity/Positive capacity) is around 5. Pouch cells were subjected to 100 kPa pressure during charging/discharging.

3.3. Results and discussion

3.3.1. Materials characterisations

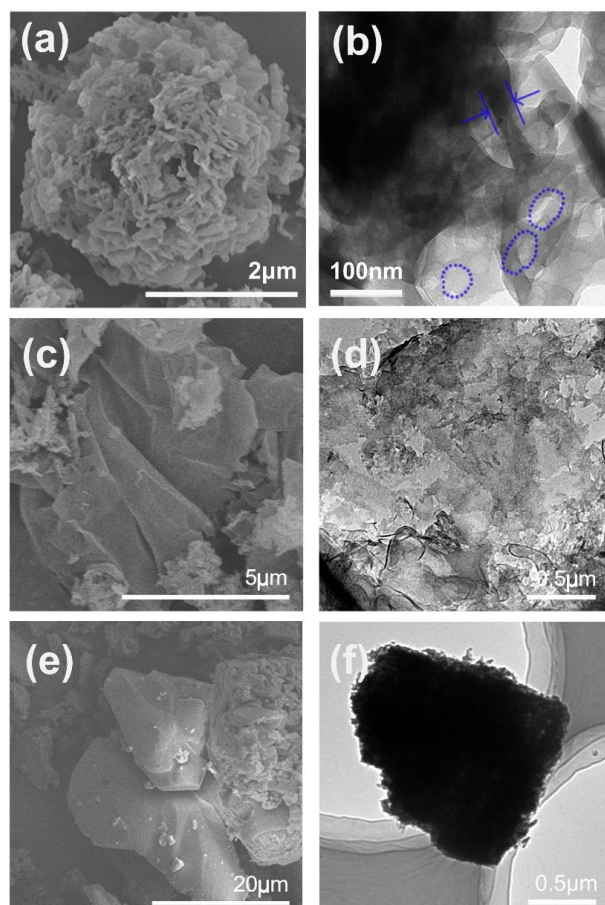


Figure 3.1. (a) SEM image and (b) TEM image of PCNM. (c) SEM image and (d) TEM image of SCN. (e) SEM image and (f) TEM image of BCN (The blue dashed circle is the pores of PCNM).

Porous $g\text{-C}_3\text{N}_4$ microspheres were synthesised by thermal polycondensation of supramolecular aggregates of melamine and cyanuric acid according to previous work by Liu et al.²⁰⁶ SEM image (Fig. 3.1a) illustrates that each $g\text{-C}_3\text{N}_4$ microsphere has porous and flower-like morphology with a typical diameter of $\sim 3.5 \mu\text{m}$. 2D $g\text{-C}_3\text{N}_4$ nanosheets with an average thickness of $\sim 40 \text{ nm}$ aggregate randomly in the microspheres to form porous structures with nanometer-scale pore sizes. The 3D

geometry made up of 2D nanosheets is predicted to be more robust than individual 2D g-C₃N₄ nanosheets. Also, as demonstrated in the TEM image (Fig. 3.1b), porous 3D architecture assembled by 2D g-C₃N₄ nanosheets has a higher surface area and more voids than BCN owing to the bendable and random layout of 2D nanosheet units. This porous property benefits electrolyte penetration and adsorption and provides more space for Li deposition. For comparison, two other g-C₃N₄ samples of SCN and BCN with different morphologies were also synthesised according to the method provided in the experimental section, whose morphology is presented in Fig. 3.1c-d and Fig. 3.1e-f. SCN exhibits typical laminar morphology, as displayed in the SEM and TEM images (Fig. 3.1c-d), similar to graphene. It has a lateral size of several microns and a thickness of tens of nanometres. The as-prepared BCN sample shows typical particle morphology with irregular shapes and sizes ranging from several to a few dozen microns (Fig. 3.1e). The solid internal structure of BCN particles can be discerned by TEM (Fig. 3.1f), which is different from the porous structure of PCNM.

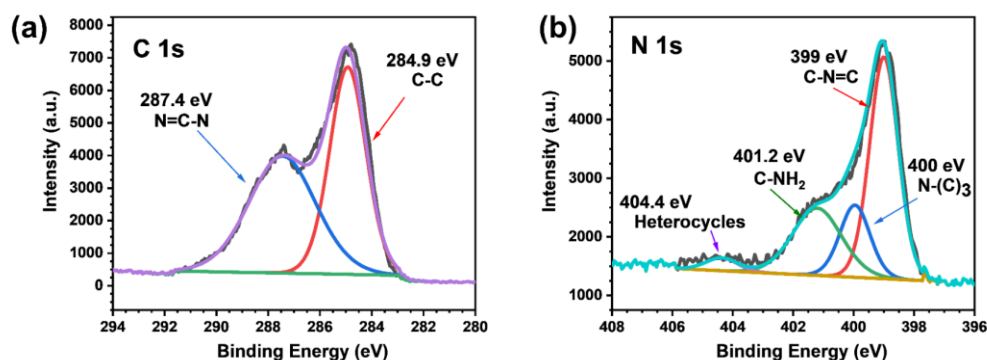


Figure 3.2. (a) C 1s and (b) N 1s XPS spectra of PCNM.

Table 3.1. Atomic concentration and mass concentration of C and N elements in PCNM determined by TEM and XPS.

Element	Mass Concentration (%) TEM	Atomic Concentration (%) TEM	Atomic Concentration (%) XPS	Mass Concentration (%) XPS

C K	42.83	46.63	55.78	51.96
N K	57.17	53.37	44.22	48.04
Total	100.00	100.00	100.00	100.00

XPS analysis was performed to determine the surface chemical composition and electronic states of PCNM, and the results are shown in Fig. 3.2. Two peaks centred at 284.9 and 287.4 eV can be found in the C 1s spectrum of PCNM (Fig. 3.2a), which are assigned to graphitic carbon (C-C) in g-C₃N₄ and sp²-hybridised carbon (N=C-N)²⁰⁷ in the aromatic ring attached to the -NH₂ or -NH group,^{207, 208} respectively. The high-resolution spectrum of porous microspheres also displays remarkable N 1s signals, which can be deconvoluted into four peaks at 399.0, 400.0, 401.2, and 404.4 eV, corresponding to sp²-nitrogen in triazine ring (C=N-C),¹³⁰ tertiary N bonded to C atoms in the form of N-(C)₃ or H-N-(C)₂,²⁰⁹ terminal amino groups (C-NHx)²¹⁰ and heterocycles, respectively (Fig. 3.2b). These results further confirm the existence of abundant N elements as Lewis-base sites in PCNM. Meanwhile, the atomic percentage of N (53.37%) measured by TEM (Table 3.1) is higher than the atomic percentage of N (44.22%) measured by XPS, which may be due to the synthetic defect during the calcination process of PCNM.

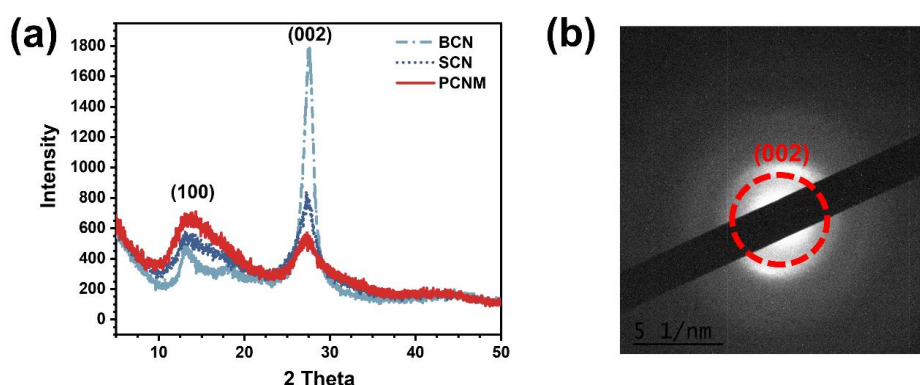


Figure 3.3. (a) X-ray diffraction patterns of BCN (light blue short dashed dot), SCN (dark blue short dot), and PCNM (red line) and (b) SAED pattern of PCNM (The red

dashed circle is the diffraction ring corresponding to (002) face of PCNMs; 5 1/nm is the reciprocal space scale, and it represents that the length of the scale bar is 1/5 nm).

Typical XRD patterns of BCN, SCN, and PCNM samples are displayed in Fig. 3.3a. All three samples have two characteristic peaks at 13.2° ($d=0.675$ nm) and 27.5° ($d=0.325$ nm), corresponding to the diffraction of the (100) (inter-planar stacking) and (002) (in-planar structural packing motif) crystal plane of g-C₃N₄, respectively.^{131, 211, 212} The diffraction peaks of PCNM have the largest full width at half maxima compared with those of BCN and SCN, suggesting the smallest crystal size of g-C₃N₄ in PCNM. Based on the Debye-Scherrer equation, the crystal size of g-C₃N₄ in PCNM along the (002) crystal plane is calculated to be ~35 nm, which is in good agreement with the thickness of the g-C₃N₄ nanosheets in this sample as shown in TEM (Fig. 3.1b). The interplanar spacing computed from the XRD patterns agrees with the selected area electron diffraction (SAED) rings illustrated in Fig. 3.3b.

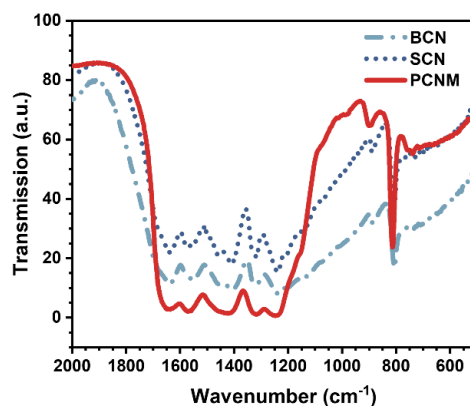


Figure 3.4. FT-IR spectra of BCN (light blue short dashed dot), SCN (dark blue short dot), and PCNM (red line).

The FT-IR spectra for all synthesised samples are depicted in Fig. 3.4. All carbon nitride samples show almost identical peaks in the range of 1200–1650 cm⁻¹, which corresponds to the typical stretching vibration of aromatic rings in carbon nitride. The

peak at $\sim 1662\text{ cm}^{-1}$ is assigned to the stretching vibration of C-N. The peaks at 1216 cm^{-1} , 1310 cm^{-1} and 1405 cm^{-1} belong to the stretching vibration of C-N in aromatic hydrocarbons, and the peak appearing at 807 cm^{-1} corresponds to the combined vibration of the triazine unit.²¹³⁻²¹⁵ All these peaks confirm the successful synthesis of g-C₃N₄ in combination with XRD and XPS results.

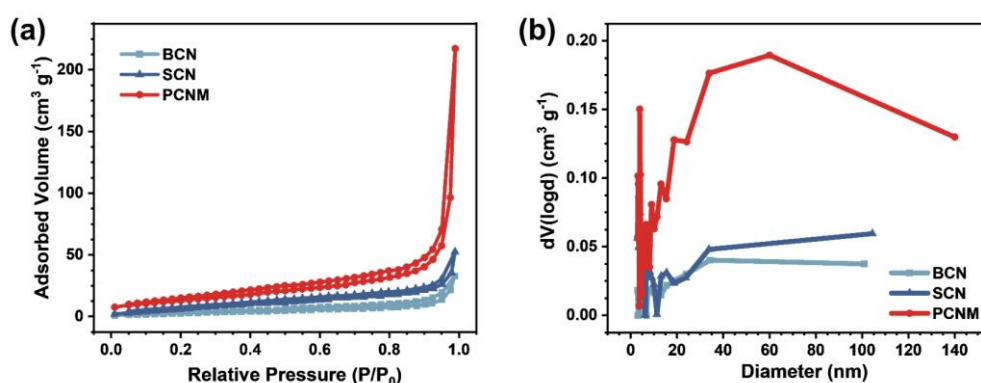


Figure 3.5. (a) Nitrogen adsorption and desorption isotherms and (b) the pore size distribution data of BCN (light blue line), SCN (dark blue line), and PCNM (red line).

Table 3.2. Specific surface area and pore volume of BCN, SCN, and PCNM.

Items	Specific Surface Area (m ² g ⁻¹)	Pore Volume (cm ³ g ⁻¹)
BCN	13.157	5.084e-02
PCNM	49.314	3.361e-01
SCN	33.645	8.143e-02

To further understand the pore structure over different g-C₃N₄ materials, which is important in Li⁺ regulation, detailed pore structure was characterised by nitrogen adsorption and desorption isotherms (Fig. 3.5a). It is found that the adsorption quantity increases linearly with rising relative pressure to 0.9 and then increases exponentially to atmospheric pressure, suggesting that a broad range of pores have been formed.

Compared to SCN and BCN, hysteresis between the adsorption and desorption branches in the exponentially increased section can be observed obviously in PCNM, suggesting it possesses a more mesoporous structure. The type of hysteresis loop of PCNM is probably assigned to H3 (IUPAC), which elucidates the presence of wedge-shaped pores resulting from loosely packed nanosheets. Pore size distribution data (Fig. 3.5b) using Barrett–Joyner–Halenda (BJH) model also proves that PCNM possesses a broad pore size distribution ranging from 2 to 140 nm. In particular, PCNM possesses a large number of mesopores especially for a pore size of 4nm, and there are also many large pores with pore sizes greater than 50nm which is in good agreement with the size of nanopores observed in the TEM image (Fig 3.1b). PCNM also possesses the largest Brunauer–Emmett–Teller (BET) specific surface area ($49.3 \text{ m}^2 \text{ g}^{-1}$) and pore volume ($\sim 0.3 \text{ cm}^3 \text{ g}^{-1}$) among three g-C₃N₄ samples (Table 3.2), which is contributed by its unique morphology. The abundant nano-sized pores (<150 nm) in PCNM endow suitable space to effectively develop the uniformity of Li⁺ flux based on the Debye length law.

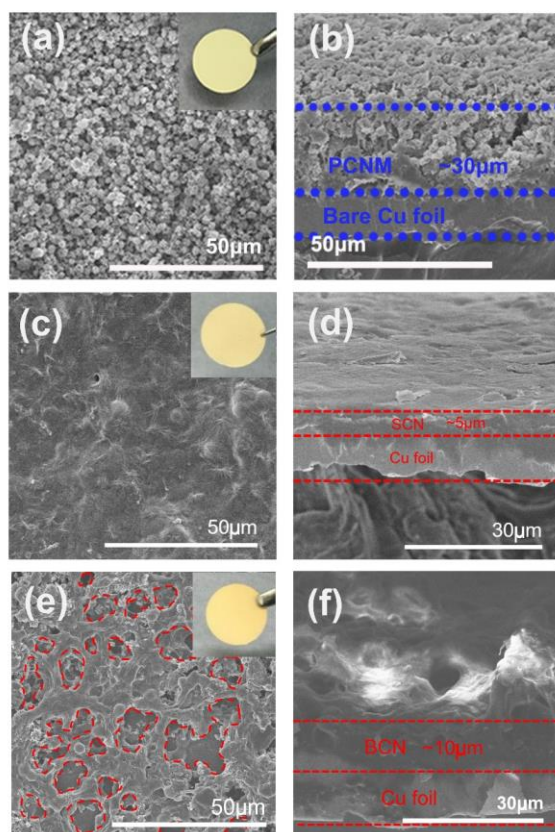


Figure 3.6. (a) Top-view and (b) cross-section view SEM images of Cu@PCNM. The inset of (a) shows the optical photograph of Cu@PCNM. (c) Top-view and (d) cross-section view SEM images of Cu@SCN. The inset of (c) is the optical photograph of Cu@SCN. (e) Top-view and (f) cross-section view SEM images of Cu@BCN. The inset of (e) is the optical photograph of Cu@BCN (The red dashed circle represents the pores of Cu@BCN).

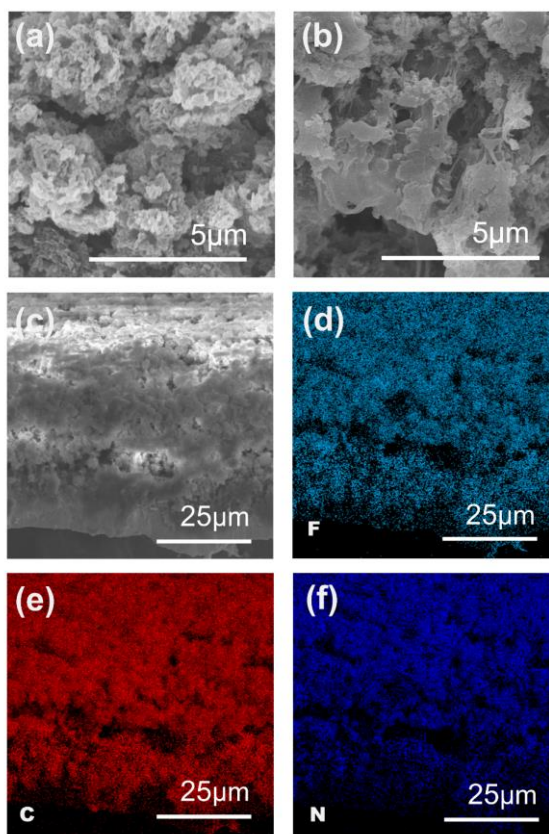


Figure 3.7. (a) Top-view and (b) cross-section view SEM images of Cu@PCNM. EDS mapping of the cross-section of the PCNM coating layer on Cu for (c) SEM image, (d) F, (e) C, and (f) N element.

The as-prepared PCNM powders were mixed with PVDF in NMP solvent to form a slurry which was subsequently cast on a Cu foil to form a coating layer of the 3D scaffold. A light-yellow coating can be observed in the inset image of Fig. 3.6a. As illustrated in Fig. 3.6a-b, the coating with a thickness of $\sim 30 \mu\text{m}$ displays a relatively smooth surface. Following the same preparation process, SCN with sheet-like morphology forms a flat coating layer with a much lower thickness of $\sim 5 \mu\text{m}$ than that of PCNM (Fig. 3.6c-d). In contrast, the BCN coating layer (Fig. 3.6e-f) exhibits a rough surface with larger pores, which can be attributed to the large particle size of BCN structural units. Notably, random packing of PCNM particles in this coating layer forms inter-particle pores (Fig. 3.7a-b), along with internal nanopores inside each $\text{g-C}_3\text{N}_4$ microsphere. Uniform distribution of N, C, and F (from PVDF) elements over the entire

coating layer are found via energy-dispersive spectroscopy (EDS) mapping as presented in Fig. 3.7c-f. The morphology of coating layers using three different g-C₃N₄ materials is expected to have distinct effects on Li deposition behaviour. SCN coating layer composed of densely stacked g-C₃N₄ nanosheets cannot provide extra space to accommodate deposited Li and fail to release stress originating from Li dendrites despite abundant N-containing functional groups. Therefore, the physical alleviation of Li dendrites is still not possible with an SCN coating. The BCN's large particle size creates relatively large cavities in the coating layer, which may not effectively facilitate chemical homogenization based on the Debye length law. It is believed that PCNM coating can provide abundant space to accommodate/guide Li growth. Besides, pristine nanoscale pores in PCNM can effectively homogenise the Li⁺ distribution. Thus, dense, flat Li deposits can be highly expected based on such physical and chemical synergic regulation mechanisms in the case of PCNM.

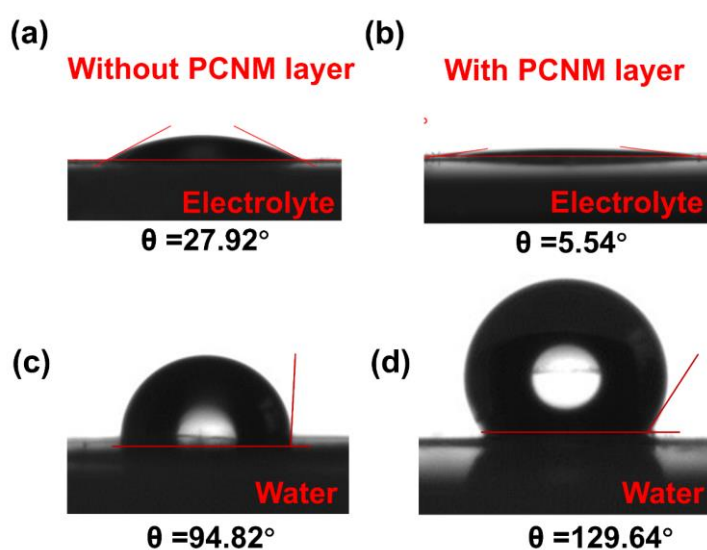


Figure 3.8. Contact angles of electrolyte toward (a) bare Cu foil and (b) Cu@PCNM. Contact angles of water toward (c) bare Cu foil and (d) Cu@PCNM.

To understand further the interaction between the electrolyte and the PCNM coating, the wettability between these two is measured using contact angle methods. Results in

Fig. 3.8a-b manifest that the presence of the PCNM layer results in a sharp reduction of contact angle from 27.92° to 5.54° , suggesting a marked improvement of the electrolyte wettability. While Cu foil and Li foil (24.7°)¹⁰⁵ remain comparatively poor wettability with ether-based electrolytes. It is reported that electrolyte wettability is closely related to the uptake amount of liquid electrolytes. Hence, higher electrolyte concentration strongly impacts the distribution of Li^+ flux over the entire Cu/Li surface during cycling.²¹⁶ It is believed that such a superior electrolyte wettability of the PCNM layer is beneficial to obtain the uniform Li^+ flux and relieve uneven Li^+ transport and deposition. Interestingly, as shown in Fig. 3.8c-d PCNM layer exhibits a higher level of water-repellency than Cu foil, which probably prevents Li from contacting water and thereby reduces safety risks in LMRBs when utilizing Li foil@PCNM.

3.3.2. Morphology of Li plating

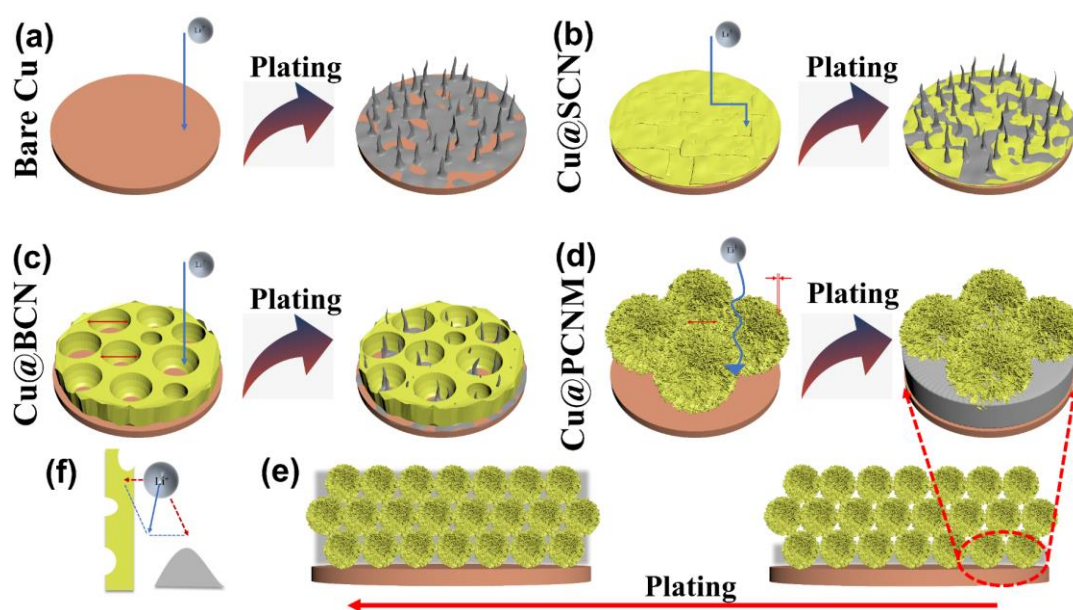


Figure 3.9. Diagrams showing the morphology of electrodeposited Li on (a) bare Cu foil, (b) Cu@SCN, (c) Cu@BCN and (d), and (e) Li plating process on Cu@PCNM; (f) Schematic diagram of PCNMs in regulating Li ion flux (The red dashed line is the interaction force between Li ion and electric field/PCNM and the blue solid line is real

Li ion movement route).

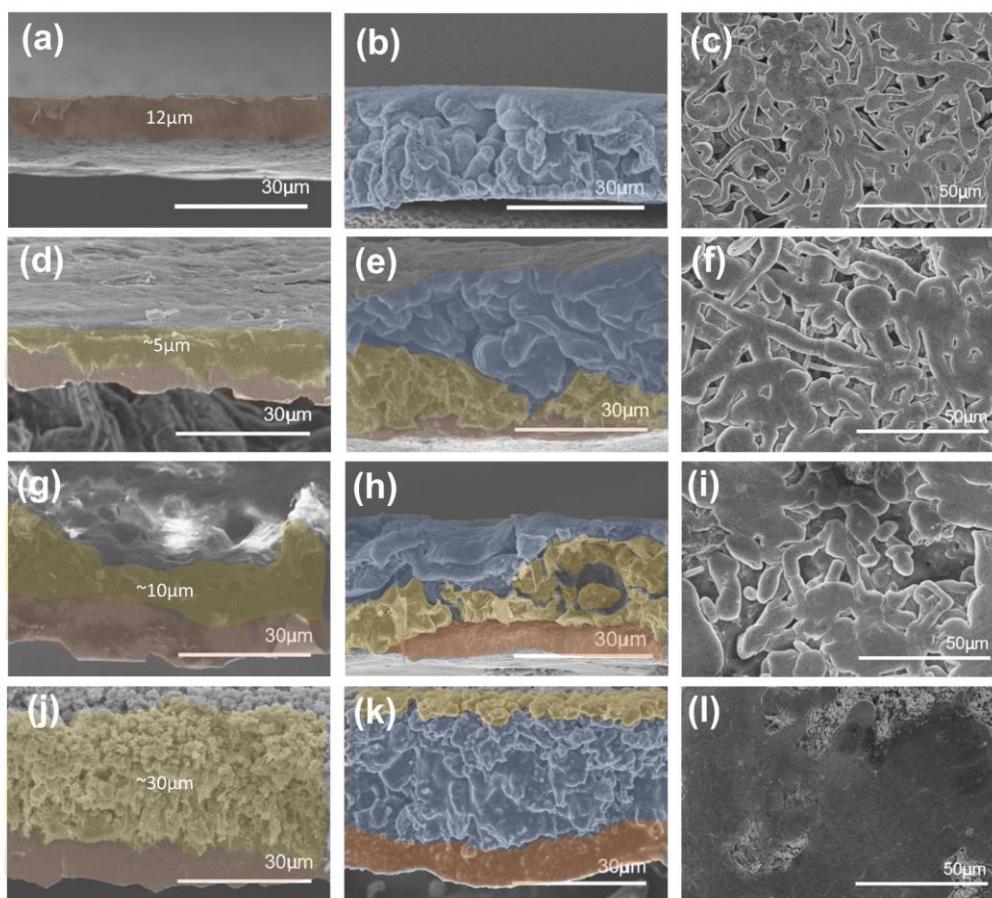


Figure 3.10. (a) SEM image of bare Cu foil. (b) Cross-section view and (c) top-view SEM images of Cu foil after plating Li with 5.0 mAh cm^{-2} . (d) SEM image of Cu@SCN. (e) Cross-section view and (f) top-view SEM images of Cu@SCN after plating Li with 5.0 mAh cm^{-2} . (g) SEM image of Cu@BCN. (h) Cross-section view and (i) top-view SEM images of Cu@BCN after plating Li with 5.0 mAh cm^{-2} . (j) SEM image of Cu@PCNM. (k) Cross-section view and (l) top-view SEM images of Cu@PCNM after plating Li with 5.0 mAh cm^{-2} . The regions marked with light blue, light red, and light yellow colours correspond with plated Li, Cu foil, and g-C₃N₄ coatings, respectively. The current density is 1 mA cm^{-2} .

Fig. 3.9 and Fig. 3.10 perform different morphologies of plated LM on bare Cu foil, Cu@SCN, Cu@BCN, and Cu@PCNM electrode (Li@Cu@SCN, Li@Cu@BCN, and

Li@Cu@PCNM). Noticeably, without lithiophilic decoration, Li^+ tends to deposit on spots where the cracks of SEI appear, and tips of surface bumps emerged on the surface of bare Cu foil (Fig. 3.9a).²¹⁷ By further depositing Li onto the existing Li whiskers, a thick and porous dendritic morphology is formed, as illustrated in Fig. 3.10a-c. This morphology results in ongoing electrolyte consumption and an escalation of irreversible Li. Due to the lack of enough space to accommodate Li growth and eliminate stress generated from Li dendrites, the SCN layer would be easily pierced, and remarkable Li dendrites still can be observed on Cu@SCN (Fig. 3.9b and Fig. 3.10d-f), especially at high deposition capacity, i.e. 5 mAh cm^{-2} . More importantly, due to the absence of vertical depth of g- C_3N_4 walls in SCN coating, Li^+ cannot be affected effectively and only pass through the gaps between g- C_3N_4 nanosheets to deposit on Cu foil. Although a porous structure is formed in the BCN coating due to random stacking of g- C_3N_4 particles (Fig. 3.10g and Fig. 3.6e-f), the Li^+ flux cannot be efficiently affected by the surface Lewis-base sites of BCN particles because of the large micrometre scale pore size (Fig. 3.9c), still leading to the formation of porous and dendritic Li (Fig. 3.10h-i). Only when there exist nanometre-scale pores that tailor Li^+ diffusion behaviour and micrometre-scale pores that provide space for Li deposition at the same time can the Li^+ flux be homogenised, and dense and flat deposition of Li be successfully developed. This scenario is observed in the Cu@PCNM electrode (Fig. 3.9d and Fig. 3.10j-l). Homogenised Li^+ flux is ascribed to the fact the effective interaction between Li ions and PCNMs gives rise to a shift in the migration path where Li ions that were originally deposited on the tip (Fig. 3.9f).

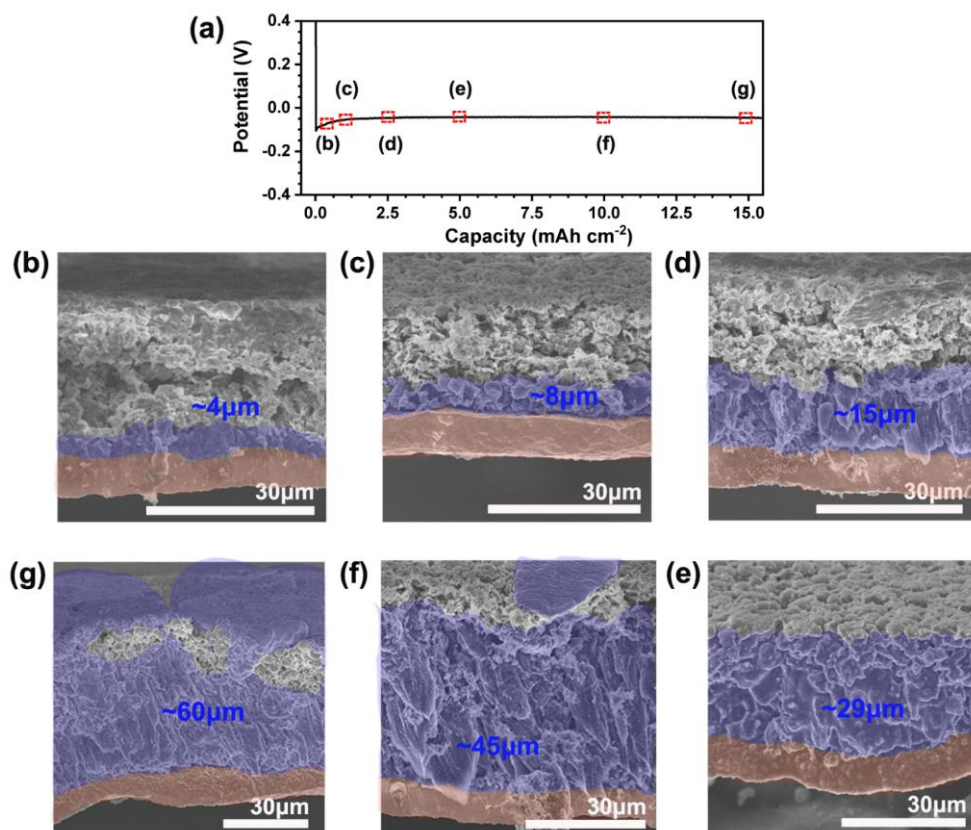


Figure 3.11. Morphology evolution of the Cu@PCNM electrode during Li plating with capacities from 0.5 to 15 mAh cm⁻². (a) Discharge curve of the Cu@PCNM electrode. Cross-section view SEM images of the Cu@PCNM electrode after plating with (b) 0.5 mAh cm⁻², (c) 1 mAh cm⁻², (d) 2.5 mAh cm⁻², (e) 5 mAh cm⁻², (f) 10 mAh cm⁻² and (g) 15 mAh cm⁻² of Li. The current density is 1 mA cm⁻².

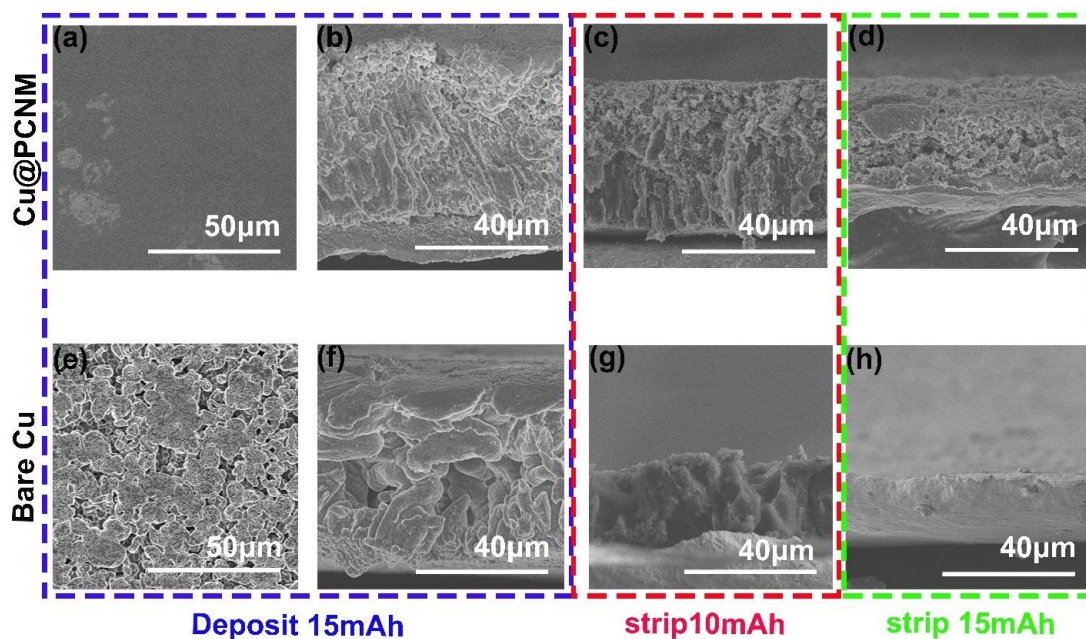


Figure 3.12. Comparison of morphology evolution during Li plating/stripping on (a-d) Cu@PCNM and (e-h) bare Cu foil with different deposition and stripping capacities. (a) and (e) are top-view SEM images, and others are cross-section view SEM images.

To clearly illustrate Li deposition behaviour within PCNM, the morphology of the Cu@PCNM electrode at different deposition capacities (from 0.5 to 15 mAh cm⁻²) was characterised (Fig. 3.11). It is observed that PCNM can accommodate the maximum Li deposition areal capacity of ~5 mAh cm⁻². Below 5 mAh cm⁻², Li tends to form a filling-like deposition within the interparticle pores (Fig. 3.11b-e), as presented in Fig. 3.9e. When the areal capacity of deposition exceeds 5 mAh cm⁻², the electrodeposited Li growth remains planar while continuing to form on the surface of the PCNM coating layer (Fig. 3.11f-g). Such behaviour is probably due to the enriched Li⁺ at the electrode/electrolyte interface induced by abundant Lewis-base sites in PCNM. Even when the Li deposition areal capacity reaches 15 mAh cm⁻², the surface of the plated LM on Cu@PCNM is still smooth. In contrast, deposited Li shows a porous dendrite morphology on bare Cu (Fig. 3.12). Notably, the plated LM can strip from the Cu@PCNM reversibly, making the matrix recover to its pristine morphology (Fig. 3.12a-d) and confirming its structural robustness.

3.3.3. SEI characterisations

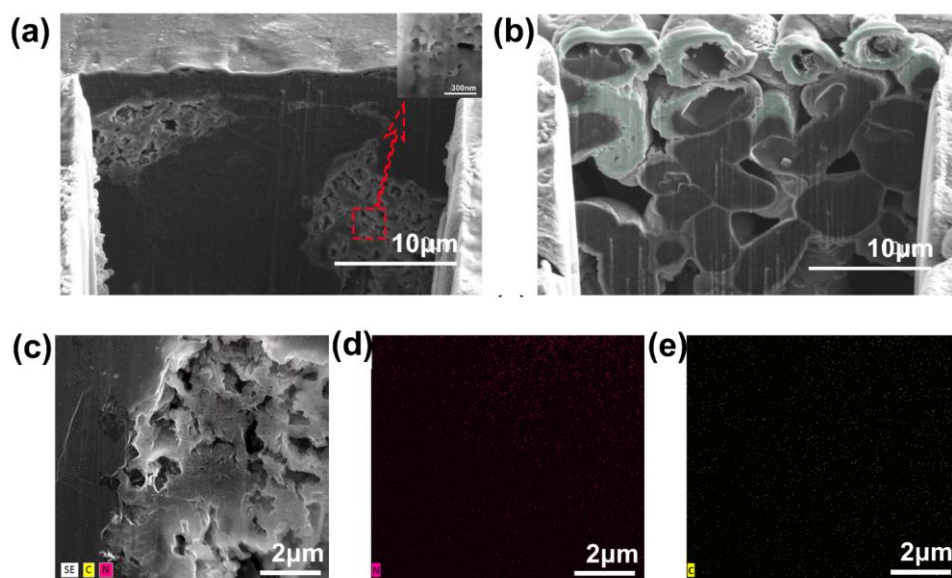


Figure 3.13. Cross-sectional FIB-SEM images of (a) Cu@PCNM and (b) bare Cu with plating 15 mAh cm^{-2} at 1 mA cm^{-2} . EDS mapping regarding the local FIB-SEM image of Li@Cu@PCNM for (c) SEM image, (d) N, and (e) C element distribution. Light green districts in (b) represent the thick SEI layer.

To clarify the specific morphology of the deposited Li, *ex-situ* FIB-SEM characterisation was further conducted over Cu@PCNM (Fig. 3.13a) and bare Cu (Fig. 3.13b) with the plating areal capacity of 15 mAh cm^{-2} . The cross-section view of the FIB-SEM image reveals that the interparticle pores of PCNM coating are almost filled with Li (Fig. 3.13a), while partial nanopores inside g-C₃N₄ microspheres are still left. The results of EDS mapping (Fig. 3.13c-e) support the domination of the N element in the porous areas, thereby confirming that the porous regions correspond to g-C₃N₄ materials instead of porous Li. The above results indicate that Li⁺ not only diffuses through but also partially deposits within pores assembled by g-C₃N₄ nanosheets, which demonstrates that micro/nano hybrid channels in PCNM are highly integrated with Li. These results support our assertion that ample nanopores in PCNM can synergise the formation of uniform Li⁺ flux and guide dense Li growth, which can result in enhanced

stability and reversibility of the cycling performance. In striking contrast, the porous and dendritic structure of electrodeposited Li is generated on bare Cu foil. Besides, remarkably thick SEI wrapping on Li dendrites is largely attributed to the uneven Li⁺ deposition and electrolyte decomposition, as well as the formation of by-products, resulting in poor cycling stability and a dramatic drop in CE.

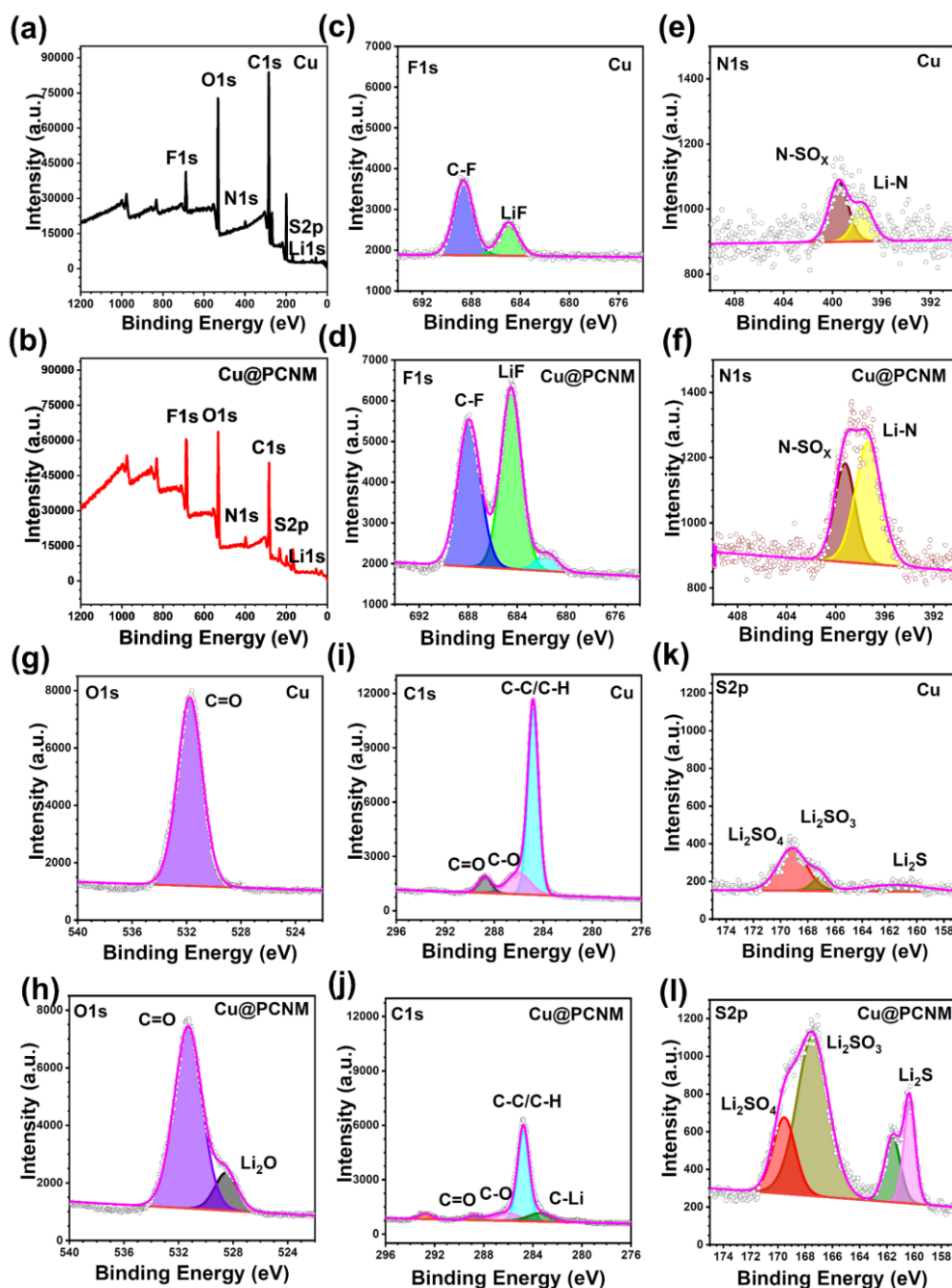


Figure 3.14. XPS Full spectra of the surface of deposited LM on (a) bare Cu foil and

(b) Cu@PCNM. (c, d) F 1s, (e, f) N 1s, (g, h) O 1s and (i, j) C 1s and (k, l) S 2p XPS spectra of the surface of plated Li on Cu foil coated with (d, f, h, j and l) and without PCNM (c, e, g, i and k).

To gain a deeper comprehension of the impact of PCNM in the regulation of Li plating, XPS was conducted to investigate the surface composition of the SEI of newly deposited Li on Cu@PCNM and bare Cu (Fig. 3.14). The full spectrum is presented in Fig. 3.14a-b. In F 1s spectra (Fig. 3.14c-d), Li-F and C-F signals are observed in both electrodes, which result from the decomposition of LiTFSI salt.¹⁴¹ LiF is well-known as an excellent SEI component for its high interfacial energy toward Li and high mechanical strength. Therefore, it is efficient to suppress dendrite growth, which contributes to uniform Li deposition. Cu@PCNM shows a stronger Li-F signal compared to bare Cu, indicating that N-containing Lewis-base sites in PCNM enhance the concentration of TFSI anions at the deposition interface. This strong interaction with Li⁺ forms a robust SEI. Meanwhile, the contents of LiN_xO_y/N-SO_x and Li-N (Li₃N) species on Li@Cu@PCNM are also higher than those on Li@Cu (Fig. 3.14e-f), revealing that increasing amounts of NO₃⁻/TFSI⁻ have been reduced to form the resulting SEI in the presence of PCNM. As Li₃N is a superconductor of Li⁺,^{218, 219} Li₃N-enriched SEI on Li@Cu@PCNM can improve Li⁺ transportation for better Li plating/stripping behaviour. In addition, the newly emerged Li-O signal (Li₂O) on Li@Cu@PCNM verifies that the decomposition of NO₃⁻ facilitates the formation of more inorganic Li₂O grains in the SEI (Fig. 3.14g-h).

Notably, the top surface of the SEI formed in the bare Cu foil has much stronger C-C/C-H (284.8 eV), C-O (286.3 eV), and C=O (288 eV)²²⁰ signals compared with Li@Cu@PCNM, indicating huge electrochemical degradation of organic solvent during Li plating (Fig. 3.14i-j). Furthermore, higher content of Li₂S-O_x (Li₂SO₄, Li₂SO₃, and Li₂S signal at ~169.5, ~167, and ~160.35 eV, respectively) resulting from electrochemical reduction of TFSI⁻ (Fig. 3.14k-l) also further proves the PCNM-driven

enhancement in cation and anion concentration, which plays an essential role in constructing robust and stable SEI. In brief, an increase in inorganic composition (Li-F, Li-N, and Li-O) and a reduction in organic composition (C-C/C-H) verifies the formation of a more robust SEI when PCNM coating is employed. The primary reason for this phenomenon can be attributed to the accumulation of anions at the interface, stemming from the chemical adsorption of Li^+ facilitated by the Lewis-base sites present in $\text{g-C}_3\text{N}_4$. The sturdy and high Li^+ conductive nature of such a SEI could potentially serve as a critical factor in enabling dendrite-free Li plating/stripping processes over extended cycling periods.

3.3.4. Electrochemical performances of half cells

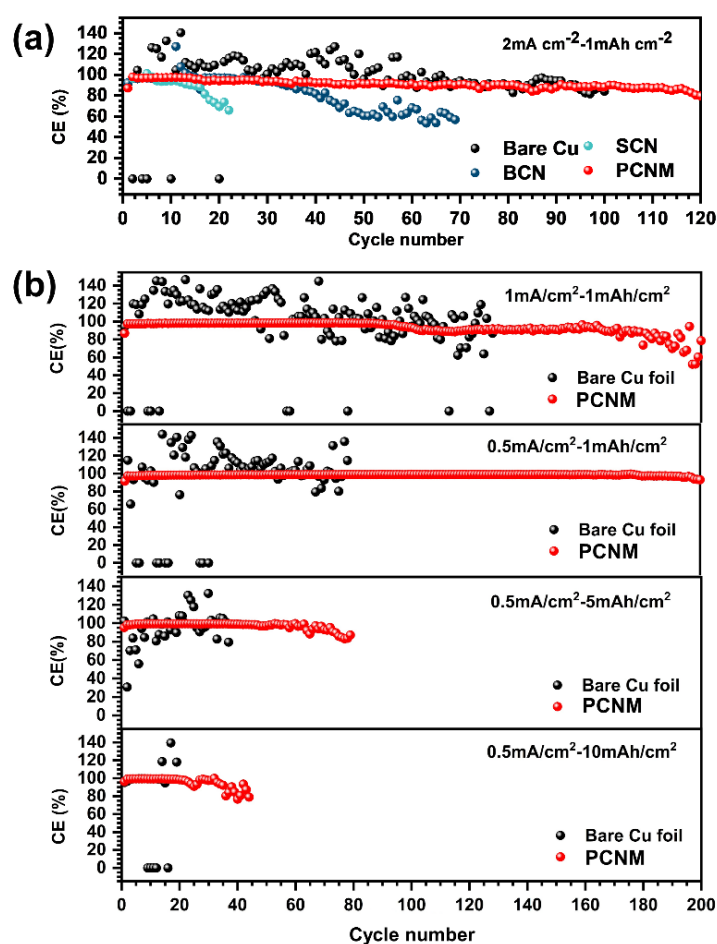


Figure 3.15. (a) CE Comparison of Li plating on/stripping on bare Cu foil electrode and Cu foil coated with SCN, BCN, and PCNM with an areal capacity of 1.0 mAh cm^{-2}

² at 2.0 mA cm⁻². (b) Comparison of CE of Li plating on/stripping over Cu foil coated with and without PCNM with 1.0 mAh cm⁻² at 1.0 mA cm⁻² and 0.5 mA cm⁻², and with 5 mAh cm⁻² and 10 mAh cm⁻² at 0.5 mA cm⁻².

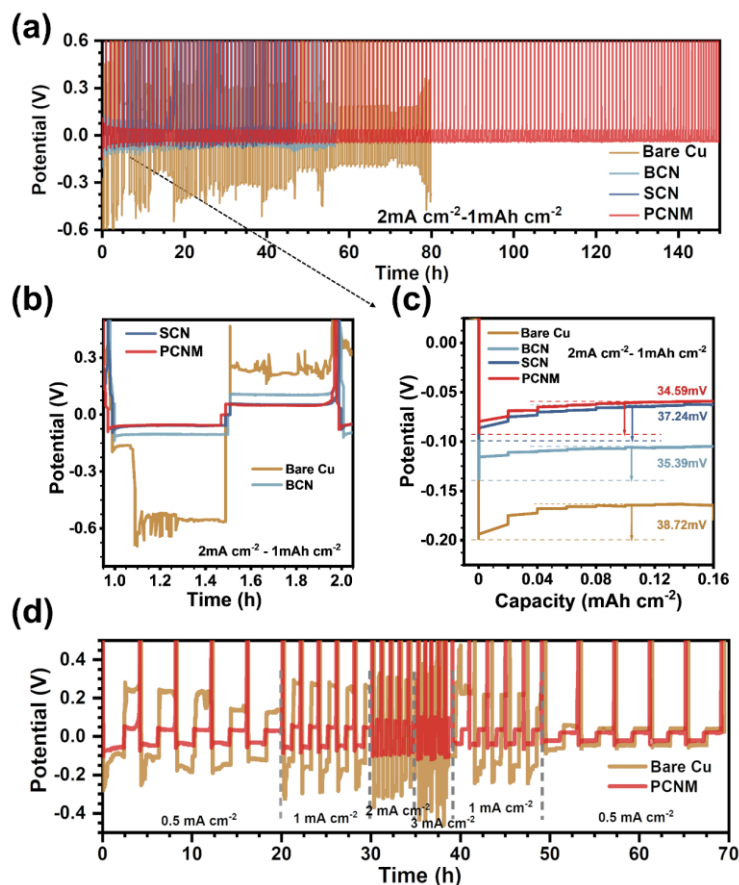


Figure 3.16. Comparison of (a) potential profiles, (b) magnified potential profiles within the plating time range of 0-2 h, and (c) nucleation overpotential of Li plating on/stripping from bare Cu foil electrode and Cu foil coated with SCN, BCN, and PCNM with an areal capacity of 1.0 mAh cm⁻² at 2.0 mA cm⁻². (d) Comparison of Li plating/stripping potential profiles on Cu foil coated with and without PCNM at different current densities ranging from 0.5 to 3 mA cm⁻² with an areal capacity of 1 mAh cm⁻².

In this chapter, this ether-based electrolyte (1 M LiTFSI in DOL/DME (V/V = 1:1) with

2.0 wt% LiNO₃) is applied for Li||Cu or Li||Li symmetric cells. LiTFSI as Lithium salt, DME and DOL as the solvent, and LiNO₃ as an additive are commonly used for ether-based electrolytes.^{105, 113, 221} Ether solvent can form oligomers on the Li surface with good flexibility and strong binding affinity.²²² The LiTFSI has high solubility and high ionic conductivity in ether solvent (DME) and it assists the generation of Li-F in the SEI.²²³ DOL is often reported to coordinate with DME to form a more stable SEI.²²⁴ Ring-opening polymerization of DOL takes place within electrochemical cells, resulting in the formation of solid-state polymer batteries that demonstrate excellent properties for interfacial charge transport.²²⁵ LiNO₃ only shows high solubility in ether (DME) solvent, and it helps form Li-N components in the SEI.²²² Both Li-F and Li-N can further enhance the inorganic components of the SEI, thereby facilitating the formation of an SEI with a bilayer configuration and dendrite-free Li deposition²²⁶. Moreover, ether-based electrolytes can promote the formation of larger LM nuclei, helping to reduce the exposed surface area to the electrolyte.²²⁶ Therefore, this ether-based electrolyte is applied for Li||Cu or Li||Li symmetric cells that do not require a high-voltage environment in Chapter 3.

Fig. 3.15 and Fig.3.16 display the CE and long-term electrochemical stability in a half-cell configuration composed of metallic Li as the counter electrode coupled with different working electrodes (bare Cu foil, Cu@SCN, Cu@BCN, and Cu@PCNM). Among all electrodes, Cu foil displays the most serious fluctuation in CE and marked overcharge behaviour within 60 cycles at a high current density (2.0 mA cm⁻² with 1.0 mAh cm⁻²), which could potentially be attributed to the uncontrolled Li dendrite-induced depletion of the electrolyte and generation of by-product (Fig. 3.13b). The CE of Cu@SCN drops rapidly in the initial 20 cycles. Cu@BCN maintains comparatively stable CE with larger than 80% within 40 cycles. In comparison, the CE of the Cu@PCNM cell keeps stable for over 100 cycles (Fig. 3.15a). The CE with current density varying from 0.5 mA cm⁻² to 1 mA cm⁻² at 1 mAh cm⁻² was also studied (Fig. 3.15b). The Cu@PCNM cell achieves comparatively higher and more stable CE of >90%

at 1 mA/cm² and >98% at 0.5 mA cm⁻² before 170 cycles. With a high areal capacity of 5 mAh cm⁻² at 0.5 mA cm⁻², Cu@PCNM still maintains a high CE value of 98% before 60 cycles. Even at an ultrahigh areal capacity of 10 mAh cm⁻², the high CE (>97%) before 30 cycles is obtained. Conversely, the cycling stability of the CE for Cu foil rapidly diminishes following only a few cycles under the aforementioned conditions. Similarly, as exhibited in Fig. 3.16a, Cu@PCNM has the most stable overpotential (<35 mV) over long-term cycling. Fig. 3.16b shows the magnified potential profiles from 0 to 2h. The overpotential of Cu@SCN is almost the same as that of Cu@PCNM, which is less than Cu@BCN's by ~30mV, probably due to the affinity of 2D g-C₃N₄ nanosheets in SCN with interfacial Li⁺. Bare Cu foil shows drastic potential fluctuation and an increasing overpotential as the test time increases. Li nucleation behaviours were further explored via the potential-capacity profiles in Fig. 3.16c. Cu@PCNM exhibits the smallest nucleation overpotential of 34.59 mV. The highest and most stable CE of Cu@PCNM implies that the effective transient Li-N bonds formed due to abundant nanopores in PCNM induce stabilised and uniform Li⁺ distribution near the deposition sites, which gives rise to dense deposition morphology with little dendrites and a reduced overpotential.¹³⁶ Different current densities were applied on the Li||Cu cells using Cu@PCNM and bare Cu foil (Fig. 3.16d). Observation reveals that the potential hysteresis of Cu@PCNM rises only marginally from ~30 mV to ~95 mV as the current density escalates from 0.5 mA cm⁻² to 3 mA cm⁻². In contrast, Cu foil shows dramatic hysteresis change from ~127 mV to ~300 mV. Also, the excellent reversible property is confirmed on the Cu@PCNM electrode. The unstable potential profile of bare Cu foil implies the formation of excessive SEI and catastrophic structural evolution, which contribute to the drastic enlargement of potential hysteresis at high current densities.²²⁷

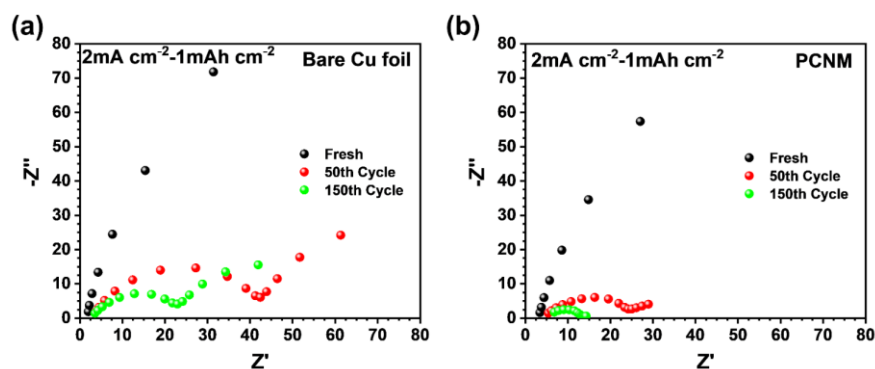


Figure 3.17. The EIS of (a) bare Cu foil electrode and (b) Cu@PCNM before cycling and after 50 and 150 cycles.

The cycling performance of cells strongly relies on the stability of SEI on the electrode materials. Thus, the interfacial stability of the SEI was further studied by EIS (Fig. 3.17a-b). After 50 and 150 cycles, Cu@PCNM reveals a smaller semicircle than Cu foil in the high-frequency range, suggesting that the SEI generated on Cu@PCNM features a reduced interface impedance and charge-transfer resistance in comparison to that formed on Cu foil. This observation highlights that the uniform Li deposition over Cu@PCNM accelerates the establishment of a homogeneous and low-resistance SEI layer.

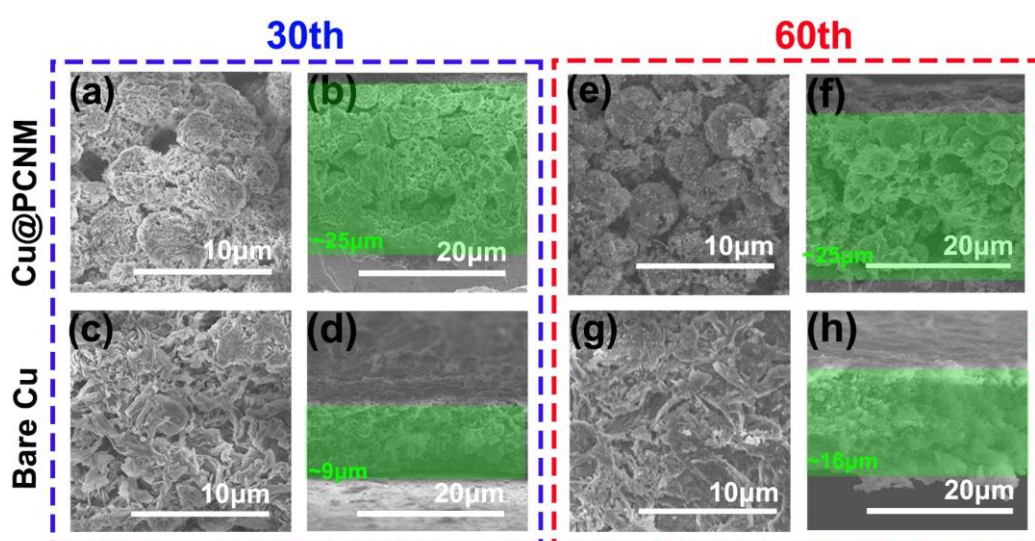


Figure 3.18. (a, c, e, and g) Top view and (b, d, f, h) cross-section view SEM images

of Cu@PCNM and bare Cu after (a-d) 30 cycles and (e-h) 60 cycles with an areal capacity of 2 mAh cm⁻² at 1.0 mA cm⁻². The regions marked with light green colour correspond with PCNM coatings and “dead Li” respectively.

Morphology of Cu@PCNM and bare Cu after 30 and 60 cycles (Fig. 3.18a-h) with an areal capacity of 2.0 mAh cm⁻² at 1.0 mA cm⁻² was measured. Apparent dendrite-like “dead Li” continuously accumulates on Cu foil during plating/stripping processes, contributing to the volume expansion (~16 μm after 60 cycles), increasing internal resistance, and electrolyte consumption. In contrast, PCNM maintains its comparatively intact structure and does not show accumulation of “dead Li” on its surface even after 60 cycles. This highlights the critical role of PCNM in inhibiting the formation of Li dendrites and reducing volume changes during charging/discharging.

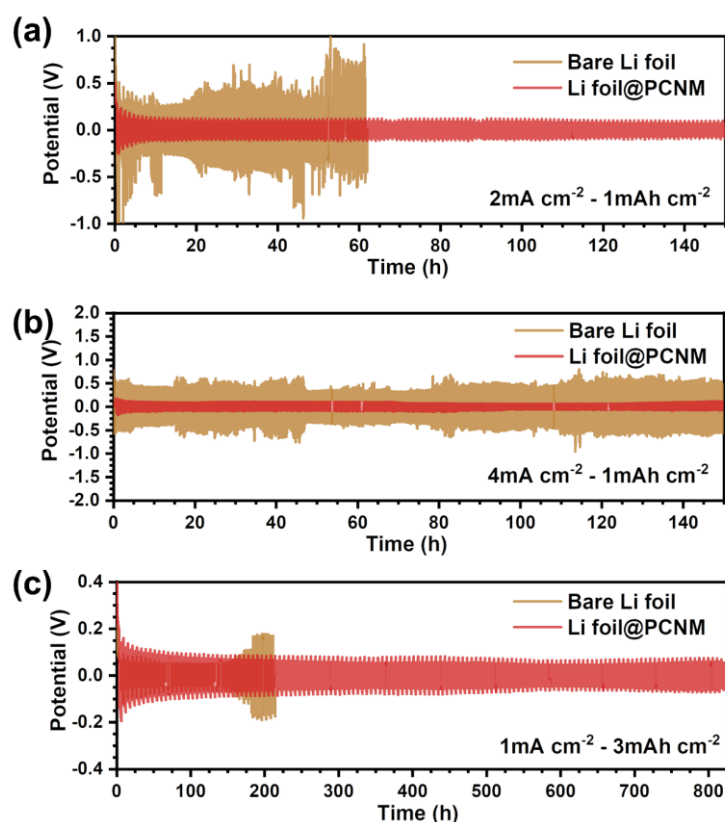


Figure 3.19. The galvanostatic plating/stripping profiles of Li||Li symmetrical cells with an areal capacity of (a) 1.0 mAh cm⁻² at 2.0 mA cm⁻², (b) 1.0 mAh cm⁻² at 4.0 mA

cm⁻² and (c) 3.0 mAh cm⁻² at 1.0 mA cm⁻² using Li foil@PCNM, and bare Li foil electrodes.

To employ PCNM in actual LMRBs, PCNM is coated on Li foil to form a composite LMNE. Long-term cycling stability and the stripping/plating process of symmetric cells assembled with identical Li foil@PCNM electrodes were investigated at high current densities and high capacity. As presented in Fig. 3.19a, Li foil symmetric cell shows a high potential hysteresis (~250 mV) in the initial stage, which is much higher than that of the Li foil@PCNM symmetric cell (~85 mV). As the cycling continues, the potential hysteresis of the Li symmetric cell rapidly increases to about 500 mV, accompanied by apparent potential fluctuation appearing after 20 h, which possibly implies the failure of the cell. This may be due to the irregular growth of dendrites on the surface of the Li foil during the stripping/plating. Then, Li dendrites with large surface areas continuously react with the electrolyte to form the SEI and partially “dead Li”, leading to growing internal resistance.

By contrast, the Li foil@PCNM symmetrical cell exhibits greater consistency during cycling over a longer period, enduring beyond 140 cycles. This greater stability can be attributed to the uniform Li⁺ flux induced by nanopores and the confined Li deposition promoted by PCNM. As shown in Fig. 3.19b, Li foil@PCNM symmetric cell also exhibits superior cycling performance under higher current density (4 mA cm⁻²-1mAh cm⁻²). With an increasing areal capacity to 3 mAh cm⁻², the Li foil@PCNM cell still exhibits a low overpotential of ~45 mV and good cycling stability with more than 800 hours (Fig. 3.19c). Li foil symmetric cell displays a steady overpotential (~45 mV) in the initial stage, followed by a sudden boost after 150 cycles due to possible short circuits.

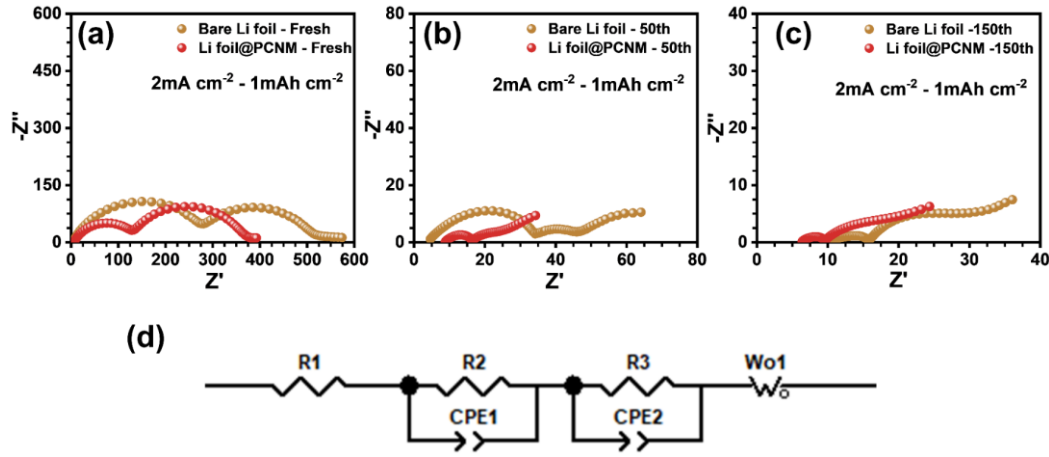


Figure 3.20. The EIS of the bare Li foil and Li foil@PCNM (a) before cycling and after (b) 50 and (c) 150 cycles with an areal capacity of 1.0 mAh cm⁻² at 2.0 mA cm⁻². (d) applied fitting resistance model: R1: R₀ (Ohmic resistance); R2: R_{SEI} (Migration resistance of Li⁺ through the SEI); R3: R_{ct} (Charge transfer resistance); Wo1: Warburg (Li⁺ diffusion resistance); CPE1/CPE2: Constant phase element (Conventional double-layer and passivation film capacitance).

Table 3.3. Fitting resistance data of the galvanostatic plating/stripping in symmetrical cells using Li@PCNM or bare Li foil with an areal capacity of 1.0 mAh cm⁻² at 2.0 mA cm⁻².

Sample	R1 (Ω)	R2 (Ω)	R3 (Ω)
Li foil@PCNM-fresh	6.531	128	242.6
Bare Li foil-fresh	4.396	280.3	252
Li foil@PCNM-50th	8.033	4.468	0.0010753
Bare Li foil-50th	4.146	30.71	4.551
Li foil@PCNM-150th	6.388	3.046	9.142
Bare Li foil-150th	10.75	4.972	12.33

The stability of SEI interface in Li foil@PCNM and bare Li foil during cycling (2 mA cm⁻² - 1 mAh cm⁻²) was analysed by EIS (Fig. 3.20). Notably, Li foil@PCNM shows lower interfacial resistance (128 Ω) before cycling compared to bare Li foil (280.3 Ω).

Specific resistance data derived from the fitting process are listed in Table 3.3. After 50 cycles and 150 cycles, Li foil@PCNM still performs much smaller interfacial resistance of 4.468 Ω and 3.046 Ω , respectively, which benefits from the fact that nanopore-driven uniform Li^+ distribution due to effective transient Li-N bonds and intact and stable electrode structure during cycling due to interparticle pore induced low volume changes.²²⁸

3.3.5. Li ions regulation by g- C_3N_4 materials

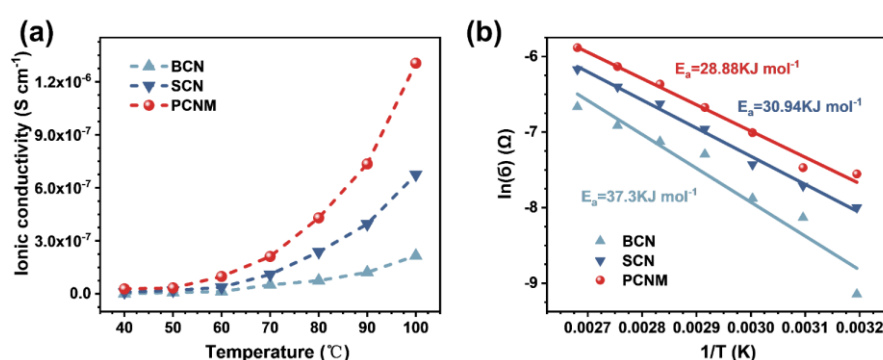


Figure 3.21. (a) Temperature-dependent ionic conductivity plots and (b) corresponding activation energy of Cu@SCN, Cu@BCN, and Cu@PCNM.

Table 3.4-1. Fitting resistance data of the BCN/SCN/PCNM&LiTFSI@Cu.

Items	T ($^{\circ}\text{C}$)	40	50	60	70
BCN	R(Ω)	728122	70349	39227	10232
	σ (S cm^{-1})	7.13916E-10	7.38913E-09	1.32515E-08	5.08032E-08
SCN	R(Ω)	51954	26784	13993	4731
	σ (S cm^{-1})	1.00054E-08	1.94078E-08	3.71484E-08	1.09875E-07
PCNM	R(Ω)	58318	48112	16555	7681
	σ (S cm^{-1})	2.78547E-08	3.37635E-08	9.81233E-08	2.11487E-07

Table 3.4-2. Fitting resistance data of the BCN/SCN/PCNM&LiTFSI@Cu.

Items	T (°C)	80	90	100	Thickness (μm)
BCN	R(Ω)	6948	4271	2414	~8
	σ (S cm^{-1})	7.48155E-08	1.21709E-07	2.15335E-07	
SCN	R(Ω)	2191	1316	770	~8
	σ (S cm^{-1})	2.37252E-07	3.94999E-07	6.75088E-07	
PCNM	R(Ω)	3778	2210	1245	~25
	σ (S cm^{-1})	4.29971E-07	7.35037E-07	1.30476E-06	

The difference in interaction with Li^+ of different g- C_3N_4 materials was characterised by measuring the Li^+ conductivity (corresponding to Li^+ transfer kinetics) of PVDF/LiTFSI-based solid-state electrolyte added with BCN, SCN, or PCNM powders (see details in the experimental section). g- C_3N_4 materials can facilitate Li^+ transportation in PVDF matrices owing to site-to-site hopping of Li^+ via Lewis-base sites in g- C_3N_4 .¹⁷² The morphology and pore structure of g- C_3N_4 materials have varying effects on Li^+ and can result in different ion transportation abilities. It is believed that enhancement in Li^+ conductivity is ascribed to more efficient interaction with Li^+ of g- C_3N_4 . According to Fig. 3.21a, the ionic conductivity of solid-state electrolytes with different g- C_3N_4 materials all increase with increasing temperature from 40°C to 100°C. PCNM-based one achieves the most superior ionic conductivity compared with the other two (Table 3.4). The activation energy of g- C_3N_4 materials is calculated via temperature-dependent EIS tests. Data acquired from all cases were fitted to straight lines using the following Arrhenius equation:

$$\frac{T}{R_{ct}} = A \exp\left(-\frac{E_a}{RT}\right) \quad (3.2)$$

where E_a is the activation energy, T is the absolute temperature, R is the gas constant (8.314J (mol·K)⁻¹), R_{ct} is the interfacial Li^+ transfer resistance, and A the pre-exponential factor²²⁹. The activation energy upon PCNM, SCN, and BCN are valued at 28.88, 30.94, and 37.30 kJ mol⁻¹, respectively (Fig. 3.21b), further verifying the

prominent role of PCNM with unique pore structure plays in interaction with Li^+ than that of BCN and SCN.

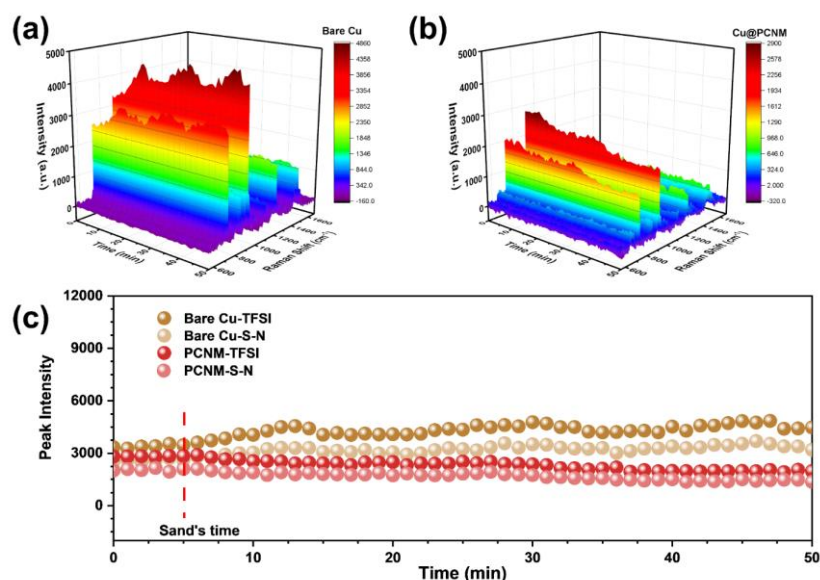


Figure 3.22. *In-situ* Raman spectra of (a) bare Cu foil and (b) Cu@PCNM; (c) Summary of intensity evolution of Raman peaks of electrolytes in the cells using Cu foil coated with and without PCNM in charging process at 1mA cm^{-2} .

Raman spectroscopy is a powerful tool to probe the polarizable surface in vibrational energy levels.²³⁰ It is reported that the average Li^+ concentration near the surface (less than $10\ \mu\text{m}$ above the surface) of plated Li can be increased via strong Li^+ affinity (e.g., Li-N).¹⁹⁷ This can efficiently compensate for Li^+ depletion and mitigate the surface concentration difference, which leads to more uniform local current density distribution and Li-plating morphology. However, near interfacial ($<300\ \mu\text{m}$) Li^+ flux distribution/fluctuation related closely to the concentration gradient change of Li^+ upon strong Li^+ affinity remains unknown. In addition, detecting concentration gradient change of the Li^+ flux is a more convenient way to investigate Li deposition behaviour, especially with some materials whose laser-induced signal will be shielded by excited fluorescence signal. Therefore, *in-situ* Raman spectroscopy was conducted in a Li||Cu cell to confirm the PCNM-regulated uniform Li^+ flux. The laser beam was set parallel

to the Cu foil or Cu@PCNM and was focused near the interface of the electrodes (~ 300 μm above the surface) to detect the concentration gradient change of ion flux. The operando Raman spectra were measured during the Li plating process at the current density of 1 mA cm^{-2} with the areal capacity of 1 mAh cm^{-2} . Before the electrochemical plating process, the Raman spectrum of the electrolyte in Fig. 3.22a-b shows featured bands at 741 cm^{-1} and 941 cm^{-1} , corresponding to the S-N stretching in coordinated TFSI and Li-coordinated solvent band, respectively, whose intensities can indirectly represent the Li^+ concentration.^{230, 231} The peak intensity of S-N and TFSI regarding bare Cu foil and Cu@PCNM is summarised in Fig. 3.22c.

The peak intensity of TFSI initially keeps at ~ 3000 on both electrodes. Bare Cu foil fluctuates from 3200 to 4900 with a range of ~ 1700 , while Cu@PCNM varies within only ~ 1000 during charging. Meanwhile, the peak intensity of S-N keeps at ~ 2300 at the beginning of both electrodes, followed by fluctuating within a range of ~ 1200 on bare Cu foil and ~ 700 on Cu@PCNM electrode, respectively. At the beginning of the plating (~ 5 min), initial stable nucleation and deposition play a dominant role in stabilizing the Li^+ flux near the interfacial area on bare Cu foil and Cu@PCNM before the formation of Li dendrites. Therefore, the peak intensities keep relatively stable during this period. It is referred that sphere-like Li seeds grow initially on Cu foil, followed by continuing preferential deposition on the Li seeds to form Li dendrites.²¹⁷ As the deposition proceeds, according to the dendrite growth model proposed by Chazalviel,⁶⁶ the concentration of Li^+ in the vicinity ($< 10 \mu\text{m}$) of the negatode will drop to zero at Sand's time, leading to the apparent concentration gradient. Consequently, the Li-dendrite-induced concentration gradient is reported to intensify the highly local disturbance of the Li^+ flux near the interfacial area of the negatode,¹⁹⁷ leading to the formidable fluctuation of the Li^+ flux. Thus, bare Cu foil shows a large fluctuation range of ~ 1700 and ~ 1200 in TFSI and S-N, respectively. In contrast, PCNM with N-rich Lewis-base sites and nano-channels can serve as a regulator to continually smooth the concentration of Li^+ flux¹⁹⁷ and ensure even ion flux in the vicinity of the

electrochemical interface, resulting in dendrite-free deposition and weakening local disturbance of Li^+ . Consequently, a reduced fluctuation in peak intensity, of approximate values of 1000 and 700 for TFSI and S-N, respectively, was noted owing to the improved stability of Li^+ flux in proximity to the negatrode.

3.4.6. Electrochemical performances of full cells

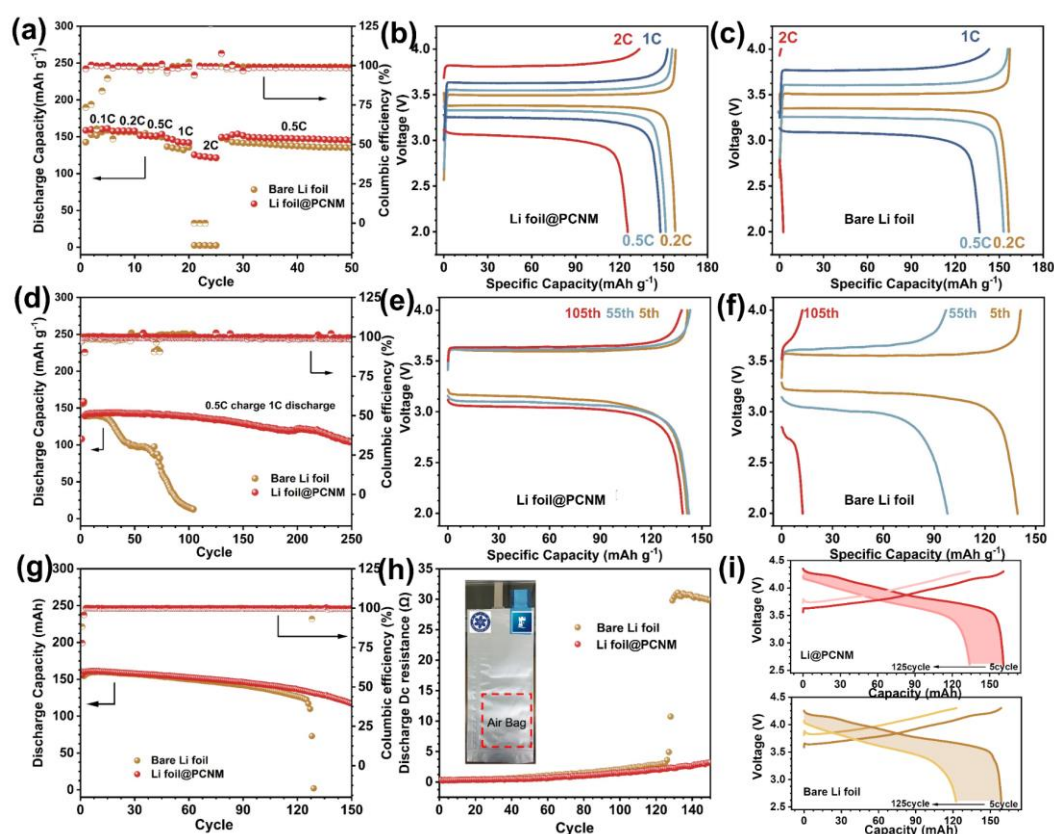


Figure 3.23. Performances of Li foil@PCNM in coin full cells and pouch cells. (a) Rate capability and (d) cycling performance of Li foil@PCNM and bare Li foil paired with high areal capacity LFP positrodes ($\sim 2 \text{mAh cm}^{-2}$). Voltage profiles of (b) Li foil@PCNM||LFP full cell and (c) bare Li foil||LFP full cell from 0.2C to 2C. Voltage profiles of (e) Li foil@PCNM||LFP full cell and (f) bare Li foil||LFP full cell at the 5th, the 55th, and the 105th cycle. (g) Cycling performance and (h) *in-situ* discharge internal resistance profiles of Li foil@PCNM and bare Li foil paired with high areal capacity NCM 811 positrodes ($\sim 3.75 \text{mAh/cm}^2$). (i) Voltage profiles of Li foil@PCNM||NCM 811 pouch cell and bare Li foil||NCM 811 pouch cells from the 5th to the 125th cycle.

For full batteries, we mainly adopted ester-based electrolytes and incorporated FEC additives into pouch cells to help form a better SEI. Although ether-based electrolytes have demonstrated many advantages in regulating LM deposition, ether-based electrolytes are severely hampered by their high flammability and low oxidation potential ($<4\text{V}$ vs. Li^+/Li). Thus, it is not suitable for full cells with high voltage ($>4\text{V}$). For full-cell, EC and DMC are commonly used as ester-based solvents, which can withstand higher voltage.²³² LiPF_6 is a commonly used fluorine-containing Li salt in commercial ester-based electrolytes based on its excellent comprehensive performance e.g. low corrosion towards Al current collector, high solubility and low price.²³³ Therefore, this electrolyte composition (LiPF_6 in a mixed solution of EC and DMC) was chosen to test full-cell performance (the positive was LFP) in this chapter. In addition, FEC as an additive can further help form Li-F components on the surface of LMNE and optimize cycling performance.²³² Therefore, an electrolyte containing FEC is used in pouch cells (the positive was NCM811) to improve its cycling performance and obtain more practical operating conditions.

To verify the practical performance of PCNM in full cells, long-term cycling and rate performance of full cells assembled with bare Li foil or Li foil@PCNM negative (20 mAh cm^{-2}) and LFP ($\sim 2 \text{mAh cm}^{-2}$) positive were tested. Compared with bare Li foil, Li foil@PCNM composite negative performs better rate capability, as illustrated in Fig. 3.23a. Especially at a high rate of 2C, the cell using Li foil@PCNM still delivers a high specific capacity of $\sim 125 \text{mAh g}^{-1}$, which is much higher than that of a bare Li foil cell ($\sim 5 \text{mAh g}^{-1}$), revealing the stable discharge capacity at high rates owing to the PCNM-driven stable Li^+ flux. Fig. 3.23b shows that the capacity retention of the full cell composed of bare Li foil undergoes a sharp drop to less than 10% after 100 cycles. In contrast, the full cell with Li foil@PCNM composite negative exhibits much higher capacity retention of $\sim 97\%$ after 100 cycles and $\sim 80\%$ after even more than 200 cycles. Compared with bare Li foil cell, Li foil@PCNM-based full cell exhibits lower voltage

hysteresis at all different charge/discharge rates of 0.1, 0.2, 0.5, 1, and 2C, and much more stable voltage hysteresis from the 5th to the 105th cycle (Fig. 3.23c-f). The improved rate capability and cycling stability of Li foil@PCNM can be ascribed to the nano-channel-induced uniform and stabilised Li⁺ flux and confined growth of Li in PCNM, which leads to much smaller polarisation and fast and uniform Li⁺ transportation.

The compatibility and practical feasibility of the Li foil@PCNM composite negatode (20 mAh cm⁻²) were further evaluated by pairing it with the NCM 811 positrode (~3.75 mAh cm⁻² on each side) in a pouch-type full cell with a designed initial capacity of ~0.16 Ah and electrolyte mass of ~0.96 g. Li foil||NCM 811 cells show apparent capacity and CE decay after 120 cycles at 0.2C, followed by a sudden drop, while Li foil@PCNM cell can maintain high capacity retention of ~73% after 150 cycles under the same condition (Fig. 3.23g). Fig. 3.23h displays a comparison of the internal resistances of pouch cells that are *in-situ* monitored to showcase how PCNM functions in reducing the electrochemical polarisation of cells during cycling. In the first 20 cycles, the internal resistance of Li foil||NCM 811 and Li foil@PCNM||NCM 811 pouch cells show a similar rising trend (increasing from ~0.2 Ω to ~0.4 Ω). Nevertheless, the internal resistance of Li foil||NCM 811 cell suffers from a dramatic increase to ~30 Ω after 130 cycles, while that of Li foil@PCNM||NCM 811 cells only gradually rises to ~2.7 Ω after more than 140 cycles. Smaller capacity decay (~25 mAh) can also be found in Li foil@PCNM||NCM 811 cells than that in bare Li foil||NCM 811 cells (almost doubled) from the 5th to the 125th cycle (Fig. 3.23i). More stable internal resistance and better cycling stability of Li foil@PCNM||NCM 811 pouch cells than that of Li foil||NCM 811 cells can be ascribed to the inhibition of “dead Li” and generation of more robust SEI by the PCNM coating.

3.4. Conclusions

In this work, we first investigated the influence of morphology over g-C₃N₄ materials on Li deposition/dissolution behaviour. Although the SCN layer can provide an effective interaction with Li⁺ during electrolyte penetration, its 2D lamellar structure lacks the mechanical strength to accommodate Li growth and absorb the increased stress caused by Li dendrite growth. Though a large space was found within the BCN coating layer, efficient interaction between Li⁺ and nitrogen atoms in g-C₃N₄ was limited due to the large pore size. In comparison, the 3D porous framework of the PCNM coating layer containing both nano- and micro-pores was more favourable for physical regulation of Li deposition to rapidly absorb the stress change and guide Li growth, resulting in suppression of volume variation. Meanwhile, nanopores in PCNM can facilitate chemical interaction between Li⁺ and N-containing functional groups, leading to homogenizing Li⁺ distribution based on the Debye-length law. The above physical-chemical synergic regulation strategy can promote dendrite-free Li plating. Resultantly, dense and stable deposits and highly reversible plating/stripping behaviour over the PCNM-decorated Cu foil/Li foil were fully confirmed in three different coin cells, i.e., Cu@PCNM||Li, Li foil@PCNM||Li foil@PCNM and Li foil@PCNM||LFP, and a pouch cell, i.e., Li foil@PCNM||NCM 811. This research provides novel insight into the rational structure design of lithiophilic materials for modifying LMNEs toward stable and long-life LMRBs.

Chapter4

Solvent Modification of Porous-Carbon-Nitride-Microsphere-based Coating Slurry on Lithium Metal Negative Electrode for Improved Lithium Deposition/Dissolution

This chapter reports a new method where Dimethylacetamide (DMAC) was used as a solvent to promote the self-driven chemical reaction between polyvinylidene fluoride (PVDF) and Li to form Li-F. Thus, a Li-F-rich layer was built in advance on the surface of the Li foil@PCNM electrode to reduce direct contact with the electrolyte, leading to enhanced electrochemical performances of symmetric cells and full cells.

4.1. Introduction

As discussed in Chapter 3, a uniform lithiophilic coating layer with both nanometre and micrometre pores not only provides a physical 3D porous framework to absorb volume changes and guide Li growth but also renders suitable chemical interaction distance to homogenise the Li^+ flux based on Debye length law effectively.²³⁴ Thus, such a physical-chemical synergic regulation strategy using PCNM can achieve dendrite-free Li plating. Nevertheless, it is still difficult to avoid the direct contact between electrolyte and LM, which can lead to continuous side reactions and affect the long cycling performance of the battery.

The construction of an inert artificial SEI layer with high Li^+ conductivity is one of the

most effective methods to shield the direct contact of LM toward electrolyte and alleviate the side reactions²³⁵ among widely proposed Li dendrite mitigation strategies such as current collector engineering,²³⁶ surface protection,²³⁷ and electrolyte modification.²³⁸ The organic SEI layer (e.g., polydimethylsiloxane²³⁹) or inorganic SEI layer (e.g., LiPON²⁴⁰ or LiF²⁴¹), or alloy SEI layer (e.g., Li-Hg²⁴²) or their hybrid SEI layer (e.g., inorganic/alloy SEI layer²³⁷ or organic/inorganic SEI layer²¹⁹) are currently reported to isolate the direct contact of electrolyte towards LM and allow uniform Li⁺ flux through this inert artificial protection layer. Inorganic components (such as Li-F) are widely employed in artificial SEI due to their high mechanical strength, low solubility, wide band gap (8.9 eV, fruitfully preventing electron tunnelling), and extra wide voltage window (up to 6.4 V vs. Li/Li⁺), effectively preventing LM from corrosion by the electrolyte. When LiF is mixed with other inorganic components such as Li₃N, Li₂O, Li₂CO₃, and LiOH on the nanoscale, higher Li⁺ conductivity can be highly guaranteed.²⁴³ A polymer such as PVDF can *in-situ* react with LM to form Li-F composition via self-driven chemical reaction, which can be regarded as a typical dehydrogenation and defluorination process of PVDF.²⁴⁴ Consequently, the implementation of this technique in large-scale LM coating processes utilizing PVDF slurry is also deemed viable to form Li-F components on LM.

However, generating a substantial number of Li-F components solely through the coating process is a challenging task. The traditional preparation process never considers the contact area or chemical reaction between PVDF and Li. For example, NMP, commonly used as a solvent in LIBs, especially for positrodes, is relatively stable and can hardly help form Li-F on LM. Thus, solvents as critical components are often neglected.

Solvents can affect the degree of *in-situ* reaction, distribution of active materials, and stabilisation of the LM interface, which may affect the pre-construction of Li-F-rich SEI on LM. For example, DMF with a low boiling point can increase the volatilization

rate of the solvent,²⁴⁵ which may affect the self-driven reaction between Li and PVDF. Thus, a suitable solvent can provide complete contact and promote the chemical reaction between LM and PVDF solution, leading to an enhanced amount of Li-F.

As such, we intend to employ a well-suited solvent to develop an initial Li-F enriched layer atop the Li@PCNM surface, thus creating an inert and artificial SEI layer. This approach aims to reduce direct contact between the electrolyte and Li@PCNM, thereby enabling more effective suppression of adverse interfacial reactions. The ideal coating solvent for Li-metal-based *in-situ* reaction is expected to follow the points below. Firstly, the solvent can keep comparatively stable with LM. Secondly, it should have excellent solubility toward materials such as binders. Thirdly, low cost and high safety are also essential for large-scale production. Lastly, extra function is highly expected, especially for facilitating the *in-situ* reaction. According to the above rules, considering that the generation of Li-F belongs to PVDF dehydrofluorination reaction, the selected solvent should preferably possess active sites such as the Lewis base site, and should also have a low boiling point and comparatively high chemical stability. DMAC and DMF are new solvents that can replace NMP because of their low cost, low boiling point, low surface tension and good chemical stability. Through the utilization of this solvent, it is feasible to reduce battery production expenses without compromising electrode stability.²⁴⁵ In addition, DMAC and DMF also have similar molecular structures (containing the N atom as Lewis base site and carbonyl groups), which may facilitate the generation of Li-F.²⁴⁶ Therefore, in this chapter, we will compare DMAC and DMF with conventional NMP solvents, and focus on the stability toward LM and the impact of three solvents on surface Li-F generation. Results showed that DMAC can be used as a solvent to promote the self-driven chemical reaction between PVDF (binder) and LM in this chapter, as illustrated in Fig. 4.1. In comparison with DMF and NMP, DMAC not only keeps comparatively stable with LM, but it also effectively facilitates the formation of Li-F during coating. Finally, the electrochemical performances, such as long-term cycling, were enhanced.

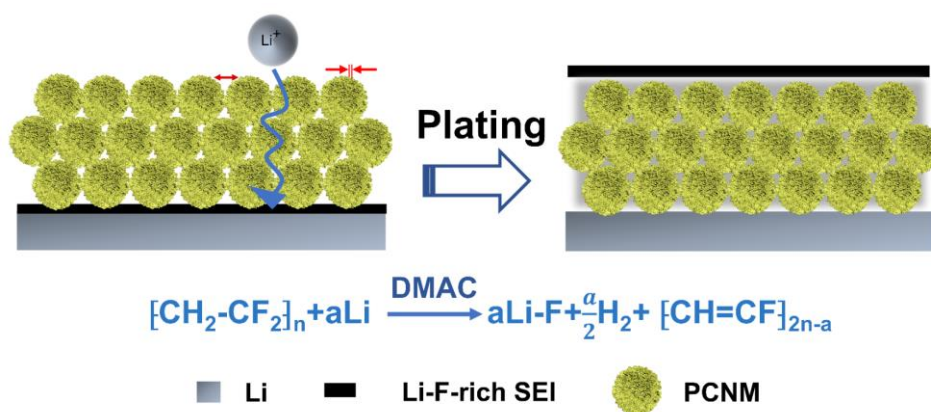


Figure 4.1. Diagrams showing the mechanism of electrodeposited Li on Li@PCNM-DMAC and self-driven chemical reaction between Li and PVDF.

4.2. Experimental section

4.2.1. Electrodes preparation

Fabrication of Li foil@PCNM (or Li@PCNM-NMP), Li@PCNM-DMF, and Li@PCNM-DMAC. The as-prepared PCNM powders were mixed with PVDF in NMP, DMF, and DMAC, respectively, with a 1:1 mass ratio of PCNM to PVDF. After stirring for 10 h, PCNM slurry was quickly cast on 100 μm thick Li foil with a thickness of 200 μm in the ultra-dry clean room (Dew point: below -45°C , cleanliness level: 100,000) at room temperature followed by vacuum-dried at 80°C for 6h. The as-obtained Li foil@PCNM (or Li@PCNM-NMP), Li@PCNM-DMF, and Li@PCNM-DMAC were punched into 14 mm circular or 47 mm \times 57 mm rectangular discs, respectively, as the negatode.

4.2.2. Electrochemical Measurements

Two-electrode coin half cells (Bare Li foil vs. Bare Li foil or Li@PCNM-DMAC vs. Li@PCNM-DMAC). Standard CR2032 coin-type cells were assembled in an Ar-filled

glove box with O₂ and H₂O content below 1 ppm. For Li||Li symmetrical coin cells, two identical 14 mm discs of bare Li foil or Li@PCNM-DMAC were assembled into symmetrical coin cells with polypropylene (Celgard 2500) as the separator. The electrolyte with 1 M LiPF₆ in EC/DMC=1:1 by volume with 2 wt% FEC was employed. The electrolyte of 75 μL is added to each coin cell. All coin cells were shelved for 8 h before testing. The galvanostatic performances were conducted at 25 °C using the Land CT 2100A system (Jinnuo Wuhan Corp, China). Li was plated galvanostatically with the capacity of 1 mAh cm⁻² on the bare Li foil or Li@PCNM-DMAC and then stripped galvanostatically with the same capacities of 1 mAh cm⁻² at different current densities (1-3mA cm⁻²). EIS was measured by an electrochemical workstation (Solartron 1470E) using CR2032-type coin cells. The frequency range was chosen between 1 MHz and 0.01 Hz.

Two-electrode coin full cells (LFP vs. Bare Li foil or LFP vs. Li@PCNM-NMP (same as Li@PCNM) or LFP vs. Li@PCNM-DMAC). The as-prepared 14 mm discs of bare Li foil or Li@PCNM-NMP or Li@PCNM-DMAC and LFP were employed as the negatropes and positropes, respectively. The areal loading of the LFP positrode was 12 mg cm⁻², corresponding to an areal capacity of ~2 mAh cm⁻². The areal loading of the bare Li foil or Li@PCNM-NMP or Li@PCNM-DMAC negatrode was 20 mAh cm⁻². Celgard 2500 was used as the separator (25μm). The electrolyte used herein was 1 M LiPF₆ in EC/DMC=1:1 by volume with 2 wt% FEC. Electrolyte injection is fixed at 75 μL in each coin cell. All coin cells were shelved for 8 h before testing. The LFP-based full cells were galvanostatically charged up to 4 V at 0.5C and then galvanostatically discharged to 2.0 V at 1C.

Two-electrode coin full cells (NCM 811 vs. Bare Li foil or NCM811 vs. Li@PCNM-DMAC). The as-prepared 14 mm discs of bare Li foil or Li@PCNM-DMAC and NCM811 were employed as the negatropes and positropes, respectively. The areal loading of the NCM 811 positrode was ~20 mg cm⁻², corresponding to an areal capacity

of $\sim 4 \text{ mAh cm}^{-2}$. The areal loading of the bare Li foil or Li@PCNM-DMAC negatrod was 20 mAh cm^{-2} . Celgard 2500 was used as the separator ($25 \mu\text{m}$). The electrolyte used herein was 1 M LiPF_6 in EC/DMC=1:1 by volume with 2 wt% FEC. Electrolyte injection is fixed at $75 \mu\text{L}$ in each coin cell. All coin cells were shelved for 8 h before testing. The NCM 811-based full cells were galvanostatically charged up to 4.3 V and then galvanostatically discharged to 2.6 V at various rates from 0.1 to 3C. The cycling performances of the cells were tested by charging at 0.1 C and discharging at 0.3 C within the voltage range from 2.6 to 4.3 V.

Pouch cells (NCM 811 vs. Bare Li foil or NCM 811 vs. Li@PCNM-DMAC). As-prepared bare Li foil or Li@PCNM-DMAC with a size of $47 \text{ mm} \times 57 \text{ mm}$ was employed as the negatrod (20 mAh cm^{-2}). As-prepared NCM 811 electrodes with a size of $43 \text{ mm} \times 53 \text{ mm}$ were applied as the positrod. Single-side areal loading of the positrod was $\sim 20 \text{ mg cm}^{-2}$, corresponding to the areal capacity of $\sim 3.75 \text{ mAh cm}^{-2}$. Celgard 2500 was used as the separator ($25 \mu\text{m}$). Pouch cells are fabricated within $\sim 30 \text{ min}$ in the ultra-dry clean room (Dew point: below -45°C , cleanliness level: 100,000) at room temperature. The electrolyte with 1 M LiPF_6 in EC/DMC=1:1 by volume with 2 wt% FEC was used (6 g Ah^{-1}). After injecting the electrolyte, full cells were at least stored for two days to achieve full infiltration of electrolytes into pores of separators and positrodes. The NCM 811-based pouch cells were galvanostatically tested by charging at 0.1 C and discharging at 0.3 C within the voltage range from 2.6 to 4.3 V. N/P ratio is around 5. Pouch cells were subjected to 100 kPa pressure during charging/discharging.

4.3. Results and discussion

4.3.1. Materials characterisations

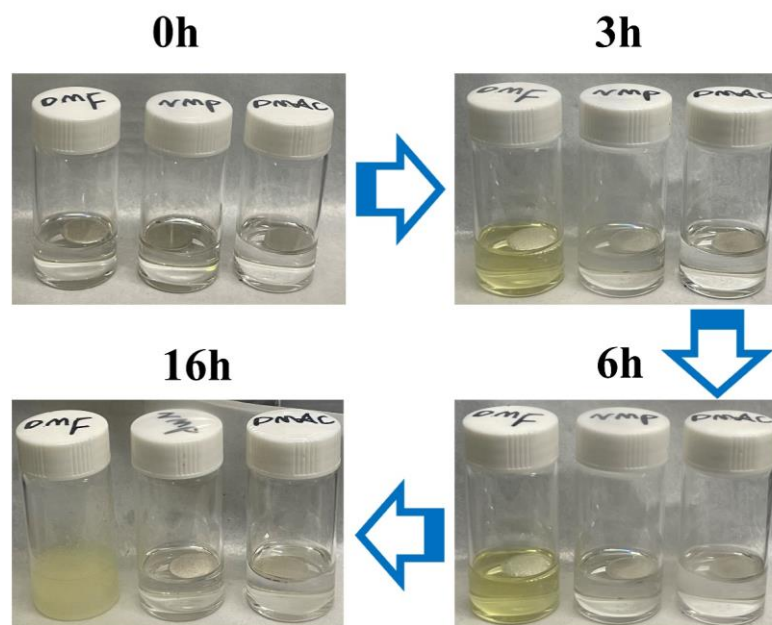
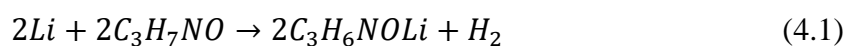


Figure 4.2. Digital photographs showing the time-dependent corrosion behaviour between LM and DMF, NMP, and DMAC.

To determine the stability of Li and prevent any significant corrosion, the corrosion performance between LM and DMF, NMP, or DMAC was evaluated, as depicted in Fig. 4.2. In the beginning, Li discs with 0.5 mm in thickness and 16.0 mm in diameter were immersed in DMF, NMP, and DMAC respectively. After 3h, the colour of DMF containing Li changes from colourless to light yellow. Curiously, the Li disc is fully dissolved in DMF after 16h, demonstrating a fast reaction between Li and DMF and implying that DMF is unsuitable as a coating solvent on LM. The possible chemical reaction can be found in equation (4.1). There is no change in the colour of NMP and DMAC within 16h, showing that LM can keep pretty stable with them.



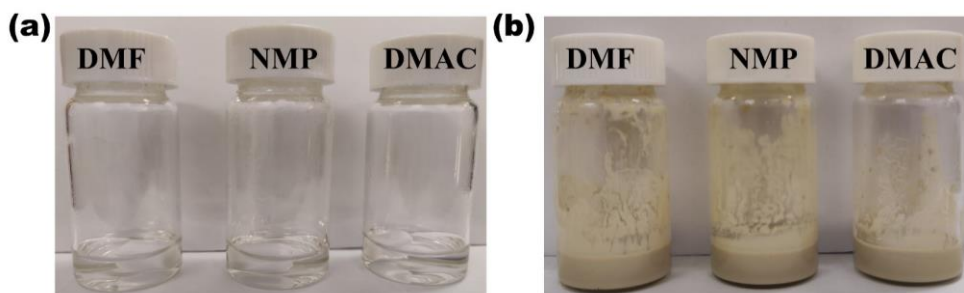


Figure 4.3. (a) Uniform and stable PVDF solution and (b) coating slurry (PVDF+PCNMs) using DMF, NMP, and DMAC, respectively.

To further evaluate the dissolution condition of PVDF and PCNMs in different solvents, the relevant solutions were separately prepared. As presented in Fig. 4.3a, PVDF can be fully dissolved in DMF, NMP, or DMAC to form a uniform and stable PVDF solution. Fig. 4.3b illustrates that PCNMs can be uniformly dispersed in three types of PVDF solutions, resulting in a highly stable coating slurry. Based on the aforementioned results, it can be inferred that DMF, NMP, or DMAC satisfy the criteria of uniformity and stability for the coating slurry.

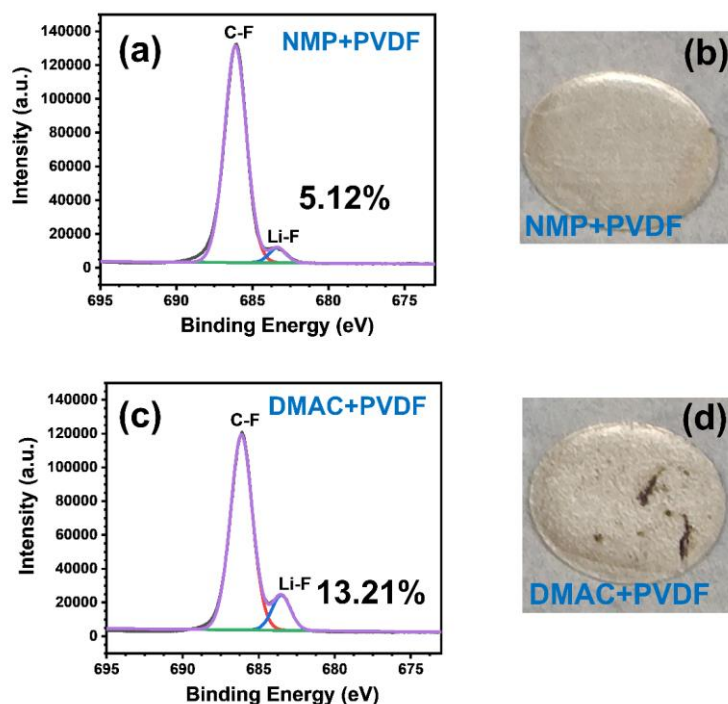


Figure 4.4. (a) F 1s XPS spectra and (b) optical photos of Li foil coated with PVDF

solution using NMP as a solvent. (c) F 1s XPS spectra and (d) optical photos of Li foil coated with PVDF solution using DMAC as a solvent.

To further clarify the effect of solvents on the self-driven reaction between LM and PVDF, XPS analysis was performed to determine the surface chemical composition of LM drop-coated with PVDF slurry containing NMP or DMAC respectively (Li@PVDF-NMP and Li@PVDF-DMAC in Fig. 4.4). In the F 1s spectra (Fig. 4.4a and Fig. 4.4c), Li-F and C-F signals are observed in both Li electrodes, which verifies that Li-F can result from the self-driven reaction between Li and PVDF. Compared with Li@PVDF-NMP, Li@PVDF-DMAC has more than two times larger Li-F content (13.21%), showing that the formation of Li-F can be facilitated effectively using DMAC as a solvent. In addition, a few black substances can be observed in the optical photos of Li@PVDF-DMAC (Fig. 4.4d), which is ascribed to the physical optical effect resulting from an increase in LM roughness.

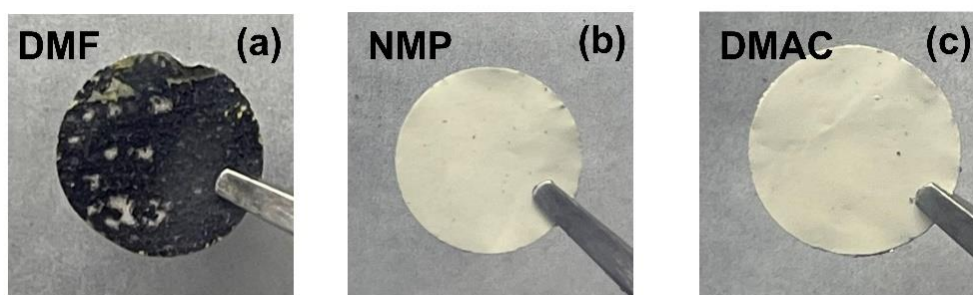


Figure 4.5. Comparison of optical photos of Li@PCNM using (a) DMF, (b) NMP, and (c) DMAC as solvents.

The as-prepared PCNM powders were mixed with PVDF in NMP, DMF, and DMAC, respectively, with a 1:1 mass ratio of PCNM to PVDF, to form a coating slurry. Li@PCNM-DMF, Li@PCNM-NMP, and Li@PCNM-DMAC were prepared by casting the above slurry on a 100 μm thick Li foil. Fig. 4.5a exhibits that black substances on the surface of LM using DMF-based coating slurry are formed, which

strongly supports our claim that there is strong corrosion between DMF and Li foil. This corrosion can lead to an extremely uneven LM surface, which may result in a black colour area. Thus, DMF is not an appropriate solvent for coating on LM. While the bright yellow colour of PCNMs can be found in Li@PCNM-NMP and Li@PCNM-DMAC (Fig. 4.5b-c), suggesting LM is sufficiently stable in DMAC and NMP-based slurry, and DMAC and NMP are feasible options as coating solvents.

From the reaction mechanism, it is speculated that three solvents are likely to promote the reaction between Li and PVDF. Shen et al.²⁴⁶ found that the La atom of $\text{Li}_{6.75}\text{La}_3\text{Zr}_{1.75}\text{Ta}_{0.25}\text{O}_{12}$ could complex with the N atom and C=O group of DMF/DMAC/NMP along with electrons enriching at the N atom, which has like a Lewis base and induced the chemical dehydrofluorination of the PVDF skeleton. When LM is present, the dehydrofluorination of the PVDF will further promote the generation of Li-F and $[\text{CH}=\text{CF}]_n$.²⁴⁷ Therefore, the presence of the N atom and C=O group in DMAC, NMP, and DMF may promote the generation of Li-F through their active catalytic sites.

Although three solvents can theoretically promote the generation of Li-F, the difference in solvents may be closely related to the stability toward LM and the solvation structure formed by the solvent with PVDF.

The three solvents show different stability to LM, which may be mainly due to the difference in molecular structure. Among them, DMF is the most unstable for LM, which makes it difficult to use as a coating solvent. This may be due to the presence of hydrogen on the carbon connecting the carbonyl group, which makes DMF highly active. This carbon-hydrogen bond may be easily attacked by LM, leading to bond breaking and decomposition.²⁴⁷ There are no hydrogen bonds in the carbon connecting with the carbonyl group for the other two solvents, so it may help them maintain a relatively stable state. However, after approximately 48 hours, LM will also undergo

dissolution in DMAC, but it won't occur in NMP. This proves that the stability of DMAC towards LM is an intermediate condition, and chain molecules are still easily reduced by LM. The high stability of NMP may be ascribed to the molecular ring structure which increases the stability of the molecular structure.

The difference in solvation structure formed by different solvents with PVDF may be the main reason for the difference in Li-F generation, and the stability of solvents on LM is likely to further affect the generation of Li-F. The solvation structure formed by NMP around PVDF may be the most stable. In addition, NMP exhibits the strongest stability towards LM. Therefore, NMP will form a very stable solvated shell layer to avoid excessive contact between Li and PVDF. Compared to NMP, the molecular solvation structure formed by DMAC may be weaker, thus enabling Li preferentially to contact PVDF more easily. In addition, due to the intermediate stability of DMAC, LM may first react slowly with this solvated shell layer, which may gradually weaken the solvated structure formed by DMAC and ultimately accelerate the interface contact between PVDF and LM. Lastly, when DMF solution containing PVDF contact with LM, the solvation structure formed by DMF with PVDF is the weakest, and the solvation shell of DMF will preferentially bring violent side reactions with LM,²⁴⁷ accelerating the unevenness of LM. Although PVDF can easily contact LM and even produce Li-F, the violent side reactions on the surface have destroyed the stability of the electrode interface, making it difficult to be used as an electrode.

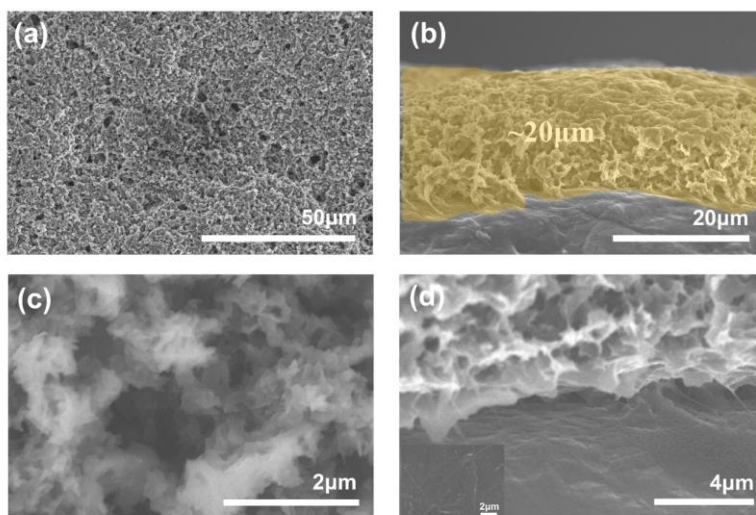


Figure 4.6. (a) The top-view and (b) cross-section view SEM images of Li@PCNM-DMAC. (c) The top-view and (d) cross-section view high-magnification SEM images of Li@PCNM-DMAC. The inset of (d) is an SEM image of the bare Li.

The morphology of Li@PCNM-DMAC was further characterised. The coating with a thickness of $\sim 20 \mu\text{m}$ displays a relatively smooth surface (Fig. 4.6a-b). Similarly, the high-magnification SEM image (Fig. 4.6c) shows that random packing of PCNM particles in this flat coating layer forms inter-particle pores, along with internal nanopores inside each g- C_3N_4 microsphere. This hierarchical pore structure can fully guarantee the physical-chemical synergic regulation strategy mentioned in Chapter 3 for achieving dendrite-free Li plating. As depicted in the high-magnification SEM image (Fig. 4.6d), the LM interface beneath the PCNM layer appears rougher in comparison to bare Li foil (inset of (d)). This phenomenon may be attributed to the self-driven chemical reaction. Briefly, the above characteristics further confirm that DMAC keeps stable with LM and effectively facilitates the formation of Li-F during the self-driven chemical reaction between LM and PVDF.

4.3.2. Morphology of Li plating

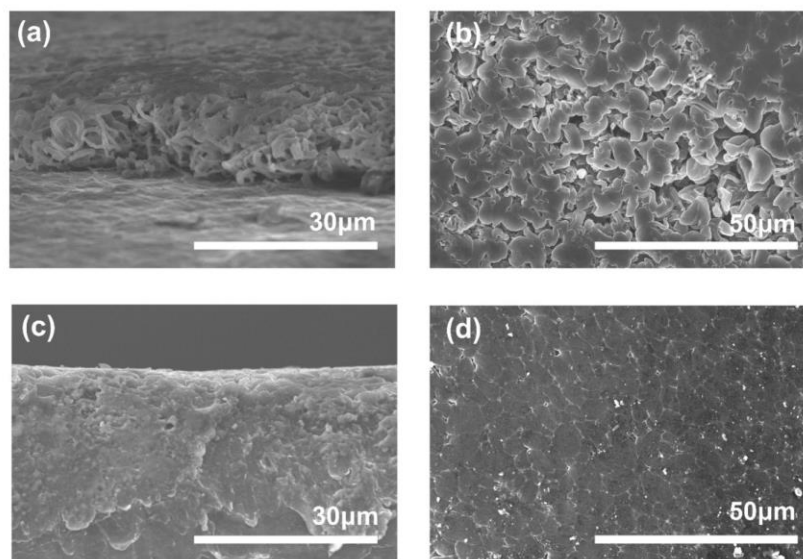


Figure 4.7. (a) Cross-section view and (b) top-view SEM images of bare Li foil after plating with 3.0 mAh cm^{-2} of Li. (c) Cross-section view and (d) top-view SEM images of Li@PCNM-DMAC after plating with 3.0 mAh cm^{-2} of Li. The current density is 0.5 mA cm^{-2} .

The deposition morphology of Li plays a crucial role in determining electrochemical performance metrics such as long-term cycling endurance. Fig. 4.7 exhibits different morphologies of metallic Li plated on bare Li foil and Li@PCNM-DMAC with a capacity of 3 mAh cm^{-2} at 0.5 mA cm^{-2} . It can be found in the cross-section view of bare Li foil (Fig. 4.7a) that the plated Li has an apparent dendrite-like morphology. The dendritic morphology of Li, further confirmed in Fig. 4.7b, can dramatically increase electrolyte consumption and give rise to a considerable volume expansion. In remarkable contrast, Li tends to form a filling-like deposition within the interparticle pores of PCNM, as presented in Fig. 4.7c, leading to minor volume expansion. Dense and flat Li deposit is further developed, as shown in Fig. 4.7d, due to the PCNM-induced homogenised Li^+ flux. Thus, Li@PCNM-DMAC still achieves uniform Li deposition, enabling DMAC to maintain the advantages of the PCNM layer as reported in Chapter 3 without introducing adverse effects caused by the enhanced *in-situ* reaction

on plating Li.

4.3.3. Volume expansion tests

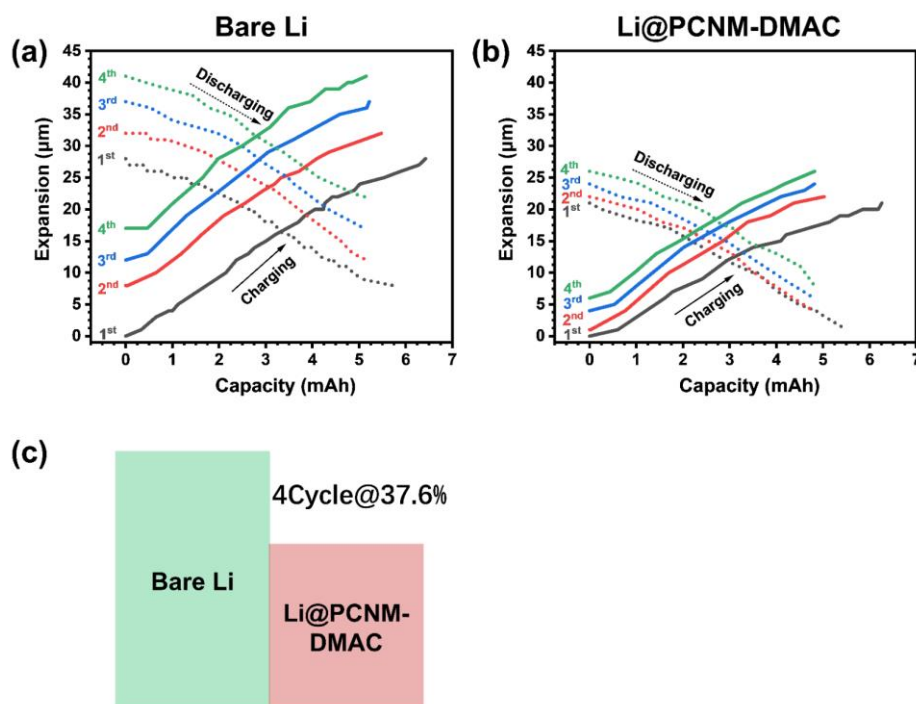


Figure 4.8. *In-situ* swelling dimension of (a) bare-Li-foil-based and (b) Li@PCNM-DMAC-based cells paired with high areal capacity NCM811 positrodes ($\sim 4 \text{ mAh cm}^{-2}$) during charging and discharging. (c) Comparison of the maximum swelling dimension of (a) bare-Li-foil-based and (b) Li@PCNM-DMAC-based full cells within 4 cycles.

The *in-situ* volume expansion of LMRB is a pretty important parameter affecting its practical application. Thus, *in-situ* swelling dimensions of bare-Li-foil-based and Li@PCNM-DMAC-based full cells paired with high areal capacity NCM811 positrodes ($\sim 4 \text{ mAh cm}^{-2}$) within 4 cycles were collected to verify further PCNMs-induced suppressed volume expansion. Fig. 4.8a shows that the bare Li foil can reach a thickness expansion of $\sim 28 \mu\text{m}$ when it is fully charged for the first time. As the cell cycling, bare Li foil arrives at a remarkable volume expansion of nearly $43 \mu\text{m}$ at the fourth circle. In addition, after 4 cycles, the cell thickness increased by $20 \mu\text{m}$ (20% of the pristine Li thickness), mainly due to the uncontrolled accumulation of porous Li

dendrites and “dead Li”. The Li@PCNM-DMAC has a thickness expansion of about 20 μm when fully charged for the first time and only increases to 25 μm at the fourth charge state, as presented in Fig. 4.8b. In addition, after 4 cycles, the cell thickness increased by only 7 μm . Dramatic reduction of volume expansion is mainly attributed to the PCNM-induced uniform Li deposition, leading to less porous “dead Li” and physical space accommodation for plated Li. Specifically, as shown in Fig. 4.8c, Li foil coated with PCNM using DMAC significantly reduced volume expansion by 37.6% within only 4 cycles compared to bare Li, which confirms the advantage of PCNM layer in suppressing the formation of Li dendrite and alleviating volume expansion.

4.3.4. Electrochemical performances of half cells

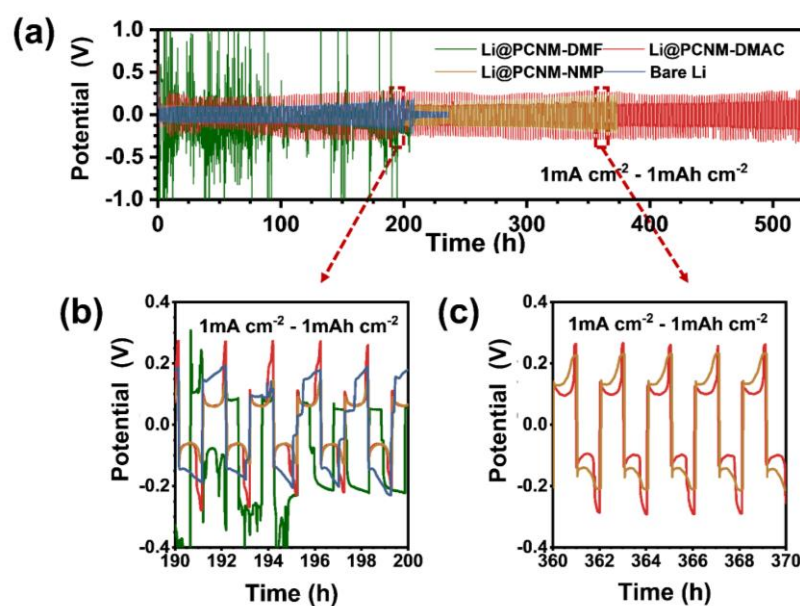


Figure 4.9. (a) The galvanostatic plating/stripping profiles of Li||Li symmetrical cells with an areal capacity of 1.0 mAh cm⁻² at 1.0 mA cm⁻² using Li@PCNM-NMP, Li@PCNM-DMF, Li@PCNM-DMAC, and bare Li foil. Magnified potential profiles within the plating/stripping time range of (b) 190-200h and (c) 360-370h.

This chapter is a further optimization of the coating layer using DMAC based on Chapter 3. To further demonstrate the modification advantages of the coating layer, especially for full cells, an ester-based electrolyte component containing FEC (LiPF₆

in a mixed solution of EC and DMC) was directly used in all cells, which makes the performance more comparable to that of the previous chapter.

Long-term cycling stability and the stripping/plating process of symmetric cells assembled with identical Li@PCNM-NMP, Li@PCNM-DMF, Li@PCNM-DMAC, or bare Li foil electrodes were tested at 1.0 mA cm^{-2} with an areal capacity of 1.0 mAh cm^{-2} . Notably, Fig. 4.9a shows that Li@PCNM-DMF symmetric cell performs an extremely abnormal charge/discharge potential curve, highly proving that DMF is unsuitable as a coating solvent on LM because of severe side reactions (Fig. 4.5a). As presented in Fig. 4.9a-b, Li foil symmetric cell shows the highest potential hysteresis ($\sim 170 \text{ mV}$) after 190h. While Li@PCNM-NMP and Li@PCNM-DMAC symmetric cells keep similar potential hysteresis ($\sim 60 \text{ mV}$), strongly verifying that reduced potential hysteresis is due to the nanopore-triggered uniform Li^+ flux and PCNM-driven confined deposition. As the cycling progresses, the potential hysteresis of the Li symmetric cell rapidly diminishes to approximately 35 mV , and no potential fluctuations are observed after 210 hours. This observation may imply that the occurrence of internal short circuits induced by Li dendrites ultimately results in the failure of the cells. The potential hysteresis of Li@PCNM-NMP symmetric cell gradually grows to $\sim 170 \text{ mV}$ which is larger than that of Li@PCNM-DMAC by $\sim 70 \text{ mV}$ at 360h (Fig. 4.9a and 4.9c), demonstrating the DMAC-facilitated Li-F-rich SEI can further reduce the formation of by-products (such as parasitic reactions generating SEI) or “dead Li”. Thus, PCNM not only renders uniform Li^+ flux and alleviated volume expansion, but DMAC-facilitated Li-F composition can also give rise to the reduction of interface resistance, further boosting the long-term cycling performance.

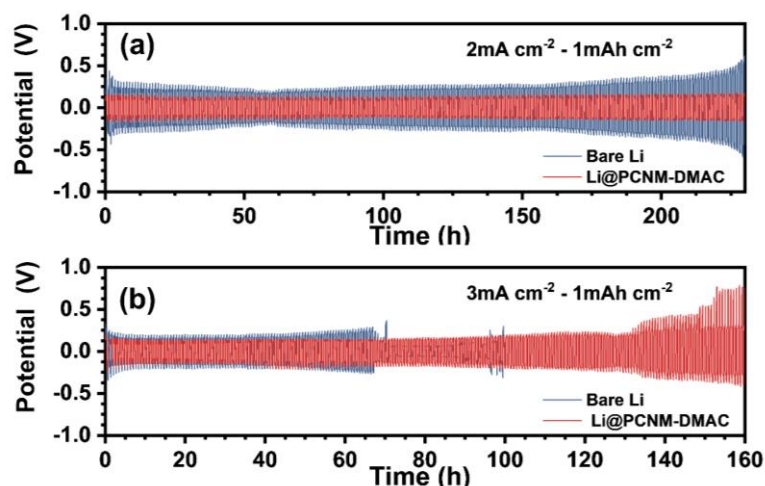


Figure 4.10. The galvanostatic plating/stripping profiles of Li||Li symmetrical cells with an areal capacity of 1.0 mAh cm⁻² at (a) 2.0 mA cm⁻² and (b) 3.0 mA cm⁻² using Li@PCNM-DMAC and bare Li foil.

Long-term cycling stability of Li@PCNM-DMAC and bare Li foil symmetric cells at high current density (2.0 mA cm⁻² and 3.0 mA cm⁻² with an areal capacity of 1.0 mAh cm⁻².) are further collected. Fig. 4.10a-b illustrates that Li@PCNM-DMAC symmetric cell also exhibits superior cycling performance with more negligible potential hysteresis (100 mV at 2.0 mA cm⁻² and ~115 mV at 3.0 mA cm⁻²) than bare Li foil under higher current density.

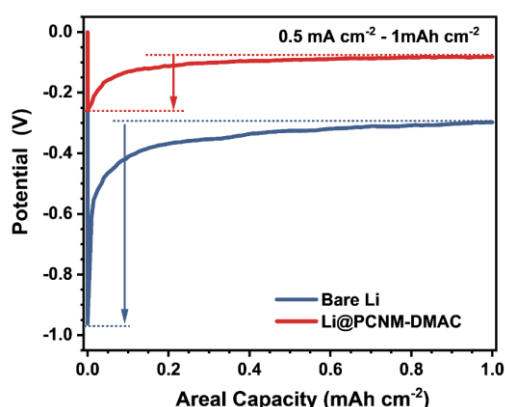


Figure 4.11. Comparison of nucleation overpotential of Li plating on bare Li foil and Li@PCNM-DMAC with an areal capacity of 1.0 mAh cm⁻² at 0.5 mA cm⁻².

Li nucleation behaviours on bare Li foil and Li@PCNM-DMAC were further investigated via the potential-capacity profiles in Fig. 4.11. Compared to bare Li foil, it has been demonstrated that Li@PCNM-DMAC displays a reduced nucleation overpotential. This serves as evidence that the lithiophilic coating layer of PCNM interacts effectively with the Li⁺ flux, leading to a decrease in the Li nucleation barrier on Li foil.

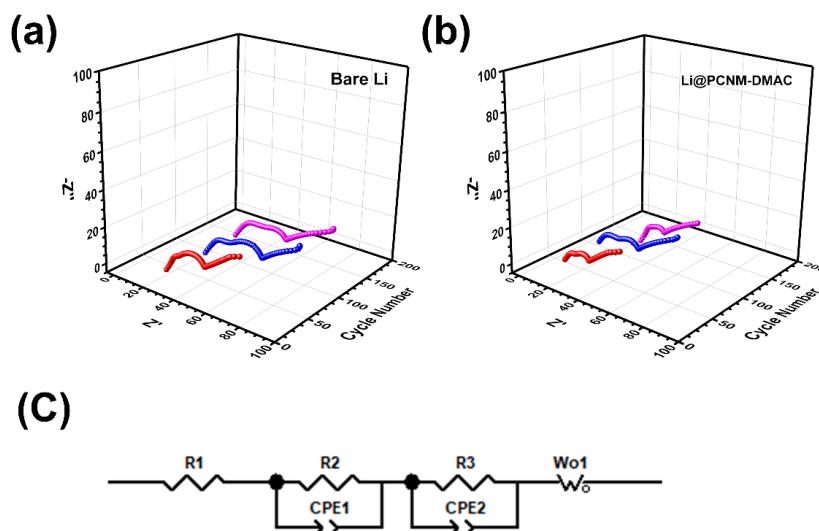


Figure 4.12. The EIS of the bare (a) Li foil and (b) Li@PCNM-DMAC after 50 cycles, 100 cycles, and 150 cycles with an areal capacity of 1.0 mAh cm⁻² at 3.0 mA cm⁻². (c) Applied fitting resistance model: R1: R₀ (Ohmic resistance); R2: R_{SEI} (Migration resistance of Li⁺ through the SEI); R3: R_{ct} (Charge transfer resistance); Wo1: Warburg (Li⁺ diffusion resistance); CPE1/CPE2: Constant phase element (Conventional double-layer and passivation film capacitance).

Table 4.1. Fitting resistance data of the galvanostatic plating/stripping in symmetrical cells using bare Li foil or Li@PCNM-DMAC with an areal capacity of 1.0 mAh cm⁻² at 3.0 mA cm⁻².

Sample	R1 (Ω)	R2 (Ω)	R3 (Ω)	WO1
Li@PCNM-DMAC-50 th	9.862	6.784	11.33	43.58
Bare Li foil-50 th	17.05	4.935	19.45	47.77

Li@PCNM-DMAC-100th	9.897	11.19	17.5	112.3
Bare Li foil-100th	21.33	14.18	24.89	103.4
Li@PCNM-DMAC -150th	20.53	5.473	9.88	94.57
Bare Li foil-150th	20.73	16.44	21.26	136.3

The stability of the SEI interface in Li@PCNM-DMAC and bare Li foil during cycling at 3 mA cm⁻² with a capacity of 1 mAh cm⁻² was analysed by EIS technology (Fig. 4.12a-c). Specific resistance data listed in Table 4.1 is derived from the fitting process (Fig. 4.12c). During cell cycling, compared with bare Li foil, Li@PCNM-DMAC at the 50th, 100th, and 150th cycle performs more overwhelming advantage with pretty small interfacial SEI resistance of 6.78 Ω, 11.19 Ω and 5.47 Ω, and charge transfer resistance of 11.33 Ω, 17.5 Ω and 9.88 Ω, respectively. Decreased resistance benefits from the nanopore-driven uniform Li⁺ distribution, interparticle-pore-induced low-volume changes, and the DMAC-facilitated Li-F-rich SEI.

4.3.5. Electrochemical performances of full cells

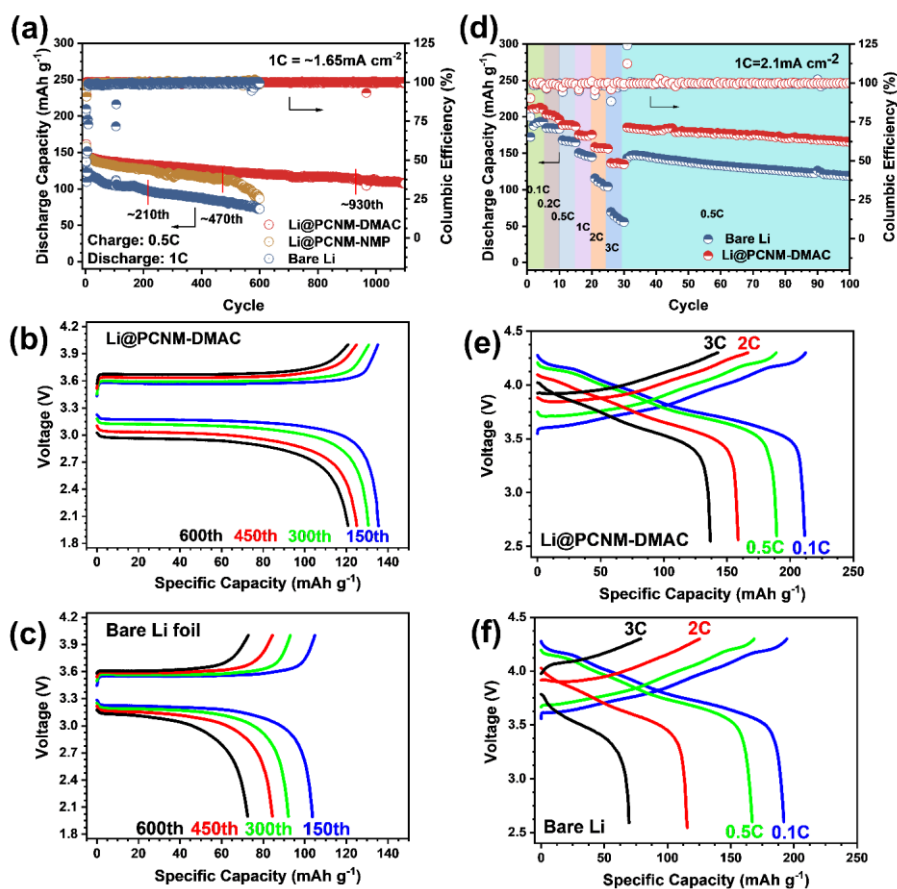


Figure 4.13. (a) Long-term cycling performance of Li@PCNM-NMP, Li@PCNM-DMAC, and bare Li foil paired with LFP positrodes ($\sim 1.7 \text{ mAh cm}^{-2}$) in coin full cell. Voltage profiles of (b) Li@PCNM-DMAC||LFP and (c) bare Li||LFP full cell at the 150th, 300th, 450th and 600th cycle. (d) The rate capability of Li@PCNM-DMAC and bare Li foil paired with LFP positrodes ($\sim 2 \text{ mAh cm}^{-2}$). Voltage profiles of (e) Li@PCNM-DMAC||LFP and (f) bare Li||LFP full cell from 0.1C to 3C.

To confirm the practical performance of Li@PCNM-DMAC in full cells, long-term cycling and rate performance of full cells assembled with bare Li foil or Li@PCNM-NMP or Li@PCNM-DMAC negatrode (20 mAh cm^{-2}) and LFP ($\sim 1.7\text{-}2 \text{ mAh cm}^{-2}$) positrode were tested. Fig. 4.13a illustrates that the capacity retention of the full cell composed of bare Li foil undergoes an apparent drop to less than 80% after ~ 210 cycles. In contrast, the full cell with Li@PCNM-NMP electrode shows much higher capacity

retention of ~88% after 210 cycles and ~80% after even more than 470 cycles, largely verifying the PCNM-driven uniform Li⁺ flux and dendrite-free Li deposition. It is believed that the self-driven reaction caused by DMAC in Fig. 4.4 can lead to more Li-F in the initial SEI of Li@PCNM-DMAC in comparison with Li@PCNM-NMP. Astonishingly, the full cell with Li@PCNM-DMAC electrode exhibits ultrahigh capacity retention until 470 cycles and approaches the capacity retention of 80% at the 930th cycle, highly confirming the fact that DMAC-induced initial Li-F-rich interface can efficaciously prevent the formation of irreversible Li and prolong the long-term cycling performance of LMRBs. Specifically, compared with bare Li foil-based full cell, Li@PCNM-DMAC-based full cell demonstrates much more steady voltage hysteresis from the 150th to the 600th cycle (Fig. 4.13b-c).

Compared with bare Li foil, Li@PCNM-DMAC also performs better rate capability, as shown in Fig. 4.13d-f. Especially at a high rate of 3C, the cell using Li@PCNM-DMAC still delivers a high specific capacity of ~135 mAh g⁻¹, which is more than 2 times larger than that of bare Li foil-based cell (~55 mAh g⁻¹). Compared with bare Li foil-based cells, Li@PCNM-DMAC-based full cell performs lower voltage hysteresis at all different charge/discharge rates of 0.1, 0.5, 2, and 3C. The above results reveal that the PCNM-driven uniform Li⁺ flux and DMAC-facilitated stable interface can give rise to stable and enhanced discharge capacity at high rates.

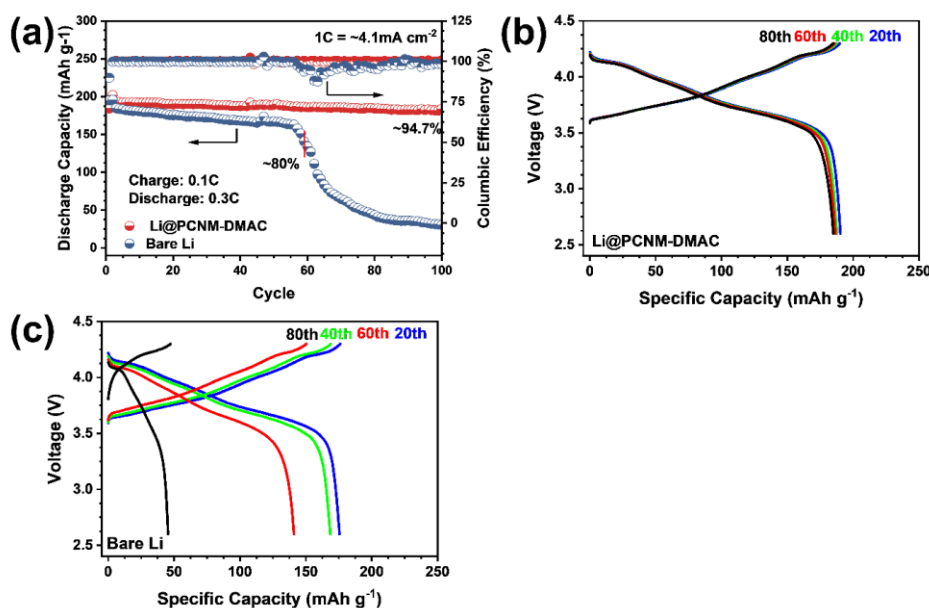


Figure 4.14. (a) Long-term cycling performance of Li@PCNM-DMAC and bare Li foil electrodes paired with high areal capacity NCM 811 positrodes ($\sim 4 \text{ mAh cm}^{-2}$) in coin full cells. Voltage profiles of (b) Li@PCNM-DMAC||NCM 811 and (c) bare Li||NCM 811 full cell at the 20th, 40th, 60th, and 80th cycle.

To further confirm the practical performance of Li@PCNM-DMAC in full cells, long-term cycling of full cells assembled with bare Li foil or Li@PCNM-DMAC negatrod (20 mAh cm⁻²) and NCM 811 ($\sim 4 \text{ mAh cm}^{-2}$) positrode were checked. Fig. 4.14a shows that the capacity retention of the full cell with bare Li foils experiences a sharp reduction to less than 80% after ~ 60 cycles. In significant contrast, the capacity retention of a full cell composed with Li@PCNM-DMAC can approach $\sim 95\%$ at the 100th cycle. Meanwhile, compared with bare Li foil-based full cell, Li@PCNM-DMAC-based full cell possesses steady voltage hysteresis from the 20th to the 80th cycle, as illustrated in Fig. 4.14b-c. This tremendous discrepancy can be attributed to the nano-channel-induced uniform and stabilised Li⁺ flux and confined growth of Li in PCNM, as well as a stable Li-F-rich interface, leading to a much smaller polarisation, higher discharge capacity, and better capacity retention.

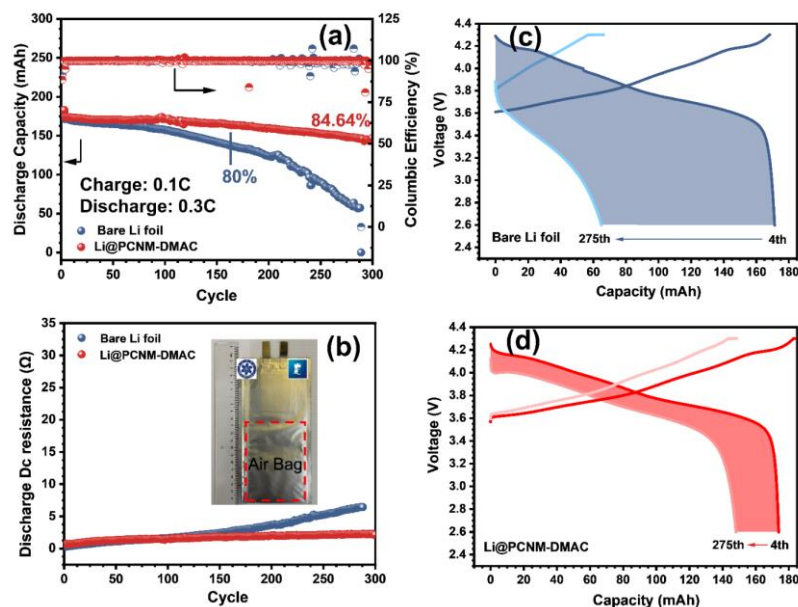


Figure 4.15. (a) Long-term cycling performance and (b) *in-situ* discharge internal resistance profiles of Li@PCNM-DMAC and bare Li foil electrodes paired with high areal capacity NCM 811 positrodes ($\sim 4 \text{ mAh cm}^{-2}$) in pouch cell. Voltage profiles of (c) bare Li foil||NCM 811 and (d) Li@PCNM-DMAC||NCM 811 pouch cells from the 4th to the 275th cycle.

The compatibility and practical feasibility of the Li@PCNM-DMAC (20 mAh cm^{-2}) were further investigated by pairing it with the NCM 811 positrode ($\sim 4 \text{ mAh cm}^{-2}$ on each side) in a pouch full cell with a designed initial capacity of $\sim 0.17 \text{ Ah}$ and electrolyte mass of $\sim 1.02 \text{ g}$. Fig. 4.15a shows that Li foil-based pouch full cell illustrates apparent capacity decay after 100 cycles, followed by a rapid drop to 136.4 mAh g^{-1} at the 166th cycle (capacity retention of 80%). In comparison, Li@PCNM-DMAC-based pouch full cell can keep strikingly high capacity retention of $\sim 84.6\%$ after 300 cycles under the same condition.

Fig. 4.15b compares the internal resistances of two pouch cells, which are *in-situ* monitored to exhibit the modified coating layer on lowering the electrochemical polarisation during cycling. Li foil-based and Li@PCNM-DMAC-based pouch cells have a similar rising trend with increasing to $\sim 1.5 \Omega$ from 0 to 100th cycle. Nevertheless,

the internal resistance of Li foil-based pouch cells suffers from impressive growth to 6 Ω , while that of Li@PCNM-DMAC-based pouch cells only slowly rise by $\sim 0.5 \Omega$ within the 100th-300^h cycle. This result reveals that the Li@PCNM-DMAC electrode can effectively alleviate the Li dendrite or “dead Li”-induced internal resistance. Smaller capacity decay (~ 25 mAh) can also be observed in Li@PCNM-DMAC-based pouch cells than that of bare Li foil-based pouch cells (more than 4 times) from the 4th to the 275th cycle (Fig. 4.15c-d). More stable internal resistance and significantly superior cycling stability of Li@PCNM-DMAC-based pouch cells than that of Li foil-based pouch cells can be ascribed to the inhibition of “dead Li” and suppressed electrolyte consumption by the PCNM coating.

4.4. Conclusions

In this work, we have first evaluated the influence of different solvents (DMF, NMP, and DMAC) of PCNMs slurry on the surface composition of LM and related electrochemical performance. DMF is not suitable as the solvent of PCNMs slurry because of the severe side reactions between DMF and LM, which highly affect the electrochemical performance of cells. Although NMP can keep pretty stable with LM, it can hardly provide any extra help for the *in-situ* formation of Li-F-rich SEI on LM. DMAC not only keeps comparatively stable with LM but also effectively facilitates the formation of Li-F during coating via a self-driven chemical reaction between PVDF (binder) and LM. This facilitated reaction may be ascribed to the special solvation structure formed by DMAC with PVDF and moderate structural stability toward LM. Thus, DMAC can fully promise the advantage of PCNMs in effectively homogenizing Li⁺ flow and achieving dendrite-free Li deposits, as well as effectively suppressing the volume expansion. Meanwhile, the electrochemical performance of symmetric half and full cells, especially for long-term cycling depending on a more stable interface on Li@PCNM-DMAC, are highly enhanced.

Chapter5

CNT/PVDF Composite Coating Layer on Cu with a Synergy of Uniform Current Distribution and Stress Releasing for Improving Reversible Li Plating/Stripping

This chapter reports the fabrication of the novel Cu foil with a relatively dense coating layer composed of CNTs network and a soft functional polymer PVDF. PVDF can shield the contact between the internal surface of the 3D CNTs and the electrolyte. Simultaneously, the Li-F-rich SEI resulting from the partial reduction of PVDF, and the soft nature of the coating layer release the accumulated internal stress in the parallel direction to the current collector surface. As a result, Li deposition without mosses and whiskers has been achieved, leading to improved reversibility of Li deposition.

5.1. Introduction

LMRBs, where pre-placement of LMNE as the main Li resource delivers reversible electrochemical plating/stripping, are considered the next generation beyond LIBs. However, the pre-placement of LMNE especially for thickness larger than 500 μ m will have a detrimental impact on the specific energy and cycling performance of the battery,²⁴⁸ and lead to notable concerns regarding manufacturing costs and safety.²⁴⁹ Furthermore, it is imperative to take into consideration the potential for initial corrosion of the electrolyte on the LMNE during the standing period, as this may greatly impact subsequent Li deposition. Last but not least, the practice of utilizing LMRBs to evaluate the authentic efficacy of materials in controlling reversible Li deposition is deemed unscientific.

Theoretically, LM-free is viable for LMRBs, called “lithium metal rechargeable batteries with lithium-metal-free negatode” (LMFRBs) where Li-contained positrode provides Li resources.²⁵⁰ Compared with conventional LMRBs, LMFRBs have performed greatly profound advantages owing to their higher specific energy and lower manufacturing cost. The concern of potential electrolyte corrosion on the LMNE during the standing period is also non-existent. Meanwhile, the use of LMFRBs provides a more scientifically valid evaluation method to determine the authentic performance of materials in regulating reversible Li deposition. Thus, in this chapter, based on the above advantages we decide to focus on the construction of LMFRBs.

However, the implementation of LMNE in LMFRBs is also impeded by their unavoidable formation of polymorphous Li deposits, e.g., whiskers, mosses, or dendrites.^{35, 251} The morphologies of Li polymorphs and their evolution trends are highly dependent on the interfacial current distribution and internal stress release form, which are intrinsically related to the heterogeneous nucleation and growth stages of Li. During the heterogeneous nucleation stage, inhomogeneity of the local interfacial current distribution in the current collector can indeed initially result in a local Li⁺ concentration void, consequently further leading to the formation of non-uniform Li nucleation seeds (Fig. 5.1). During the growth stage, inhomogeneity of the local interfacial current distribution can cause the high local current density which is a key factor in Li dendrite formation. Based on Chazalviel’s space charge model,⁶⁶ an applied current density (J_{acd}) would lead to different ion concentration gradient behaviours.⁷⁰ The concentrations of anions and Li⁺ near and at the negatode surface will decrease to zero at the Sand’s time (τ), making electroplating becomes unstable. A sudden drop in salt concentration near the negatode will trigger the formation of tip-growing dendrites.^{35, 186, 252}

Furthermore, Li deposition-induced internal stress is another important driving force for Li whisker/mosses growth with a preferential crystallographic orientation,

especially at low current densities.^{253, 254} It is proposed in a pioneering model that the inhomogeneous Li deposits on the negative electrode under the influence of the SEI layer initially result in a gradual accumulation of stress. Afterwards, the SEI layer breaks up so as to release the upward stress to the current collector surface, and LM sticks out in the shape of whiskers.⁶⁸

To alleviate the formation of polymorphous Li deposits and improve CE for LMFRBs, various strategies have been reported to be efficient, such as current collector engineering (e.g., 3D current collector or soft substrate design),^{236, 251, 254-260} artificial interface design (e.g., SEI with high Li⁺ diffusion),²⁶¹⁻²⁶³ electrolyte formulations (e.g., local high concentration).^{74, 264, 265} A current collector as an indispensable component in LMFRBs is vital to promoting the electrochemical performance by adjusting current density and establishing stable SEI during charging/discharging^{257, 262} whether in the current collector engineering or artificial interface design.

2D-type current collectors such as Cu foil are a common choice in LMFRBs. However, bare Cu foil cannot provide excellent interfacial current distribution and internal stress release in the horizontal direction to the current collector surface to help achieve dendrite-free Li deposits. Many experimental results^{135, 197, 217} show that Li dendrites can easily occur on Cu foil, which may be mainly ascribed to the local inhomogeneities of the current density. The interfacial current distribution of Cu foil can be highly affected by its tiny surface morphology changes, especially for the ultrathin Cu foil. Moreover, the metal-based surface is more likely to be passivated by air or electrolyte to form the insulating oxide or hydroxide, further deteriorating the interfacial current distribution on the Cu foil.^{104, 266} In addition, Cu foil has a very high Young's modulus, which is not conducive to the horizontal internal stress release to the current collector surface and easily leads to whisker/mosses-like Li deposits during LM growth.²⁵⁴ The lack of excellent SEI further intensifies irregular Li deposits.

According to the currently reported literatures,²⁶⁷⁻²⁷¹ the 3D skeleton has been proven to efficiently reduce J_{acd} relying on their large surface area, which effectively manipulates the heterogeneous nucleation of Li and mitigates the growth of Li dendrites. For instance, Zuo et al.¹¹⁷ utilized a graphitised carbon fibre electrode as a multifunctional 3D carbon-based current collector to decrease the effective current density, thereby achieving an extended cycling lifespan for LMNE. It is also proved that the carbon nanotubes (CNTs) network can effectively eliminate the internal accumulated stress.²⁷²

Nevertheless, the enlarged electroactive surface area of the 3D current collector serving as a “double-edged sword” can induce more considerable electrolyte decomposition at the current collector–electrolyte interface than typical Cu foil current collectors.^{257, 273} Meanwhile, more electrolyte is required to infiltrate the 3D current collector as well, which will affect the energy density and specific energy of LMFRBs. 3D current collectors also still face up the challenge of tip-effect²⁷⁴ toward Li^+ . In addition, the SEI repeatedly forms by Li intercalation/deposition in carbon-based 3D skeleton will not only consume the inherent Li source in LMFRBs, but Li-intercalation-induced SEI may also affect the stability of subsequent Li deposition.

Therefore, we aim to homogenise interfacial current distribution using a 3D carbon-based skeleton. Simultaneously, introducing a soft functional polymer shields the contact between the active surface of the 3D carbon-based framework and the electrolyte and prevents the pores within the 3D carbon-based framework from absorbing the electrolyte to overcome the side effects and retain the uniform current density distribution. Also, an integrated soft substrate can horizontally release the accumulation of stress and mitigate mosses/whisker-like Li deposits.

Herein, as shown in Fig. 5.1, we demonstrate a simple method using PVDF as the “soft functional filler” in the slurry of CNTs to cast the carbon-based mixture interfacial layer

on the Cu foil to protect the Cu substrate and homogenise current distribution. CNTs are an ideal host candidate to redistribute highly current based on their nanometre-scale tube-like morphology. Compared with carbon fibres with diameters on the micrometre scale, nanometre-sized CNTs are more efficient in modulating Li^+ transportation with a diameter of ~ 0.3 nm. In addition, carbon materials perform much better resistance toward corrosion of oxygen or electrolyte compared with metal-based materials.^{266, 275} As for the functional polymer, the CNTs can be wrapped well by PVDF with a proper amount to form a relatively dense coating layer that reduces the porosity of CNTs, suppressing the repeated generation of SEI and retaining the homogenised interfacial current distribution. Spontaneously, the Li-F component derived from the partial reduction of PVDF by the deposited Li in SEI can be formed. Thus, not only can the entire soft substrate horizontally release the accumulation of Li internal stress, but the robust SEI can also further avoid upward stress release to the current collector surface, resulting in stress-mitigating mosses/whisker-free Li deposits. The utilization of CNTs induces a nano-redistributed uniform current distribution and the use of a soft substrate mitigates stress release, which in turn, promotes the formation of a favourable SEI layer. These factors collectively lead to improved Li deposition/dissolution and result in a highly stable cycling performance of LMFRBs.

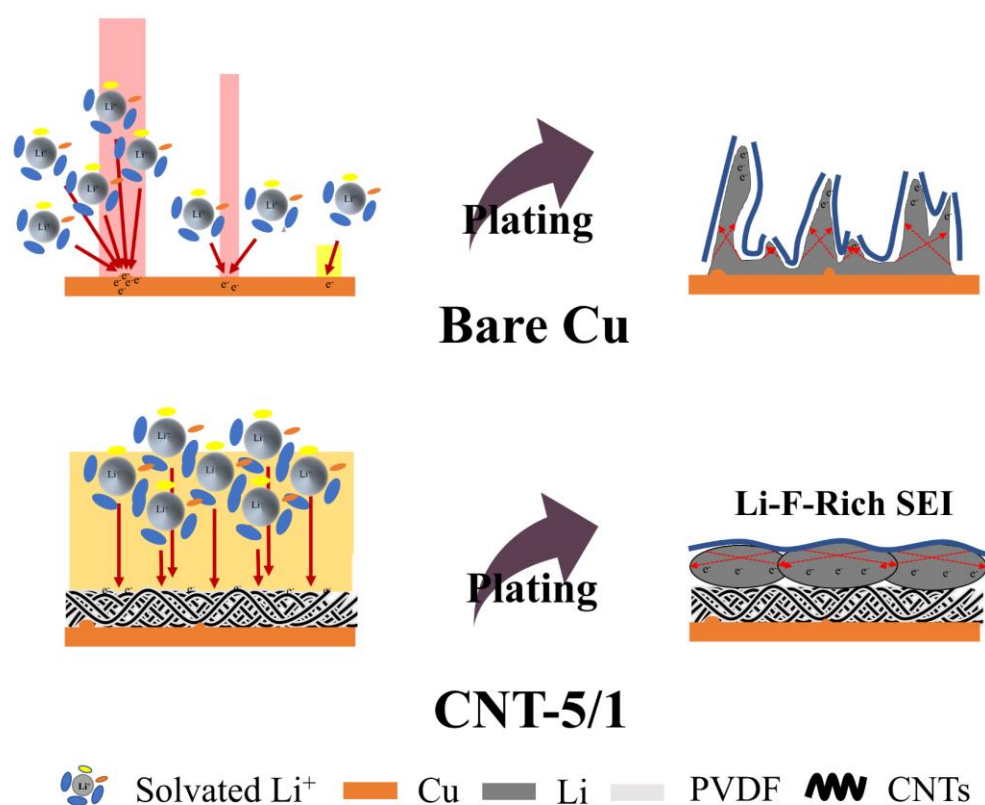


Figure 5.1. Schematic diagrams showing the morphology of electrodeposited Li on bare Cu foil and CNT-5/1. Red area: high current strength; yellow area: low current strength; orange area: medium current strength.

5.2. Experimental section

5.2.1. Electrodes preparation

Fabrication of Cu coated with a mixture of CNTs and PVDF (CNT-X/1). CNTs slurry with 4.3 wt% CNTs dispersed in NMP (solvent) and PVDF powder (MW:1,000,000) (mass ratio of PVDF: CNTs =X:1, X= 0, 0.5, 2.5, 5, 7.5) were mixed and stirred for 24 h. The slurry was cast on a Cu foil with a thickness of 200 μm (mass ratio of PVDF: CNTs = 0/0.5:1), 500 μm (mass ratio of PVDF: CNTs =2.5:1), or 700 μm (mass ratio of PVDF: CNTs = 5/7.5:1), and vacuum-dried at 80 $^{\circ}\text{C}$ for 6 h. The as-obtained electrodes were denoted as CNT-X/1 (X = 0, 0.5, 2.5, 5, and 7.5), respectively.

Fabrication of Cu coated with a mixture of CNTs, PEO, and PAN (CNT-5/1-PEO and CNT-5/1-PAN). The same CNTs slurry was mixed with PEO (MW:2,000,000) or PAN (MW:150,000) powder (mass ratio of PEO/PAN: CNTs =5:1) and heated at 80 °C for 30 min before stirring for 24 h. The slurry was cast on a Cu foil with a thickness of 700 μm and vacuum-dried at 80 °C for 6 h. The as-obtained electrodes were denoted as CNT-5/1-PEO and CNT-5/1-PAN, respectively. The as-obtained CNT-X/1 (X = 0, 0.5, 2.5, 5, and 7.5) and CNT-5/1-PEO & CNT-5/1-PAN electrodes were punched into disks of 14 mm in diameter for the electrochemical measurements.

5.2.2. Electrochemical Measurements

Two-electrode coin half cells (Li vs. CNT-X/1 (X = 0, 0.5, 2.5, 5, and 7.5) or CNT-5/1-PEO or CNT-5/1-PAN). Standard CR2032 coin-type cells were assembled in an Ar-filled glove box with H₂O and O₂ content below 1 ppm. For the Li||Cu coin half cell, a 0.5 mm thick Li disc with a diameter of 16.0 mm was applied as both the counter and reference electrode. The as-obtained 14 mm discs of CNT-X/1 (X = 0, 0.5, 2.5, 5, and 7.5), CNT-5/1-PEO and CNT-5/1-PAN were employed as the working electrode. The Celgard 2500-type polypropylene membrane with a thickness of 25 μm was applied as the separator. 1 M LiTFSI in DOL/DME (v/v = 1:1) with 2.0 wt.% LiNO₃ additive was employed as the electrolyte in coin half cells. 75 μL electrolyte was added to each cell. The galvanostatic performances were conducted at 25 °C using the Land CT 2100A system (Jinnuo Wuhan Corp, China). Li was plated galvanostatically with capacities of 1 or 3 mAh cm⁻² and then stripped galvanostatically by a cut-off potential of 0.5 V vs. Li/Li⁺ at different current densities on the two-electrode coin half cells. CV and EIS were tested by an electrochemical workstation (Solartron 1470E) using CR2032-type coin cells. The voltage range of CV was chosen from 2V to -0.25V with a scan rate of 0.1 mV s⁻¹. The frequency range was set between 1 MHz and 0.01 Hz.

Two-electrode coin full cells (LFP vs. Bare Cu or CNT-0/1 or CNT-5/1). The as-obtained 14 mm discs of bare Cu & CNT-X/1 (X = 0, 0.5, 2.5, 5, and 7.5) and LFP were

employed as the current collector (in the negatode) and the positrode. The areal loading of the LFP positrode was 12 mg cm^{-2} , corresponding to an areal capacity of $\sim 2 \text{ mAh cm}^{-2}$. The Celgard 2500-type polypropylene membrane with a thickness of $25 \text{ }\mu\text{m}$ was applied as the separator. 1 M LiTFSI in DOL/DME ($v/v = 1:1$) with $2.0 \text{ wt.}\%$ LiNO_3 additive was employed as the alternative electrolyte in partial LFP-based coin full cells. 4 M LiFSI in DME was employed as the alternative electrolyte in partial LFP-based coin full cells. Electrolyte injection is fixed at $75 \text{ }\mu\text{L}$ in each coin cell. All coin cells were shelved for 8 h before testing. The LFP-based full cells were galvanostatically charged up to 4 V at 0.5C and then galvanostatically discharged to 2.0 V at 1C .

Two-electrode coin full cells (NCM 811 vs. Bare Cu or CNT-0/1 or CNT-5/1). The as-obtained 14 mm discs of bare Cu & CNT-X/1 ($X = 0, 0.5, 2.5, 5, \text{ and } 7.5$) and LFP were employed as the current collector (in the negatode) and the positrode. The areal capacity of the NCM 811 positrode was $\sim 2 \text{ mAh cm}^{-2}$ or $4 \sim 2 \text{ mAh}$. The Celgard 2500-type polypropylene membrane with a thickness of $25 \text{ }\mu\text{m}$ was applied as the separator. 1 M LiPF_6 in EC and DMC (EC: DMC=3: 7, v/v) with $2 \text{ wt}\%$ FEC (Zhangjiagang Guotai-Huarong New Chemical Materials Co., Ltd) as the electrolyte in NCM 811-based coin full cells. Electrolyte injection is fixed at $75 \text{ }\mu\text{L}$ in each coin cell. All coin cells were shelved for 8 h before testing. The cycling performances of the NCM 811-based coin full cells were tested by charging at 0.5 C and discharging at 1 C within the voltage range from 2.6 to 4.3 V .

5.3. Results and discussion

5.3.1. Materials characterisations

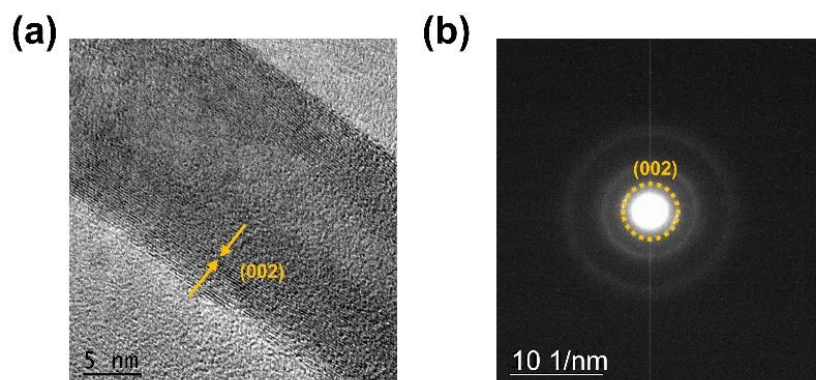


Figure 5.2. (a) High-magnification TEM and (b) selected area electron diffraction (SAED) pattern of CNTs. (The yellow dashed circle is the diffraction ring corresponding to (002) face of multi-wall CNTs; 10 1/nm is the reciprocal space scale, and it represents that the length of the scale bar is 1/10 nm)

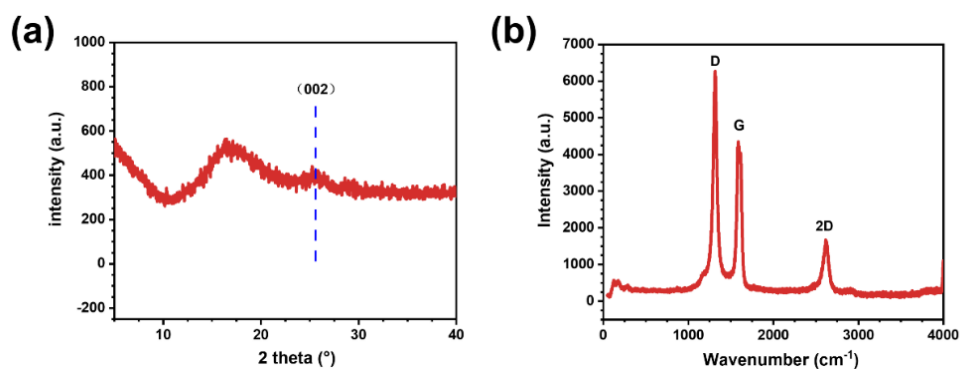


Figure 5.3. (a) X-ray diffraction pattern and (b) Raman spectrum of CNTs.

As shown in Fig. 5.2a, CNTs with a diameter of ~ 10 nm are used as the conductor, guaranteeing that the interfacial current distribution can be sufficiently subdivided by the CNTs network. Furthermore, multiple wall structures can be found in CNTs, which provide little storage space to store Li^+ and form lithophilic LiC_x on the surface of CNT-based electrodes.²⁷⁶ The interlayer spacing of CNTs within multiple walls

calculated from the selected area electron diffraction (SAED) rings presented in Fig. 5.2b is in accordance with the result obtained from the XRD patterns (Fig. 5.3a). However, as displayed in Fig. 5.3b, a large number of defects ($I_D/I_G=1.5$) exist in the multiple wall structure, suggesting defect-induced stronger adsorption toward Li^+ may lead to the growth of inactive Li during charging.²⁷⁷

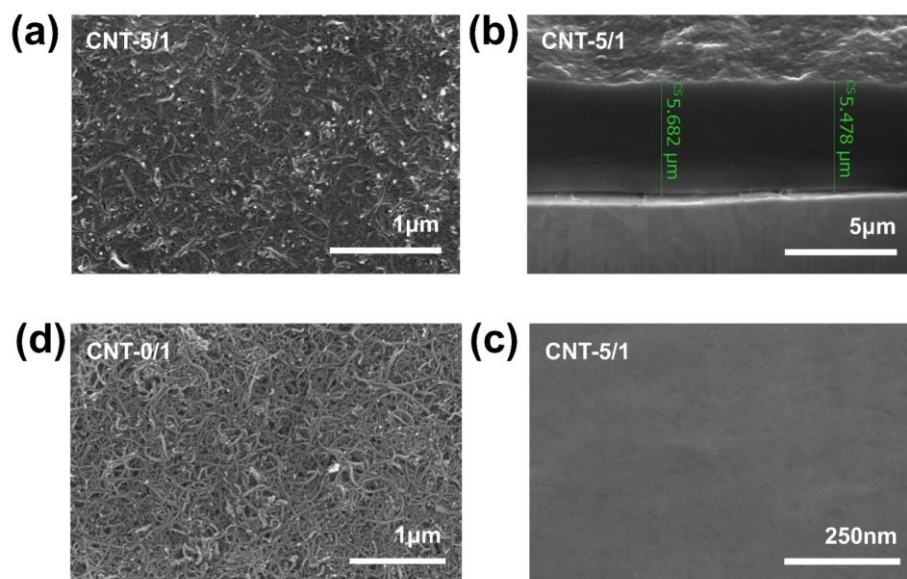


Figure 5.4. (a) Top-view and (b) cross-section view SEM images of CNT-5/1. (c) High-magnification SEM image of the cross-section view of CNT-5/1. (d) Top-view SEM image of CNT-0/1.

The well-dispersed CNTs slurry was mixed with PVDF in NMP solvent with a certain ratio to form a hybrid slurry, and then the mixture was cast on a Cu foil to form a coating layer with a thickness of $\sim 5.5 \mu\text{m}$. CNTs network structure can be found in Fig. 5.4a. The partial pores within the interlaced CNTs are landfilled by PVDF, which can be further proved by the cross-section view of CNT-5/1 that shows densification and non-porous features (Fig. 5.4b and Fig. 5.4c). On the contrary, typical porous structures constructed by intertwined CNTs networks are verified without PVDF in Fig. 5.4d. It is conjectured that surface electrochemical deposition rather than internal electrochemical reaction is more likely to occur within CNT-5/1, leading to a decrease

in the repeated formation of SEI. Meanwhile, the metal-based interface can be completely protected by the carbon-based mixture coating layer due to the non-porosity during cycling, which implies that the metal's interfacial current distribution and chemical environment can be reconstructed effectively by a CNT-based mixture coating layer.

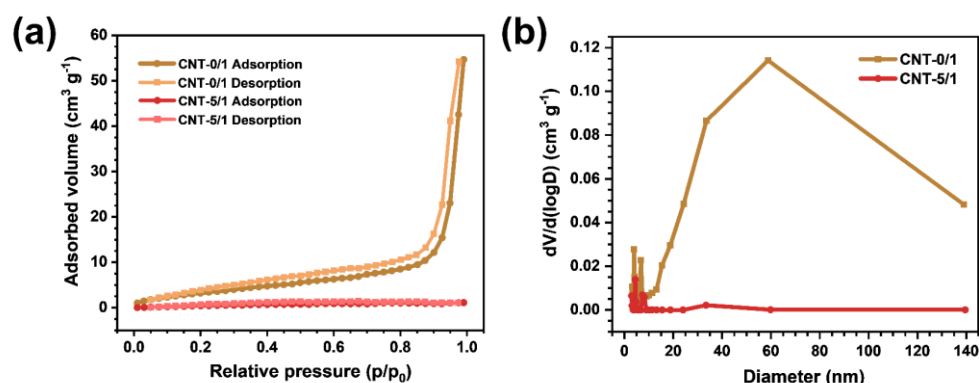


Figure 5.5. (a) Nitrogen adsorption and desorption isotherms and (b) the pore size distribution data of CNT-0/1 (yellow line) and CNT-5/1 (red line).

Table 5.1. Specific surface area, pore volume, and pore size of CNT-X/1 (X = 0, 0.5, 2.5 and 5) and PVDF.

Sample	Surface area (m ² /g)	Pore volume (cm ³ /g)	Average pore size (nm)
CNT-0/1	191.14	1.2	25.13
CNT-0.5/1	81.76	0.63	30.67
CNT-2.5/1	21.69	0.014	2.56
CNT-5/1	13.53	0.0082	2.41
PVDF	8.13	0.057	27.30

To further understand the change in pore structure caused by the introduction of PVDF over CNT-based electrodes, detailed pore structure, and surface area were characterised by nitrogen adsorption and desorption isotherms. Fig. 5.5a illustrates that the adsorption

quantity increases linearly with rising relative pressure to 0.9 and then exponentially to atmospheric pressure for CNT-0/1, suggesting that a broad range of pores have been formed. The type of the hysteresis loop of CNT-0/1 is probably attributed to H3 (IUPAC). It is further proved that CNT-0/1 possesses a broad pore size distribution ranging from 2 to 140 nm by the pore size distribution data (Fig. 5.5b) using the BJH model. Particularly, the pore size of 60 nm is dominant in CNT-0/1, which is also in good accordance with the pore size observed in the SEM image (Fig. 5.4d). Inversely, compared with CNT-0/1, the adsorption quantity of CNT-5/1 remains almost constant with rising pressure, revealing that nearly no pores are formed. Pore size distribution data of CNT-5/1 further confirms the non-porosity feature, which is highly in agreement with the cross-section SEM image of the sample (Fig. 5.4b and Fig. 5.4c). With the content of PVDF increasing (≤ 5), CNT-5/1 also possesses the smallest specific surface area ($13.5 \text{ m}^2 \text{ g}^{-1}$), pore volume ($0.00171 \text{ cm}^3 \text{ g}^{-1}$), and average pore size (2.41 nm) among other CNT-based mixture electrodes (Table 5.1), which is ascribed to the filled pores by PVDF.

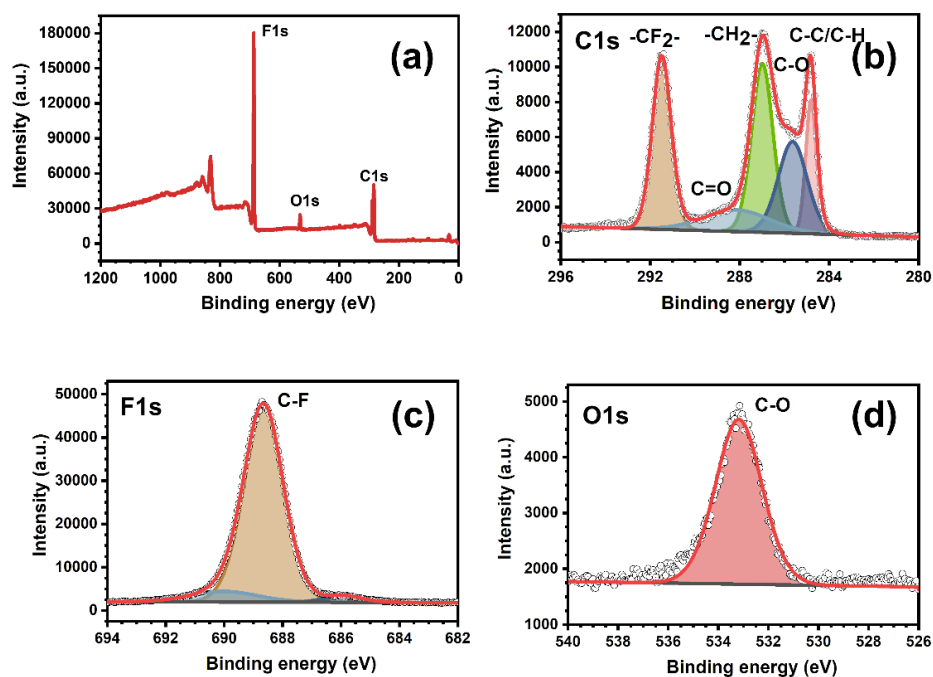


Figure 5.6. XPS result of CNT-5/1. (a) full spectrum, (b) C 1s, (c) F 1s and (d) O 1s.

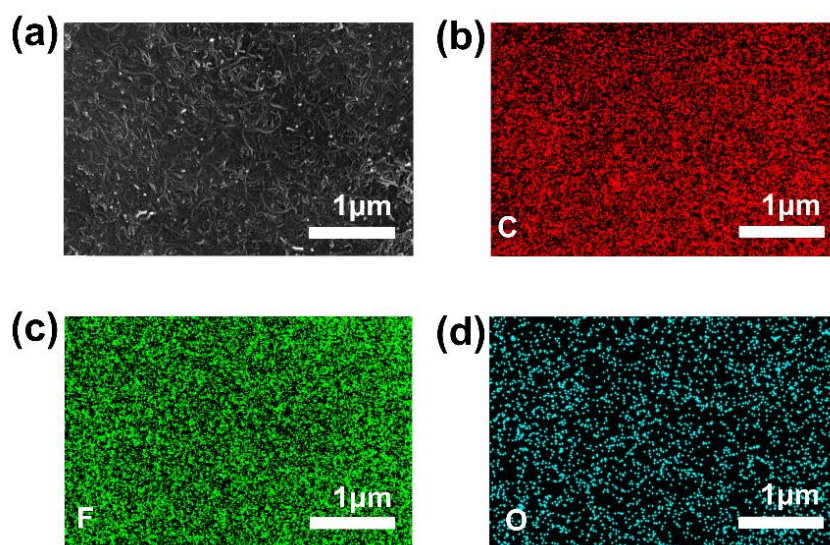


Figure 5.7. EDS mapping for (a) SEM image and (b) C, (c) F, and (d) O elements on the surface of CNT-5/1.

XPS analysis and EDS mapping were carried out to investigate further the chemical composition and electronic states on the surface of CNT-5/1. Fig. 5.6a shows that the F, C, and O elements dominate in the full spectrum. Two peaks at 291.5 eV and 287 eV which are assigned to the $-\text{CF}_2-$ and $-\text{CH}_2-$ respectively in the C1s spectrum (Fig. 5.6b) and one peak at 688.5 eV which is ascribed to the C-F in the F1s spectrum (Fig. 5.6c) of CNT-5/1 confirm the existence of PVDF. Two peaks at 288 eV and 285.5 eV corresponding to the C=O and C-O in the C1s spectrum (Fig. 5.6b) and one peak at 533 eV corresponding to the C-O in the O1s spectrum (Fig. 5.6d) of CNT-5/1 verify the existence of oxygen as a lithiophilic element in CNTs,¹²⁷ which can make CNTs more lithiophilic and decrease the Li deposition barrier.^{138, 278} The uniform distribution of F, C, and O elements over the entire coating layer is found via EDS mapping, as demonstrated in Fig. 5.7, which also agrees with the XPS results. It is predicted that abundant F and O elements can sufficiently interact with Li^+ and form robust SEI components such as Li-F during the electrochemical deposition of Li.²³⁴

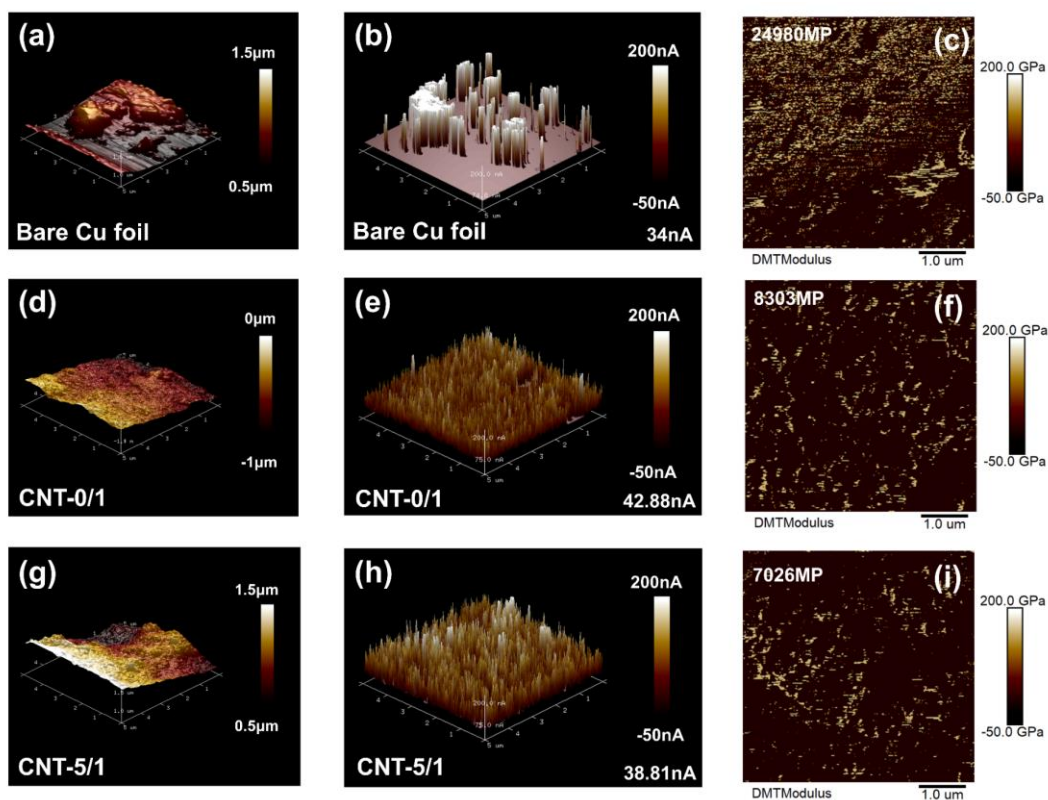


Figure 5.8. Surficial morphology, surface current distribution, and DMT modulus over (a), (b), and (c) bare Cu, (d), (e) and (f) CNT-0/1, and (g), (h) and (i) CNT-5/1 through AFM characterisation.

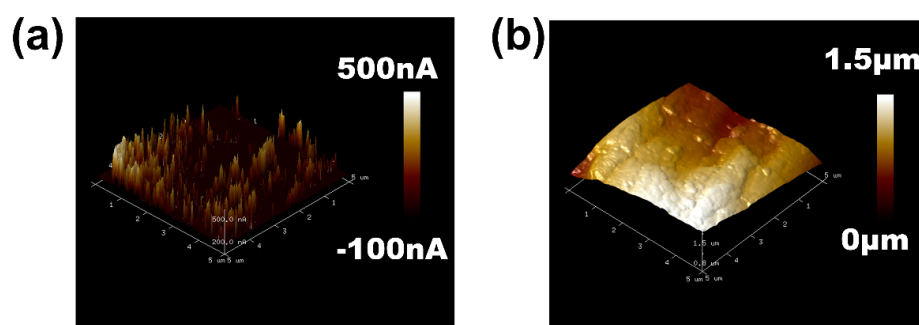


Figure 5.9. (a) Surface current distribution and (b) morphology of the bare Cu after being washed by HCl.

AFM is further conducted to obtain the surface morphology, current distribution, and DMT modulus of prepared electrodes (Fig. 5.8). Surface current distribution plays an important role in regulating the initial Li^+ flux over the electrode. Non-uniform

interfacial current distribution can be detected in the bare Cu foil (Fig. 5.8b). When 200 mV is applied, irregular conductive sites and locally ultrahigh current with even more than 200 nA will easily result in concentrated Li^+ flux and the formation of Li dendrites during the deposition process. More importantly, after being washed by HCl (Fig. 5.9), bare Cu foil shows a substantially improved interfacial current distribution, proving the non-uniform interfacial current distribution on bare Cu foil is partially attributed to the formation of Cu_xO or $\text{Cu}(\text{OH})_x$.²⁶⁶ In addition, even if the inert substance is eliminated by HCl (Fig. 5.9), bare Cu foil is still difficult to show uniform current distributions.

On the contrary, uniform conductive sites are distributed on the surface of CNT-0/1 (Fig. 5.8e) owing to the network formed by CNTs. The current keeps at nearly the same level of ~ 43 nA. The above results demonstrate that CNTs possess superior conductivity and a nano-tube morphology that makes them an optimal conductor for effectively dividing and stabilizing the interfacial current distribution. It is worth noting that the excellent stability of CNTs in the air also contributes to the steady and uniform interfacial current distribution. As presented in Fig. 5.8h, CNT-5/1 performs an exceptionally similar interfacial current distribution compared to CNT-0/1 except for the reduction of the current by ~ 4 nA, which illustrates the interfacial current re-distribution induced by CNTs cannot be dramatically affected by the introduction of non-conductive linear polymer (PVDF). Thus, a CNT-based electrode relying on uniform interfacial current distribution is prone to homogenise the Li^+ and eliminate the Li dendrites. The newly formed surface of the CNT-based electrode remains smooth (Fig. 5.8a, 5.8d and 5.8g), proving that CNTs and PVDF are well integrated. The lowest DMT module can be observed in the case of CNT-5/1 in Fig. 5.8c, 5.8f and 5.8i among all electrodes, which suggests that CNT-5/1 may exhibit the most favourable conformal capability toward Li and efficaciously remove accumulated stress generated by Li dendrites as presented in Fig. 5.1.

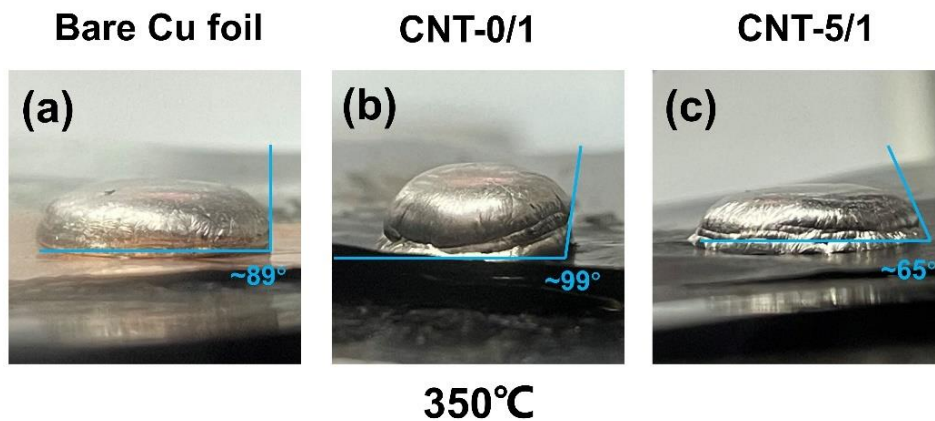


Figure 5.10. Contact angles of Li toward (a) bare Cu foil, (b) CNT-0/1, and (c) CNT-5/1 at 350°C.

To further determine the interaction between Li and the CNT-based mixture electrode, the wettability between these two is measured using contact angle methods at 350°C. Results in Fig. 5.10 manifest that the CNT-0/1 performs the largest contact angle ($\sim 99^\circ$) due to the previously reported lithiophobic feature of carbon materials.²¹⁷ Inversely, the smallest contact angle ($\sim 65^\circ$) can be found in the CNT-5/1, which illustrates that PVDF probably facilitates the adaptability of surface energy between Li and CNT-based electrodes and is beneficial to alleviating Li dendrite.

5.3.2. Initial SEI characterisations

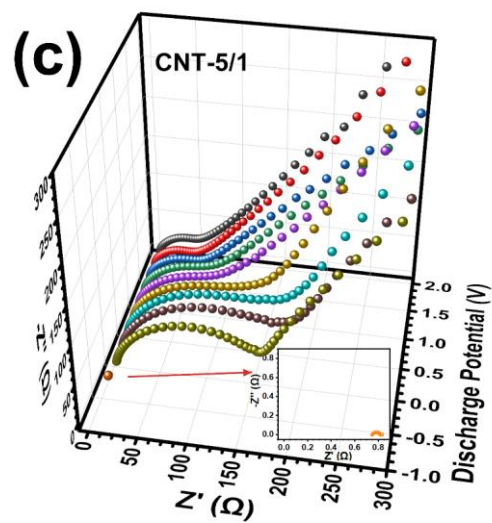
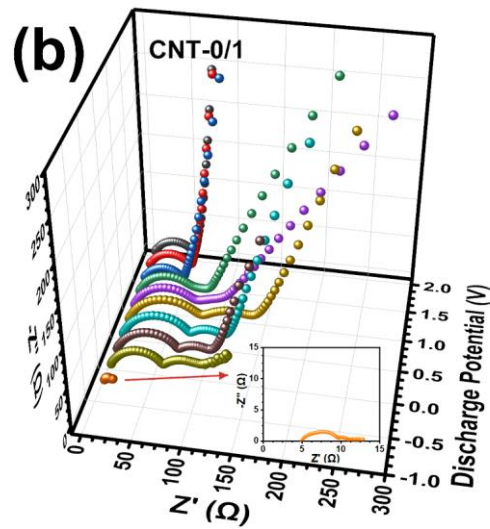
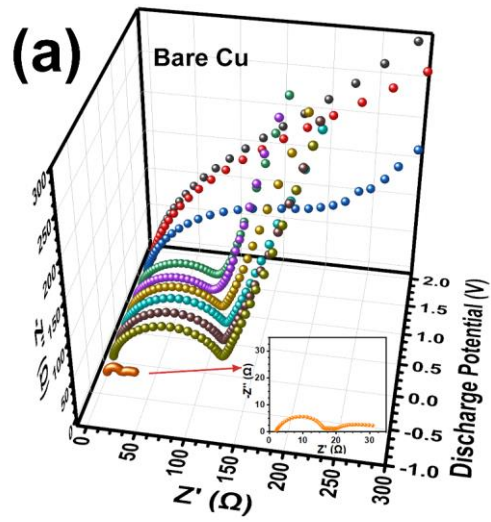


Figure 5.11. EIS evolution with discharging from 2V to -0.25V at $0.1 \text{ mV}\cdot\text{s}^{-1}$ over (a) bare Cu, (b) CNT-0/1, and (c) CNT-5/1.

SEI formed on the current collector is highly important because it influences the evolution of the Li deposit morphology and subsequent cycling performance. The *ex-situ* EIS measurement during the first plating process is conducted to explore the SEI evolution on the fresh bare Cu foil and CNT-based electrodes. As shown in Fig. 5.11a, three periods (2~1.25V, 1.25~0V, and 0~-0.25V) with different shapes in Nyquist plots of bare Cu can be seen, implying that there are three stages in SEI evolution during plating. In the potential range of 2V-1.25V, the interfacial charge type gradually varies from the EDL behaviour to the pseudocapacitive behaviour, which reveals that the formation of initial SEI can break diffusion-limited behaviour on the surface of bare Cu foil.²⁷⁹ With potential decreasing to 0 V, the diameter of the semicircles in the high-frequency regions gradually increases, representing that charge transfer resistance (R_{ct}) is elevated. It is inferred that the generation of negative charges on Cu's surface intends to repel anions and increasing adsorbed solvated Li^+ groups probably hinder the subsequent Li^+ diffusion into the surface of the electrode. Finally, when the potential drops to -0.25V, there is a sharp reduction in the R_{ct} , suggesting that fast ion transportation channels are formed due to the Li electrodeposition and the comparatively stable SEI formation.²⁸⁰

It is found that there are also three different potential range stages (2~1V, 1~0V, and 0~-0.25V) in the case of CNT-0/1 due to the intercalation and deposition behaviour of CNTs (Fig. 5.11b). Within 2V-1V, CNT-0/1 performs simple pseudocapacitive behaviour. New resistance (SEI resistance/ R_{SEI}) is generated when the potential reduces from 1V to 0 V due to the formation of intercalation-triggered SEI. Overall, the R_{ct} of CNT-0/1 performs more dramatic fluctuation in the potential range of 2V-0V. When Li^+ begins to deposit (potential < 0 V), the comparatively stable and new SEI is formed based on the sharp reduction of the R_{ct} at -0.25V. Predictably, repeated generations of

SEI can consume more active Li sources. Although the CNTs network is regarded as the 3D current collector, the small space within the CNTs network is hard to accommodate Li deposition with a large volume. Thus, most Li deposits will confront a similar deteriorating deposition environment with Cu foil. By contrast, a similar trend can be observed in CNT-5/1 in these two potential range stages (2~0V and 0~-0.25V) (Fig. 5.11c) compared with bare Cu (1~0V and 0~-0.25V), implying that Li deposit is more likely to occur on the surface of CNT-5/1 rather than intercalation in CNTs. Probably, CNT-5/1 could show higher reversible capacity due to the lack of intercalation/internal-deposition-induced SEI formation. The above result also illustrates that Li deposition on the electrode surface other than inside is more beneficial to achieving stable SEI in the CNT-based electrodes, possibly attributed to the enlarged electrode area that leads to the growing SEI and complex deposition environment. It is noteworthy that, among all electrodes, CNT-5/1 exhibits the minimum Rct when discharging to -0.25V. This finding suggests that the Li deposit-derived SEI on CNT-5/1 is superior, benefitting from the uniform current distribution and the functional filler effect induced by PVDF during plating.

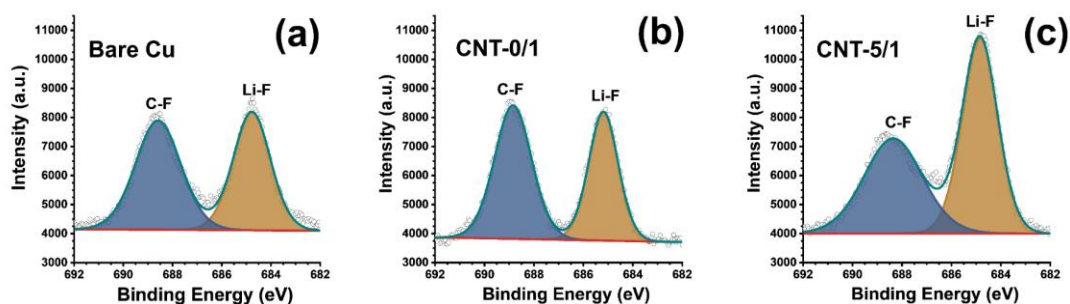


Figure 5.12. XPS spectra of the F 1s of plated Li (1 mAh cm^{-2} at 0.5 mA cm^{-2}) on (a) bare Cu, (b) CNT-0/1, and (c) CNT-5/1.

XPS is further carried out to verify the SEI component in bare Cu foil and CNT-based electrodes with a plating areal capacity of 1 mAh cm^{-2} . In F 1s spectra (Fig. 5.12a-c), Li-F and C-F signals are obtained in all electrodes, resulting from LiTFSI salt

decomposition.¹⁴¹ Li-F is well-known as an excellent SEI component owing to its high interfacial energy toward Li and high mechanical strength. Thus, Li-F-rich SEI is more efficient for uniform Li deposition. According to the reported literature,^{244, 281} the Li-F coating can be fabricated by the *in-situ* reaction between Li and fluoropolymer (e.g., polytetrafluoroethylene or PVDF). The highest intensity of the Li-F signal in the CNT-5/1 implies partial PVDF as a film-forming polymer is involved in the electrochemical deposition process, forming robust SEI.

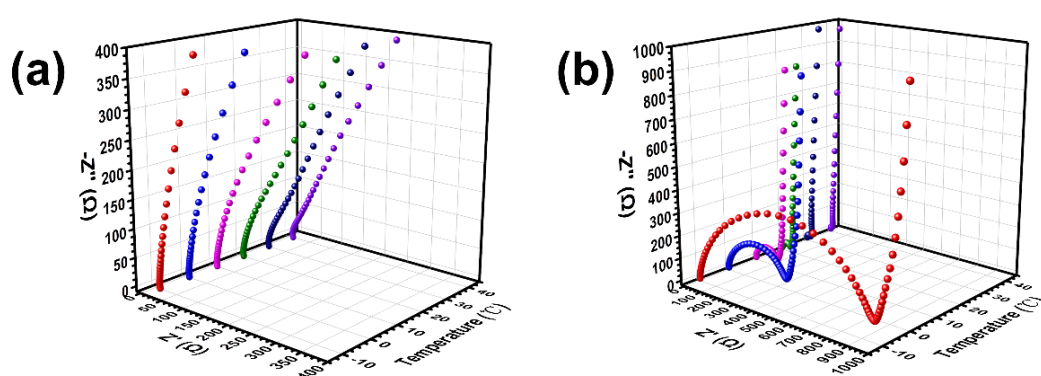


Figure 5.13. The EIS of (a) fresh bare Cu foil and (b) fresh CNT-5/1 under different temperatures ranging from -10°C to 40°C.

Nyquist plots regarding the fresh Cu foil and CNT-5/1 under different temperatures (-10°C-40°C) were measured to confirm the interaction between Li^+ and PVDF (Fig. 5.13). It is observed that the R_{ct} in CNT-5/1 reduces dramatically with increasing temperature. In comparison, the EIS of the bare Cu foil keeps almost the same within 50 degrees. These results support our claim that the R_{CT} in CNT-5/1 is mainly due to the interaction between PVDF and solvated Li^+ rather than simple contact resistance occurring at the current collector/active material interface. Furthermore, all Ohmic impedance data of CNT-5/1 are extremely small when the temperature rises from -10°C to 40°C, demonstrating that PVDF cannot give rise to considerably high internal resistance in the batteries.

5.3.3. Morphology of Li plating

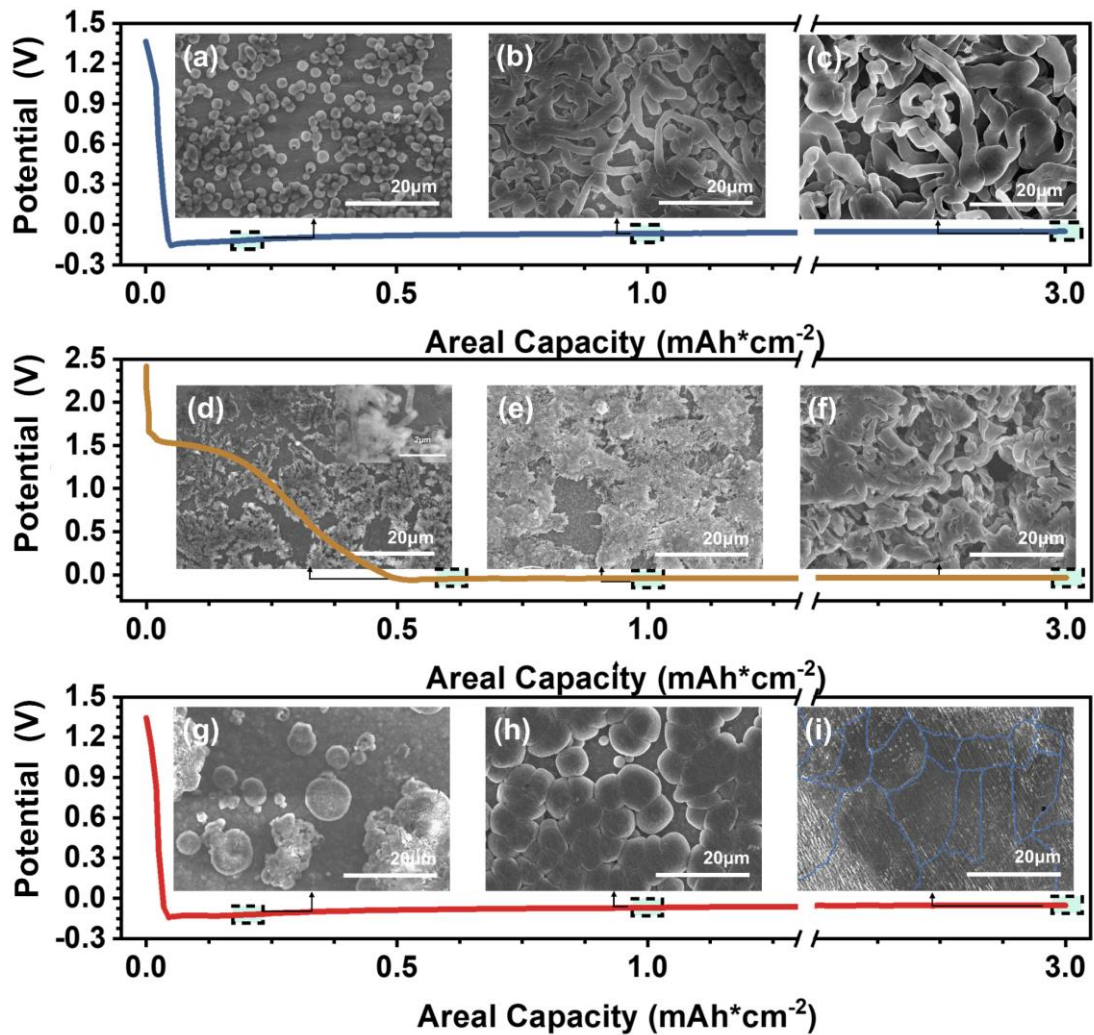


Figure 5.14. Li deposition morphology with capacities from 0.2 to 3 mAh cm⁻² on the bare Cu, CNT-0/1, and CNT-5/1. Top-view SEM images of the bare Cu, CNT-0/1, and CNT-5/1 electrode after plating with (a), (d), and (g) 0.2 mAh cm⁻², (b), (e), and (h) 1 mAh cm⁻² and (c), (f) and (i) 3 mAh cm⁻² of Li (The blue dashed line represents the boundary between the spliced LM particles). The current density is 0.5 mA cm⁻².

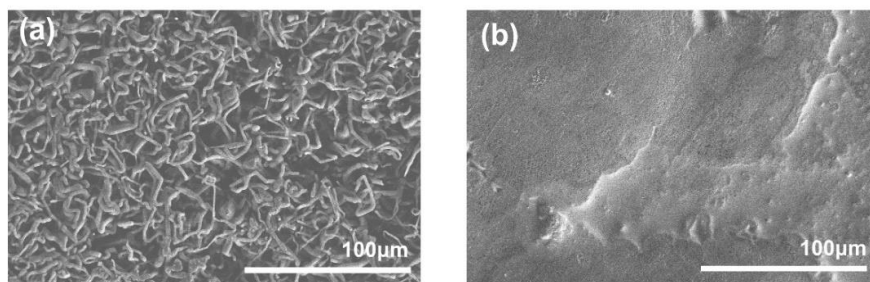


Figure 5.15. Top-view SEM images of electrodeposited Li with 3.0 mAh cm^{-2} at 0.5 mA cm^{-2} on (a) Cu and (b) CNT-5/1.

Fig. 5.14 exhibits morphology evolution during Li plating with capacities from 0.2 to 3 mAh cm^{-2} on bare Cu foil, CNT-0/1 and CNT-5/1 electrodes (Li@Cu, Li@CNT-0/1, and Li@CNT-5/1). Notably, without the help of uniform interfacial current distribution, as mentioned in others' work,¹¹³ Li^+ tends to deposit on spots where current strength is pretty high, and Li grains with a size of $\sim 2 \text{ }\mu\text{m}$ (Fig. 5.14a) gradually form at the beginning of Li plating (0.2 mAh cm^{-2}). Meanwhile, incomplete SEI can be formed owing to the local high interfacial current distribution and accumulated internal stress. After that, Li^+ will be continuously attracted, and accumulated internal stress will be released in the incomplete SEI to form a local whisker protrusion (1 mAh cm^{-2} in Fig. 5.14b). Furthermore, tips-effect²²⁷ also further intensifies the formation of dendrite-like Li. Finally, the mossy-type (whisker and dendrite) Li network can be affirmed with a capacity growing to 3 mAh cm^{-2} in Fig. 5.14c. Fig. 5.15a further confirms the generation of dendrite-like Li in a large area over the bare Cu.

Fig. 5.14d-f reveals that insertion/adsorption toward Li^+ contributes to the main capacity at the initial of plating (0.5 mAh cm^{-2}) in CNT-0/1. Li does not deposit in the form of flocculent-type Li until it reaches the areal capacity of 0.5 mAh cm^{-2} (Fig. 5.14d-e), implying the intercalation behaviour of Li in CNTs may not be conducive to the subsequent deposition of Li. Compared with Li deposition on Cu foil, the side reactions occurring on the carbon-based 3D surface may negatively affect subsequent Li deposition, which implies that the further application of carbon materials with a large

surface area in LMRBs requires more careful consideration. Isotropic surface growth and local whisker protrusion can be found on CNT-0/1 as well when capacity is further increased to 3 mAh cm⁻² (Fig. 5.14f), proving the formation of incomplete SEI upon deposited Li or the SEI may easily be interrupted by Li deposits on CNT-0/1.²⁵² The above result is possibly due to the fact that SEI originated from the insertion/adsorption of Li⁺ in CNTs can greatly affect subsequent Li plating. Therefore, achieving a uniform interfacial current distribution is crucial for homogenizing Li deposition, and creating a favourable deposition environment, such as an excellent SEI, is equally important for uniform Li plating.

Fig. 5.14g reveals that the size of Li grains can horizontally grow to more than ~10 μm with a capacity of 0.2 mAh cm⁻². With a further increase of capacity, large Li particles gradually become crowded and then splice into a dense and dendrite-free bulk (Fig. 5.14h-i), which is further proved by the image with a larger view (Fig. 5.15b). The above results can be attributed to the uniform interfacial current distribution (Fig. 5.8h), Li-F-rich SEI, and internal stress release in the horizontal direction to the current collector surface. More importantly, the potential curve (Fig. 5.14g-i) shows that the insertion/adsorption of Li⁺ in CNTs almost disappears due to the blocking effect from PVDF toward Li⁺. Thus, insertion/adsorption-induced side effects (e.g., generation of unstable SEI) can be effectively avoided in CNT-5/1.

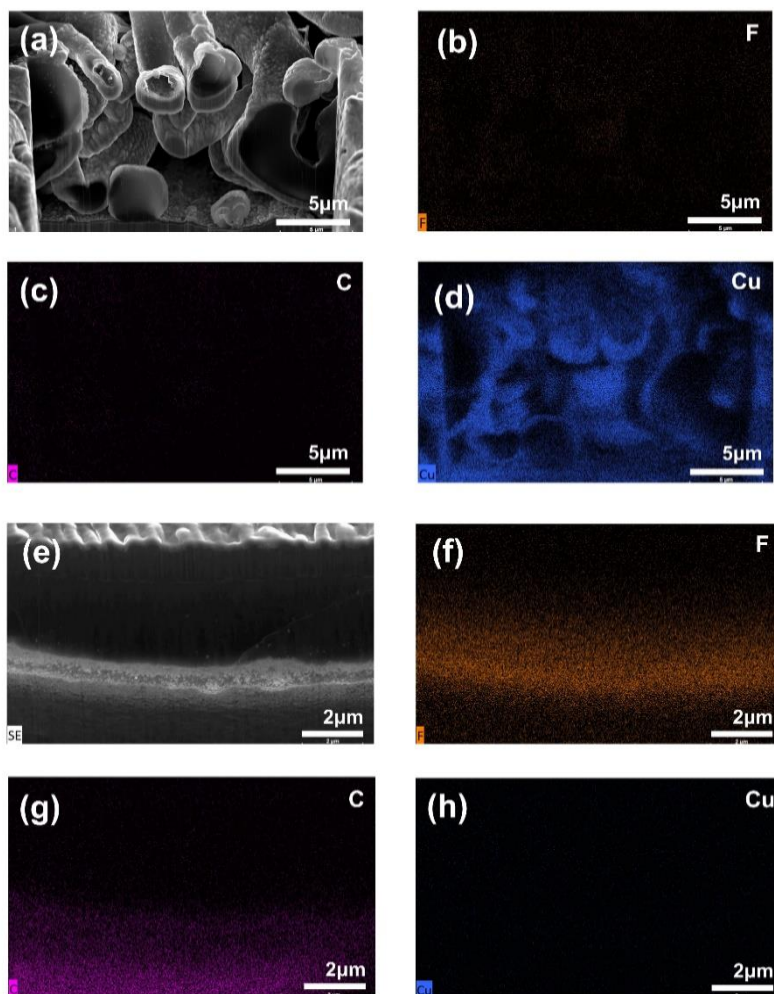


Figure 5.16. Cross-section view (a) bare Cu with related EDS mapping of (b) F, (c) C, and (d) Cu, and cross-section view of (e) CNT-5/1 with related EDS mapping of (f) F, (g) C and (h) Cu after Li plating with an areal capacity of 3 mAh cm^{-2} .

Ex-situ FIB-SEM characterisation was further carried out to detect the specific morphology of the deposited Li on bare Cu and CNT-5/1 with a plating areal capacity of 3 mAh cm^{-2} (Fig. 5.16). Fig. 5.16a presents that the porous and dendrite-like structure of electrodeposited Li is generated on bare Cu foil. Besides, remarkably thick SEI wrapping on dendrite-like Li is attributed to the uneven Li^+ deposition and electrolyte decomposition and the formation of by-products, resulting in poor cycling stability and a dramatic drop in CE.²³⁴ Corresponding EDS mapping result (Fig. 5.16b-d) illustrates that C and F can hardly be found, while Cu accounts for the biggest element distribution

in Li@Cu, which strongly supports our previous claim and other researchers' findings^{266, 282} that Cu will be electrochemically corroded during plating. In striking contrast, dense and dendrite-free Li plating can be observed in Li@CNT-5/1 (Fig. 5.16e). More notably, F exhibits obvious gradient distribution characteristics compared to the C element (Fig. 5.16f-h), which strongly verifies that partial PVDF may be electrochemically reduced with deposited Li or uniform interfacial current distribution promotes the reductive decomposition of even anions flux in the electrolyte to form Li-F. This finding is also proved by the XPS result in Fig. 5.12c. In addition, nearly no Cu element can be found in Li@CNT-5/1 (Fig. 5.16h), which indicates that CNT-5/1 can effectively prevent Cu from electrochemical corrosion. Our results support the notion that a uniform interfacial current distribution, soft-substrate-induced stress mitigation, and favourable SEI in CNT-5/1 are crucial for achieving dendrite-free Li.

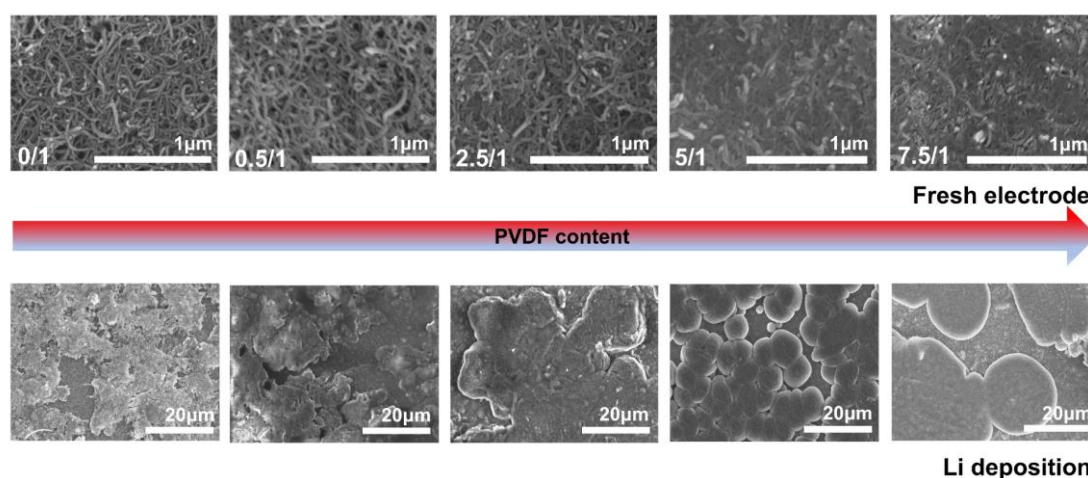


Figure 5.17. Top-view SEM images of fresh CNT-based electrodes with different PVDF contents (CNT-X/1 ($X = 0, 0.5, 2.5, 5$ and 7.5)) (upper), and Li plated electrodes with 1 mAh cm^{-2} at 0.5 mA cm^{-2} (down).

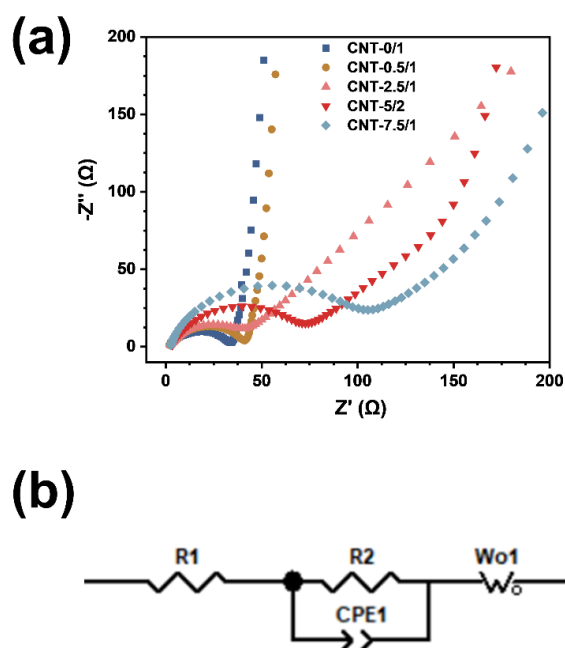


Figure 5.18. (a) EIS of the fresh CNT-based electrodes added with different PVDF contents (CNT-X/1 ($X = 0, 0.5, 2.5, 5,$ and 7.5)). (b) applied fitting resistance model: $R1:R_0$ (Ohmic resistance); $R2: R_{ct}$ (Charge transfer resistance); $CPE1$: Constant phase element (Conventional double-layer and passivation film capacitance); $Wo1$: Warburg (Li^+ diffusion resistance)

Table 5.2. Fitting resistance data of fresh CNT-based electrodes with different PVDF contents (CNT-X/1 ($X = 0, 0.5, 2.5, 5,$ and 7.5)) in $Li||Cu$ coin half cell.

Sample	R1 (Ω)	R2 (Ω)	WO1-R (Ω)
CNT-0/1	1.32	33.54	-
CNT-0.5/1	1.214	41.37	-
CNT-2.5/1	1.669	48.85	189.4
CNT-5/1	2.927	75.01	267.9
CNT-7.5/1	2.263	107.7	291.6

A comparison of electrochemical deposit morphology on CNT-based electrodes with different PVDF contents (CNT-X/1 ($X = 0, 0.5, 2.5, 5,$ and 7.5)) is further explored (Fig. 5.17). The typical porous structure can be found in CNT-0/1 and CNT-0.5/1 when

introducing a very small amount of PVDF or not. Then, there is a significant reduction in porosity with PVDF content growing, verifying that PVDF can make electrode densification and reduce the space for transportation of Li^+ inside the CNTs network. In addition, augmented R_{ct} elucidates that the interaction between solvated Li^+ and PVDF is further enhanced due to the increasing amount of PVDF (Fig. 5.18 and Table 5.2). These top-view SEM images about CNT-X/1 ($X = 0, 0.5, 2.5, 5,$ and 7.5) are in good accordance with the surface area presented in Table 5.1. The deposition morphology of Li on CNT-X/1 ($X = 0, 0.5, 2.5, 5,$ and 7.5) can be classified into two categories. When X is smaller than 2.5, the deposited Li shows the flocculent-type morphology, while Li is deposited much more flatly with a dendrite-free morphology when X reaches 5 and 7.5. The above results confirm that the introduction of PVDF with a suitable proportion ($X > 2.5$) can effectively avoid the intercalation of Li^+ in CNTs and induce horizontal internal stress release in deposited Li.

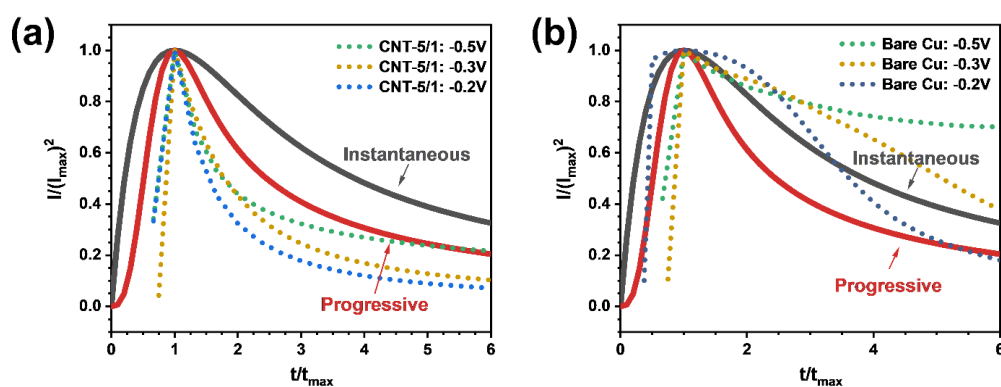


Figure 5.19. t/t_{\max} - $I/I_{\max})^2$ plots of the (a) fresh CNT-5/1 and (b) fresh bare Cu foil under different voltages (-0.2V, -0.3V, and -0.5V).

Fig. 5.19 demonstrates that CNT-5/1 follows progressive nucleation mode, while Cu foil obeys instantaneous nucleation mode,²⁸³ which further implies Li intends to continuously grow based on the initially formed nucleus on CNT-5/1 and the growing Li particles begin to splice when they touch the adjacent ones.

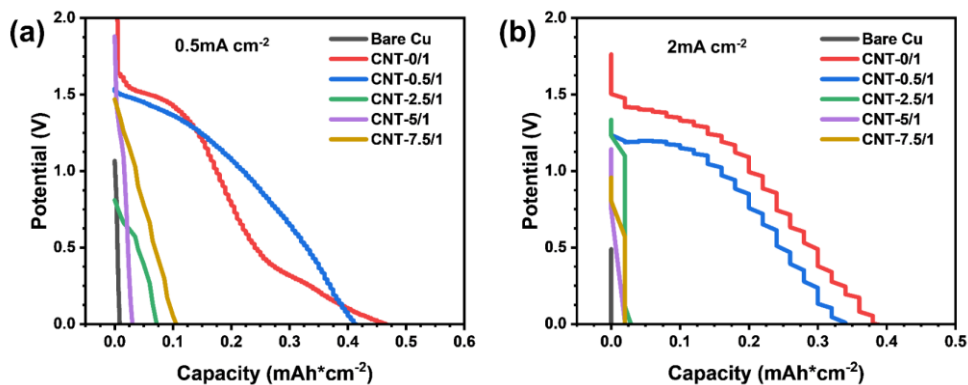


Figure 5.20. Lithiation capacity (>0V) of the CNT-X/1 ($X = 0, 0.5, 2.5, 5,$ and 7.5) at (a) 0.5 mA cm^{-2} and (b) 2 mA cm^{-2} .

Comparing the lithiation capacity (>0V) of different CNT-based electrodes is highly feasible to understand the area of CNTs exposed to the electrolyte. Fig. 5.20 shows that the lithiation capacity of CNT-based electrodes exhibits a generally decreasing trend with the content of PVDF increasing at 0.5 mA cm^{-2} and 2 mA cm^{-2} . CNT-0/1 and CNT-0.5/1 have the first and second largest lithiation capacity, respectively, while CNT-5/1 shows the smallest one, confirming the extra area of CNTs contacting electrolyte can be effectively shielded via introducing a certain amount of PVDF.

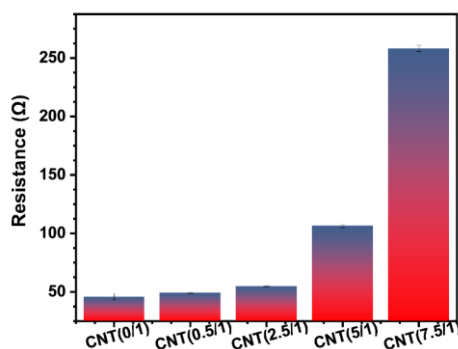


Figure 5.21. The electrical resistance of CNT-X/1 ($X = 0, 0.5, 2.5, 5,$ and 7.5).

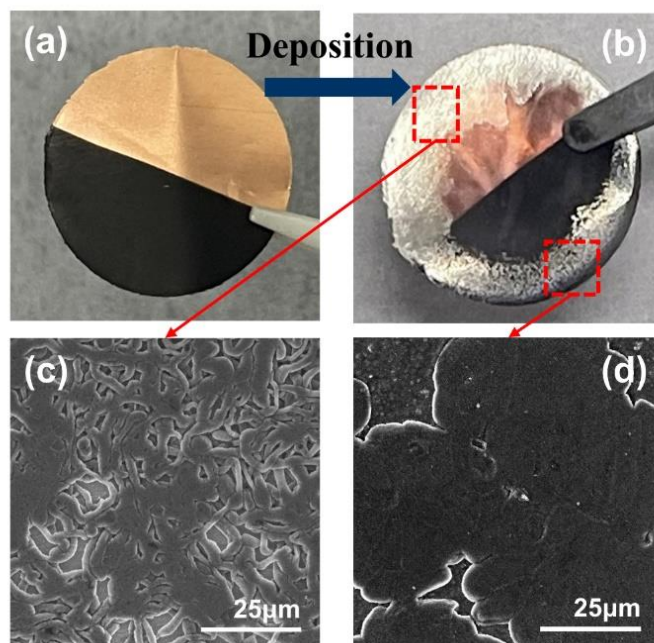


Figure 5.22. Optical photographs of Cu foil with half coated with CNT-5/1 (a) before and (b) after Li plating. SEM images of electroplated Li on (c) bare Cu and (d) CNT-5/1 coated Cu.

It cannot be denied that electric resistance is enhanced when introducing PVDF into the CNTs network (Fig. 5.21). Therefore, the effect of conductivity between CNT-based electrodes and bare Cu foil on the Li plating process should be clarified. Fig. 5.22a-b illustrates that electric resistance in the CNT-based electrodes has no great effect on the Li deposition process. Li^+ does not deposit preferentially on the current collector where there is low resistance. Also, porous dendrite-like Li can still be found on the uncoated Cu foil (Fig. 5.22c). In contrast, Cu coated with CNT-5/1 induces a planar deposition manner (Fig. 5.22d), proving that CNT-based electrodes can efficaciously inhibit the formation of dendritic Li.

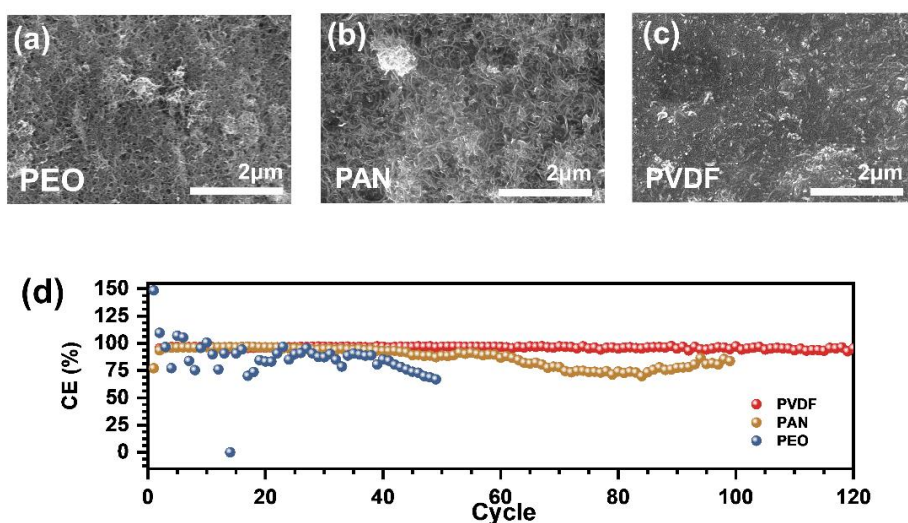


Figure 5.23. Top-view SEM images of fresh CNT-based electrodes added with (a) PEO, (b) PAN, and (c) PVDF. (d) comparison of CE of Li plating on/stripping from the above electrodes with a capacity of 1 mAh cm^{-2} at 2 mA cm^{-2} .

Different polymers such as PAN and PEO were added into CNTs (PAN or PEO: CNTs= 5:1, m:m) as a comparison with PVDF (Fig. 5.23). The addition of PEO to CNT-based electrodes results in a porous structure, as illustrated in Fig. 5.23a. This differs from the structure obtained using PVDF in the electrode. Such a porous structure may induce enhanced swelling of PEO by the electrolyte. That is why a considerable fluctuation of CE of the cell with the PEO-containing electrode at the first 5 cycles exists. No apparent morphology differences exist in the CNT-based electrode added with PAN or PVDF (Fig. 5.23b-c). However, the PAN-containing electrode shows inferior cycling performance compared with PVDF, further confirming PVDF is an ideal robust SEI film-forming polymer relying on the electrochemical formation of Li-F and excellent electrochemical stability in the battery (Fig. 5.23d).

5.3.4. Half-cell electrochemical performances of CNT-based electrodes

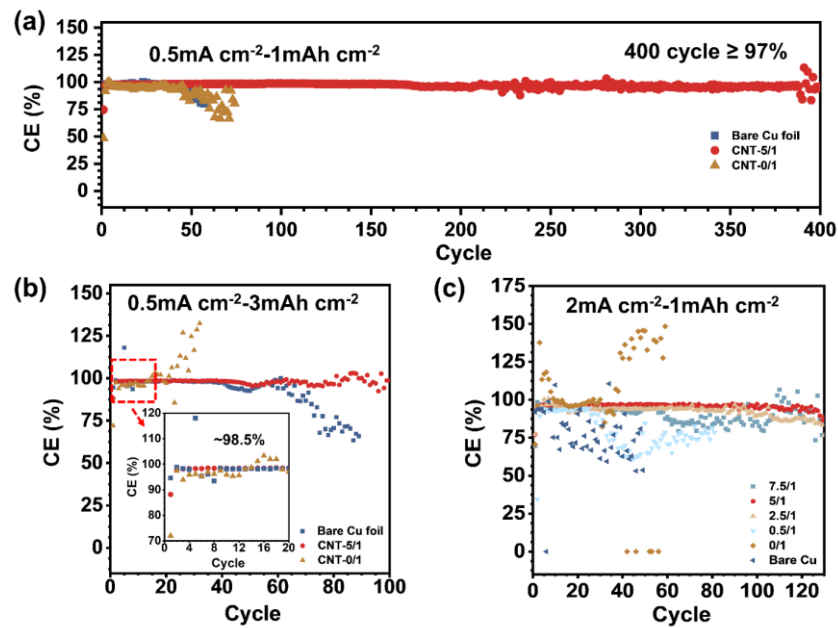


Figure 5.24. Comparison of CE of Li plating on/stripping with a capacity of (a) 1 mAh cm⁻² and (b) 3 mAh cm⁻² at 0.5 mA cm⁻² over bare Cu, CNT-0/1, and CNT-5/1. (c) CE of Li plating on/stripping from Cu coated with CNTs and PVDF with mass ratio (PVDF/CNTs) from 0 to 7.5 with a capacity of 1 mAh cm⁻² at 2 mA cm⁻².

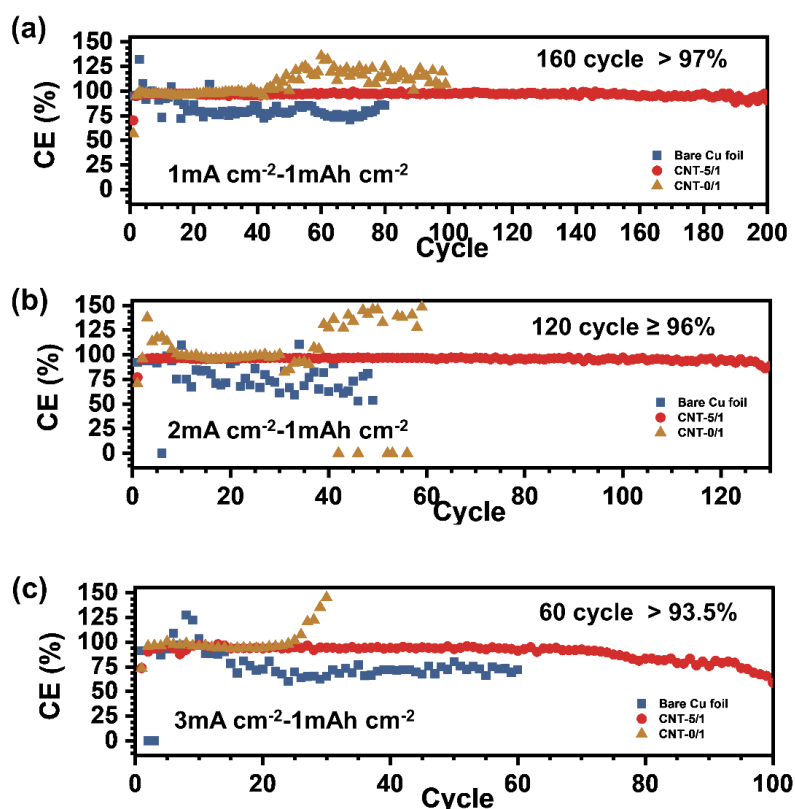


Figure 5.25. Comparison of CE of Li plating on/stripping over bare Cu foil, CNT-0/1 and CNT-5/1 with 1.0 mAh cm^{-2} at (a) 1 mA cm^{-2} , (b) 2 mA cm^{-2} and (c) 3 mA cm^{-2} .

In this chapter, 1 M LiTFSI in DOL/DME ($v/v = 1:1$) with $2.0 \text{ wt.}\% \text{ LiNO}_3$ was directly utilized in the half cells. It was reported in the literature that ether-based electrolytes have lower dielectric constants,^{284, 285} which may enable them more sensitive to the current density distribution in the current collector. That is to say, a more uniform current density distribution on the current collector may be more appropriate for ether-based electrolytes. Moreover, considering that this ether-based electrolyte exhibits better compatibility with LM deposition/dissolution, thus electrolyte composition consisting of 1 M LiTFSI in DOL/DME ($v/v = 1:1$) with $2.0 \text{ wt.}\% \text{ LiNO}_3$ was directly utilized in the half cells.

The CE and long-term electrochemical stability in a half cell composed of different working electrodes (bare Cu foil and CNT-based electrodes) coupled with Li foil as the counter electrode are further investigated. Among all electrodes, as reported in the

literature,¹⁰⁴ Cu foil shows the most serious decay in CE with current density varying from 0.5 mA cm^{-2} to 3 mA cm^{-2} at 1 mAh cm^{-2} as displayed in Fig. 5.24a, Fig. 5.24c and Fig. 5.25. With current density increasing from 0.5 mA cm^{-2} to 3 mA cm^{-2} at 1 mAh cm^{-2} , CE of bare Cu foil drops rapidly from more than 97% for ~ 40 cycles to around 90% for only 5 cycles before overcharge takes place, which may be ascribed to the uncontrolled Li dendrite/whisker-induced electrolyte depletion and generation of by-products (Fig. 16a) owing to the lack of uniform interfacial current distribution. CNTs-coated Cu maintains comparatively stable CE ($\sim 94\%$ within 20 cycles) at high current density (3 mA cm^{-2}), implying uniform interfacial current distribution improves Li deposition. However, apparent overcharge or CE fading is still found in CNT-0/1 due to the lack of stable SEI film-forming polymer and large surface area-induced overgrowth of SEI. In comparison, the CNT-5/1 cell maintains the most stable CE with a larger than the average of 97% within 400 cycles and CE with a larger than the average of 93.5% within 60 cycles at 0.5 mA cm^{-2} (Fig. 5.24a) and 3 mA cm^{-2} (Fig. 5.25c) with a capacity of 1 mAh cm^{-2} , respectively. A larger deposition capacity (3 mAh cm^{-2}) is carried out to investigate its practical application in full cells (Fig. 5.24b). CNT-5/1 still exhibits superior cycling performance and the highest CE of 98.5% in the first 20 cycles at 0.5 mA cm^{-2} .

A comparison of cycling lifetime on CNT-based electrodes with different PVDF contents (CNT-X/1 ($X = 0, 0.5, 2.5, 5,$ and 7.5)) was conducted (Fig. 5.24c). Increasing the PVDF content in CNT-based electrodes effectively prolongs their cycling lifetime and improves their CE value. Fig. 5.24c illustrates that CNT-5/1 maintains the highest CE value in all CNT-based electrodes, which indicates the mass ratio of PVDF/CNTs=5/1 is probably the best proportion to achieve the dendrite-free and high reversible Li deposition owing to the least surface area (Table 5.1), PVDF-induced favourable SEI and comparably appropriate interface impedance.

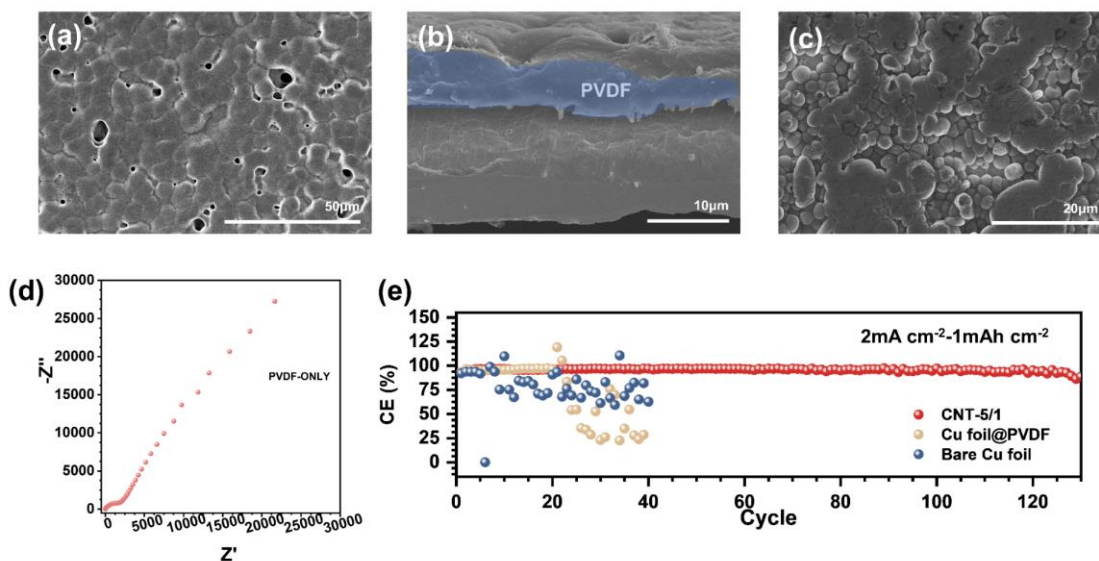


Figure 5.26. (a) Top-view and (b) cross-sectional view SEM images of Cu coated with PVDF only (Cu@PVDF). (c) Top-view SEM image of Li plated Cu@PVDF with a capacity of 1 mAh cm⁻² at 0.5 mA cm⁻². (d) EIS of the fresh Cu@PVDF electrode. (e) CE of Li plating on/stripping from bare Cu, Cu@PVDF, and CNT-5/1 with a capacity of 1.0 mAh cm⁻² at 2.0 mA cm⁻².

Cu foil was coated with only PVDF (Cu@PVDF) to check the function of CNTs. Pores are observed in the top-view SEM images (Fig. 5.26a-b) of Cu@PVDF, proving that the PVDF coating layer is not completely dense. Flat Li deposits can be observed on the Cu@PVDF (Fig. 5.26c), revealing that PVDF plays a crucial role in facilitating dough-type Li deposits owing to the internal stress release in the horizontal direction to the current collector surface.²⁴⁴ The rather large R_{ct} (Fig. 5.26d) elucidates that the interfacial impedance between solvated Li⁺ and PVDF may greatly increase, which may affect the electrochemical redox of Li⁺. It is concluded that CNTs can help adjust the formation of pore structure and reduce the barrier in the redox ability of Li⁺ via the uniform interfacial current distribution. As a result, Cu@PVDF can keep only short cycling times (~20 cycles) even with high CE because of an extremely high barrier in the redox ability of Li⁺ without a uniform current distribution contributed by CNTs (Fig. 5.26e).

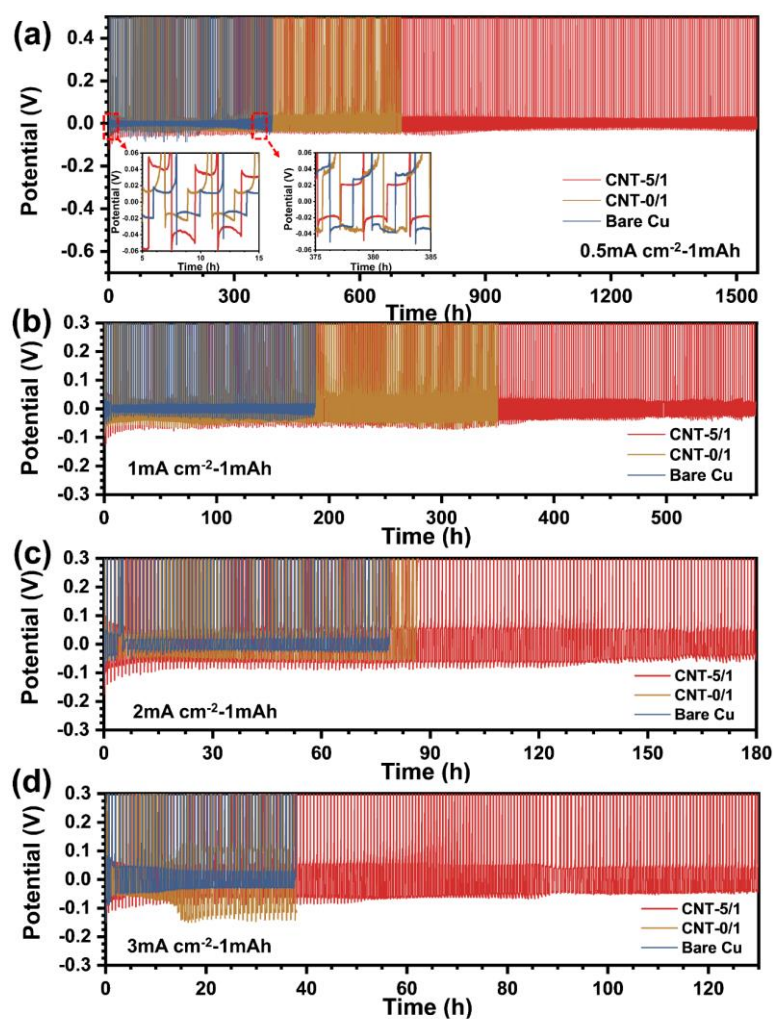


Figure 5.27. (a) Comparison of potential profiles of Li plating on/stripping from bare Cu, CNT-0/1, and CNT-5/1 with a capacity of 1 mAh cm^{-2} at (a) 0.5 mA cm^{-2} , (b) 1 mA cm^{-2} , (c) 2 mA cm^{-2} and (d) 3 mA cm^{-2} .

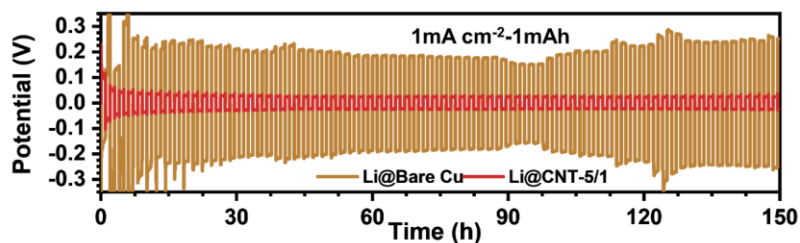


Figure 5.28. Cycling performance of Li@Bare Cu and Li@CNT-5/1 at 1 mA cm^{-2} with 1 mAh cm^{-2} . Li is pre-deposited on bare Cu and CNT-5/1 with 5 mAh cm^{-2} to fabricate Li@Bare Cu and Li@CNT-5/1, respectively.

Similarly, as displayed in Fig. 5.27a, CNT-5/1 performs the most stable overpotential (<20 mV) over long-term cycling (more than 1500 h) at 0.5 mA cm^{-2} with a capacity of 1 mAh cm^{-2} . Notably, the overpotential of CNT-5/1 keeps the highest value before stabilizing at $\sim 20 \text{ mV}$ in the first 10 cycles among 3 electrodes, which is attributed to the fact that there is an obvious film-forming process derived from the electrochemical reduction of PVDF and Li in CNT-5/1. Thus, this film-forming-induced polarisation reveals that the strong complexation between solvated Li^+ and PVDF can facilitate planar Li deposition. For example, it has been reported that cyanide is used to increase polarisation in the electroplating industry to improve the flatness and brightness of the electroplated metal.²⁸⁶ Similar behaviour in CNT-5/1 can be found at different current densities (Fig. 5.27b-d). The cycling performance of symmetrical cells using Li@CNT-5/1 was measured to reveal the long-term stability of CNT-5/1 further. Li was pre-deposited on the bare Cu and CNT-5/1 with a capacity of $\sim 5 \text{ mAh cm}^{-2}$ to fabricate Li@Bare Cu and Li@CNT-5/1, respectively. As shown in Fig. 5.28, the Li@CNT-5/1-based symmetric cell also exhibits superior cycling performance with a much smaller overpotential than the Li@Bare Cu-based one at 1 mA cm^{-2} with an areal capacity of 1 mAh cm^{-2} .

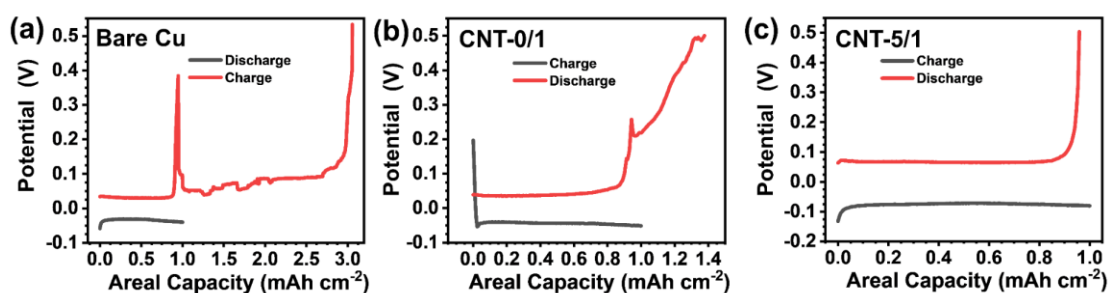


Figure 5.29. Potential profiles at the 4th cycle of Li plating/stripping with an areal capacity of 1 mAh cm^{-2} at 2 mA cm^{-2} on (a) bare Cu, (b) CNT-0/1, and (c) CNT-5/1.

The Li dendrite/whisker-induced overcharge phenomenon in half cells with bare Cu or CNT-0/1 electrode during the stripping process can be seen in Fig. 5.29a-c since

continuous side reactions between porous Li dendrites and electrolytes contribute to the spurious capacity, further confirming dense Li deposition can be achieved in CNT-5/1.

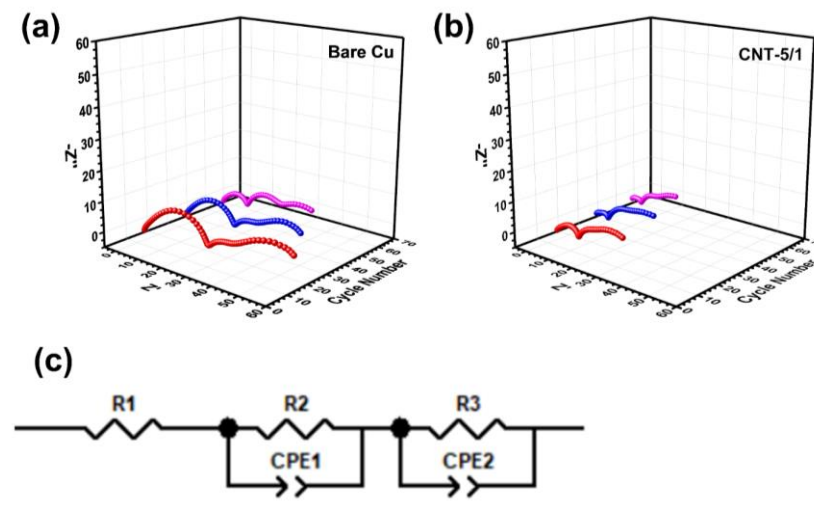


Figure 5.30. EIS of (a) bare Cu and (b) CNT-5/1 after 10, 30, and 50 cycles with an areal capacity of 1 mAh cm^{-2} at 1 mA cm^{-2} . (c) applied fitting resistance model: R1:R₀ (Ohmic resistance); R2: R_{SEI} (Migration resistance of Li⁺ through the SEI); R3: R_{ct} (Charge transfer resistance); CPE1/CPE2: Constant phase element (Conventional double-layer and passivation film capacitance).

Table 5.3. Fitting resistance data of galvanostatic plating/stripping in symmetrical cells using CNT-5/1 or Cu foil with an areal capacity of 1.0 mAh cm^{-2} at 1 mA cm^{-2} .

Sample	R1 (Ω)	R2 (Ω)	R3 (Ω)
CNT-5/1-10 th	4.243	10.42	25.51
Bare Cu foil-10 th	3.481	27.52	61.08
CNT-5/1-30 th	2.926	6.39	25.99
Bare Cu foil-30 th	3.669	21.44	50.6
CNT-5/1-50 th	1.848	5.068	24.44
Bare Cu foil-50 th	3.588	10.7	34.98

Cycling performance is strongly decided by the stability of SEI on the electrode

materials. Thus, the interfacial stability of the SEI was further investigated by EIS (Fig. 5.30a-b). After 10, 30, and 50 cycles, CNT-5/1 exhibits smaller semicircles in the high-frequency and medium-frequency ranges than bare Cu foil (Table 5.3). These results indicate that the SEI formed on CNT-5/1 has a smaller interface impedance, such as R_{ct} than the SEI formed on the Cu foil. This result confirms that a uniform current distribution and PVDF introduction can facilitate the formation of a stable SEI layer with low resistance during Li deposition/dissolution.

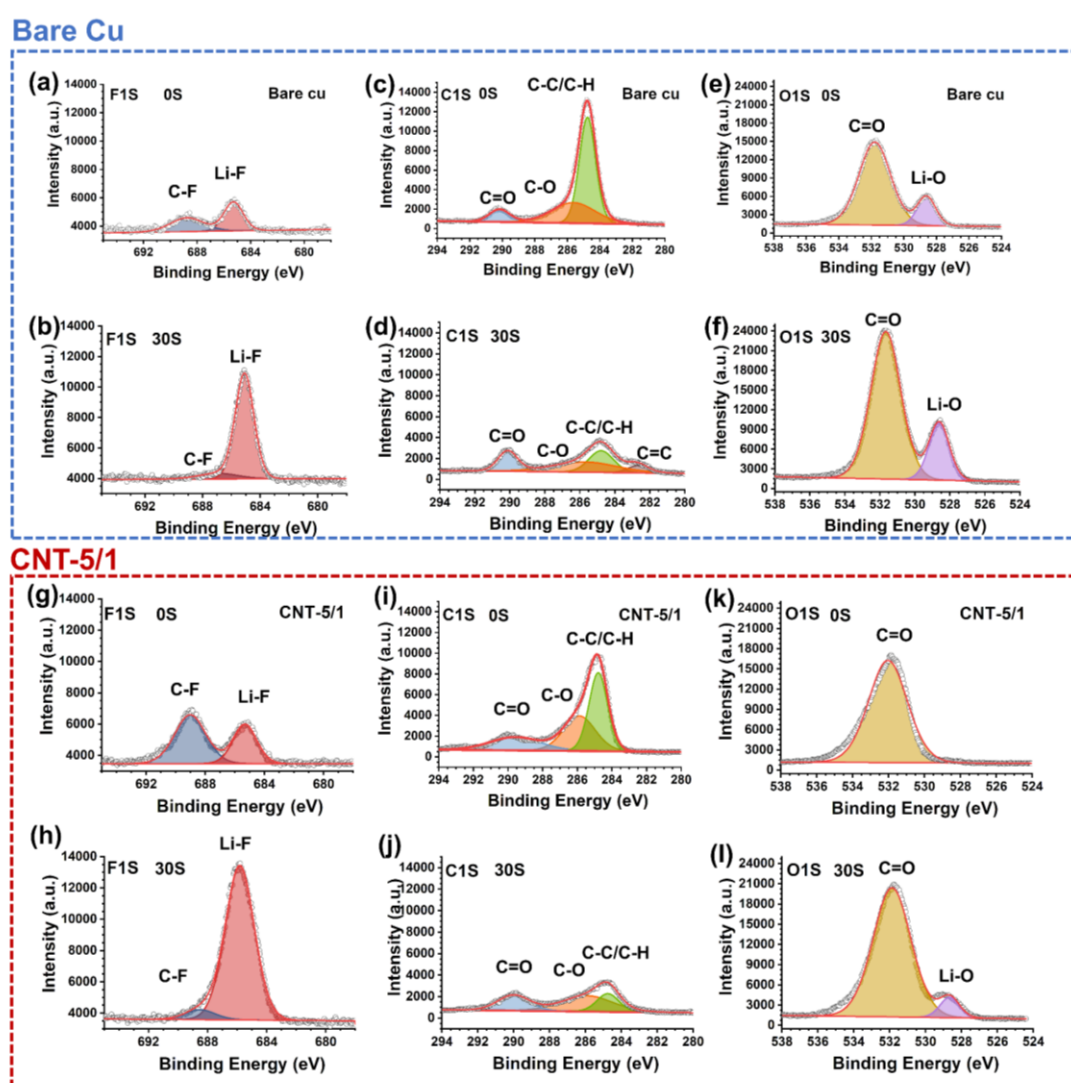


Figure 5.31. F 1s, C 1s, and O 1s XPS spectra of (a, b), (c, d), and (e, f) bare Cu and (g, h), (i, j), and (k, l) CNT-5/1 electrodes with 30 cycles of Li plating/stripping with a capacity of 1 mAh cm^{-2} at 1 mA cm^{-2} before (a, c, e, g, i, and k) and after the 30s of

etching (b, d, f, h, j, and l).

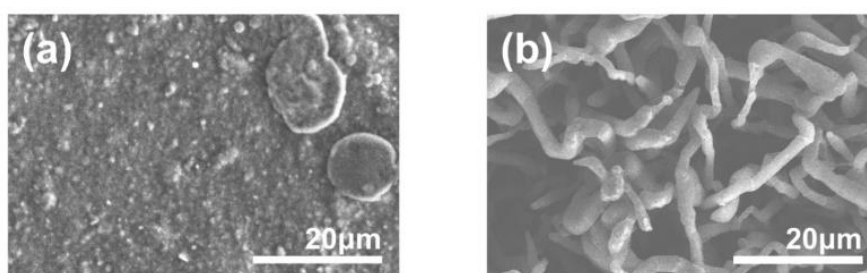


Figure 5.32. Top-view SEM images of (a) CNT-5/1 and (b) bare Cu after 30 cycles of Li plating/stripping with an areal capacity of 1.0 mAh cm^{-2} at 1.0 mA cm^{-2} .

After 30 cycles, the interfacial SEI component was further investigated (Fig. 5.31). There is an apparent growth of the Li-F intensity in the interior of SEI than that on the surface in both Cu and CNT-5/1 after 30 cycles. Compared to the bare Cu, CNT-5/1 has a higher Li-F intensity in the internal SEI component, which is more favourable for good cycling performance. This result is in accordance with the EIS results (Fig. 5.30). Furthermore, more carbonaceous components (e.g., C-C/C-H) and more oxygenated components (e.g., C=O or Li-O) can be observed in the C1s and O1s spectra of bare Cu, which is ascribed to the more electrochemical side reactions between Li and electrolyte on the bare Cu foil. Morphology of CNT-5/1 and bare Cu after 30 cycles (Fig. 5.32a-b) with an areal capacity of 1 mAh cm^{-2} at 1.0 mA cm^{-2} was characterised. Apparent dendrite-like “dead Li” continuously accumulates on the Cu foil during the plating/stripping processes, resulting in increased internal resistance, huge electrolyte consumption, and capacity fading. In comparison, only little bulk-like “dead Li” is discerned in CNT-5/1 after 30 cycles, revealing the essential role that the CNT-based electrode plays in suppressing the formation of Li dendrites. The generation of SEI involving a reaction between Li and CNTs or PVDF can be regarded as the dominant form of irreversible Li during cycling.

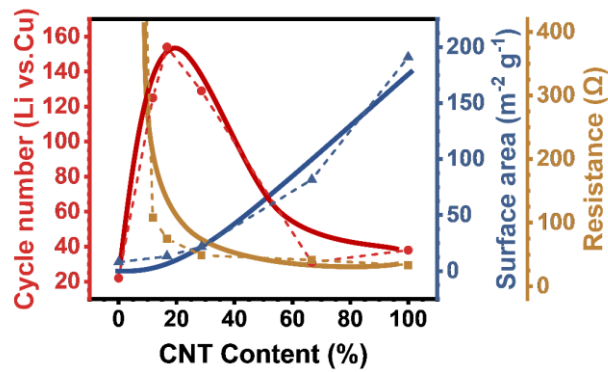


Figure 5.33. The summary diagram of the relationship between cycling performance, resistance, surface area, and CNT contents. Dots are original data, and solid lines are rough-fitting curves.

The relation between the cycling performance, resistance and surface area, and different CNTs contents are further clarified in Fig. 5.33. The cycling performance in CNT-based electrodes strongly depends on the surface area and PVDF-induced impedance (R_{ct}). Low impedance may lead to a high reaction rate, easily resulting in Li dendrite as a result of a diffusion-limited rate. By contrast, high impedance usually gives rise to a reaction-limited rate. But it can enhance the barrier of Li^+ redox. Thus, comparatively appropriate impedance is key to balancing reaction-limited and diffusion-limited rates for CNT-5/1. The huge specific surface area in the current collector of LMFRBs can consume too much active Li and electrolyte, dramatically reducing discharging capacity. In addition, a large specific surface area often implies spatial structure distribution with small pores. Li deposition/dissolution may be highly affected by pore size.²⁷⁴ The requirement of specific energy and tip-effect²⁷⁴ may limit the inside space usage in the 3D current collector. Most Li may still undergo host-free deposition, which does not help establish stable SEI and release the accumulated internal stress. Therefore, the current collector of LMFRBs with the appropriate specific surface area also plays a relatively important role in battery performance.

5.3.5. Full-cell electrochemical performances of CNT-based electrodes

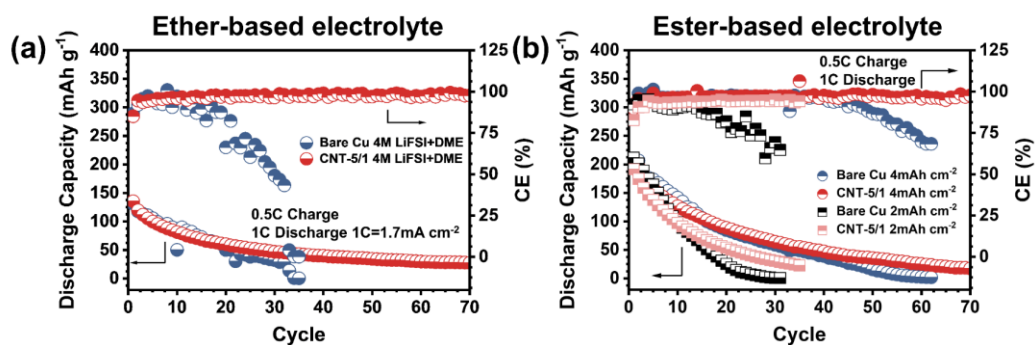


Figure 5.34. (a) Cycling performance of bare Cu and CNT-5/1 paired with high areal capacity LiFePO₄ positrodes ($\sim 1.7 \text{ mAh cm}^{-2}$) in the ether-based electrolyte. (b) Cycling performance of bare Cu and CNT-5/1 paired with high areal capacity NCM811 positrodes ($\sim 2 \text{ mAh cm}^{-2}$ and $\sim 4 \text{ mAh cm}^{-2}$) in the esters-based electrolyte.

In this chapter, 4 M LiFSI in DME electrolyte was employed in the full cell. It is reported that the high-concentration ether-based electrolyte can better suppress dendrite growth and increase the voltage window of the battery.¹⁴⁹ Therefore, a 4 M LiFSI in DME electrolyte was employed in the full cell.¹⁴⁹ Additionally, a full cell test was conducted using 1 M LiPF₆ in a mixed solution of EC and DMC with 2 wt% FEC, to evaluate its performance in the ester-based electrolyte.

To obtain the practical performance of CNT-based electrodes in full cells, long-term cycling of LMFRBs assembled with bare Cu foil or CNT-5/1 and LiFePO₄ ($\sim 1.7 \text{ mAh cm}^{-2}$) positrodes were tested in electrolyte with a high concentration of Li salt in ether electrolyte. Fig. 5.34a displays that the full cell composed of bare Cu foil capacity retention undergoes a sharp drop to less than 5% within 40 cycles. In contrast, the full cell with CNT-5/1 shows much higher capacity retention of $\sim 34\%$ after 40 cycles. The practical performance of a CNT-based electrode in full cells composed of NCM811 positrode with a larger areal capacity (2 mAh cm^{-2} and 4 mAh cm^{-2}) in the esters-based electrolyte was further investigated. Full cells assembled with CNT-5/1 still perform

better cycling performance compared to bare Cu (Fig. 5.34b). Thus, uniform current distribution and soft-substrate-induced internal stress release in the horizontal direction and favourable SEI can contribute to the long cycling performance of CNT-5/1.

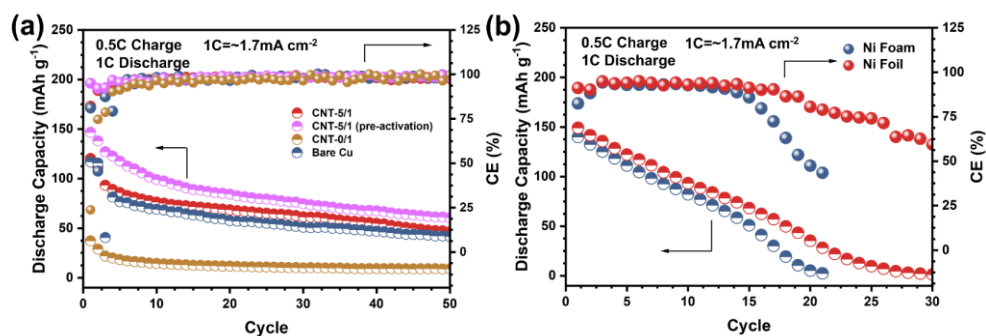


Figure 5.35. (a) Cycling performance of bare Cu, CNT-0/1, CNT-5/1, and CNT-5/1 with pre-activation capacity of 2 mAh cm⁻² at 0.5 mA cm⁻² for 2 cycles paired with LiFePO₄ positrodes (~1.7 mAh cm⁻²) in the ethers-based electrolyte. (b) Cycling performance of bare Ni foil and Ni foam paired with LiFePO₄ positrodes (~1.7 mAh cm⁻²) in the esters-based electrolyte.

The large surface area of CNTs leading to serious capacity fading is clarified upon common ether-based electrolytes. Full cells containing CNT-0/1 show a sharp decline in capacity retention within the first 10 cycles due to the formation of significant amounts of irreversible Li (Fig. 5.35a). The pre-activation process in CNT-5/1 is carried out so that the influence on discharge capacity due to the generation of initial SEI can be eliminated. Firstly, Li||CNT-5/1 cell is assembled and cycled 2 times with 2 mAh cm⁻² at 0.5 mA cm⁻² to pre-form SEI on CNT-5/1. Then, full cells assembled with pre-activated CNT-5/1 current collector and LiFePO₄ positrode are tested. It is found that after the pre-activation process, the discharge capacity of CNT-5/1 promotes dramatically by ~20 mAh g⁻¹ within 50 cycles compared with the pristine one, which implies when the capacity is further increased, the SEI can still support a good cycling performance, and the generation of SEI can be regarded as the dominant form of

irreversible Li on the CNT-5/1 (Fig. 5.35a). To specifically uncover capacity fading caused by large surface area in LMFRBs, Ni foil and Ni foam are used as 2D and 3D current collectors, respectively. It is widely reported that Li dendrites can be effectively alleviated by a 3D current collector relying on reduced local current density.^{104, 287} However, the discharge capacity of Ni foil-based LMFRBs (typical 2D current collector) is higher than that of Ni foam-based LMFRBs (3D current collector) during cycling in Fig. 5.35b, indicating that SEI proliferation caused by a large surface area in 3D current collector will affect seriously discharge capacity and cycling performance of LMFRBs. It can be conjectured that there may be different forms of irreversible Li in Ni foil (“dead Li” is dominant) and Ni foam (SEI proliferation is dominant) during cycling. Thus, the above result reflects that in LMFRBs, we cannot focus only on dendrite elimination but also on capacity fading due to SEI proliferation in the current collector design. Thus, the appropriate surface area in the current collector is more important for the practical application of LMFRBs, confirming that reducing the surface area of CNTs is a viable method to improve its practical application in LMFRBs.

5.4. Conclusions

It has been concluded that the implementation of a CNT network can effectively establish a uniform and well-subdivided current distribution in the nanoscale, resulting in a uniform Li^+ flux and preventing localized ion concentration voids. Meanwhile, the introduction of PVDF can lower the porous structure of the electrode to reduce the CNT-induced side effects (including SEI proliferation and severe Li dendrite growth), and PVDF serves as a Li-F-rich SEI film-forming polymer to facilitate the internal stress release in the horizontal direction to the current collector surface in deposited Li. The synergistic effect between CNTs and PVDF contributes to improved Li deposition/dissolution behaviours, resulting in stable cycling performance of the LMFRBs. Our findings suggest that using a 2D-type current collector with uniform current distribution and soft substrate provides a viable choice for applying LMFRBs.

Chapter6

Free-standing and Low-Density Composite of Graphene and PVDF as Promoting Current Collector for Reversible Lithium Deposition

This chapter displays a method for the preparation of novel free-standing graphene/PVDF composite carbon-based current collectors (CBCCs). Graphene sheets are tightly stacked to reduce the surface area and suppress lithiation. PVDF facilitates the formation of the sturdy free-standing film and hinders Li^+ insertion and electrolyte penetration to reinforce the mechanical strength of the CBCCs. The Li-F-rich SEI can improve the stability of SEI and minimise electrolyte decomposition owing to PVDF's introduction. Cu tabs can be bonded firmly to the CBCCs with acceptable resistance, promising practical application. Therefore, basic requirements such as high conductivity, sufficient mechanical strength, viable tab welding, and improved Li deposition and dissolution in cells have been satisfactorily achieved using this CBCC.

6.1. Introduction

The current collector as an essential component is worth focusing on in LMFRBs since they can highly impact the reversibility of Li deposition. Not only can the current collector play a role in conducting electrons, but also directly affects the Li deposition behaviour on the substrate.^{249, 258}

Cu foils are a commonly used current collector in LIBs and, indeed function well due to their high conductivity and good mechanical property. However, as we found in

Chapter 5, Cu foil is inappropriate to serve as a suitable deposition substrate for Li in LMFRBs as it is prone to be corroded by air or electrolyte, which will destroy the formation of a robust SEI and increase the irreversible capacity. Non-uniform current distribution on the Cu foil can further exacerbate Li deposition. Additionally, it is commonly overlooked that galvanic corrosion between the metal-based current collector and electroplated Li in the presence of electrolyte leads to Li dissolution and reduction of cell capacity.²⁷⁵ Equally important, the heavy Cu foil can impair the specific energy of the LMFRBs. For past years, researchers have employed numerous strategies to modify Cu foil, such as plating a tin layer,²⁵⁵ growing multilayer graphene via chemical vapour deposition,²⁸⁸ and coating PAN fibre array via electrospinning.¹⁹⁰ However, these strategies are too complicated to apply in the industry. Meanwhile, the mass loading and thickness of modified current collectors can hardly meet the specific energy requirement at the cell level.²⁵⁸ For example, the weight of CNT-5/1 (Chapter 5) is not relatively light ($\sim 20 \text{ mg/cm}^2$) because of the Cu substrate.

It has been extensively proposed that highly conductive and light-weight carbon-based current collectors (CBCCs) such as graphene paper,²⁸⁹ carbon cloth,¹¹¹ or carbon nanotubes (CNTs) films²⁷⁰ can replace Cu foil in LIBs with the advantage of raising specific energy. Furthermore, carbon materials perform better resistance toward corrosion by air or electrolyte,^{266, 275} better heat dissipation (high thermal conductivity) capability, and more uniform current distribution than metal-based current collectors.²⁹⁰

Nevertheless, the implementation of CBCCs is still hindered due to two inherent issues. Unlike metallic materials that melt at high temperatures, carbon materials are difficult to be melted. Consequently, the conventional welding process does not apply to connecting carbon materials and metal tabs, which poses a big problem for the practical application of CBCCs. The other issue is related to the deposition behaviours of Li on carbon substrates. Firstly, due to their lithiophobic property,²¹⁷ pure carbon substrates for stable Li deposition/dissolution are challenging. Because the basal plane of graphitic

carbon materials has a high energy barrier for Li nucleation, Li deposits tend to form a dendritic morphology, leading to fragile SEI.²¹⁷ Secondly, the intercalation-induced and deposition-induced SEI growth on carbon materials with large surface area (e.g., CNTs or carbon cloth) consumes a large part of the limited Li inventory in LMFRB, leading to severe capacity fading, especially in the initial cycles.²⁹¹ Thirdly, it is found that Li⁺ insertion (lithiation) in graphitic carbon materials will easily give rise to degradation of the mechanical properties.²⁹² Also, electrolytes penetrate the body of CBCCs, usually leading to dramatic volume expansion. Thus cracking or even pulverisation of CBCCs may occur during cycling, which makes it difficult to sustain a long cycling life.²⁹³ In addition, the Li⁺ intercalation-induced SEI may hurt subsequent Li deposition. Thus, ideally, CBCCs should preferably possess a relatively small effective surface area to reduce the lithiation behaviour as much as possible. CBCCs should also have good mechanical strength to satisfy long-term cycling. Meanwhile, robust SEI on carbon materials should also be built. Finally, it is necessary to achieve a stable connection with low resistance between CBCCs and metallic tabs for practical applications.

Inspired by what we have done in Chapter 5,²⁹⁴ we propose a simple strategy of using polyvinylidene fluoride (PVDF) as an excellent binder/film-forming additive in the graphene slurry to cast the free-standing graphene-based current collector after partially etching Cu substrate (Fig. 6.1a) in this chapter. CNTs with 1D structure are replaced by Graphene sheets with 2D structure and high electrical conductivity. It is because Graphene sheets can be tightly stacked, which considerably reduces the electrochemically reactive surface area to improve the initial CE and decrease the formation of extra SEI. Meanwhile, the lithiation behaviour of graphene can also be effectively hindered, bringing about benefits to the mechanical strength of the current collector. PVDF can not only sufficiently bind the graphene sheets to form the sturdy free-standing film but also hinder the Li⁺ insertion in graphene sheets to maintain good mechanical properties for the CBCCs during cycling. Meanwhile, the Li-F components derived from the partial reduction of PVDF by the deposited Li in SEI can promote Li

deposition/dissolution, declining the lithiophobicity-induced fragile SEI and improving the Li reversibility of LMFRBs. Also, this SEI can further minimise the electrolyte decomposition owing to PVDF's low Fermi level, which can suppress electron transfer to the electrolyte. It is also worth mentioning that by partially etching Cu substrate, Cu tabs can be bonded firmly to the graphene-based current collectors with acceptable resistance, guaranteeing its practical application in pouch cells. Therefore, it is shown in Fig. 6.1b that Li deposits on the Cu foil with apparent Li dendrites due to the continuous formation of fragile and unstable SEI. Ultimately, "dead Li" which can highly block the Li^+ passing to the surface of Cu, will be formed after cycles, leading to the failure of the battery. Higher resistance to corrosion by air or electrolyte and a more uniform current distribution guarantee a more stable deposition environment on the graphene-based current collector. Meanwhile, PVDF-induced Li-F-rich SEI triggers uniform Li^+ flux and achieves dendrite-free deposits (Fig. 6.1c). Thus, improved Li deposition/dissolution behaviour and high specific energy are delivered using this free-standing CBCC simultaneously.

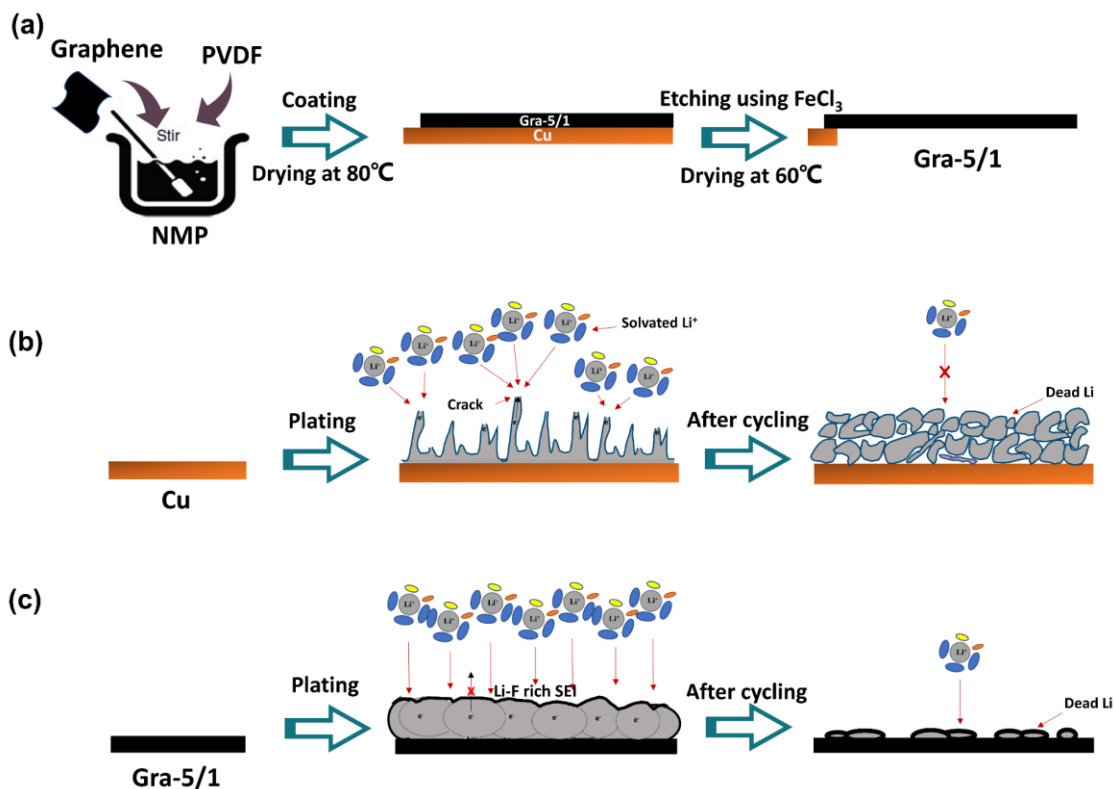


Figure 6.1. (a) Schematic illustration showing the preparation process of free-standing Gra-5/1. Schematic diagrams showing the morphology of electrodeposited Li and “dead Li” after cycling on (b) bare Cu foil and (c) Gra-5-1.

6.2. Experimental section

6.2.1. Electrodes preparation

Fabrication of the graphene/PVDF composite current collectors (Gra-X/1).

Graphene powder which was stored in an oven at 80 °C for at least 24 h before use, and PVDF (MW:1,000,000) solution (6 wt% in NMP) (mass ratio of PVDF: graphene =X:1, X= 1, 5, and 10) were mixed to make the graphene slurry. The slurry with a thickness of 100 μm (mass ratio of PVDF: graphene = 1:1) or 700 μm (mass ratio of PVDF: graphene =5:1) or 1000 μm (mass ratio of PVDF: graphene = 10:1) was respectively cast on a Cu foil and vacuum-dried at 80 °C for 6 h. The as-obtained electrodes were denoted as Gra-X/1-Cu (X = 1, 5, 10), respectively. The graphene current collector

without PVDF (denoted as Gra-0/1-Cu) was also prepared by mixing graphene, CMC, and SBR with a weight ratio of 90 : 5 : 5 to form a homogeneous slurry which was then cast with a thickness of 100 μm on Cu foil and vacuum-dried at 80 $^{\circ}\text{C}$ for 6 h. The as-prepared graphene-based electrodes were soaked in a solution containing 1M FeCl_3 and HCl (37 wt%) with the same volume ratio to partially remove the Cu substrate, followed by washing three times with deionised water and vacuum-dried at 80 $^{\circ}\text{C}$ for 6 h. The as-prepared free-standing graphene-based current collectors were denoted as Gra-X/1 (mass ratio of PVDF: graphene =X:1, X= 0, 1, 5, 10).

Fabrication of the composite current collector of graphene and PAN (Gra-5/1-PAN-Cu). Graphene powder was stored in an oven at 80 $^{\circ}\text{C}$ for at least 24 h before use, and PAN (MW:150,000) solution (6 wt% in NMP) (mass ratio of PAN: graphene =5:1) was mixed to make the graphene slurry. The slurry with a thickness of 700 μm was cast on a Cu foil and vacuum-dried at 80 $^{\circ}\text{C}$ for 6 h. The as-obtained electrodes were denoted as Gra-5/1-PAN-Cu.

The as-prepared Gra-X/1-Cu or Gra-X/1 (X = 0, 1, 5, and 10) or Gra-5/1-PAN-Cu were punched into 14 mm discs or cut to 47 mm \times 57 mm or 64 mm \times 74 mm sheets, respectively for application as the current collectors in coin-type or pouch-type cells. Other CBCCs such as carbon cloth (Suzhou Siner Technology Co., Ltd.), CNTs film (Nanjing Yuanchang New Materials Co., Ltd.), expanded graphite paper (Hefei Aoqi Electronic Technology Co., Ltd.), graphene paper (prepared by vacuum filtration of aqueous graphene slurry), and graphite paper (Ningbo Morsh Technology Co., Ltd.) were punched into 14 mm discs or cut to 47 mm \times 57 mm sheets.

6.2.2. Electrochemical Measurements

Two-electrode coin half cells (Li vs. Gra-X/1 or Gra-X/1-Cu (X = 0, 1, 5, and 10) or Gra-5/1-PAN-Cu). Standard CR2032 coin-type cells were assembled in an Ar-filled glove box with H_2O and O_2 content below 1 ppm. For the Li||Cu or Li||C coin half cell,

a 0.5 mm thick Li disc with a diameter of 16.0 mm was applied as both the counter and reference electrode. The as-obtained 14 mm discs of Gra-X/1 or Gra-X/1-Cu (X = 0, 1, 5, and 10) or Gra-5/1-PAN-Cu were employed as the working electrode. The Celgard 2500-type polypropylene membrane with a thickness of 25 μm was applied as the separator. 1 M LiPF_6 in fluoroethylene carbonate and Ethyl Methyl Carbonate (FEC: EMC=1: 5, v/v) (Zhangjiagang Guotai-Huarong New Chemical Materials Co., Ltd) was employed as the ester-based electrolyte in Li||Cu or Li||C coin half cells. 75 μL electrolyte was added to each cell. All coin cells were shelved for 8 h before testing. The batteries were first cycled at 0-3.0 V (versus Li/Li⁺) at 0.1 mA cm^{-2} for ten cycles to remove surface contamination in Li||Cu or Li||C coin half cell. The galvanostatic performances were conducted at 25 °C using the Land CT 2100A system (Jinnuo Wuhan Corp, China). Li was plated galvanostatically with capacities of 1 or 3 mAh cm^{-2} and then stripped galvanostatically with a cut-off potential of 0.5 V vs. Li/Li⁺ at different current densities. CV and EIS were tested by an electrochemical workstation (Solartron 1470E) using CR2032-type coin cells. The voltage range of CV was chosen from 2 V to -0.25 V with a scan rate of 0.1 mV s^{-1} . The frequency range was set between 1 MHz and 0.01 Hz.

Two-electrode coin full cells (LFP or NCM 811 vs. Cu or Gra-X/1 or Gra-X/1-Cu (X = 0, 1, 5, and 10)). For Cu or Gra-X/1 or Gra-X/1-Cu (X = 0, 1, 5, and 10) ||LFP or NCM 811 coin full cells, the as-prepared 14 mm discs of Cu or Gra-X/1 or Gra-X/1-Cu (X = 0, 1, 5 and 10) and LFP or NCM 811 were employed as the current collectors and positrodes, respectively. Celgard 2500 was used as the separator (25 μm). The electrolyte used herein was 1 M LiPF_6 in a mixed solution of FEC and EMC (volume ratio of 1:5). Electrolyte injection was fixed at 75 μL in each coin cell. All coin cells were shelved for 8 h before testing. The cycling performances of the LFP-based full cells were galvanostatically charged up to 4 V at 0.5 C and then galvanostatically discharged to 2.0 V at 1C. The NCM 811-based full cells were galvanostatically charged up to 4.3 V and then galvanostatically discharged to 2.6 V at various rates from

0.1 C to 2 C. Cycling performances of the cells were tested by charging at 0.1 C and discharging at 0.2 C within the voltage range from 2.6 to 4.3 V.

Pouch cells (NCM 811 or LR-NCM 114 vs. Gra-5/1 or Gra-5/1-Cu or Gra-5/1-PAN-Cu). Gra-5/1, Gra-5/1-Cu, or Gra-5/1-PAN-Cu with a size of 47 mm × 57 mm or 64 mm × 74 mm were employed as the current collectors. As-prepared NCM 811 electrodes with 43 mm × 53 mm were applied as the positive electrode. Celgard 2500 was used as the separator (25 μm). Pouch cells are fabricated in the ultra-dry clean room (Dew point: below -45°C, cleanliness level: 100,000) at room temperature. 1 M LiPF₆ in FEC/EMC=1:5 by volume was used as the electrolyte (6 g Ah⁻¹). Alternatively, lithium bis(fluorosulfonyl)imide (LiFSI), DMC, and 1,1,2,2-Tetrafluoroethyl-2,2,3,3-tetrafluoropropylether (TTE) in a molar ratio of 3:4:1 with 1wt% lithium difluoro(oxalato)borate (LiDFOB) were used as a modified electrolyte. After injecting the electrolyte, full cells were at least stored for two days to achieve full infiltration of electrolytes into pores of separators and positive electrodes. The NCM 811-based pouch cells were galvanostatically charged up to 4.3 V and then galvanostatically discharged to 2.6 V at 0.1 or 0.2 C. The LR-NCM 114-based pouch cells with a positive electrode size of 62 mm × 72 mm were galvanostatically charged up to 4.6 V at 0.1C and then galvanostatically discharged to 2.6 V at 0.1 C. Pouch cells were subjected to 100 kPa pressure during charging/discharging.

6.3. Results and discussion

6.3.1. Physical characterisations of Graphene-based current collectors

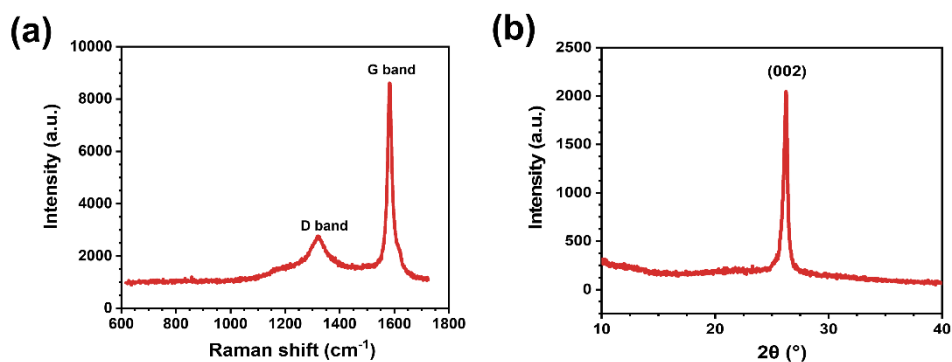


Figure 6.2. (a) Raman spectra and (b) X-ray diffraction pattern of graphene powders.

Highly conductive graphene nanosheets prepared by an intercalation and exfoliation method without an oxidation process were used as the raw material to prepare the CBCC. The graphitic structures of graphene materials were characterised by Raman spectroscopy and X-ray diffraction (Fig. 6.2a-b). Two sharp peaks at 1321 and 1584 cm⁻¹ in Fig. 6.2a are indexed as the D and G bands, respectively. A low-intensity ratio of 0.32 between the two bands (I_D/I_G) indicates the well-ordered graphitic structure, confirming the high electric conductivity of graphene materials. The XRD result (Fig. 6.2b) verifies the multilayer structure of the graphene materials as reflected by the characteristic (002) diffraction peak of graphite centred at 26.2° ($d=0.34$ nm).

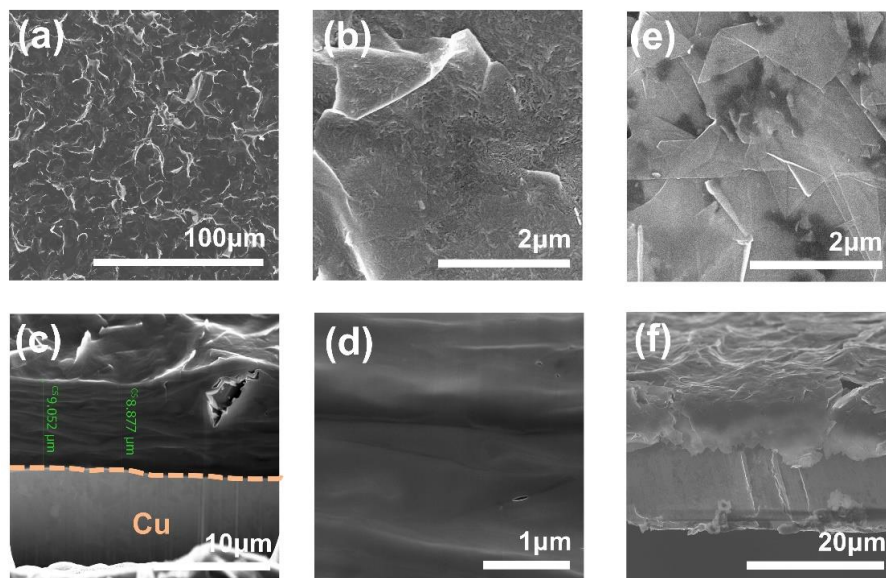


Figure 6.3. (a) Top-view of normal-magnification and (b) High-magnification SEM images of Gra-5/1. (c) FIB cross-section view of normal-magnification and (d) High-magnification SEM images of Gra-5/1. (e) Top-view and (f) cross-section view of SEM image of Gra-0/1.



Figure 6.4. Optical photographs showing the appearance and weight of bare Cu (left) and Gra-5/1 (right).

The graphene powders were mixed with PVDF in NMP solvent with a certain ratio to form a homogeneous slurry. Then the mixture was cast on a Cu foil, as illustrated in Fig. 6.1a, to form a coating layer after drying. Finally, the free-standing graphene-based

current collector was prepared by etching the Cu foil using FeCl_3 solution. Wrinkled graphene sheets are observed on the surface of Gra-5/1 (Fig. 6.3a). A magnified SEM image (Fig. 6.3b) shows that PVDF is attached tightly to the surface of graphene, which guarantees that Li^+ /metal can react with PVDF during deposition and mitigate the lithiophobic property of carbon materials. The cross-section view of Gra-5/1 in Fig. 6.3c-d shows that the thickness of the as-prepared Gra-5/1 is $\sim 9 \mu\text{m}$. Graphene sheets with warping edges can be observed in Fig. 6.3a, possibly owing to the introduction of PVDF or the use of NMP solvent in the slurry compared to Gra-0/1 in Fig. 6.3e (using water as the solvent). The graphene-only coating layer with the same thickness of $\sim 9 \mu\text{m}$ (see Fig. 6.3f) was fabricated to make a comparison. Notably, the thickness of graphene-based composite electrodes can be easily controlled on a small scale ($<10 \mu\text{m}$) by adjusting the coating thickness, which is beneficial to further improve specific energy without sacrificing cost. On the contrary, the thickness and cost of conventional Cu foil are typically inversely proportional, especially on a small thickness scale ($<6 \mu\text{m}$).²⁹⁵ Fig. 6.3c also manifests the homogeneous mixing of graphene sheets and PVDF. In addition, there are very few pores in the magnified FIB cross-section view of Gra-5/1 in Fig. 6.3d, approving that the obtained Gra-5/1 is non-porous and can prevent Li^+ inserting/depositing into the CBCC interior. The small surface area of Gra-5/1 can also suppress large irreversible Li consumption due to SEI formation. As shown in Fig. 6.4, Gra-5/1 ($\sim 2.5 \text{ mg cm}^{-2}$) is almost 8 times lighter than the conventional Cu foil of the same size ($47 \text{ mm} \times 57 \text{ mm}$), which is helpful to increase the specific energy of the battery.

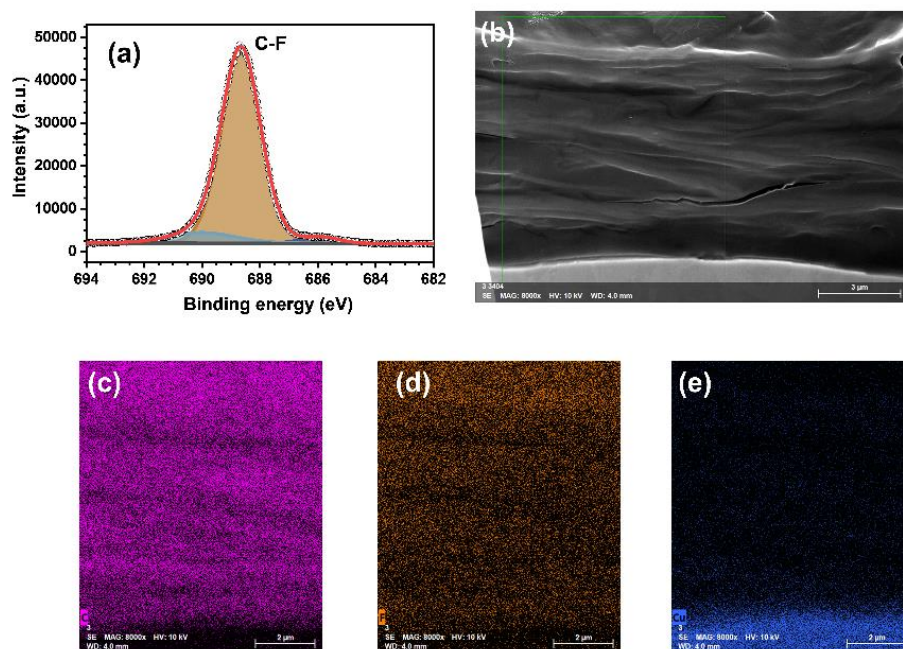


Figure 6.5. (a) XPS spectra of the F 1s over the fresh Gra-5/1. EDS mapping of the (b) cross-section view for (c) C, (d) F, and (e) Cu element of Gra-5/1.

XPS analysis and EDS mapping were carried out to investigate further the chemical composition and electronic states on the surface of Gra-5/1 (Fig. 6.5). One peak at 688.5 eV in the F1s spectrum of Gra-5/1 (Fig. 6.5a), which is ascribed to the C-F and proves the existence of PVDF. The uniform distribution of F and C elements over the entire coating layer is found via EDS mapping, as demonstrated in Fig. 6.5b-e, which also agrees with the XPS results. It has been verified that F atoms can interact with Li^+ to form robust SEI components such as Li-F during the electrochemical deposition²³⁴.

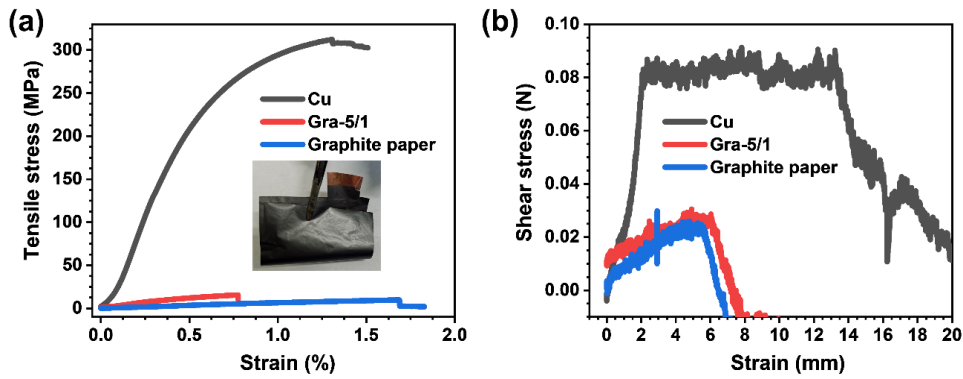


Figure 6.6. (a) Specific tensile strength and (b) specific shear strength of Cu, Gra-5/1, and graphite paper. The inset photograph of (a) shows the flexibility of the Gra-5/1.

Mechanical properties of Gra-5/1 were also investigated to evaluate its adaptability to the manufacturing procedures of practical cells (Fig. 6.6). Though the tensile and shear stress of the CBCCs are lower than that of Cu foil (Fig. 6.6), the mechanical strength of the as-prepared Gra-5/1 (0.75% at a tensile stress of 15 MPa and 6.5 mm at a shear stress of 0.03 N) is sufficient to withstand the changes of the mechanical stress in the battery during charging/discharging, as well as the production process. Interestingly, in comparison with the graphite paper (1.65% at a tensile stress of 10 MPa and 5.5 mm at a shear stress of 0.025 N) which is produced by carbonisation and graphitisation of polyimide polymers film at high temperatures (Fig. 6.6a-b), the free-standing Gra-5/1 shows better mechanical properties, which is ascribed to the PVDF molecules that bond graphene sheets. The excellent flexibility of Gra-5/1 is demonstrated by a bending process with 180 degrees, as shown in the inset of Fig. 6.6a.

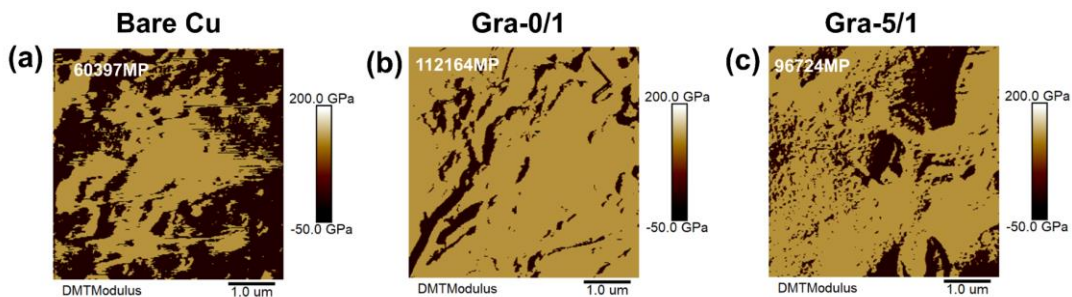


Figure 6.7. DMT modulus over (a) bare Cu, (b) Gra-0/1, and (c) Gra-5/1 through AFM

characterisation.

To characterise surface stiffness distribution, more mechanical characterisation, such as DMT modulus, is collected through AFM over bare Cu, Gra-0/1, and Gra-5/1 (Fig. 6.7a-c). Gra-0/1 has the remarkably highest micro stiffness (Young's modulus of 112.1 GPa), confirming the excellent mechanical properties of graphene materials.²⁹⁶ Interestingly, the incorporation of PVDF decreases Young's modulus of Gra-5/1 to 96.7 GPa (Fig. 6.7b-c) owing to the soft nature of PVDF while keeping good flexibility.

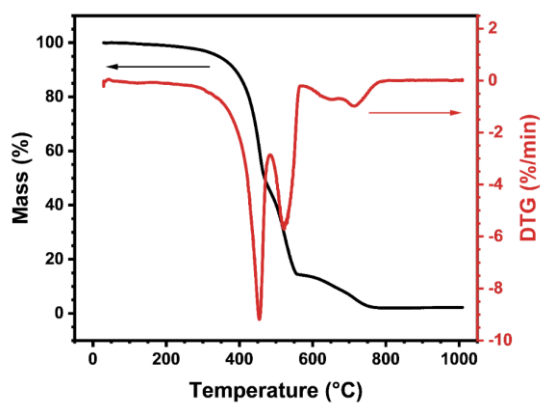


Figure 6.8. TGA and relevant derivative curves of the Gra-5/1.

The thermal stability of graphene-based current collectors is evaluated by TGA (Fig. 6.8). Gra-5/1 can withstand temperatures up to 400 °C in an air atmosphere, which is far beyond the normal operating temperatures (<60 °C) of batteries.

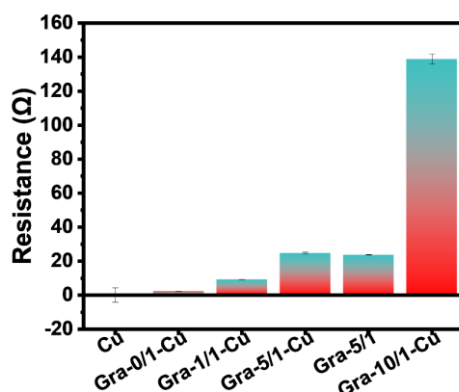


Figure 6.9. Resistance of Gra-X/1-Cu (X = 0, 1, 5, and 10), Gra- 5/1, and bare Cu foil.

The resistance of CBCCs is an important parameter affecting the battery's energy conversion efficiency and thermal management. Fig. 6.9 shows that the resistance of different graphene-based current collectors strongly depends on the PVDF mass ratio. Specifically, Gra-0/1 with no PVDF exhibits excellent electrical conductivity (resistance of $\sim 2 \Omega$). As the proportion of PVDF increases, the electrode resistance increases slowly to $\sim 24 \Omega$ (Gra-5/1). When the PVDF/graphene mass ratio reaches 10 (Gra-10/1), the resistance increases sharply to about 138Ω . Predictably, Gra-10/1 may not be suitable as the current collector, as it may substantially increase the battery's internal resistance.

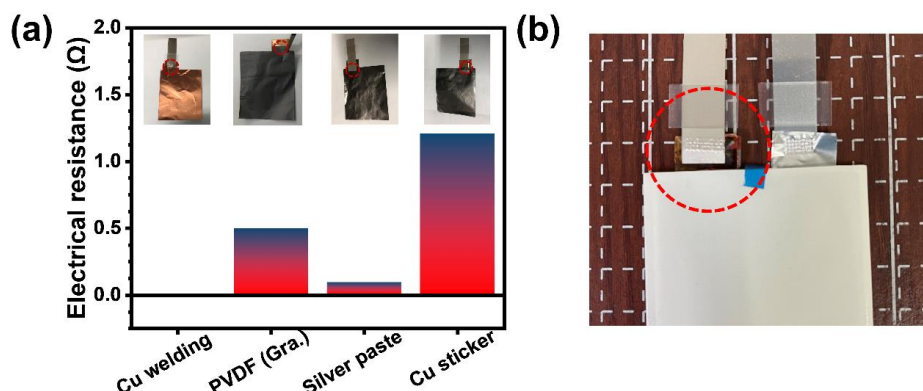


Figure 6.10. (a) Contact resistance between different current collectors and metallic tabs using different connecting methods. The inset optical photographs show the

appearance of different samples. (b) Optical photograph showing the tabs welded on the Gra-5/1 in a practical pouch cell.

The stable connection between carbon and metallic materials with low resistance should be first considered to apply the CBCCs in practical pouch cells. Inspired by our previous coating operations on Cu foils,²⁹⁴ we found strong adhesion and acceptable contact resistance between PVDF-containing conductive carbon coatings and Cu foil. Therefore, we decide to leave a small piece of metallic Cu on the end of the graphene-based current collector via the coating and etching process to enable tab welding of the CBCCs. The contact resistance between Gra-5/1 and Cu (Fig. 6.10a) is almost equivalent to the contact resistance between Gra-5/1 and welded metallic tab (Fig. 6.10b), verifying the reliability of this design in practical pouch cells. The connection resistances using alternative connection strategies (such as using a Cu sticker or silver paste as binding materials between metallic tabs and graphite paper) were also tested (Fig. 6.10a), all of which fall in an acceptable level for pouch cell applications. Considering the cost and convenience of fabricating multi-layer pouch cells, tab connection by ultrasonic welding was adopted in our experiments.

Overall, this free-standing CBCC is qualified to undertake the basic function of the current collector and show certain processability and practical application potentials in pouch cells.

6.3.2. The adaptability of Graphene-based electrodes to cell operating conditions



Figure 6.11. Contact angles of electrolyte toward (a) Cu foil and (b) Gra-5/1.

To further estimate the feasibility of the as-fabricated Gra-5/1 as the current collector in practical cells, its adaptability, including wettability in the electrolyte was clarified. The contact angle of the electrolyte on both Cu foil and Gra-5/1 was measured (Fig. 6.11a-b) to understand better the interaction between the electrolyte and the graphene/PVDF composite current collector. Results show that Gra-5/1 demonstrates considerably better wettability (contact angle of 4°) toward carbonate ester electrolyte than Cu foil (contact angle of 23.5°). It was reported that the electrolyte wettability is closely related to the uptake amount of liquid electrolyte and then influences the distribution of Li^+ flux over the surface of the current collector during cycling.¹³⁷ Therefore, such a superior electrolyte wettability is beneficial for uniform Li^+ flux and mitigating uneven Li deposition.

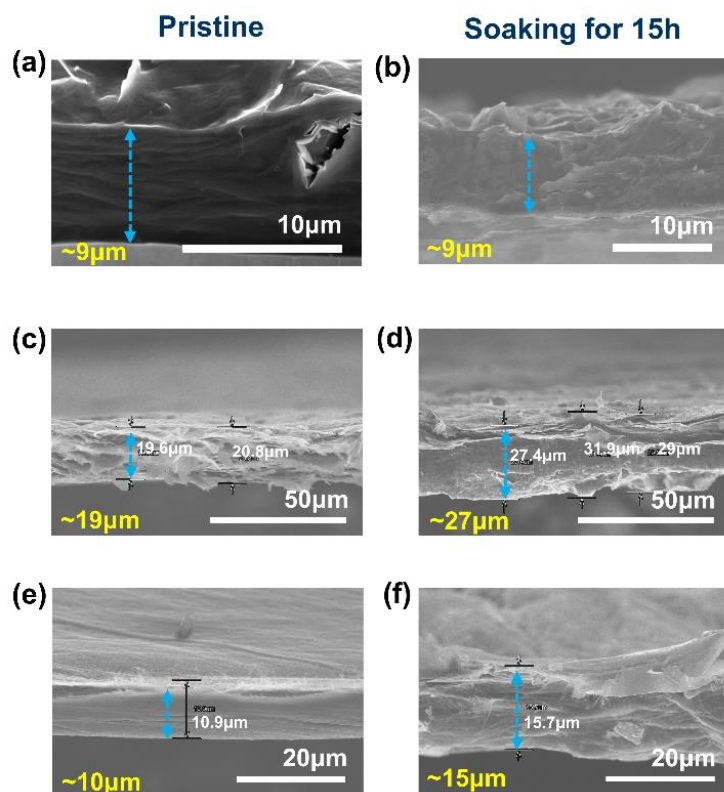


Figure 6.12. Cross-section views SEM images of (a), (b) Gra-5/1, (c), (d) graphene paper and (e), (f) carbon nanotube film before soaking and after soaking in the electrolyte solution for 15h, respectively.

Another typical parameter for characterizing the stability of materials is swelling behaviour, as electrolyte penetration may cause the expansion of CBCCs and strength reduction. Thus, to further evaluate the stability of Gra-5/1 in the electrolyte, the swelling behaviour of Gra-5/1 was measured by soaking it in the electrolyte solution for 15h. Fig. 6.12a-b illustrates there is no apparent swelling in Gra-5/1, implying PVDF can keep Gra-5/1 stable in the electrolyte by preventing the electrolyte from entering the interior of the current collector. The swelling behaviours of other CBCCs, such as graphene paper and CNTs film, are obtained to compare with Gra-5/1. Inversely, there is apparent swelling in both CBCCs, as illustrated in Fig. 6.12c-f. The volume of graphene paper expands by ~30%, and the volume of CNTs film increases by 50%, verifying that PVDF can shield the invasion of electrolytes into the interior of carbon frameworks.

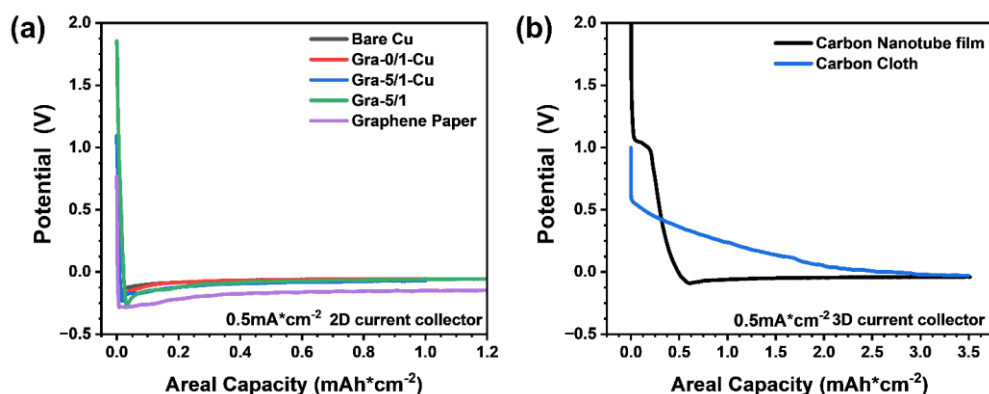


Figure 6.13. (a) Potential profiles of Li plating on the 2D current collector: bare Cu foil, Gra-0/1-Cu, Gra-5/1-Cu, Gra-5/1, and the graphene paper at 0.5 mA cm⁻². (b) Potential profiles of Li plating on the 3D current collector: carbon cloth and carbon nanotube film with an areal capacity of 3.5 mAh cm⁻² at 0.5 mA cm⁻².

Lithiation/intercalation behaviour is rather common in graphite-type materials, but it will damage the mechanical strength of CBCCs.²⁹² Thus, the lithiation behaviour of Gra-5/1 and other free-standing CBCCs is investigated (Fig. 6.13a-b). Interestingly, Gra-0/1, Gra-5/1, and graphene paper show similar metal-deposition-like behaviour without apparent lithiation potential (Fig. 6.13a), proving that there is nearly no Li⁺ intercalation behaviour. It is probably because that horizontally stacked graphene can forcefully hinder Li⁺ intercalation into carbon interlayer. This is a good signal for the CBCCs to maintain their mechanical strength. However, commercial carbon cloth and CNTs film have apparent lithiation behaviour (Fig. 6.13b), implying that their mechanical strength can be largely affected during cycling. The potential profile of Li plating on CNT/PVDF composite electrode (CNT-5/1) reveals that PVDF can reduce the Li⁺ insertion/deposition in the internal CBCCs (Fig. 5.20).

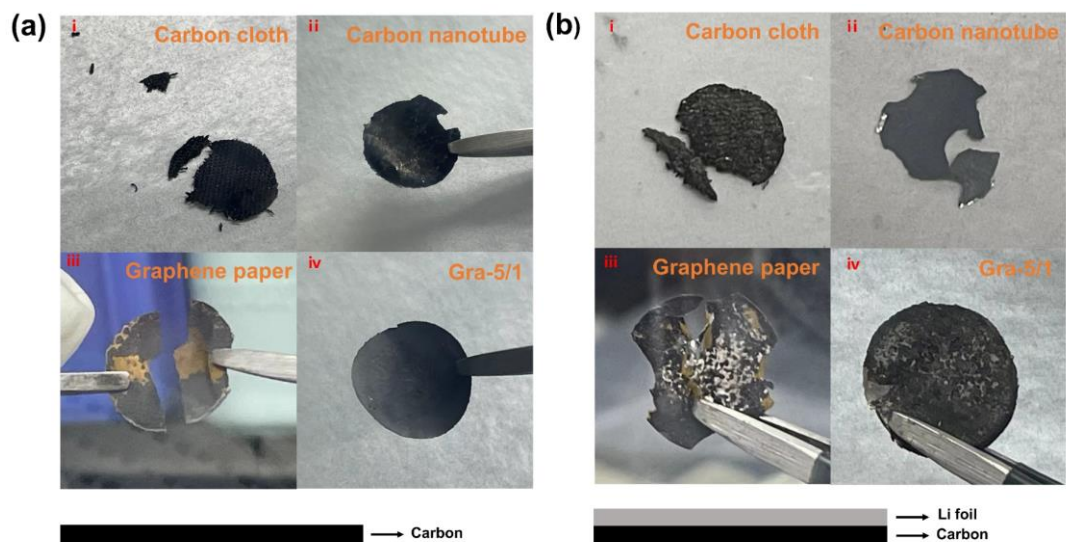


Figure 6.14. Optical photograph of (i) the carbon cloth, (ii) carbon nanotube film, (iii) graphene paper, and (iv) Gra-5/1 after (a) 20 cycles of direct deposition/dissolution and (b) 30 cycles with Li foil covering on the upper surface at 0.5 mA cm^{-2} with a capacity of 3.5 mAh cm^{-2} .



Figure 6.15. The optical photograph shows the flexibility of Gra-5/1 after 100 cycles of deposition/dissolution in a full pouch cell.

To explore the stability of Gra-5/1 after cycling, we assembled Li||C coin half cells using commercial carbon cloth, CNTs film, graphene paper, and Gra-5/1, respectively, as CBCCs to make a comparison. Fig. 6.14a shows that carbon cloth, CNTs film, and graphene paper fragmented after cycling. Breakage of carbon cloth and CNTs film can

be ascribed to the fact that lithiated CBCCs are too stiff to endure the volume change of Li deposit, which deteriorates their mechanical strength. The toughness reduction in graphene sheets is probably due to the volume expansion caused by electrolyte infiltration. In contrast, intact Gra-5/1 can be maintained after cycling, strongly confirming that no intercalation behaviour and PVDF-induced electrolyte shield/structural reinforcement can maintain the mechanical strength of CBCCs.

Furthermore, CBCCs covered with Li foil were tested to investigate the stability of Gra-5/1 toward Li, as shown in Fig. 6.14b. Similarly, only Gra-5/1 can keep the most favourable mechanical strength and electrode integrity after 30 cycles with a capacity of 3.5 mAh cm^{-2} at 0.5 mA cm^{-2} due to the PVDF-induced sturdy structure and minimum Li^+ intercalation. Afterwards, the flexibility of cycled Gra-5/1 was verified by a simple bending process, as shown in Fig. 6.15. Results show that similar to the fresh Gra-5/1 (Fig. 6.6a), the cycled Gra-5/1 still maintains excellent flexibility after 100 cycles in a pouch cell, which elucidates that this free-standing graphene-based composite current collector is strong enough to endure the Li deposition/dissolution.

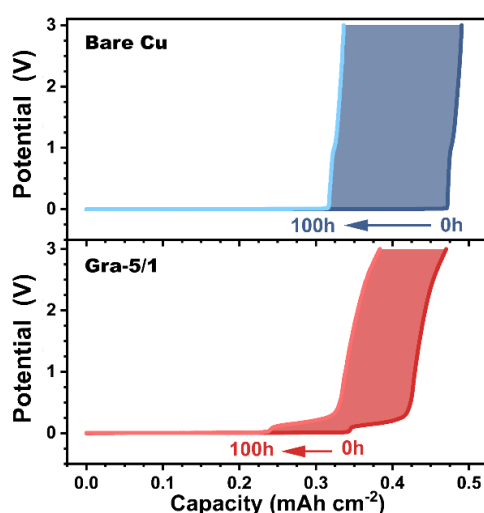


Figure 6.16. Potential profiles showing the capacity difference in comparison of galvanic corrosion before and after standing for 100h over the bare Cu and Gra-5/1 with plating Li at $0.01 \text{ mA cm}^{-2}/0.5 \text{ mA cm}^{-2}$ and stripping Li at 0.01 mA cm^{-2} .

The Li||Cu and Li||C coin half cells were assembled, respectively, to further confirm the galvanic corrosion between the metal-based current collector and electroplated Li in the presence of an electrolyte, which can result in Li dissolution and reduction of delivered capacity.²⁷⁵ The electroplated Li was allowed to stand for 0h and 100h before charging. Fig. 6.16 shows that after standing for 100 hours, the capacity of both cells declines significantly, revealing that there are obvious side reactions between electroplated Li and electrolyte. Furthermore, Gra-5/1-based cells perform lower capacity reduction (by ~30%) than Cu-based cells, which strongly verifies the application of Gra-5/1 can effectively avoid metal-induced corrosion behaviour. Therefore, the Gra-5/1 current collector has high stability and reliability toward electrolyte and LM, indicating that it can be applied in pouch cells.

6.3.3. SEI and Li deposit characterisations

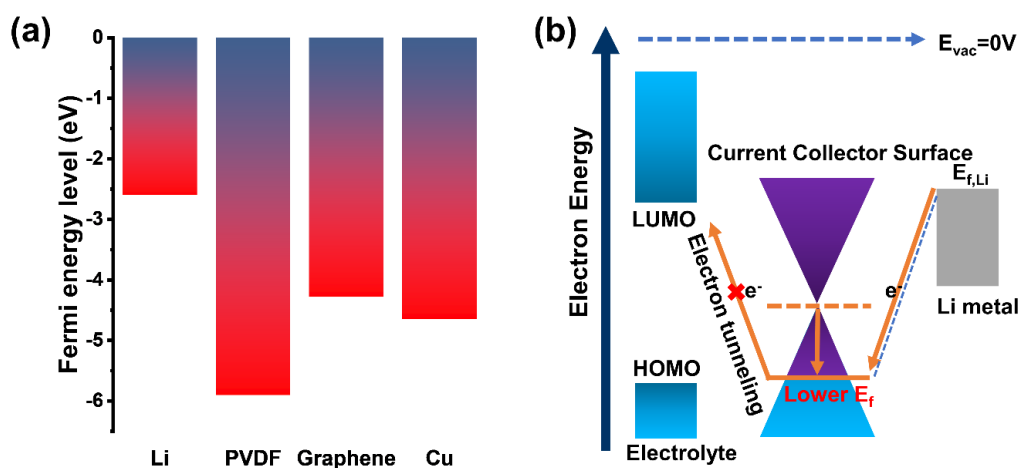


Figure 6.17. (a) Simulation result of Fermi energy level over Li, graphene, PVDF, and Cu. (b) Mechanism of lower Fermi level in suppressing electron transfer to the electrolyte on the Cu and Gra-5/1.

The property and composition of SEI have a strong effect on Li plating/stripping behaviours. Electronic insulation is one of the most important properties of SEI that can

prevent electrolyte reduction. It was reported that the electron insulating property of the SEI relies on the thickness (d) of SEI and Fermi level (E_f) of the electrode surface, as shown in equation (6.1):²⁹⁷

$$T = \frac{16E_f\Delta E_t}{(E_f+\Delta E_t)^2} e^{-\frac{4\pi d}{h}\sqrt{2m\Delta E_t}} \quad (6.1)$$

where T is the electron tunnelling probability for complete electron insulation (namely, $T = e^{-40}$),²⁹⁷ ΔE_t represents the electron tunnelling barrier, m is the mass of an electron, and h is Planck's constant. Thus, the calculation of E_f was conducted to investigate the SEI stability of graphene-based electrodes, especially toward electrolytes (Fig. 6.17a). Based on tunnelling theory in quantum mechanics, the disparity in the SEI thickness between Cu foil and Gra-5/1 can be clarified further. It is found that Li has the highest E_f of -2.65 eV,²⁹⁸ which is higher than graphene (-4.28 eV) and bare Cu (-4.65 eV).²⁹⁹,³⁰⁰ Thus, the electrolyte is easily reduced by Li via transferring electrons to the lowest unoccupied molecular orbital (LUMO) of the electrolyte. Notably, PVDF has the lowest E_f (-5.90 eV), reflecting that PVDF has the highest antioxidant capability. Fig. 6.3b shows that PVDF is mainly attached to the surface of Gra-5/1 in the form of a thin film. Thus, the E_f of the Gra-5/1 surface approximately equals the E_f of PVDF, which initially provides a relatively stable electrode interface. Equation (1) can be simplified as $T \sim e^{-d\sqrt{\Delta E_t}}$ through the Wentzel–Kramers–Brillouin approximation in quantum tunnelling theory.^{257, 297} It is found that since ΔE_t increases with decreasing E_f , lower E_f means that electro-insulation can be achieved with a smaller thickness of SEI. In other words, the electrode with lower E_f is more likely to suppress the electron tunnelling behaviour. Therefore, Gra-5/1 performs the best interfacial compatibility toward the electrolyte because it can suppress electron transfer to the LUMO of the electrolyte (Fig. 6.17b).²⁵⁷ Briefly, Gra-5/1 can alleviate electrolyte decomposition, limit SEI growth and facilitate the formation of excellent SEI owing to the lower E_f -induced reduced electron tunnelling probability.

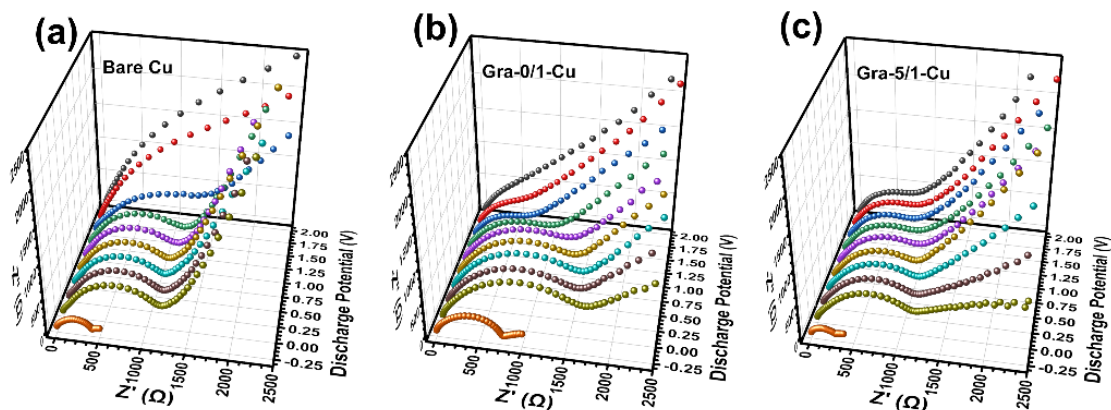


Figure 6.18. EIS evolution with discharging from 2V to -0.25V at 0.1 mV·s⁻¹ over (a) bare Cu, (b) Gra-0/1-Cu, and (c) Gra-5/1-Cu.

The EIS in the first plating process was measured to explore the SEI evolution on the fresh electrode of bare Cu, Gra-0/1-Cu, and Gra-5/1-Cu. As shown in Fig. 6.18a-c, there are three evident potential ranges (2 - 1.5 V, 1.5 - 0 V, and 0 - -0.25 V) in the Nyquist plots of bare Cu and Gra-0/1-Cu, implying that there are three glaring changes in SEI evolution during plating. In the range of 2 V - 1.5 V, the interfacial reaction gradually varies from the EDL behaviour to the pseudocapacitive-like behaviour, which reveals that the formation of initial SEI can break diffusion-limited behaviour on the surface of Cu and carbon.²⁷⁹ With potential decreasing to 0 V, the diameter of the semicircles in the high-frequency region of the Nyquist plots gradually increases, representing that R_{ct} is elevated. It is inferred that the precursor of SEI derived from the fast reaction between reduced Li^+ and electrolyte or adsorption of active cationic clusters probably hinders the Li^+ diffusion into the surface of the electrode and becomes densified.²⁸⁰ Finally, when the potential drops to -0.25 V, there is a sharp reduction in the R_{ct} , suggesting that the fast ion transportation channels are formed due to the formation of comparatively stable SEI. By contrast, only two distinct stages (2 - 0 V and 0 - -0.25 V) can be observed in Gra-5/1-Cu. The R_{ct} gradually increases when discharging to 0 V, implying that PVDF is involved in the Li^+ reduction process during the formation of initial SEI. Notably, the R_{ct} of Gra-5/1-Cu is the smallest among all electrodes when discharging to -0.25 V, revealing that PVDF plays a critical role in the evolution of

stable SEI.

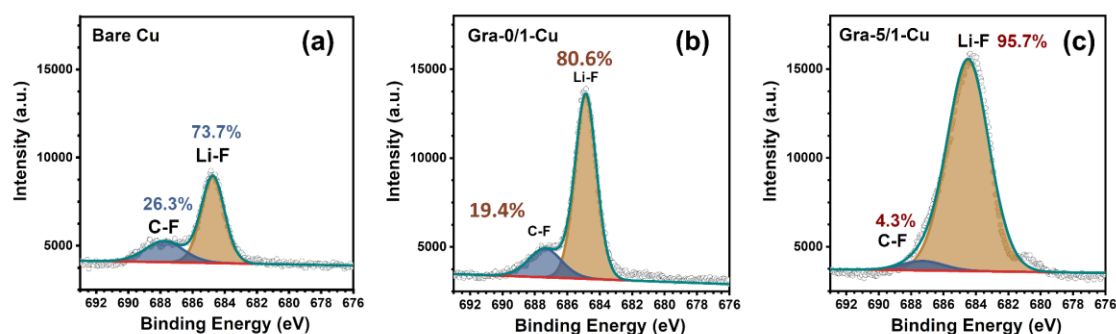


Figure 6.19. XPS spectra of the F 1s of plated 1 mAh cm^{-2} Li at 0.5 mA cm^{-2} on (a) bare Cu, (b) Gra-0/1-Cu, and (c) Gra-5/1-Cu.

XPS was further conducted to verify the SEI component in Cu foil and Gra-5/1-Cu with Li plating areal capacity of 1 mAh cm^{-2} . In F 1s spectra (Fig. 6.19a-c), Li-F and C-F signals are observed in all electrodes, resulting from the decomposition of FEC or LiPF_6 .²⁶² Li-F is well-known as an excellent SEI component owing to its high interfacial energy toward Li and high mechanical strength, which helps suppress Li dendrites. Thus, Li-F-rich SEI is more efficient for uniform Li deposition. According to the literature,^{244, 281} the Li-F components can be obtained by the *in-situ* reaction between Li and fluoropolymer (e.g., polytetrafluoroethylene or PVDF). Thus, it is inspired that the highest intensity of the Li-F signal (95.7%) in the Gra-5/1 implies partial PVDF as a film-forming polymer could be involved in the electrochemical deposition process and result in the formation of robust SEI. Li-F is also widely suggested to prevent electron tunnelling due to its low solubility and wide band gap (8.9 eV), which verifies that Gra-5/1 can suppress electron transfer to the electrolyte. In contrast, the lowest intensity of the Li-F signal (73.7%) for bare Cu confirms the formation of comparatively unstable SEI.

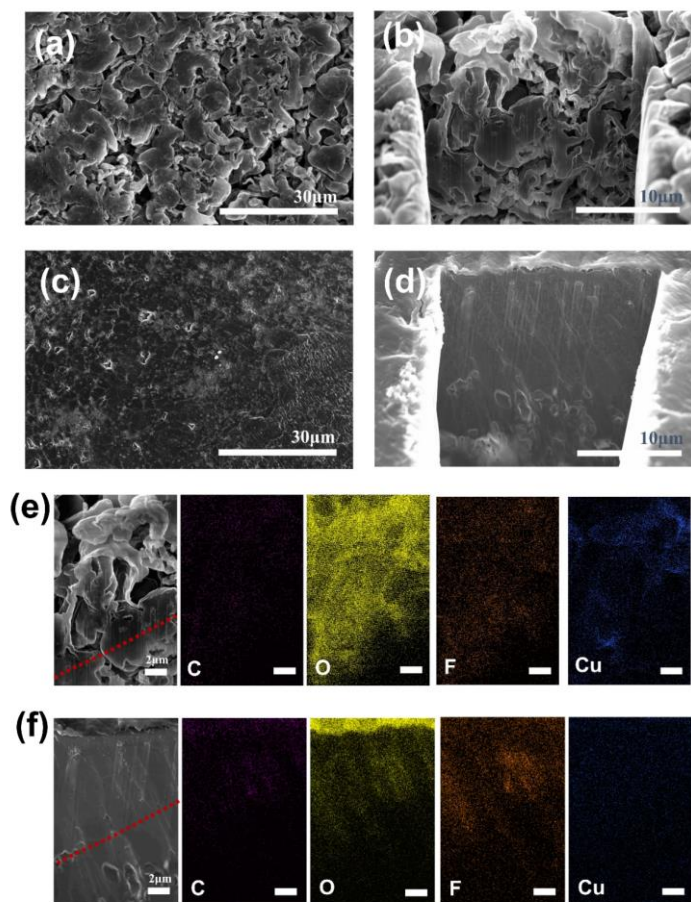


Figure 6.20. Top-view and cross-section view SEM images and corresponding EDS mapping for C, O, F, and Cu elements of (a, b, e) bare Cu, and (c, d, f) Gra-5/1-Cu with a plating areal capacity of 3 mAh cm^{-2} . The current density is 0.5 mA cm^{-2} .

Ex-situ FIB-SEM characterisation was further carried out to investigate the morphology of the deposited Li on bare Cu and Gra-5/1-Cu with a plating areal capacity of 3 mAh cm^{-2} (Li@Cu and Li@Gra-5/1-Cu) (Fig. 6.20a-d). Fig. 6.20a and Fig. 6.20b present that the porous and dendritic structure of electrodeposited Li is generated on bare Cu foil, which can accelerate the capacity attenuation in Cu-foil-based LMFRBs. Besides, remarkably thick SEI covering on porous dendrite-like Li is attributed to the uneven Li^+ deposition and electrolyte decomposition due to the SEI with a higher electron tunnelling probability, as well as the formation of by-products, resulting in poor cycling stability and a dramatic drop in CE.²³⁴ Related EDS mapping result (Fig. 6.20e) illustrates that F and C are subordinate, while O and Cu account for the two most

significant elements in Li@Cu. The high content of Cu strongly supports our previous claim that Cu can be easily electrochemically corroded during plating, while the strong signal of O (mainly originated from electrolyte decomposition) implies that Li dendrites accelerate the electrolyte decomposition and increase irreversible Li capacity. In striking contrast, Fig. 6.20c shows that Li particles tend to splice into dense and dendrite-free bulks on Gra-5/1-Cu, which can reduce the contact area between electrolyte and Li. The dense and dendrite-free cross-section view of Li plating can also be observed in Fig. 6.20d. More notably, the F element is comparatively dominant in the case of Gra-5/1-Cu (Fig. 6.20f), which highly supports that partial PVDF can be electrochemically reduced by Li to form extra Li-F. This finding is also in accordance with the XPS result in Fig. 6.19c. In addition, nearly no Cu element can be found in Li@Gra-5/1-Cu, which indicates that Gra-5/1 can effectively prevent Cu from electrochemical corrosion. The result above confirms our hypothesis that PVDF-induced favourable SEI and lower E_f -induced shielding of side reaction can achieve uniform dendrite-free Li deposit on Gra-5/1.

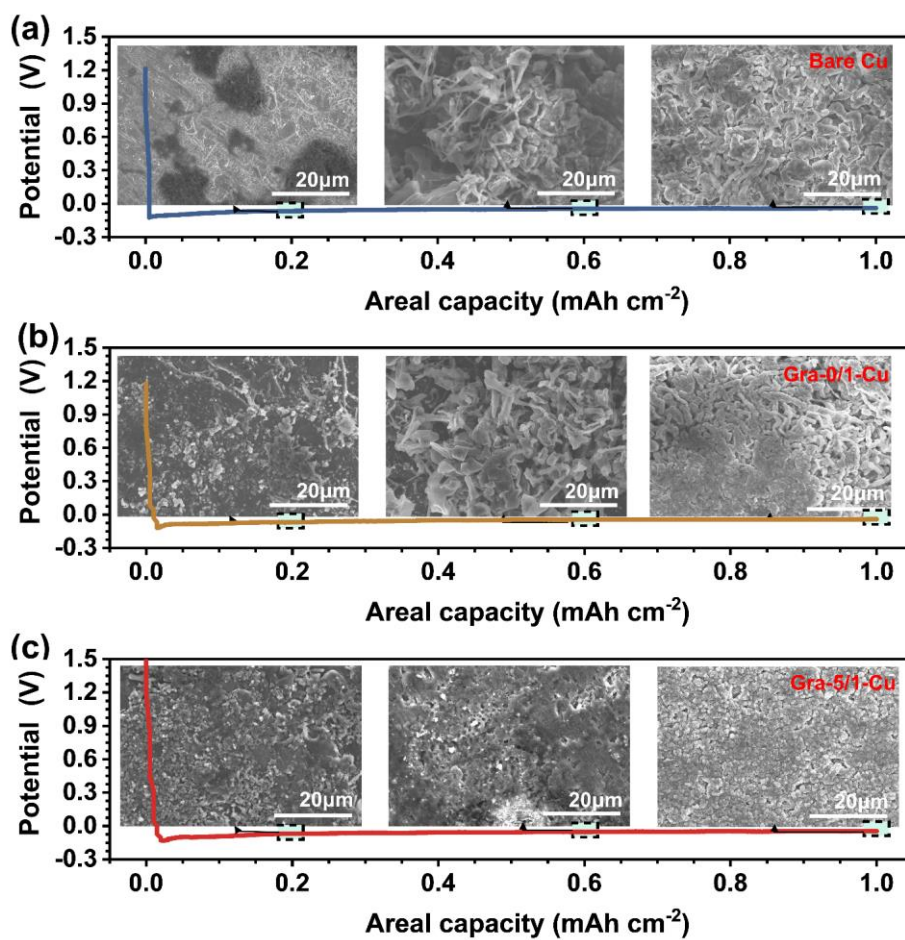


Figure 6.21. LM deposition morphology evolution with capacities from 0.2 to 1 mAh cm⁻² on the bare Cu and Gra-based electrodes. Top-view SEM images of the (a) bare Cu, (b) Gra-0/1-Cu, and (c) Gra-5/1-Cu electrode after plating with 0.2 mAh cm⁻², 0.6 mAh cm⁻² and 1.0 mAh cm⁻² of Li. The current density is 0.5 mA cm⁻².

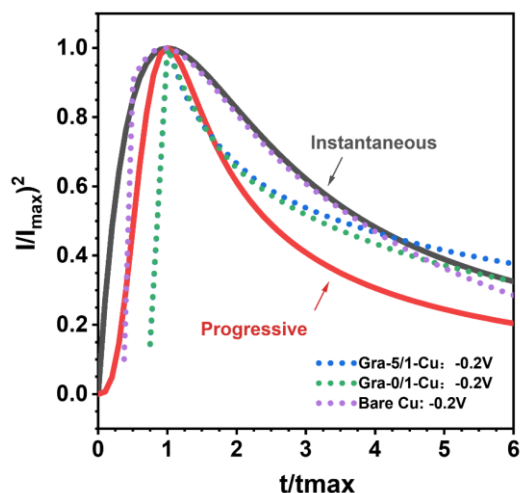


Figure 6.22. t/t_{\max} - $I/I(\max)^2$ plots of the fresh bare Cu, fresh Gra-0/1-Cu, and fresh Gra-5/1-Cu.

The basic interfacial electrochemical characterisation of the newly prepared electrode was carried out to explore the evolution of Li deposition, which plays an essential role in the following cycle. Fig. 6.21 exhibits morphology evolution during Li plating with capacities from 0.2 to 1 mAh cm⁻² on bare Cu foil, Gra-0/1-Cu, and Gra-5/1-Cu (Li@Cu, Li@Gra-0/1-Cu, and Li@Gra-5/1-Cu). As Li⁺ tends to deposit on spots with high electric strength, slender dendrite-like Li is easy to find (0.2 mAh cm⁻²) on bare Cu, as shown in Fig. 6.21a, due to the uneven electric field distribution of Cu foil. As a result, incomplete SEI can be formed owing to the non-uniform Li deposition and continuously attract Li⁺ to form local whisker protrusion (0.6 mAh cm⁻²). Furthermore, tips-effect²²⁷ also further intensifies the formation of dendrite-like Li. Finally, the mossy-type (whisker and dendrite) Li network can be observed when the plating capacity grows to 1 mAh cm⁻². Fig. 6.21b reveals that larger Li particles are observed on Gra-0/1-Cu than Cu foil. However, with discharging capacity increasing to 0.6 mAh cm⁻² or 1 mAh cm⁻², mossy-type (whisker and dendrite) Li networks still form due to the lack of robust SEI. Similar to Gra-0/1-Cu, Fig. 6.21c reveals that Li can horizontally grow with small particles with diameters of ~2 μm on Gra-5/1-Cu with a capacity of 0.2 mAh cm⁻². Li particles become crowded and spliced into a dense, dendrite-free

plane when the plating capacity increases. Fig. 6.22 demonstrates that the Gra-5/1-Cu follows the progressive nucleation form. While, Cu foil obeys instantaneous nucleation form,²⁸³ which confirms that Li intends to continuously grow on the formed nucleus in Gra-5/1 and grow into a whole.

In brief, Cu as a deposition substrate possesses a higher Fermi energy level and lower anti-corrosion toward air/electrolyte, which can further deteriorate the electric field distribution and hinder the establishment of stable SEI. Thus, it is not an appropriate current collector to deposit Li. Meanwhile, lacking film-forming polymer makes it more difficult to stabilise Li deposition. While Gra-5/1 with high anti-corrosion not only preferably guarantees a good deposition environment but also facilitates the formation of robust and electron-retarding SEI with the assistance of PVDF with the lowest Fermi energy level. Thus, extra electrolyte decomposition and Li inventory consumption can be impeded, resulting in uniform dendrite-free Li deposition.

6.3.4. Electrochemical performances of Graphene-based electrodes of half and full cells

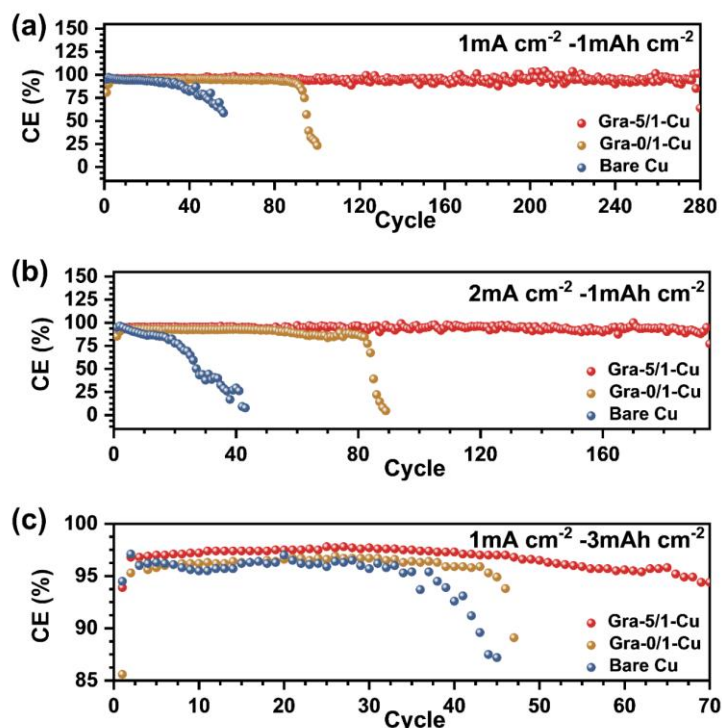


Figure 6.23. Comparison of CE of Li plating on/stripping with the capacity of 1 mAh cm⁻² at (a) 1 mA cm⁻² and (b) 2 mA cm⁻² and with the capacity of (c) 3 mAh cm⁻² at 1 mA cm⁻² over bare Cu, Gra-0/1-Cu, and Gra-5/1-Cu under ester-based electrolyte.

In this chapter, considering that ester-based electrolytes have a higher dielectric constant and better practical significance, electrolytes consisting of 1 M LiPF₆ in the mixture of FEC and DMC with 2 wt% FEC were used in all cells, and EC was eliminated to further improve the wettability of the electrolyte and stability.²³²

CE and long-term electrochemical stability of half cells containing different working electrodes (Cu foil and graphene-based electrodes) coupled with Li foil as the counter electrode was tested. Cu is not etched in the graphene-based electrodes to eliminate the influence of internal stress in the coin cells. Among all electrodes, Cu foil shows the most severe decay in CE, with current density varying from 1 mA cm⁻² to 2 mA cm⁻² at

1 mAh cm⁻² (Fig. 6.23a-b). With current density increasing from 1 mA cm⁻² to 2 mA cm⁻², CE of bare Cu drops rapidly from an average of ~94% for ~30 cycles to around 90% for only 10 cycles before significant dropping, which may be ascribed to the dramatic enhancement of internal resistance resulting from accumulated “dead Li” or uncontrolled Li-dendrite-induced electrolyte depletion (Fig. 6.20) due to the fragile SEI resulting from higher electron tunnelling probability. Gra-0/1-Cu keeps comparatively stable CE with an average of ~94.5% within 80 cycles at 1 mA cm⁻² with a capacity of 1 mAh cm⁻² (Fig. 6.23a), which implies that the high anti-corrosion ability of graphene and uniform electric field contribute efficaciously to improved Li deposition behaviour. However, apparent fading in CE is still found in Gra-0/1-Cu due to the lack of stable SEI film-forming polymer. In comparison, the Gra-5/1-Cu cell maintains the most stable CE with an average value of ~96% for more than 250 cycles at 1 mA cm⁻² and ~95% for around 100 cycles at 2 mA cm⁻² with a capacity of 1 mAh cm⁻² (Fig. 6.23a-b). A larger deposition capacity (3 mAh cm⁻²) was employed to test their practical application in full cells (Fig. 6.23c). Gra-5/1-Cu still exhibits superior cycling performance at 1 mA cm⁻² with the highest CE (~98%).

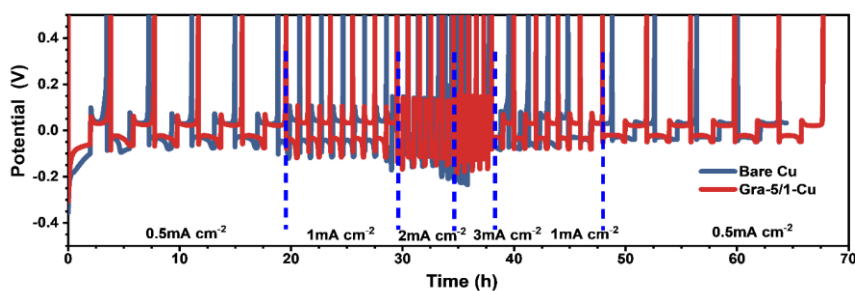


Figure 6.24. Comparison of Li plating/stripping potential profiles on Cu foil and Gra-5/1-Cu at different current densities ranging from 0.5 to 3 mA cm⁻² with 1 mAh cm⁻².

Potential hysteresis and reversibility were studied using bare Cu foil and Gra-5/1-Cu in half cells (Fig. 6.24). The potential hysteresis of Gra-5/1-Cu only grew from ~25 mV to ~70 mV, with current density increasing from 0.5 to 3 mA cm⁻². In contrast, Cu foil

shows dramatic hysteresis change by ~ 200 mV. The above results ultimately prove that the Gra-5/1 electrode can actively form excellent SEI and mitigate the side reactions to stabilise Li deposition.

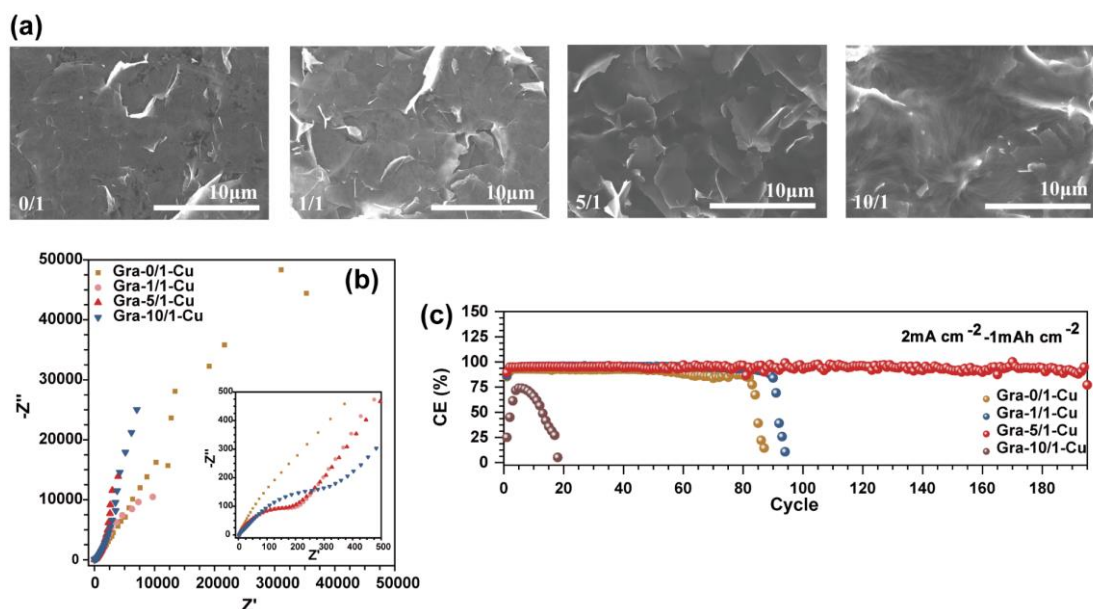


Figure 6.25. (a) Top-view SEM images, (b) EIS, and (c) related CE of Li plating on/stripping with the capacity of 1 mAh cm^{-2} at 2 mA cm^{-2} over fresh Gra-X/1-Cu ($X = 0, 1, 5,$ and 10).

A comparison of cycling lifetime on graphene-based current collectors with different PVDF contents (Gra-X/1 ($X = 0, 1, 5,$ and 10)) is shown in Fig. 6.25a-c. Augmented R_{ct} elucidates that the interaction between Li^+ and PVDF is enhanced due to the increasing proportion of PVDF (Fig. 6.25b), which is consistent with the resistance results (Fig. 6.9). The results of cycling lifetime in Fig. 6.25c show that, with PVDF content growing (within 0-5), cycling lifetime is efficiently prolonged, and CE value is improved in graphene-based electrodes. Nevertheless, when PVDF content is further increased (Gra-10/1-Cu), the worst cycling lifetime and the lowest CE value can be found, confirming that too much PVDF can hinder Li^+ reduction and substantially affect the electrochemical performance of the cell due to the high resistance (Fig. 6.9). Fig. 6.25c also illustrates that Gra-5/1-Cu maintains the highest CE value among all

graphene-based electrodes, which indicates that the mass ratio of PVDF/graphene=5/1 is probably the best proportion to achieve the dendrite-free and high reversible Li deposit owing to the comparably appropriate interface impedance and electronic conductivity of the material. Low impedance may lead to a high reaction rate, easily resulting in Li dendrite as a result of a diffusion-limited rate. By contrast, high impedance usually gives rise to a reaction-limited rate. Although a lower reaction rate can distribute Li ions evenly on the surface of the electrode, a large amount of PVDF can highly enhance the barrier of Li⁺ redox, leading to enhanced internal resistance and great energy consumption. Thus, comparatively appropriate impedance is key to balancing reaction-limited and diffusion-limited rates for Gra-5/1.

Another possible point is relevant to the electronic conductivity of the material. Fig. 6.10 shows that when the PVDF/graphene mass ratio reaches 10 (Gra-10/1), the resistance increases sharply to about 138 Ω . Fig. 6.25a shows that graphene materials are almost entirely covered by PVDF on Gra-10/1, revealing conductive areas are highly shielded by PVDF. This condition is also similar to the Cu@PVDF electrode (Fig. 5.26). During only several cycles, this limited conductive area can be gradually blocked by accumulated isolated “dead Li”, leading to the lowest CE. A similar electrochemical performance of Cu@PVDF can also be found in Fig. 5.26.

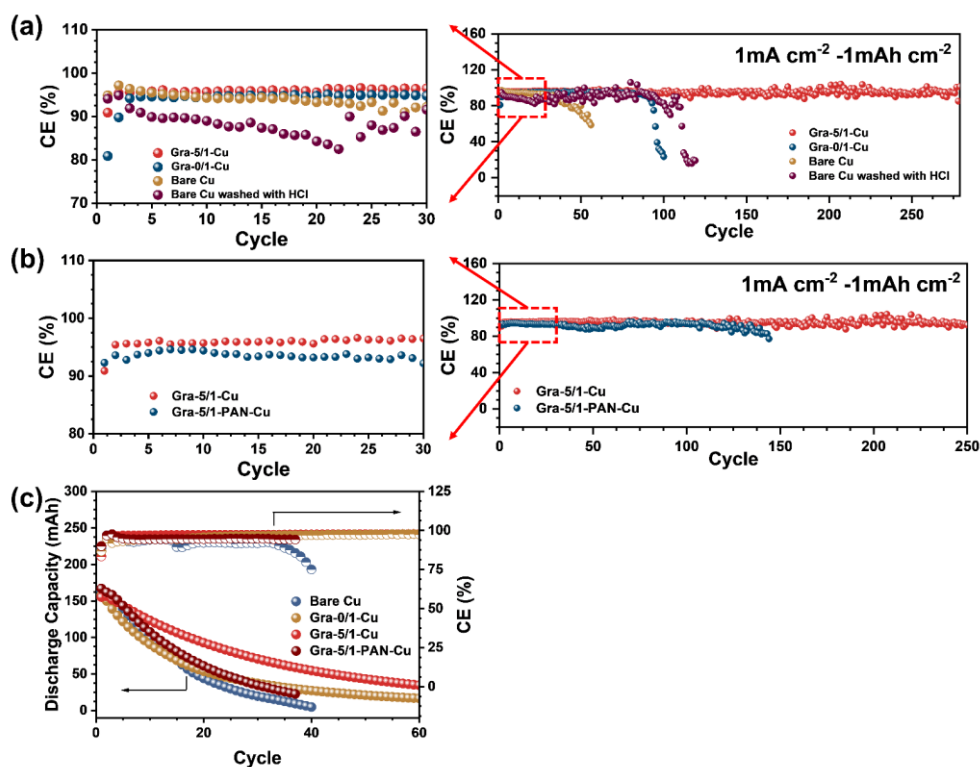


Figure 6.26. Comparison of CE of Li plating on/stripping with 1 mAh cm^{-2} at 1 mA cm^{-2} over (a) bare Cu, Gra-0/1-Cu, Gra-5/1-Cu, and Cu foil washed with HCl and (b) over Gra-5/1-Cu and Gra-5/1-PAN-Cu. (c) Cycling performance of pouch cell assembled with Cu foil, Gra-0/1-Cu, Gra-5/1-Cu, and Gra-5/1-PAN-Cu current collectors and high areal capacity NCM 811 positrodes ($\sim 4 \text{ mAh cm}^{-2}$).

To clarify the effect of copper oxide or hydroxide which comes from a side reaction between air and Cu on the surface of bare Cu on the cycling performance, the Li||Cu cell was assembled using Cu foil washed with HCl. Fig. 6.26a shows the cycling lifetime is prolonged, but the CE of the initial cycle for the washed Cu is drastically reduced to 85%. Thus, such a poor CE indicates that the limited active Li in LMFRBs will be significantly consumed by washed Cu. It also verifies the fact that poor cycling of Cu foil is due to the lack of robust and insulating SEI, other than surface contaminant only. In addition, compared with Gra-0/1-Cu, higher initial CE can be found in Gra-5/1-Cu, strongly confirming that PVDF can prevent Li^+ from entering the internal area of Gra-5/1 and decrease the formation of initial irreversible Li. The graphene-based

current collector using PAN instead of PVDF was prepared (Gra-5/1-PAN-Cu) to explore further the polymer's function (Fig. 6.26b). The Gra-5/1-PAN-Cu also achieves a relatively long cycling lifetime (>140 cycles). However, the CE within the first 30 cycles is lower than Gra-5/1 by ~3%, confirming that PVDF is an ideal film-forming additive.

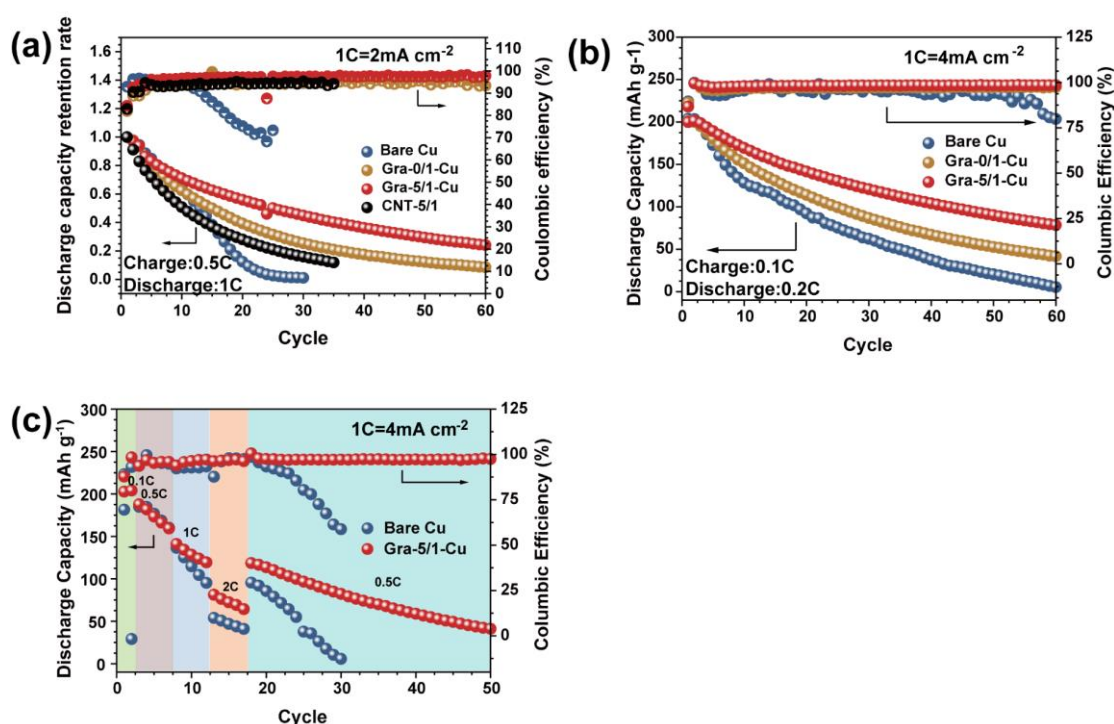


Figure 6.27. (a) Cycling performance of LM-free coin full cell assembled with bare Cu, Gra-0/1-Cu, Gra-5/1-Cu, and CNT-5/1 with an areal capacity of $\sim 2\text{ mAh cm}^{-2}$. (b) Cycling performance of full cells assembled with bare Cu, Gra-0/1-Cu, and Gra-5/1-Cu with an areal capacity of $\sim 4\text{ mAh cm}^{-2}$. (c) The rate capability of full cells assembled with bare Cu and Gra-5/1-Cu from 0.1 C to 2 C with an areal capacity of $\sim 4\text{ mAh cm}^{-2}$.

To evaluate the performance of Gra-5/1-Cu in full cells, long-term cycling and rate performance of coin full cells assembled with bare Cu foil or Gra-0/1-Cu or Gra-5/1-Cu and LiFePO₄ ($\sim 2\text{ mAh cm}^{-2}$) (Fig. 6.27a) or NCM 811 ($\sim 4\text{ mAh cm}^{-2}$) positrode (Fig. 6.27b-c) were tested. Fig. 6.27a shows that the capacity retention of the LFP-based full cell composed of Cu foil undergoes a sharp drop to less than 15% after only 20

cycles. A slightly improved cycling stability of 45% capacity retention at 20 cycles with a mitigated capacity fade rate was obtained with Gra-0/1-Cu, likely due to the more uniform electric field distribution. In contrast, the cycling stability of the LMFRBs was dramatically improved to ~65% capacity retention after 20 cycles with Gra-5/1-Cu, demonstrating its efficacy in stabilizing the Li deposition/dissolution in a full cell. In addition, the capacity retention of Gra-5/1-Cu is always higher than that of CNT-5/1 during cycling, verifying CNTs can induce more capacity loss because of large electrochemically reactive surface area. Similarly, the Cu and Gra-0/1-Cu-based full cells show significantly fast capacity fade to ~45% and ~57% capacity retention, respectively, with an areal capacity of 4 mAh cm⁻² (Fig. 6.27b). By striking contrast, Gra-5/1-Cu still maintains the highest capacity retention of ~71%. Gra-5/1-Cu also performs better rate capability than bare Cu foil, as illustrated in Fig. 6.27c. Especially at a high rate of 2 C, the cell using Gra-5/1-Cu still delivers a high specific capacity of ~76.9 mAh·g⁻¹, much higher than that of a bare Cu foil cell (~46.9 mAh·g⁻¹). The higher discharge capacity at high rates is ascribed to the PVDF-induced stable SEI and uniform Li deposition.

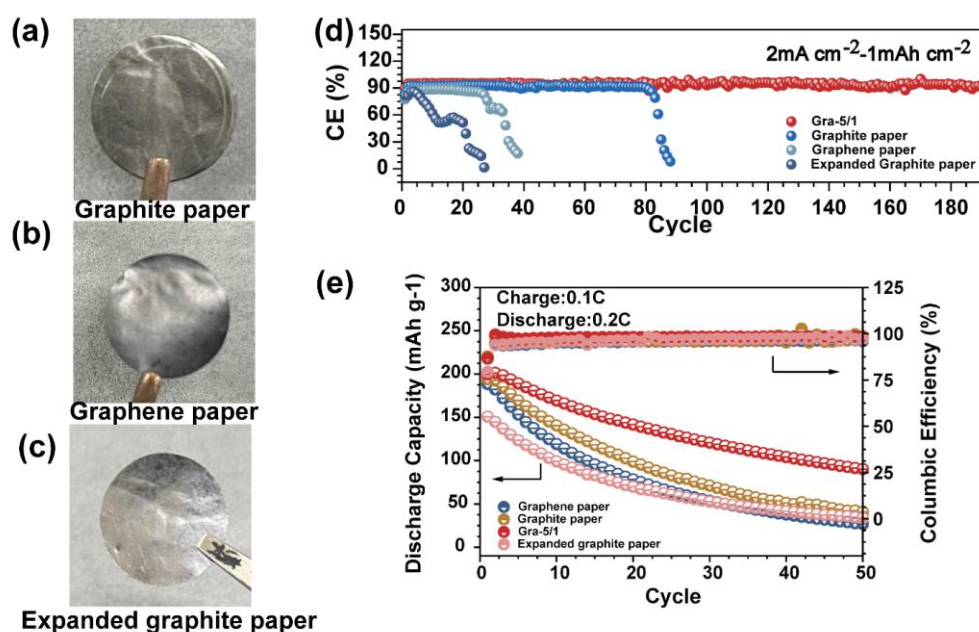


Figure 6.28. Optical photograph of the fresh (a) graphite paper, (b) graphene paper, and

(c) expanded graphite paper. (d) Comparison of CE of Li plating on/stripping with 1 mAh cm^{-2} at 2 mA cm^{-2} over the Gra-5/1, graphite paper, graphene paper, and expanded graphite paper. (e) Cycling performance of coin full cell assembled with Gra-5/1, graphite paper, graphene paper, and expanded graphite paper current collectors and high areal capacity NCM 811 positrodes ($\sim 4 \text{ mAh cm}^{-2}$).

To further investigate the advantage of Gra-5/1 as a CBCC in Li deposition/dissolution, coin half/full cells were assembled using graphite paper, graphene paper, and expanded graphite paper as pristine 2D CBCCs with no PVDF (Fig. 6.28a-c). Fig. 6.28d shows that the cell with Gra-5/1 delivers the longest cycling lifetime (>180 cycles) and the highest CE with 1 mAh cm^{-2} at 2 mA cm^{-2} . Meanwhile, the cell with Gra-5/1 achieves the highest capacity retention after 50 cycles, as shown in Fig. 6.28e. Thus, Gra-5/1 can achieve the *in-situ* construction of the favourable SEI and facilitate the Li deposition/dissolution with the help of PVDF.

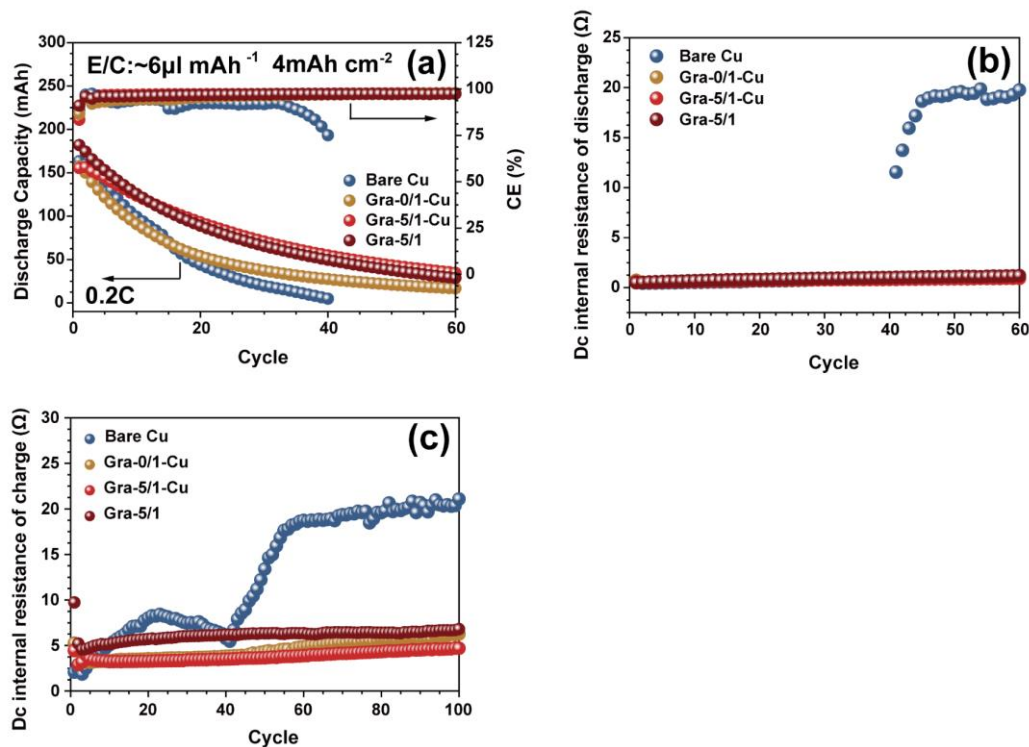


Figure 6.29. (a) Cycling performance and *in-situ* (b) discharge and (c) charge internal

resistance profiles of pouch cells assembled with bare Cu, Gra-0/1-Cu, Gra-5/1-Cu, and Gra-5/1 and high areal capacity NCM 811 positrodes ($\sim 4 \text{ mAh cm}^{-2}$).

To further verify the practical applicability of the Gra-5/1 as the CBCC, we assembled pouch cells by using an NCM811 positrode with a high areal capacity ($\sim 4 \text{ mAh cm}^{-2}$) with a designed capacity of $\sim 0.16 \text{ Ah}$ and normal ester-based electrolyte mass of $\sim 0.96 \text{ g}$ (Fig. 6.29a). Cu foil||NCM 811 cells show the fastest capacity retention and CE decay within the first 40 cycles at 0.2 C, while both Gra-5/1-Cu and Gra-5/1||NCM 811 cells can maintain similar capacity change and the highest capacity retention within the first 40 cycles under the same condition, which confirms the fact that Cu substrate does not affect the electrochemical behaviour of Gra-5/1. The Gra-5/1-PAN-Cu||NCM 811 pouch cells were also assembled, which display much worse capacity retention than PVDF-based Gra-5/1-Cu within 40 cycles (Fig. 6.26c), verifying that PVDF is an ideal film-forming additive. Fig. 6.29b-c compares the internal resistances of pouch cells during cycling, which are *in-situ* monitored to demonstrate the electrochemical resistances of cells during cycling. In the first 40 cycles, the internal discharge resistance of Cu foil||NCM 811, Gra-0/1-Cu||NCM 811, Gra-5/1-Cu||NCM 811, and Gra-5/1||NCM 811 pouch cells show a similar rising trend (increasing from ~ 0.6 to $\sim 1 \Omega$). Nevertheless, the internal discharge resistance of Cu foil||NCM 811 cell suffers from a dramatic increase to $\sim 20 \Omega$ after 50 cycles, while other cells only gradually rise to $\sim 1.1 \Omega$ after 50 cycles. It is because increasingly accumulated “dead Li” on Cu foil can result in soaring internal resistance. What’s more, Fig. 6.29c shows that the PVDF-induced resistance can be forcefully alleviated after the activation procedure, possibly owing to the formation of crystal seed. Thus, the internal resistance of pouch cells cannot be highly affected due to the introduction of PVDF.

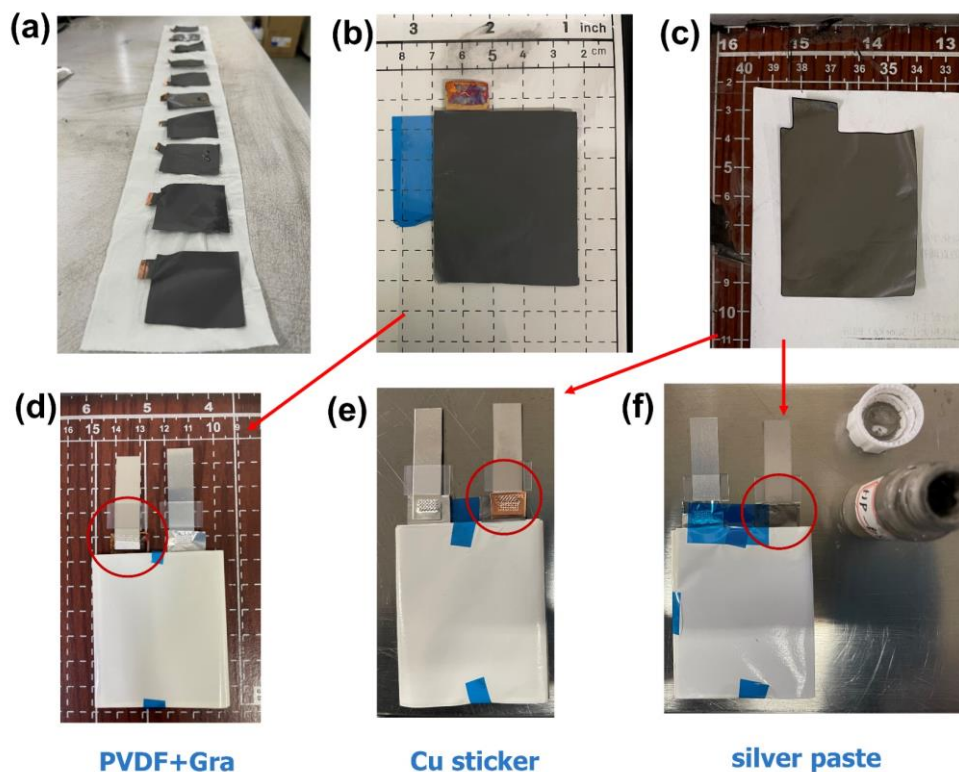


Figure 6.30. Optical photograph of (a) large-scale production of Gra-5/1 and (b) related pouch cell scale electrode (47 mm × 57mm). (c) Optical photograph of graphite paper in pouch cell. Optical photograph of welding condition over the (d) Gra-5/1 and graphite paper using (e) Cu sticker and (f) silver paste.

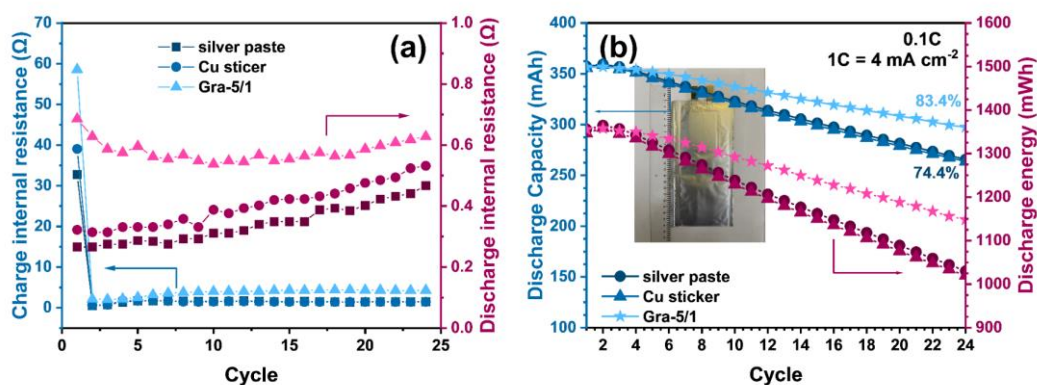


Figure 6.31. (a) *in-situ* charge and discharge internal resistance profiles and (b) cycling performance of pouch cell assembled with Gra-5/1 and graphite paper current collectors using silver and Cu sticker for the welding process and high areal capacity NCM 811 positrodes ($\sim 4 \text{ mAh cm}^{-2}$).

Based on the above-suggested tab welding technique on carbon materials (Fig. 6.10), the related carbon-based pouch cells are assembled to test their practical operation condition, as shown in the preparation procedure in Fig. 6.30. Fig. 6.31a shows that the carbon-based pouch cells do not suffer from dramatic internal resistance during cycling after the activation procedure, verifying that the above tab welding technology is suitable for the multi-layer CBCCs in the pouch cell. Furthermore, Fig. 6.31b reveals that Gra-5/1 maintains the highest capacity retention of 83.4% after 24 cycles. In comparison, graphite paper only keeps 74.5% capacity retention, demonstrating that the PVDF can efficaciously facilitate the formation of favourable SEI. Overall, it is worthy of further widening the application of CBCCs in the practical application of LMRBs due to the acceptable charge and discharge internal resistance of the above-suggested tab welding technology.

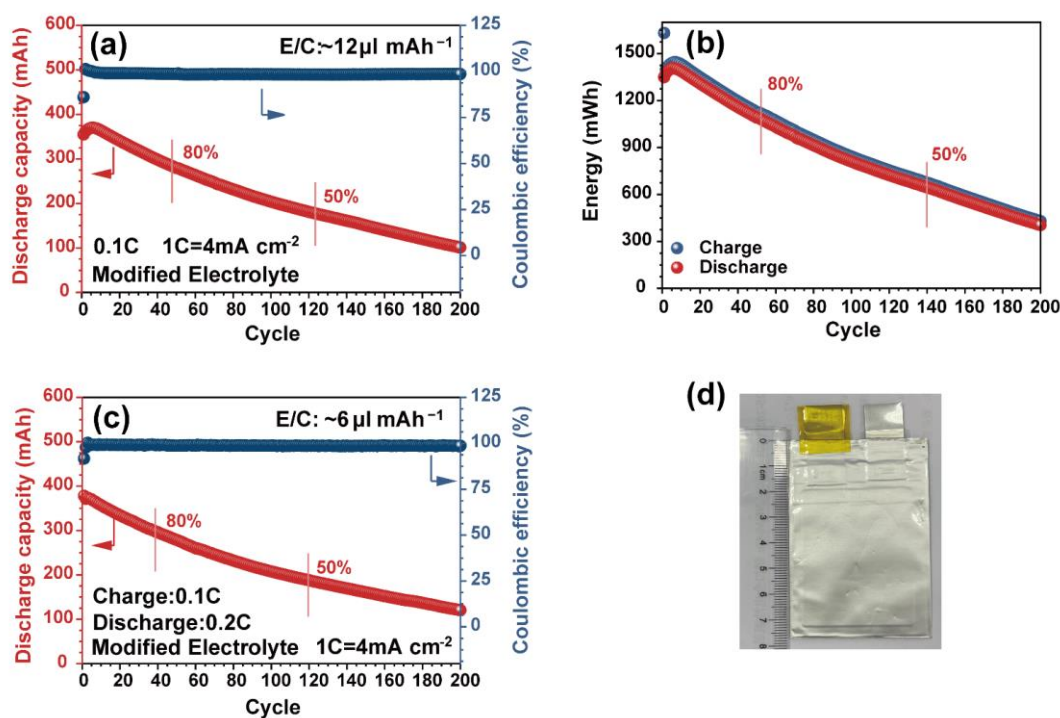


Figure 6.32. The discharge capacity and Charge and discharge energy profiles of a pouch cell assembled with Gra-5/1 and high areal capacity NCM 811 positrodes ($\sim 4 \text{mAh cm}^{-2}$) using the modified (a) and (b) rich electrolyte ($E/C: \sim 12 \mu\text{l mAh}^{-1}$) and (c)

lean electrolyte (E/C: $\sim 6 \mu\text{l mAh}^{-1}$); (d) Optical photo of the pouch cell.

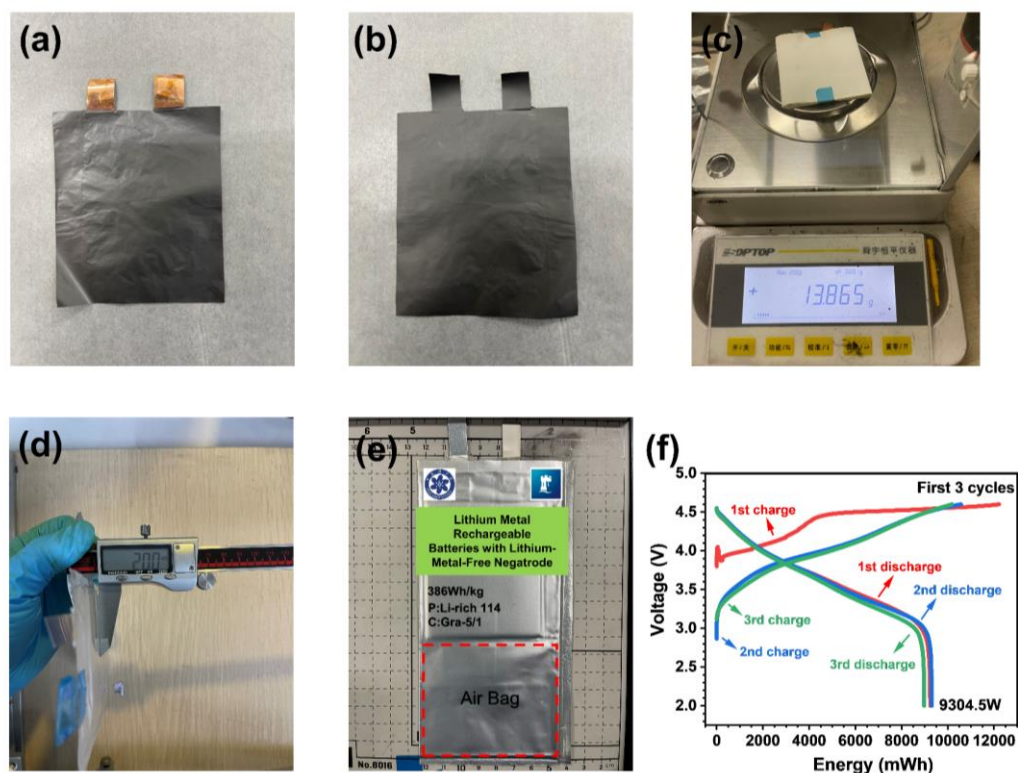


Figure 6.33. Optical photographs of the (a) front and (b) back surface of Gra-5/1 current collector ($64 \text{ mm} \times 74 \text{ mm}$) used in pouch cells. (c) The mass of the naked pouch cell without packaging, and (d) the thickness, (e) appearance, and (f) the voltage profile for the first 3 cycles of the pouch cell assembled with Gra-5/1 and high areal capacity LR-114 positrodes ($\sim 6 \text{ mAh cm}^{-2}$).

To further improve the electrochemical performance of Gra-5/1 in LMFRBs, we assembled pouch cells by using an NCM811 positrode with a capacity of $\sim 4 \text{ mAh cm}^{-2}$ with a designed initial capacity of $\sim 0.38 \text{ Ah}$. we applied local high-concentration electrolytes (TTE as diluent) as a modified electrolyte design (electrolyte to capacity ratio (E/C) of $\sim 12 \mu\text{l mAh}^{-1}$). Local high-concentration electrolytes can reduce contact between Li and solvent.^{238, 301} Also, TTE can decrease the side reaction between Li and solvent and meanwhile ensure the wettability of the electrolyte. LiFSI as high chemical stability lithium salt is dissolved in DMC (molar ratio of 3:4) to further widen the

window of voltage. Also, 1wt% LiDFOB and FSI⁻ contribute to forming excellent SEI containing Li-F and robust CEI on the LMNE and the positrode. Fig. 6.32a-b shows that the pouch cell with Gra-5/1 delivers 79% capacity retention and 81% energy retention after 50 cycles, respectively. Fig. 6.32c-d illustrates that Gra-5/1 still performs 80% capacity retention after 40 cycles, even at the lean electrolyte condition ($\sim 6 \mu\text{L mAh}^{-1}$). The 2.6 Ah level multi-layer LMFRBs with high specific energy and energy density (386 Wh/kg and 927.5 Wh/L) were assembled where LR-NCM 114 positrode (6 mAh cm^{-2}) with a size of 62 mm \times 72 mm paired with Gra-5/1 (64mm \times 74mm) (Fig. 6.33 and Table 6.1). The pouch cell achieves the discharge energy of 9.3 Wh, demonstrating that Gra-5/1 possesses excellent potential in the practical application of LMFRBs.

Table 6.1. Pouch cell details assembled with Gra-5/1 and high areal capacity LR-114 positrodes ($\sim 6 \text{ mAh cm}^{-2}$).

Items	Parameter
Pieces of the positrode	5
Pieces of Gra-5/1	6
Mass of cell stack/g	13.865 g
Mass of electrolyte (2.4g/Ah)/g	6.43 g
Total mass (no gas bag)/g	24.103 g
Total capacity/Ah	2.601 Ah
Total energy/Wh	9.3045 Wh
The specific energy of cell stack (with electrolyte)/Wh/kg	458.46Wh/kg

The specific energy (no gas bag)/Wh/kg	386Wh/kg
The energy density (no gas bag) /Wh/L	927.5Wh/L

6.3.5. Failure analysis of Graphene-based electrodes

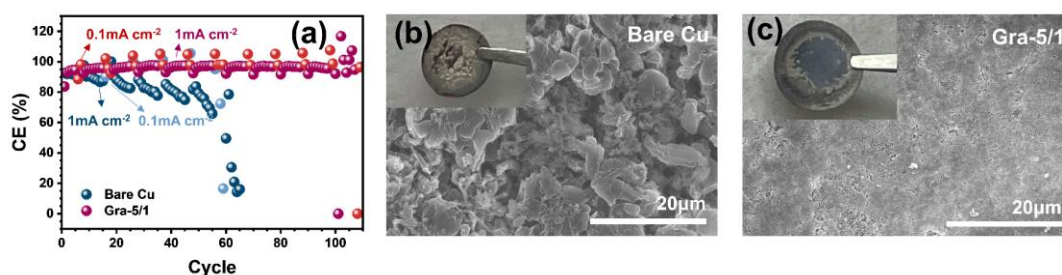


Figure 6.34. (a) CE of Li plating on/stripping with 1 mAh cm⁻² at 1/0.1 mA cm⁻² over Cu foil and Gra-5/1 under lean electrolyte conditions (~20 μL). Top-view SEM images of (b) bare Cu and (c) Gra-5/1 after 30 cycles with 1 mAh cm⁻² at 2 mA cm⁻². Inset (b) and (c) shows the optical photograph of cycled Cu and Gra-5/1.

Failure analysis on Cu foil and Gra-5/1-based batteries were conducted to understand their failure mechanism. Generally, there are three main causes for the failure of LMRBs: 1. depletion of electrolyte; 2. dramatic increase of the internal impedance due to the accumulation of “dead Li”; 3. loss of Li inventory.³⁰² For LMFRBs, the loss of Li inventory is accompanied by two possible factors (1. formation of by-products (such as SEI) caused by the reaction between Li and the electrolyte and 2. formation of “dead Li” which originates from the fracture of Li dendrites during dissolution) usually leads to serious capacity degradation.³⁰² Therefore, Li||Cu or Li||C half cells with lean electrolyte (~20 μL) and unlimited Li source were assembled to distinguish between factors 1 and 2. Meanwhile, different current densities were applied to control the Li⁺ diffusion rate. Fig. 6.34a shows that the CE of Cu foil decreases obviously after 20 cycles, but after applying a small current density, the CE rises back. The Cu foil also

exhibits a similar downward trend as shown in the flooded electrolyte condition (Fig. 6.23a). Then, when a larger current density is applied again (1 mA cm^{-2}), the downward trend of CE does not stop, demonstrating increasing internal resistance is the main factor that causes capacity decay. This growing internal impedance is probably caused by the continuous accumulation of “dead Li”. For the Gra-5/1, the CE fluctuates regularly with the increase or decrease of the current density in the first 100 cycles, but after 100 cycles, the current density has almost no effect on the CE, and the CE fluctuates violently. While Gra-5/1 can run for more than 250 cycles in the flooded electrolyte condition (Fig. 6.23a). Thus, this indicates that electrolyte depletion may be the main cause of the battery failure. This electrolyte depletion is highly ascribed to the formation of by-products for the Gra-5/1.

In summary, for LMFRBs, the loss of Li inventory in Cu-based cells is mainly because of the formation of “dead Li”, while the loss of Li inventory in Gra-5/1-based cells is mainly due to the generation of by-products. As is expected, when the Li source is sufficient, in the lean electrolyte condition, the accumulation of “dead Li” is still the main reason for the failure of the Cu-based half cell, and the failure of the Gra-5/1-based half cell is more likely due to the depletion of the electrolyte. These results also confirm that Li dendrite can be efficaciously alleviated on Gra-5/1. Morphology of bare Cu and Gra-5/1 after 30 cycles (Fig. 6.34b-c) with an areal capacity of 1 mAh cm^{-2} at 2.0 mA cm^{-2} was characterised. Apparent dendrite-like and porous “dead Li” is confirmed on the bare Cu, contributing to increased internal resistance and dramatic capacity fading. In solid comparison, only little bulk-like and dense “dead Li” is discerned in Gra-5/1 after 30 cycles, verifying depletion of electrolyte (lean electrolyte) or the formation of by-product (flooded electrolyte) could be more tightly related to the capacity decay.

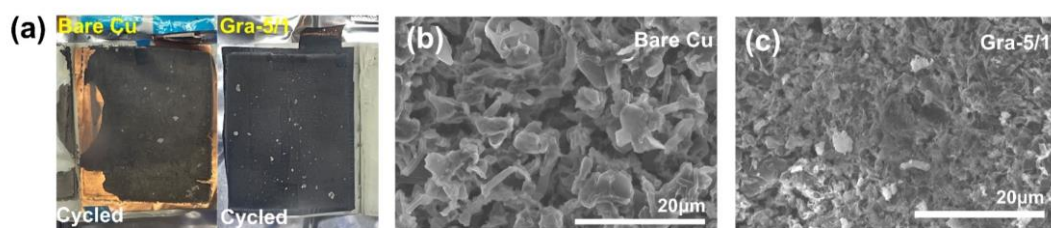


Figure 6.35. (a) The optical photographs of bare Cu and Gra-5/1, and top-view SEM images of the (b) bare Cu and (c) Gra-5/1 after 100 cycles in pouch cells.

The morphology of bare Cu and Gra-5/1 after cycling was characterised to clarify how they lose their capacity in pouch cells, as illustrated in Fig. 6.35a-c. Fig. 6.35a shows that cleaner and fewer by-products/“dead Li” can be found in the Gra-5/1 after 100 cycles compared with Cu foil, proving that PVDF-induced robust SEI can impressively suppress the generation of Li dendrites. The bare Cu and Gra-5/1 were investigated further via SEM. In the LMFRBs, the electrochemically inactive Li species (irreversible capacity) are mainly composed of “dead Li” and by-products. Fig. 6.35b confirms that the irreversible capacity of Cu-based pouch full cell is mainly ascribed to the formation of “dead Li”. While considering the high CE of Li||C coin cell (Fig. 6.23c) and reduced “dead Li” (Fig. 6.35c), the loss of capacity of the Gra-5/1-based pouch full cell is probably due to the by-products and the generation of a small part of “dead Li”. Thus, in the practical application, Gra-5/1 contributes to the improvement of cycling performance mainly due to the PVDF-triggered robust SEI alleviating the formation of Li dendrite. How to decrease the by-products/side reaction between Li and electrolyte, especially under lean electrolyte conditions, is the main challenge for Gra-5/1.

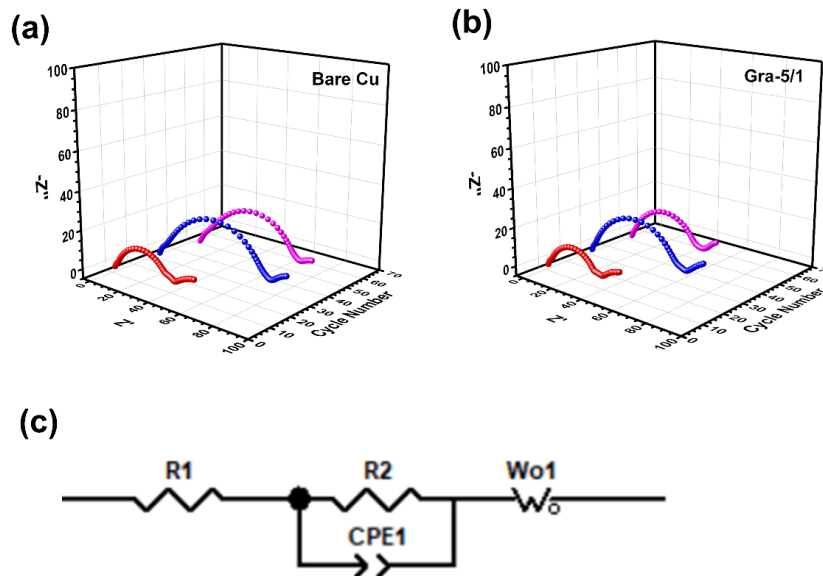


Figure 6.36. EIS of (a) the bare Cu and (b) Gra-5/1 after 10, 30, and 50 cycles with an areal capacity of 1 mAh cm^{-2} at 2 mA cm^{-2} . (c) applied fitting resistance model: R1:R0 (Ohmic resistance); R2: R_{SEI} (Migration resistance of Li^+ through the SEI); Wo1: Warburg (Li^+ diffusion resistance); CPE1/CPE2: Constant phase element (Conventional double-layer and passivation film capacitance)

Electrochemical performance is firmly determined by the electrode materials' stability of SEI. SEI properties such as conductivity and composition on the Gra-5/1 were further collected via EIS (Fig. 6.36) and XPS (Fig. 6.37-6.38) characterisation after cycling. Compared with the bare Cu foil, smaller semicircles in the high-frequency region are obtained in Gra-5/1 after 10, 30, and 50 cycles (Table 6.2), reflecting that the SEI formed on Gra-5/1 possesses a smaller interface impedance and a smaller R_{ct} than that of the Cu foil. The closer frequency may coincide with SEI resistance (R_{SEI}) and R_{ct} . This result confirms that introducing PVDF can facilitate stable SEI formation with low resistance during Li deposition/dissolution. While higher resistance in SEI formed on Cu foil also renders a negative effect on its electrochemical performance.

Table 6.2. Fitting resistance data of the galvanostatic plating/stripping in symmetrical cells using Gra-5/1 or Cu foil with an areal capacity of 1.0 mAh cm^{-2} at 2 mA cm^{-2} .

Sample	R1 (Ω)	R2 (Ω)
Gra-5/1-10 th	3.035	34.37
Bare Cu foil-10 th	2.953	38.57
Gra-5/1-30 th	4.336	59.28
Bare Cu foil-30 th	5.188	72.3
Gra-5/1-50 th	5.335	45.07
Bare Cu foil-50 th	7.493	64.84

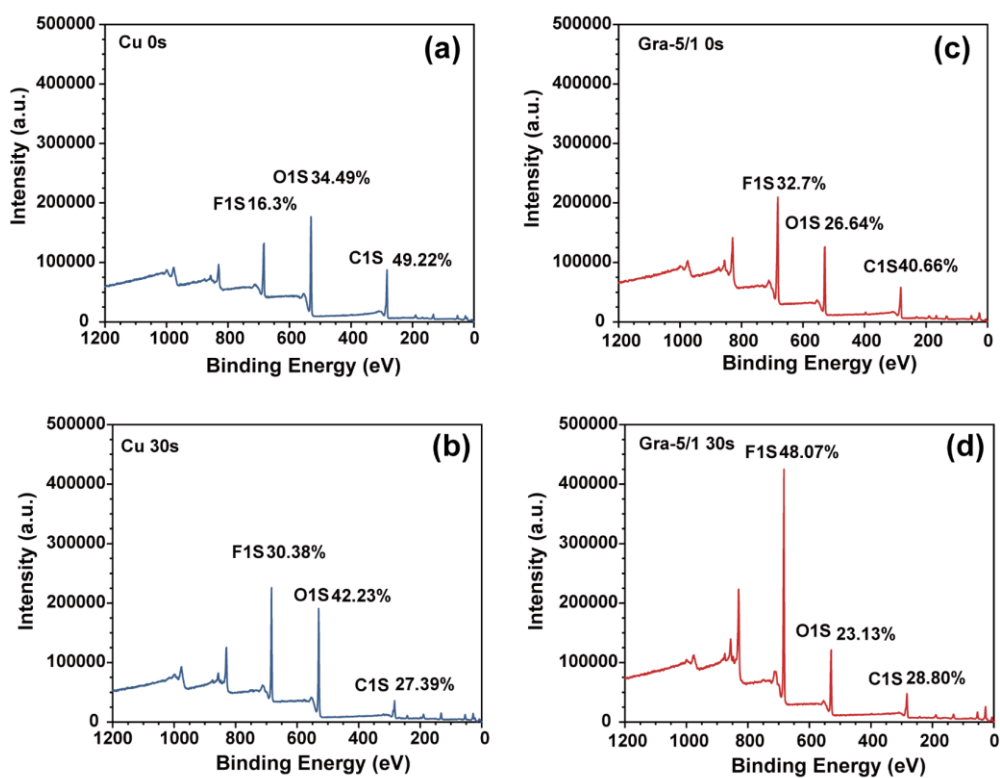


Figure 6.37. XPS full spectrum at various depths of Li plating on/stripping with 1 mAh cm^{-2} at 2 mA cm^{-2} over the (a), (b) bare Cu, and (c), (d) Gra-5/1 after 50 cycles.

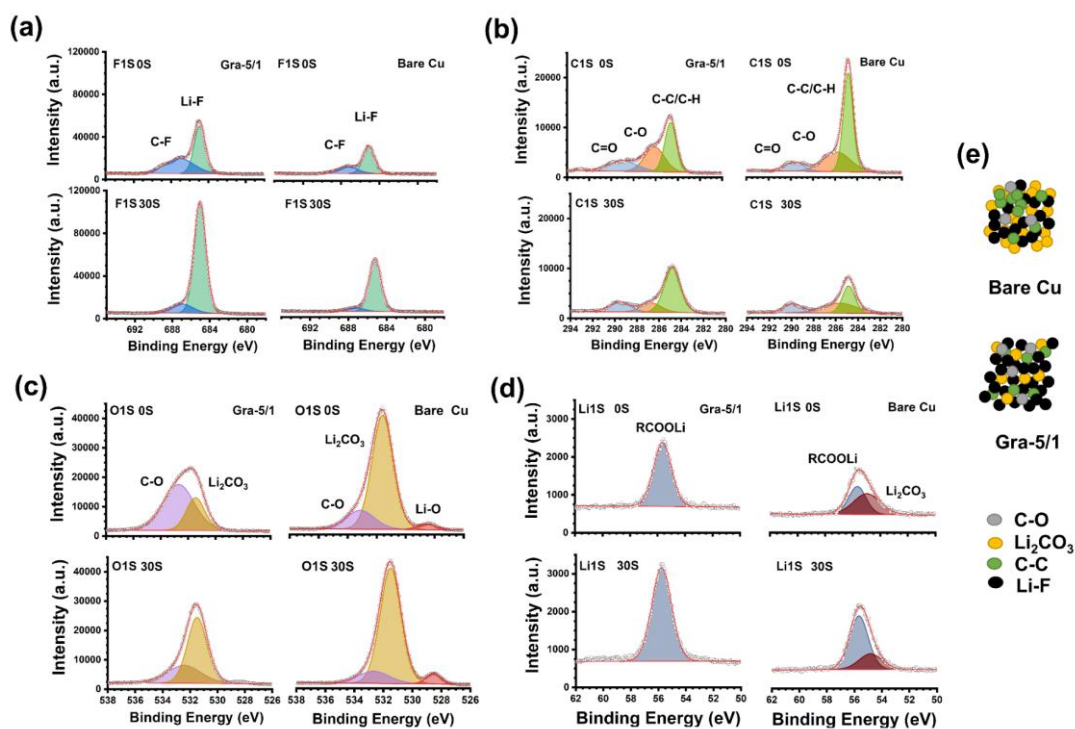


Figure 6.38. XPS spectra at different etching depths (0s and 30s) of the (a) F 1s, (b) C 1s, (c) O 1s, and (d) Li 1s of Li plating/stripping with 1 mAh cm^{-2} at 2 mA cm^{-2} over the bare Cu and Gra-5/1 after 50 cycles. (e) Illustration of the SEI compositions on the bare Cu (top) and Gra-5/1 (down).

To identify the chemical composition and stability of SEI, the half cells were evaluated after the 50th stripping/plating cycle (1 mAh cm^{-2} at 2 mA cm^{-2}), and the interfacial SEI component was further investigated (Fig. 6.37 and Fig. 6.38) at different depth and is displayed graphically via XPS. The surface SEI of bare Cu is mainly composed of organic (C–C/C–H) (Fig. 6.38b) and inorganic (Li_2CO_3) (Fig. 6.38c) substances. However, Gra-5/1 shows strong peaks of Li-F (Fig. 6.38a) and RCOOLi (Fig. 6.38d). Li-F is well-known as a favourable SEI component for its high interfacial energy toward Li and high mechanical strength.³⁰³ Therefore, it efficiently suppresses dendrite growth and contributes to uniform Li deposition. There is a more apparent growth in the intensity of Li-F after 30s' sputtering than the external SEI composition (F1S of Fig. 6.38a) in the Gra-5/1 compared to the bare Cu, implying the PVDF dispersed in graphene can facilitate the formation of Li-F and help achieve uniform Li

deposition/dissolution. Notably, the top surface of the SEI formed in the Cu foil has much stronger C–C/C–H (284.8 eV), C–O (286.2 eV), and C=O (289.5eV) signals compared with Gra-5/1, demonstrating the tremendous electrochemical degradation of organic solvent during cycling (C1s of Fig. 6.38b). While the C–C/C–H signal in the internal SEI dramatically reduces, which verifies unstable SEI formed on Cu cannot effectively stop massive electrolyte decomposition contributing to the external higher content of C–C/C–H. The stronger and similar C=O signals can be found in bare Cu before and after Ar sputtering (O1s Fig. 6.38c) compared to the Gra-5/1's, indicating that both internal and external parts of the SEI contain more organic components resulting from electrolyte decomposition. Therefore, it is indicated that numerous side reactions between the electrolyte and Li can be foreseen in Cu-foil-based LMFRBs, accelerating the dendrite formation and capacity attenuation. Compared to Gra-5/1, bare Cu shows a lower RCOOLi content and higher Li₂CO₃ in Li1S (Fig. 6.38d), implying that the RCOOLi may help Gra-5/1 reduce the electrolyte decomposition. The internal SEI of Gra-5/1 has stronger C=O signals than the external SEI, revealing that the electro-reduction of electrolytes may be efficiently inhibited by RCOOLi besides the Li-F. Fig. 6.37 shows a gradually decreased content of C-C/C-H and Li₂CO₃, an increased amount of Li-F over Gra-5/1, and both increased amounts of Li-F and Li₂CO₃ and decreased content of C-C/C-H for bare Cu along with the depth of SEI, suggesting the organic-inorganic feature of hybrid SEI as illustrated in Fig. 6.38e. It is mainly due to the PVDF-induced Li-F enriched SEI and high electron-retarding ability, which can be crucial in improving Li cycling. While vulnerable SEI on Cu will facilitate the formation of Li dendrites and “dead Li”.

Briefly, apparent Li dendrites are deposited on Cu owing to the fragile and unstable SEI. Ultimately, “dead Li” which can highly hinder the Li⁺ transporting, will be formed after several cycles, resulting in exponential failure (increased internal resistance in half cell and capacity fading in the full cell) of the battery. While PVDF-induced Li-F-rich and electron-retarding SEI triggers uniform Li⁺ flux and mitigates the formation of Li

dendrites on Gra-5/1. Thus, electrolyte depletion or the formation of by-products can lead to slow capacity decay of Gra-5/1-based LMFRBs.

6.4. Conclusions

In brief, a free-standing graphene-based current collector with a Cu tab to replace Cu foil and achieve practical application of CBCCs is fabricated. Not only can PVDF improve the mechanical strength of CBCCs, but it can also be considered an excellent film-forming polymer to help form favourable and highly insulating SEI. Graphene sheets not only have excellent electric conductivity but also provide a small surface area and hinder Li^+ insertion due to the tightly stacked 2D structure. The as-prepared Gra-5/1 satisfies the basic requirement of current collectors, such as high conductivity, sufficient mechanical strength, and viable tab welding, and also performs improved Li deposition/dissolution behaviour in pouch cells compared with Cu foil. It is believed that this free-standing CBCC with low density can furnish profound significance to practically achieve high specific energy of LMFRBs with high reversibility.

Chapter7

Conclusions and Prospect

This chapter mainly concludes the experimental result and discussion of different chapters and lists unresolved issues that require further attention in the future and provides promising suggestions about how to effectively improve the electrochemical performance of LMRBs or LMFRBs.

7.1. Conclusions

This thesis aims to achieve uniform Li deposition/dissolution and improved electrochemical performance by regulating Li^+ and electrons strategies. As for ion regulation, PCNM materials are applied to homogenise Li^+ flow on the surface of the LMNE and accommodate Li growth. To slow down the direct contact of LM toward electrolyte and alleviate the interface side reaction, Li-F-rich SEI is built on Li@PCNM electrode in advance via solvent modification. As for electron regulation, Cu foil is modified by a CNT/PVDF coating layer to realise uniform interfacial current distribution and simultaneously facilitate Li-F-rich SEI formation. To enhance the specific energy and improve the application of CBCCs, the free-standing graphene/PVDF composite current collector is prepared to replace Cu foil directly. The details are listed below.

Chapter 3. The influence of g- C_3N_4 morphology on Li deposition/dissolution behaviour has been first investigated. The 2D SCN layer could not accommodate Li growth and performed weak mechanical strength to absorb the increased stress resulting from the growing Li dendrites. The large pore size limited the efficient interaction between Li^+ and nitrogen atoms in the 3D-like BCN layer. In comparison, the 3D

porous framework of the PCNM coating layer containing both nano- and micro-pores was more favourable for physical regulation of Li deposition to rapidly absorb the stress change and guide Li growth, resulting in suppression of volume variation. Meanwhile, nanopores in PCNM can facilitate chemical interaction between Li^+ and N-containing functional groups, leading to more homogeneous Li^+ distribution based on the Debye-length law. The above physical-chemical synergic regulation strategy can promote dendrite-free Li plating. This research provides novel insight into the rational structure design of lithiophilic materials for modifying LMNEs toward stable and long-life LMRBs.

Chapter 4. The influence of different solvents (DMF, NMP, and DMAC) of PCNMs slurry on the composition of LM surfaces and related electrochemical performance have been first evaluated. DMF is not suitable as the solvent of PCNMs slurry because of the severe side reactions between DMF and LM. Although NMP is pretty stable with LM, it can hardly provide any extra help for the *in-situ* formation of Li-F-rich SEI on LM. DMAC not only keeps stable with LM but also effectively facilitates the formation of Li-F during coating via a self-driven chemical reaction between PVDF and LM. This facilitated reaction may be attributed to the distinctive solvation structure formed by DMAC with PVDF and moderate structural stability toward LM. Thus, the electrochemical performance of symmetric half cells and full cells, especially for long-term cycling which depends on a more stable interface on Li@PCNM-DMAC, is highly enhanced.

Chapter 5. A uniform and sufficiently subdivided current distribution in the nanoscale can be efficaciously formed by the CNTs network to induce uniform Li^+ flux and avoid the local ion concentration void. Meanwhile, the introduction of PVDF can lower the porous structure of the electrode to reduce the CNT-induced side effects (including SEI proliferation and severe Li dendrite growth), and PVDF serves as a Li-F-rich SEI film-forming polymer to facilitate the internal stress release in the horizontal direction to the

current collector surface. The synergistic effect between CNTs and PVDF contributes to improved Li deposition/dissolution behaviours, resulting in stable cycling performance of the LMFRBs. Our research has revealed that the utilization of a 2D-type current collector with a uniform current distribution and a soft substrate could provide a feasible option for the application of LMFRBs.

Chapter 6. A free-standing graphene-based current collector with a Cu tab is fabricated to replace Cu foil and is applied in pouch cells. Not only can PVDF improve the mechanical strength of the current collector, but it can also be considered an excellent film-forming polymer to help form favourable and highly insulating SEI. Graphene sheets with excellent electric conductivity also provide a small surface area and hinder Li⁺ insertion due to the tightly stacked 2D structure. The as-prepared Gra-5/1 satisfies the basic requirement of current collectors, such as high conductivity, sufficient mechanical strength, and viable tab welding, and also performs improved Li deposition/dissolution behaviour compared with Cu foil. This free-standing CBCC with low density can furnish profound significance to further practically achieve high specific energy of LMFRBs with high reversibility.

7.2. Prospect

In Chapter 3, the formation of large pore sizes (>2 μm) in PCNMs for accommodating LM is not precisely discussed. There is a lack of a specific relationship between the size of micropores and the ability to accommodate LM deposition. When the size of micropores is too small, LM may be difficult to enter these pores and grow, ultimately depositing outside the coating layer; If the pore size is too large, it may be difficult to achieve the localized growth of LM. Therefore, further analysis and exploration are needed in the future on how to limit the growth of LM and suppress volume expansion with a suitable micropores size.

Molecular simulation technology is an important characterisation technique for exploring chemical reaction pathways and reaction mechanisms at the micro level of molecules. In Chapter 4, the instability mechanism of DMF toward LM and the mechanism of DMAC promoting the self-driven reaction between PVDF and LM should be further elaborated through molecular simulation technology. Constructing molecular models of solvents, LM, and PVDF to simulate the formation or disappearance of molecular bonds in practical situations can provide a more convincing mechanism explanation.

In addition, in chapters 3 and 4, There are many problems with the engineering scale-up of PCNMs coating layers on LM, such as the control of the coating process. As is well known, it is necessary to ensure high specific energy for LMRBs by low N/P (Negative capacity/Positive capacity), and at the same time, low N/P can further reduce the side reaction between LM and electrolyte, thereby improving the battery cycling life.²⁴⁸ Thus, we need to use thinner Li foil (<40 μ m) to assemble the battery. It will be a challenge for PCNMs coatings to be uniformly double-sided coated on thinner Li foils. Also, it is difficult for thinner Li foil to peel off from the coating substrate due to its soft property and strong adhesion. Therefore, during the coating process, it is necessary to avoid many engineering problems such as Li foil perforation, damage, uneven coating layer, and drop of Li tab. The concentration of coating slurry and the selection of appropriate equipment may be the main entry points to address this engineering problem in future work.

In Chapter 5, both the uniform current distribution and accumulated internal stress release in the horizontal direction to the current collector caused by the soft substrate layer have a positive impact on achieving dendrite-free Li deposition. However, their influence weights should be further analysed/quantized through specific experiments/advanced characterisation techniques. In addition, the impact of these optimizations on the battery cycling process should be further explored and explained.

In Chapter 6, although etching copper foil can solve the problem of welding problem in the carbon-based current collector and obtain free-standing carbon-based current collectors for the application of pouch cells, the operation process is more dangerous due to the use of hydrochloric acid during the etching process. So, to produce Gra-5/1 on a large scale, a safer and more feasible preparation strategy should be developed. For example, graphene material can be considered to be coated on a polymer film (e.g., PET), dried, and directly removed from the film to obtain the free-standing Gra-5/1.

In addition, in Chapter 6, it is necessary to further improve Gra-5/1's cycling performance in LMFRBs. It is an ideal strategy to consider developing a solid-state electrolyte that is suitable for the G-5/1, as it can basically eliminate capacity loss caused by side reactions between LM and electrolyte. Also, the solid-state electrolyte has a high Young's modulus that can suppress the growth of Li dendrites, improving reversible Li deposition.

Last but not least, in LMRBs or LMFRBs, ions and electrons regulation strategies are indeed effective ways to alleviate Li dendrite growth. However, single ions or electrons regulation is difficult to alleviate the capacity loss of the battery. The capacity loss of LMRBs or LMFRBs usually comes from the "dead Li" caused by Li dendrites, the formation of by-products that originated from the side reaction between LM and the electrolyte, and Li inventory consumption caused by the side reactions of the positrode. In addition, the accumulation of "dead Li"-induced internal resistance and the serious consumption of electrolytes caused by the continuous generation of by-products will lead to the failure of batteries. Therefore, in addition to the Li dendrites, more attention should be paid to the side reactions between LM and electrolytes. A synergy strategy should be applied to improve the electrochemical performance of LMRBs or LMFRBs: Combining alleviating the growth of Li dendrites and deactivation treatment of the surface of the LMNE.

Reference

- [1] W. Gilliland Martha. Energy Analysis and Public Policy. *Science* **1975**, *189*, 1051-1056.
- [2] H. Kunz, N. Hagens, S. Balogh. The Influence of Output Variability from Renewable Electricity Generation on Net Energy Calculations. *Energies* **2014**, *7*, 150-172.
- [3] M. Kenneth, H. Nathan John. Energy Return on Investment: Toward a Consistent Framework. *AMBIO: A Journal of the Human Environment* **2008**, *37*, 74-79.
- [4] J. V. Paatero, P. D. Lund. Effect of energy storage on variations in wind power. *Wind Energy* **2005**, *8*, 421-441.
- [5] K. Dai, A. Bergot, C. Liang, et al. Environmental issues associated with wind energy – A review. *Renewable Energy* **2015**, *75*, 911-921.
- [6] B. K. Sahu. Wind energy developments and policies in China: A short review. *Renewable and Sustainable Energy Reviews* **2018**, *81*, 1393-1405.
- [7] S. Chu, A. Majumdar. Opportunities and challenges for a sustainable energy future. *Nature* **2012**, *488*, 294-303.
- [8] N. S. Lewis. Research opportunities to advance solar energy utilization. *Science* **2016**, *351*, add1920.
- [9] K. H. Solangi, M. R. Islam, R. Saidur, et al. A review on global solar energy policy. *Renewable and Sustainable Energy Reviews* **2011**, *15*, 2149-2163.
- [10] F. O Rourke, F. Boyle, A. Reynolds. Tidal energy update 2009. *Applied Energy* **2010**, *87*, 398-409.
- [11] E. Segura, R. Morales, J. A. Somolinos, et al. Techno-economic challenges of tidal energy conversion systems: Current status and trends. *Renewable and Sustainable Energy Reviews* **2017**, *77*, 536-550.
- [12] H.-w. Liu, S. Ma, W. Li, et al. A review on the development of tidal current energy in China. *Renewable and Sustainable Energy Reviews* **2011**, *15*, 1141-1146.
- [13] E. Barbier. Geothermal energy technology and current status: an overview. *Renewable and Sustainable Energy Reviews* **2002**, *6*, 3-65.
- [14] J. W. Lund, T. L. Boyd. Direct utilization of geothermal energy 2015 worldwide review. *Geothermics* **2016**, *60*, 66-93.
- [15] I. B. Fridleifsson. Geothermal energy for the benefit of the people. *Renewable and Sustainable Energy Reviews* **2001**, *5*, 299-312.
- [16] A. J. Nicastro. A dynamical model of a carnot cycle. *The Physics Teacher* **1983**, *21*, 463-464.
- [17] L. Y.-c. LI Hong. Short Review on Electrochemical Energy Storage. *Journal of electrochemistry* **2015**, *21*, 412-424.
- [18] J. M. Tarascon, M. Armand. Issues and challenges facing rechargeable lithium batteries. *Nature* **2001**, *414*, 359-367.
- [19] M. Armand, J. M. Tarascon. Building better batteries. *Nature* **2008**, *451*, 652-657.
- [20] M. S. Whittingham. Electrical Energy Storage and Intercalation Chemistry. *Science*

1976, 192, 1126-1127.

- [21] M. M. Thackeray, W. I. F. David, P. G. Bruce, et al. Lithium insertion into manganese spinels. *Materials Research Bulletin* **1983**, 18, 461-472.
- [22] K. Mizushima, P. C. Jones, P. J. Wiseman, et al. Li_xCoO_2 ($0 < x < 1$): A new cathode material for batteries of high energy density. *Materials Research Bulletin* **1980**, 15, 783-789.
- [23] J. B. Goodenough, H. Gao. A perspective on the Li-ion battery. *Science China Chemistry* **2019**, 62, 1555-1556.
- [24] A. K. Padhi, K. S. Nanjundaswamy, C. Masquelier, et al. Effect of Structure on the $\text{Fe}^{3+}/\text{Fe}^{2+}$ Redox Couple in Iron Phosphates. *Journal of The Electrochemical Society* **1997**, 144, 1609-1613.
- [25] M. Winter, B. Barnett, K. Xu. Before Li Ion Batteries. *Chemical Reviews* **2018**, 118, 11433-11456.
- [26] S.-T. Myung, F. Maglia, K.-J. Park, et al. Nickel-Rich Layered Cathode Materials for Automotive Lithium-Ion Batteries: Achievements and Perspectives. *ACS Energy Letters* **2016**, 2, 196-223.
- [27] Q. Wang. Study on Structural Design and Interfacial Chemistry of Lithium Metal Anode. Peking University, Beijing, 2021.
- [28] B. Dunn, H. Kamath, J.-M. Tarascon. Electrical Energy Storage for the Grid: A Battery of Choices. *Science* **2011**, 334, 928-935.
- [29] J. W. Choi, D. Aurbach. Promise and reality of post-lithium-ion batteries with high energy densities. *Nature Reviews Materials* **2016**, 1, 16013.
- [30] Y. Li, Y. Lu, P. Adelhelm, et al. Intercalation chemistry of graphite: alkali metal ions and beyond. *Chemical Society Reviews* **2019**, 48, 4655-4687.
- [31] A. Ponrouch, J. Bitenc, R. Dominko, et al. Multivalent rechargeable batteries. *Energy Storage Materials* **2019**, 20, 253-262.
- [32] X. Su, Q. Wu, J. Li, et al. Silicon-Based Nanomaterials for Lithium-Ion Batteries: A Review. *Advanced Energy Materials* **2014**, 4, 1300882.
- [33] P. Poizot, S. Laruelle, S. Grugeon, et al. Nano-sized transition-metal oxides as negative-electrode materials for lithium-ion batteries. *Nature* **2000**, 407, 496-499.
- [34] X. B. Cheng, R. Zhang, C. Z. Zhao, et al. Toward Safe Lithium Metal Anode in Rechargeable Batteries: A Review. *Chemical Reviews* **2017**, 117, 10403-10473.
- [35] D. Lin, Y. Liu, Y. Cui. Reviving the Lithium Metal Anode for High-Energy Batteries. *Nature Nanotechnology* **2017**, 12, 194-206.
- [36] A. Manthiram, Y. Fu, S. H. Chung, et al. Rechargeable lithium-sulfur batteries. *Chemical Reviews* **2014**, 114, 11751-87.
- [37] Y. X. Yin, S. Xin, Y. G. Guo, et al. Lithium-sulfur batteries: electrochemistry, materials, and prospects. *Angewandte Chemie International Edition* **2013**, 52, 13186-200.
- [38] A. Manthiram, Y. Fu, Y.-S. Su. Challenges and Prospects of Lithium-Sulfur Batteries. *Accounts of Chemical Research* **2013**, 46, 1125-1134.
- [39] F. Cheng, J. Chen. Metal-air batteries: from oxygen reduction electrochemistry to cathode catalysts. *Chemical Society Reviews* **2012**, 41, 2172-92.

- [40]J. Lu, L. Li, J. B. Park, et al. Aprotic and aqueous Li-O₂ batteries. *Chemical Reviews* **2014**, *114*, 5611-40.
- [41]P. G. Bruce, S. A. Freunberger, L. J. Hardwick, et al. Li-O₂ and Li-S batteries with high energy storage. *Nature Materials* **2011**, *11*, 19-29.
- [42]L. Yu, G. Z. Chen. High energy supercapattery with an ionic liquid solution of LiClO₄. *Faraday Discuss* **2016**, *190*, 231-40.
- [43]B. Liu, J. Chen, B. Yang, et al. Boosting the performance of lithium metal capacitors with a Li composite anode. *Journal of Materials Chemistry A* **2021**, *9*, 10722-10730.
- [44]B. Liu, J. Chen, B. Yang, et al. An ultrahigh-energy-density lithium metal capacitor. *Energy Storage Materials* **2021**, *42*, 154-163.
- [45]X. Yao, Q. Dong, Q. Cheng, et al. Why Do Lithium-Oxygen Batteries Fail: Parasitic Chemical Reactions and Their Synergistic Effect. *Angewandte Chemie International Edition* **2016**, *55*, 11344-53.
- [46]D. Geng, N. Ding, T. S. A. Hor, et al. From Lithium-Oxygen to Lithium-Air Batteries: Challenges and Opportunities. *Advanced Energy Materials* **2016**, *6*, 1502164.
- [47]R. Xu, J. Lu, K. Amine. Progress in Mechanistic Understanding and Characterization Techniques of Li-S Batteries. *Advanced Energy Materials* **2015**, *5*, 1500408.
- [48]O. Ogoke, G. Wu, X. Wang, et al. Effective strategies for stabilizing sulfur for advanced lithium-sulfur batteries. *Journal of Materials Chemistry A* **2017**, *5*, 448-469.
- [49]G. Z. Chen. Supercapacitor and supercapattery as emerging electrochemical energy stores. *International Materials Reviews* **2016**, *62*, 173-202.
- [50]W. Shimizu, S. Makino, K. Takahashi, et al. Development of a 4.2 V aqueous hybrid electrochemical capacitor based on MnO₂ positive and protected Li negative electrodes. *Journal of Power Sources* **2013**, *241*, 572-577.
- [51]W. Li, B. Song, A. Manthiram. High-voltage positive electrode materials for lithium-ion batteries. *Chemical Society Reviews* **2017**, *46*, 3006-3059.
- [52]A. Manthiram, X. Yu, S. Wang. Lithium battery chemistries enabled by solid-state electrolytes. *Nature Reviews Materials* **2017**, *2*, 16103.
- [53]R. Dominko, A. Vizintin, G. Aquilanti, et al. Polysulfides Formation in Different Electrolytes from the Perspective of X-ray Absorption Spectroscopy. *Journal of The Electrochemical Society* **2017**, *165*, A5014-A5019.
- [54]A. Aryanfar, D. J. Brooks, A. J. Colussi, et al. Thermal relaxation of lithium dendrites. *Physical Chemistry Chemical Physics* **2015**, *17*, 8000--8005.
- [55]K. Nishikawa, T. Mori, T. Nishida, et al. Li dendrite growth and Li⁺ ionic mass transfer phenomenon. *Journal of Electroanalytical Chemistry* **2011**, *661*, 84-89.
- [56]X. Sun, X. Zhang, Q. Ma, et al. Revisiting the Electroplating Process for Lithium-Metal Anodes for Lithium-Metal Batteries. *Angewandte Chemie International Edition* **2020**, *59*, 6665-6674.
- [57]E. Nakouzi, R. Sultan. Fractal structures in two-metal electrodeposition systems II: Cu and Zn. *Chaos* **2012**, *22*, 023122.
- [58]B. Li, Y. Wang, S. Yang. A Material Perspective of Rechargeable Metallic Lithium

- Anodes. *Advanced Energy Materials* **2018**, *8*, 1702296.
- [59]J. Steiger, G. Richter, M. Wenk, et al. Comparison of the growth of lithium filaments and dendrites under different conditions. *Electrochemistry Communications* **2015**, *50*, 11-14.
- [60]C. Ling, D. Banerjee, M. Matsui. Study of the electrochemical deposition of Mg in the atomic level: Why it prefers the non-dendritic morphology. *Electrochimica Acta* **2012**, *76*, 270-274.
- [61]M. Jackle, A. Gross. Microscopic properties of lithium, sodium, and magnesium battery anode materials related to possible dendrite growth. *Journal Of Chemical Physics* **2014**, *141*, 174710.
- [62]C. Sun. Study on the Optimization of Lithium-Metal Anode and its Interface for Lithium-Metal Batteries. dissertation, University of Chinese Academy of Sciences, Shanghai, 2020.
- [63]D. R. Ely, R. E. García. Heterogeneous Nucleation and Growth of Lithium Electrodeposits on Negative Electrodes. *Journal of The Electrochemical Society* **2013**, *160*, A662-A668.
- [64]N. Dong. Study of Alloying Modification and Surface Protection of Lithium Metal Anode for Lithium Secondary Batteries. dissertation, University of Chinese Academy of Sciences, Ningbo, 2020.
- [65]K. Yan, Z. Lu, H.-W. Lee, et al. Selective deposition and stable encapsulation of lithium through heterogeneous seeded growth. *Nature Energy* **2016**, *1*, 16010.
- [66]J. Chazalviel. Electrochemical Aspects of the Generation of Ramified Metallic Electrodeposits. *Physical Review A* **1990**, *42*, 7355-7367.
- [67]V. Fleury, J. N. Chazalviel, M. Rosso, et al. The role of the anions in the growth speed of fractal electrodeposits. *Journal of Electroanalytical Chemistry and Interfacial Electrochemistry* **1990**, *290*, 249-255.
- [68]J.-i. Yamaki, S.-i. Tobishima, K. Hayashi, et al. A Consideration of the Morphology of Electrochemically Deposited Lithium in an Organic Electrolyte. *Journal of Power Sources* **1998**, *74*, 219-227.
- [69]C. Monroe, J. Newman. The Effect of Interfacial Deformation on Electrodeposition Kinetics. *Journal of The Electrochemical Society* **2004**, *151*, A880.
- [70]X. Guan, A. Wang, S. Liu, et al. Controlling Nucleation in Lithium Metal Anodes. *Small* **2018**, *14*, e1801423.
- [71]P. Zou, Y. Wang, S. W. Chiang, et al. Directing lateral growth of lithium dendrites in micro-compartmented anode arrays for safe lithium metal batteries. *Nature Communications* **2018**, *9*, 464.
- [72]F. Ding, W. Xu, G. L. Graff, et al. Dendrite-free lithium deposition via self-healing electrostatic shield mechanism. *Journal of The American Chemical Society* **2013**, *135*, 4450-6.
- [73]Z. L. Brown, S. Jurng, C. C. Nguyen, et al. Effect of Fluoroethylene Carbonate Electrolytes on the Nanostructure of the Solid Electrolyte Interphase and Performance of Lithium Metal Anodes. *ACS Applied Energy Materials* **2018**, *1*, 3057-3062.
- [74]R. Weber, M. Genovese, A. J. Louli, et al. Long Cycle Life and Dendrite-Free

Lithium Morphology in Anode-Free Lithium Pouch Cells Enabled by a Dual-Salt Liquid Electrolyte. *Nature Energy* **2019**, *4*, 683-689.

[75]Z. A. Ghazi, Z. Sun, C. Sun, et al. Key Aspects of Lithium Metal Anodes for Lithium Metal Batteries. *Small* **2019**, *15*, e1900687.

[76]F. Chen. Study on the Precast and Cycle Stability of Elastic SEI Film for Metal Lithium Anode. dissertation, Harbin Institute of Technology, Haerbin, 2021.

[77]J. Wu, L. Yuan, Z. Li, et al. Air-stable means more: designing air-defendable lithium metals for safe and stable batteries. *Materials Horizons* **2020**, *7*, 2619-2634.

[78]Z. Yu, Y. Cui, Z. Bao. Design Principles of Artificial Solid Electrolyte Interphases for Lithium-Metal Anodes. *Cell Reports Physical Science* **2020**, *1*, 100119.

[79]C. Brissot, M. Rosso, J. N. Chazalviel, et al. Dendritic growth mechanisms in lithium/polymer cells. *Journal of Power Sources* **1999**, *81-82*, 925-929.

[80]M. Rosso, C. Brissot, A. Teyssot, et al. Dendrite short-circuit and fuse effect on Li/polymer/Li cells. *Electrochimica Acta* **2006**, *51*, 5334-5340.

[81]H. J. S. Sand. III. On the concentration at the electrodes in a solution, with special reference to the liberation of hydrogen by electrolysis of a mixture of copper sulphate and sulphuric acid. *The London, Edinburgh, and Dublin Philosophical Magazine and Journal of Science* **1901**, *1*, 45-79.

[82]M. Rosso, T. Gobron, C. Brissot, et al. Onset of dendritic growth in lithium/polymer cells. *Journal of Power Sources* **2001**, *97-98*, 804-806.

[83]A. Dey. Film Formation on Lithium Anode in Propylene Carbonate. *Journal of the electrochemical society* **1970**, *117*, C248.

[84]E. Peled. The Electrochemical Behavior of Alkali and Alkaline Earth Metals in Nonaqueous Battery Systems—The Solid Electrolyte Interphase Model. *Journal of The Electrochemical Society* **1979**, *126*, 2047.

[85]H. J. Chang, A. J. Ilott, N. M. Trease, et al. Correlating Microstructural Lithium Metal Growth with Electrolyte Salt Depletion in Lithium Batteries Using (⁷)Li MRI. *Journal of The American Chemical Society* **2015**, *137*, 15209-15216.

[86]J. B. Goodenough, Y. Kim. Challenges for Rechargeable Li Batteries†. *Chemistry of Materials* **2010**, *22*, 587-603.

[87]E. Peled. Advanced Model for Solid Electrolyte Interphase Electrodes in Liquid and Polymer Electrolytes. *Journal of The Electrochemical Society* **1997**, *144*, L208.

[88]S.-P. Kim, A. C. T. v. Duin, V. B. Shenoy. Effect of electrolytes on the structure and evolution of the solid electrolyte interphase (SEI) in Li-ion batteries: A molecular dynamics study. *Journal of Power Sources* **2011**, *196*, 8590-8597.

[89]S. Shi, P. Lu, Z. Liu, et al. Direct calculation of Li-ion transport in the solid electrolyte interphase. *Journal of The American Chemical Society* **2012**, *134*, 15476-87.

[90]D. Aurbach, K. Gamolsky, B. Markovsky, et al. On the use of vinylene carbonate (VC) as an additive to electrolyte solutions for Li-ion batteries. *Electrochimica Acta* **2002**, *47*, 1423-1439.

[91]D. Aurbach, E. Zinigrad, Y. Cohen, et al. A short review of failure mechanisms of lithium metal and lithiated graphite anodes in liquid electrolyte solutions. *Solid State*

Ionics **2002**, *148*, 405-416.

[92] Y. Li, W. Huang, Y. Li, et al. Correlating Structure and Function of Battery Interphases at Atomic Resolution Using Cryoelectron Microscopy. *Joule* **2018**, *2*, 2167-2177.

[93] K. Xu, A. von Cresce, U. Lee. Differentiating Contributions to “Ion Transfer” Barrier from Interphasial Resistance and Li⁺ Desolvation at Electrolyte/Graphite Interface. *Langmuir* **2010**, *26*, 11538-11543.

[94] C. Monroe, J. Newman. The Impact of Elastic Deformation on Deposition Kinetics at Lithium/Polymer Interfaces. *Journal of The Electrochemical Society* **2005**, *152*, A396.

[95] Y. He, H. Hu. Analysis of lithium ion concentration and stress in the solid electrolyte interphase on the graphite anode. *Physical Chemistry Chemical Physics* **2015**, *17*, 23565-72.

[96] Z. Liu, Y. Qi, Y. X. Lin, et al. Interfacial Study on Solid Electrolyte Interphase at Li Metal Anode: Implication for Li Dendrite Growth. *Journal of The Electrochemical Society* **2016**, *163*, A592-A598.

[97] N.-W. Li, Y.-X. Yin, C.-P. Yang, et al. An Artificial Solid Electrolyte Interphase Layer for Stable Lithium Metal Anodes. *Advanced Materials* **2016**, *28*, 1853-1858.

[98] X. Yin, W. Tang, I. D. Jung, et al. Insights into morphological evolution and cycling behaviour of lithium metal anode under mechanical pressure. *Nano Energy* **2018**, *50*, 659-664.

[99] X. Shen, R. Zhang, P. Shi, et al. How Does External Pressure Shape Li Dendrites in Li Metal Batteries? *Advanced Energy Materials* **2021**, *11*, 2003416.

[100] A. C. Thenuwara, P. P. Shetty, M. T. McDowell. Distinct Nanoscale Interphases and Morphology of Lithium Metal Electrodes Operating at Low Temperatures. *Nano Letters* **2019**, *19*, 8664-8672.

[101] J. Wang, W. Huang, A. Pei, et al. Improving cyclability of Li metal batteries at elevated temperatures and its origin revealed by cryo-electron microscopy. *Nature Energy* **2019**, *4*, 664-670.

[102] M. Huang. Study on Fine Interfacial Structure Modulation of Lithium Metal and Introduction of High Fluorine Components to Inhibit Lithium Dendrites. dissertation, University of Chinese Academy of Sciences, Shanghai, 2021.

[103] I. W. Seong, C. H. Hong, B. K. Kim, et al. The effects of current density and amount of discharge on dendrite formation in the lithium powder anode electrode. *Journal of Power Sources* **2008**, *178*, 769-773.

[104] L. L. Lu, J. Ge, J. N. Yang, et al. Free-Standing Copper Nanowire Network Current Collector for Improving Lithium Anode Performance. *Nano Letters* **2016**, *16*, 4431-4437.

[105] M. Cheng, H. Su, P. Xiong, et al. Molten Lithium-Filled Three-Dimensional Hollow Carbon Tube Mats for Stable Lithium Metal Anodes. *ACS Applied Energy Materials* **2019**, *2*, 8303-8309.

[106] H. Zhang, X. Liao, Y. Guan, et al. Lithiophilic-lithiophobic gradient interfacial layer for a highly stable lithium metal anode. *Nature Communications* **2018**, *9*, 3729.

- [107] Y. Yao, R. Xu, M. Chen, et al. Encapsulation of SeS₂ into Nitrogen-Doped Free-Standing Carbon Nanofiber Film Enabling Long Cycle Life and High Energy Density K-SeS₂ Battery. *ACS Nano* **2019**, *13*, 4695-4704.
- [108] J. Jeong, J. Chun, W.-G. Lim, et al. Mesoporous carbon host material for stable lithium metal anode. *Nanoscale* **2020**, *12*, 11818-11824.
- [109] L. Fan, H. L. Zhuang, W. Zhang, et al. Stable Lithium Electrodeposition at Ultra-High Current Densities Enabled by 3D PMF/Li Composite Anode. *Advanced Energy Materials* **2018**, *8*, 1703360.
- [110] Y. Zhang, B. Liu, E. Hitz, et al. A carbon-based 3D current collector with surface protection for Li metal anode. *Nano Research* **2017**, *10*, 1356-1365.
- [111] W. Deng, W. Zhu, X. Zhou, et al. Graphene nested porous carbon current collector for lithium metal anode with ultrahigh areal capacity. *Energy Storage Materials* **2018**, *15*, 266-273.
- [112] W. Deng, X. Zhou, Q. Fang, et al. Microscale Lithium Metal Stored inside Cellular Graphene Scaffold toward Advanced Metallic Lithium Anodes. *Advanced Energy Materials* **2018**, *8*, 1703152.
- [113] Z. Zhang, J. Wang, X. Yan, et al. In-Situ Growth of Hierarchical N-Doped CNTs/Ni Foam Scaffold for Dendrite-Free Lithium Metal Anode. *Energy Storage Materials* **2020**, *29*, 332-340.
- [114] L. Zhang, X. Yin, S. Shen, et al. Simultaneously Homogenized Electric Field and Ionic Flux for Reversible Ultrahigh-Areal-Capacity Li Deposition. *Nano Letters* **2020**, *20*, 5662-5669.
- [115] Z. Zhang, X. Zhou, Z. Liu. Conformal Coating of a Carbon Film on 3D Hosts toward Stable Lithium Anodes. *ACS Applied Energy Materials* **2021**, *4*, 7288-7297.
- [116] K. Qin, J. Baucom, D. Liu, et al. A Powder Metallurgic Approach toward High-Performance Lithium Metal Anodes. *Small* **2020**, *16*, 2000794.
- [117] T.-T. Zuo, X.-W. Wu, C.-P. Yang, et al. Graphitized Carbon Fibers as Multifunctional 3D Current Collectors for High Areal Capacity Li Anodes. *Advanced Materials* **2017**, *29*, 1700389.
- [118] G. Yang, Y. Li, Y. Tong, et al. Lithium Plating and Stripping on Carbon Nanotube Sponge. *Nano Letters* **2019**, *19*, 494-499.
- [119] N. Luo, G. J. Ji, H. F. Wang, et al. Process for a Free-Standing and Stable All-Metal Structure for Symmetrical Lithium-Oxygen Batteries. *ACS Nano* **2020**, *14*, 3281-3289.
- [120] R. Zhang, X. Chen, X. Shen, et al. Coraloid Carbon Fiber-Based Composite Lithium Anode for Robust Lithium Metal Batteries. *Joule* **2018**, *2*, 764-777.
- [121] X. Wang, Z. Wang, X. Zhang, et al. Nitrogen-Doped Defective Graphene Aerogel as Anode for all Graphene-Based Lithium Ion Capacitor. *ChemistrySelect* **2017**, *2*, 8436-8445.
- [122] L. L. Tian, S. B. Li, M. J. Zhang, et al. Cascading Boost Effect on the Capacity of Nitrogen-Doped Graphene Sheets for Li- and Na-Ion Batteries. *ACS Applied Materials & Interfaces* **2016**, *8*, 26722-26729.
- [123] Q. Guo, C. Zhang, C. Zhang, et al. Co₃O₄ modified Ag/g-C₃N₄ composite as a

- bifunctional cathode for lithium-oxygen battery. *Journal of Energy Chemistry* **2020**, *41*, 185-193.
- [124] Y. Liu, D. Lin, Z. Liang, et al. Lithium-coated polymeric matrix as a minimum volume-change and dendrite-free lithium metal anode. *Nature Communications* **2016**, *7*, 10992.
- [125] R. Zhang, X. R. Chen, X. Chen, et al. Lithiophilic Sites in Doped Graphene Guide Uniform Lithium Nucleation for Dendrite-Free Lithium Metal Anodes. *Angewandte Chemie International Edition* **2017**, *56*, 7764-7768.
- [126] B. Rani, V. K. Jindal, K. Dharamvir. Energetics of a Li Atom adsorbed on B/N doped graphene with monovacancy. *Journal of Solid State Chemistry* **2016**, *240*, 67-75.
- [127] X. Chen, X.-R. Chen, T.-Z. Hou, et al. Lithiophilicity Chemistry of Heteroatom-Doped Carbon to Guide Uniform Lithium Nucleation in Lithium Metal Anodes. *Science Advances* **2019**, *5*, eaau7728.
- [128] P. Yao, Q. Chen, Y. Mu, et al. 3D hollow reduced graphene oxide foam as a stable host for high-capacity lithium metal anodes. *Materials Chemistry Frontiers* **2019**, *3*, 339-343.
- [129] G. Huang, J. Han, F. Zhang, et al. Lithiophilic 3D Nanoporous Nitrogen-Doped Graphene for Dendrite-Free and Ultrahigh-Rate Lithium-Metal Anodes. *Advanced Materials* **2019**, *31*, 1805334.
- [130] Q. Guo, Y. Wan, B. Hu, et al. Carbon-nitride-based core-shell nanomaterials: synthesis and applications. *Journal of Materials Science: Materials in Electronics* **2018**, *29*, 20280-20301.
- [131] Q. Guo, L. Fu, T. Yan, et al. Improved photocatalytic activity of porous ZnO nanosheets by thermal deposition graphene-like g-C₃N₄ for CO₂ reduction with H₂O vapor. *Applied Surface Science* **2020**, *509*, 144773.
- [132] Y. Luo, Y. Yan, S. Zheng, et al. Graphitic carbon nitride based materials for electrochemical energy storage. *Journal of Materials Chemistry A* **2019**, *7*, 901-924.
- [133] J. Wen, J. Xie, X. Chen, et al. A review on g-C₃N₄ -based photocatalysts. *Applied Surface Science* **2017**, *391*, 72-123.
- [134] Z. Zhao, Y. Sun, F. Dong. Graphitic carbon nitride based nanocomposites: a review. *Nanoscale* **2015**, *7*, 15-37.
- [135] H. Wu, Y. Zhang, Y. Deng, et al. A Lightweight Carbon Nanofiber-Based 3D Structured Matrix with High Nitrogen-Doping Level for Lithium Metal Anodes. *Science China Materials* **2018**, *62*, 87-94.
- [136] Z. Lu, Q. Liang, B. Wang, et al. Graphitic Carbon Nitride Induced Micro-Electric Field for Dendrite-Free Lithium Metal Anodes. *Advanced Energy Materials* **2019**, *9*, 1803186.
- [137] Y. Guo, P. Niu, Y. Liu, et al. An Autotransferable g-C₃N₄ Li⁽⁺⁾ -Modulating Layer toward Stable Lithium Anodes. *Advanced Materials* **2019**, *31*, 1900342.
- [138] X. Luan, C. Wang, C. Wang, et al. Stable Lithium Deposition Enabled by an Acid-Treated g-C₃N₄ Interface Layer for a Lithium Metal Anode. *ACS Applied Materials & Interfaces* **2020**, *12*, 11265-11272.
- [139] Y. Gong, M. Li, Y. Wang. Carbon Nitride in Energy Conversion and Storage:

- Recent Advances and Future Prospects. *ChemSusChem* **2015**, *8*, 931-946.
- [140] P. Zhai, T. Wang, H. Jiang, et al. 3D Artificial Solid-Electrolyte Interphase for Lithium Metal Anodes Enabled by Insulator–Metal–Insulator Layered Heterostructures. *Advanced Materials* **2021**, *33*, 2006247.
- [141] H. Sun, G. Zhu, Y. Zhu, et al. High-Safety and High-Energy-Density Lithium Metal Batteries in a Novel Ionic-Liquid Electrolyte. *Advanced Materials* **2020**, *32*, 2001741.
- [142] W. Zhang, Q. Wu, J. Huang, et al. Colossal Granular Lithium Deposits Enabled by the Grain-Coarsening Effect for High-Efficiency Lithium Metal Full Batteries. *Advanced Materials* **2020**, *32*, 2001740.
- [143] P. Shi, F. Liu, Y. Feng, et al. The Synergetic Effect of Lithium Bisoxalatodifluorophosphate and Fluoroethylene Carbonate on Dendrite Suppression for Fast Charging Lithium Metal Batteries. *Small* **2020**, *16*, 2001989.
- [144] E. Yoo, Y. Qiao, H. Zhou. Understanding the effect of the concentration of LiNO₃ salt in Li–O₂ batteries. *Journal of Materials Chemistry A* **2019**, *7*, 18318-18323.
- [145] B. D. Adams, E. V. Carino, J. G. Connell, et al. Long term stability of Li-S batteries using high concentration lithium nitrate electrolytes. *Nano Energy* **2017**, *40*, 607-617.
- [146] H. Zheng, H. Xiang, F. Jiang, et al. Lithium Difluorophosphate-Based Dual-Salt Low Concentration Electrolytes for Lithium Metal Batteries. *Advanced Energy Materials* **2020**, *10*, 2001440.
- [147] H. Yang, J. Li, Z. Sun, et al. Reliable liquid electrolytes for lithium metal batteries. *Energy Storage Materials* **2020**, *30*, 113-129.
- [148] J. Zheng, J. A. Lochala, A. Kwok, et al. Research Progress towards Understanding the Unique Interfaces between Concentrated Electrolytes and Electrodes for Energy Storage Applications. *Advanced Science* **2017**, *4*, 1700032.
- [149] J. Qian, W. A. Henderson, W. Xu, et al. High rate and stable cycling of lithium metal anode. *Nature Communications* **2015**, *6*, 6362.
- [150] S. Chen, J. Zheng, D. Mei, et al. High-Voltage Lithium-Metal Batteries Enabled by Localized High-Concentration Electrolytes. *Advanced Materials* **2018**, *30*, 1706102.
- [151] T. Hou, G. Yang, N. N. Rajput, et al. The influence of FEC on the solvation structure and reduction reaction of LiPF₆/EC electrolytes and its implication for solid electrolyte interphase formation. *Nano Energy* **2019**, *64*, 103881.
- [152] H. Ota, Y. Sakata, Y. Otake, et al. Structural and Functional Analysis of Surface Film on Li Anode in Vinylene Carbonate-Containing Electrolyte. *Journal of The Electrochemical Society* **2004**, *151*, A1778.
- [153] G.-B. Han, J.-N. Lee, D. J. Lee, et al. Enhanced cycling performance of lithium metal secondary batteries with succinic anhydride as an electrolyte additive. *Electrochimica Acta* **2014**, *115*, 525-530.
- [154] H. Wu, Y. Cao, L. Geng, et al. In Situ Formation of Stable Interfacial Coating for High Performance Lithium Metal Anodes. *Chemistry of Materials* **2017**, *29*, 3572-3579.

- [155] Q. Wang, C. Yang, J. Yang, et al. Dendrite-Free Lithium Deposition via a Superfilling Mechanism for High-Performance Li-Metal Batteries. *Advanced Materials* **2019**, *31*, 1903248.
- [156] J. Guo, Z. Wen, M. Wu, et al. Vinylene carbonate–LiNO₃: A hybrid additive in carbonic ester electrolytes for SEI modification on Li metal anode. *Electrochemistry Communications* **2015**, *51*, 59-63.
- [157] Y. Yu, X.-B. Zhang. In Situ Coupling of Colloidal Silica and Li Salt Anion toward Stable Li Anode for Long-Cycle-Life Li-O₂ Batteries. *Matter* **2019**, *1*, 881-892.
- [158] S. Li, S. Fang, H. Dou, et al. RbF as a Dendrite-Inhibiting Additive in Lithium Metal Batteries. *ACS Applied Materials & Interfaces* **2019**, *11*, 20804-20811.
- [159] K. B. Hatzell, X. C. Chen, C. L. Cobb, et al. Challenges in Lithium Metal Anodes for Solid-State Batteries. *ACS Energy Letters* **2020**, *5*, 922-934.
- [160] C. Wang, Y. Gong, B. Liu, et al. Conformal, Nanoscale ZnO Surface Modification of Garnet-Based Solid-State Electrolyte for Lithium Metal Anodes. *Nano Letters* **2017**, *17*, 565-571.
- [161] A. Mirsakiyeva, M. Ebadi, C. M. Araujo, et al. Initial Steps in PEO Decomposition on a Li Metal Electrode. *The Journal of Physical Chemistry C* **2019**, *123*, 22851-22857.
- [162] F. Yuan, H.-Z. Chen, H.-Y. Yang, et al. PAN–PEO solid polymer electrolytes with high ionic conductivity. *Materials Chemistry and Physics* **2005**, *89*, 390-394.
- [163] J. Zhang, J. Zhao, L. Yue, et al. Safety-Reinforced Poly(Propylene Carbonate)-Based All-Solid-State Polymer Electrolyte for Ambient-Temperature Solid Polymer Lithium Batteries. *Advanced Energy Materials* **2015**, *5*, 1501082.
- [164] T.-t. He, M.-x. Jing, H. Yang, et al. Effects of gelation behavior of PPC-based electrolyte on electrochemical performance of solid state lithium battery. *SN Applied Sciences* **2019**, *1*, 205.
- [165] L. Chen, Y. Li, S.-P. Li, et al. PEO/garnet composite electrolytes for solid-state lithium batteries: From “ceramic-in-polymer” to “polymer-in-ceramic”. *Nano Energy* **2018**, *46*, 176-184.
- [166] J. Yang, X. Wang, G. Zhang, et al. High-Performance Solid Composite Polymer Electrolyte for all Solid-State Lithium Battery Through Facile Microstructure Regulation. *Frontiers In Chemistry* **2019**, *7*, 388.
- [167] G. G. Eshetu, X. Judez, C. Li, et al. Ultrahigh Performance All Solid-State Lithium Sulfur Batteries: Salt Anion's Chemistry-Induced Anomalous Synergistic Effect. *Journal of The American Chemical Society* **2018**, *140*, 9921-9933.
- [168] H.-K. Jing, L.-L. Kong, S. Liu, et al. Protected lithium anode with porous Al₂O₃ layer for lithium–sulfur battery. *Journal of Materials Chemistry A* **2015**, *3*, 12213-12219.
- [169] X. Liang, Q. Pang, I. R. Kochetkov, et al. A facile surface chemistry route to a stabilized lithium metal anode. *Nature Energy* **2017**, *2*, 17119.
- [170] G. Zheng, S. W. Lee, Z. Liang, et al. Interconnected hollow carbon nanospheres for stable lithium metal anodes. *Nature Nanotechnology* **2014**, *9*, 618-23.
- [171] J. Xie, L. Liao, Y. Gong, et al. Stitching h-BN by atomic layer deposition of

- LiF as a stable interface for lithium metal anode. *Science Advances* **2017**, *3*, eaao3170.
- [172] Y. Jeon, S. Kang, S. H. Joo, et al. Pyridinic-to-graphitic conformational change of nitrogen in graphitic carbon nitride by lithium coordination during lithium plating. *Energy Storage Materials* **2020**, *31*, 505-514.
- [173] S. Li, L. Fan, Y. Lu. Rational design of robust-flexible protective layer for safe lithium metal battery. *Energy Storage Materials* **2019**, *18*, 205-212.
- [174] J. Luo, C.-C. Fang, N.-L. Wu. High Polarity Poly(vinylidene difluoride) Thin Coating for Dendrite-Free and High-Performance Lithium Metal Anodes. *Advanced Energy Materials* **2018**, *8*, 1701482.
- [175] C. B. Bucur, A. Lita, N. Osada, et al. A soft, multilayered lithium–electrolyte interface. *Energy & Environmental Science* **2016**, *9*, 112-116.
- [176] B. Zhu, Y. Jin, X. Hu, et al. Poly(dimethylsiloxane) Thin Film as a Stable Interfacial Layer for High-Performance Lithium-Metal Battery Anodes. *Advanced Materials* **2017**, *29*, 1603755.
- [177] Z. Yu, D. G. Mackanic, W. Michaels, et al. A Dynamic, Electrolyte-Blocking, and Single-Ion-Conductive Network for Stable Lithium-Metal Anodes. *Joule* **2019**, *3*, 2761-2776.
- [178] W. Liu, W. Li, D. Zhuo, et al. Core-Shell Nanoparticle Coating as an Interfacial Layer for Dendrite-Free Lithium Metal Anodes. *ACS Central Science* **2017**, *3*, 135-140.
- [179] S. Wei, S. Choudhury, Z. Tu, et al. Electrochemical Interphases for High-Energy Storage Using Reactive Metal Anodes. *Account of Chemical Research* **2018**, *51*, 80-88.
- [180] R. Akolkar. Modeling dendrite growth during lithium electrodeposition at sub-ambient temperature. *Journal of Power Sources* **2014**, *246*, 84-89.
- [181] K. Yan, J. Wang, S. Zhao, et al. Temperature-Dependent Nucleation and Growth of Dendrite-Free Lithium Metal Anodes. *Angewandte Chemie International Edition* **2019**, *58*, 11364-11368.
- [182] H. J. Chang, N. M. Trease, A. J. Illott, et al. Investigating Li Microstructure Formation on Li Anodes for Lithium Batteries by in Situ $^6\text{Li}/^7\text{Li}$ NMR and SEM. *The Journal of Physical Chemistry C* **2015**, *119*, 16443-16451.
- [183] H. Yang, E. O. Fey, B. D. Trimm, et al. Effects of Pulse Plating on lithium electrodeposition, morphology and cycling efficiency. *Journal of Power Sources* **2014**, *272*, 900-908.
- [184] K. Shen, Z. Wang, X. Bi, et al. Magnetic Field–Suppressed Lithium Dendrite Growth for Stable Lithium-Metal Batteries. *Advanced Energy Materials* **2019**, *9*, 1900260.
- [185] S. S. Zhang. Problem, Status, and Possible Solutions for Lithium Metal Anode of Rechargeable Batteries. *ACS Applied Energy Materials* **2018**, *1*, 910-920.
- [186] P. Bai, J. Li, F. R. Brushett, et al. Transition of Lithium Growth Mechanisms in Liquid Electrolytes. *Energy & Environmental Science* **2016**, *9*, 3221-3229.
- [187] G. Kresse, J. Hafner. Ab initio molecular-dynamics simulation of the liquid-metal--amorphous-semiconductor transition in germanium. *Physical Review B* **1994**, *49*, 14251-14269.

- [188] G. Kresse, D. Joubert. From ultrasoft pseudopotentials to the projector augmented-wave method. *Physical Review B* **1999**, *59*, 1758-1775.
- [189] J. P. Perdew, K. Burke, M. Ernzerhof. Generalized Gradient Approximation Made Simple. *Physical Review Letters* **1996**, *77*, 3865-3868.
- [190] J. Lang, J. Song, L. Qi, et al. Uniform Lithium Deposition Induced by Polyacrylonitrile Submicron Fiber Array for Stable Lithium Metal Anode. *ACS Applied Materials & Interfaces* **2017**, *9*, 10360-10365.
- [191] W. Deng, S. Liang, X. Zhou, et al. Depressing the irreversible reactions on a three-dimensional interface towards a high-areal capacity lithium metal anode. *Journal of Materials Chemistry A* **2019**, *7*, 6267-6274.
- [192] Y. He, H. Xu, J. Shi, et al. Polydopamine Coating Layer Modified Current Collector for Dendrite-Free Li Metal Anode. *Energy Storage Materials* **2019**, *23*, 418-426.
- [193] C. Yang, B. Liu, F. Jiang, et al. Garnet/polymer hybrid ion-conducting protective layer for stable lithium metal anode. *Nano Research* **2017**, *10*, 4256-4265.
- [194] Q. Wu, Z. Yao, A. Du, et al. Oxygen-defect-rich coating with nanoporous texture as both anode host and artificial SEI for dendrite-mitigated lithium-metal batteries. *Journal of Materials Chemistry A* **2021**, *9*, 5606-5618.
- [195] T. Li, P. Shi, R. Zhang, et al. Dendrite-free sandwiched ultrathin lithium metal anode with even lithium plating and stripping behavior. *Nano Research* **2019**, *12*, 2224-2229.
- [196] X. Wang, Z. Pan, Y. Wu, et al. Infiltrating lithium into carbon cloth decorated with zinc oxide arrays for dendrite-free lithium metal anode. *Nano Research* **2019**, *12*, 525-529.
- [197] G. Li, Z. Liu, Q. Huang, et al. Stable Metal Battery Anodes Enabled by Polyethylenimine Sponge Hosts by Way of Electrokinetic Effects. *Nature Energy* **2018**, *3*, 1076-1083.
- [198] S. Ni, S. Tan, Q. An, et al. Three dimensional porous frameworks for lithium dendrite suppression. *Journal of Energy Chemistry* **2020**, *44*, 73-89.
- [199] Y. Huang, B. Chen, J. Duan, et al. Graphitic Carbon Nitride (g-C₃N₄): An Interface Enabler for Solid-State Lithium Metal Batteries. *Angewandte Chemie International Edition* **2020**, *59*, 3699-3704.
- [200] Q. Yang, M. Cui, J. Hu, et al. Ultrathin Defective C-N Coating to Enable Nanostructured Li Plating for Li Metal Batteries. *ACS Nano* **2020**, *14*, 1866-1878.
- [201] Y. Xu, T. Li, L. Wang, et al. Interlayered Dendrite-Free Lithium Plating for High-Performance Lithium-Metal Batteries. *Advanced Materials* **2019**, *31*, 1901662.
- [202] Y. Guo, Y. Wei, H. Li, et al. Layer Structured Materials for Advanced Energy Storage and Conversion. *Small* **2017**, *13*, 1701649.
- [203] S. Pennathur, J. G. Santiago. Electrokinetic Transport in Nanochannels. 2. Experiments. *Analytical Chemistry* **2006**, *78*, 972-973.
- [204] J. Hu, J. Tian, C. Li. Nanostructured Carbon Nitride Polymer-Reinforced Electrolyte To Enable Dendrite-Suppressed Lithium Metal Batteries. *ACS Applied Materials & Interfaces* **2017**, *9*, 11615-11625.

- [205] J. Hu, K. Chen, Z. Yao, et al. Unlocking solid-state conversion batteries reinforced by hierarchical microsphere stacked polymer electrolyte. *Science Bulletin* **2021**, *66*, 694-707.
- [206] G. Liu, M. Xue, Q. Liu, et al. Facile synthesis of C-doped hollow spherical g-C₃N₄ from supramolecular self-assembly for enhanced photoredox water splitting. *International Journal of Hydrogen Energy* **2019**, *44*, 25671-25679.
- [207] P.-Y. Kuang, Y.-Z. Su, G.-F. Chen, et al. g-C₃N₄ decorated ZnO nanorod arrays for enhanced photoelectrocatalytic performance. *Applied Surface Science* **2015**, *358*, 296-303.
- [208] Y. Liu, H. Liu, H. Zhou, et al. A Z-scheme mechanism of N-ZnO/g-C₃N₄ for enhanced H₂ evolution and photocatalytic degradation. *Applied Surface Science* **2019**, *466*, 133-140.
- [209] R. Uma, K. Ravichandran, S. Sriram, et al. Cost-effective fabrication of ZnO/g-C₃N₄ composite thin films for enhanced photocatalytic activity against three different dyes (MB, MG and RhB). *Materials Chemistry and Physics* **2017**, *201*, 147-155.
- [210] L. Li, S.-Q. Sun, Y.-X. Wang, et al. Facile synthesis of ZnO/g-C₃N₄ composites with honeycomb-like structure by H₂ bubble templates and their enhanced visible light photocatalytic performance. *Journal of Photochemistry and Photobiology A: Chemistry* **2018**, *355*, 16-24.
- [211] M. Chu, K. Hu, J. Wang, et al. Synthesis of g-C₃N₄-based photocatalysts with recyclable feature for efficient 2,4-dichlorophenol degradation and mechanisms. *Applied Catalysis B: Environmental* **2019**, *243*, 57-65.
- [212] C. Li, W. Zhao, A. Wang, et al. Multifunctional carbon nitride nano-homojunction decorated g-C₃N₄ nanocomposites for optoelectronic performances. *Applied Surface Science* **2019**, *467-468*, 1140-1147.
- [213] K. Qi, Y. Xie, R. Wang, et al. Electroless plating Ni-P cocatalyst decorated g-C₃N₄ with enhanced photocatalytic water splitting for H₂ generation. *Applied Surface Science* **2019**, *466*, 847-853.
- [214] N. Liu, N. Lu, Y. Su, et al. Fabrication of g-C₃N₄/Ti₃C₂ composite and its visible-light photocatalytic capability for ciprofloxacin degradation. *Separation and Purification Technology* **2019**, *211*, 782-789.
- [215] W. Yu, D. Xu, T. Peng. Enhanced photocatalytic activity of g-C₃N₄ for selective CO₂ reduction to CH₃OH via facile coupling of ZnO: a direct Z-scheme mechanism. *Journal of Materials Chemistry A* **2015**, *3*, 19936-19947.
- [216] M.-H. Ryou, D. J. Lee, J.-N. Lee, et al. Excellent Cycle Life of Lithium-Metal Anodes in Lithium-Ion Batteries with Mussel-Inspired Polydopamine-Coated Separators. *Advanced Energy Materials* **2012**, *2*, 645-650.
- [217] Q. Meng, B. Deng, H. Zhang, et al. Heterogeneous Nucleation and Growth of Electrodeposited Lithium Metal on the Basal Plane of Single-Layer Graphene. *Energy Storage Materials* **2019**, *16*, 419-425.
- [218] U. v. Alpen. Li₃N: A promising Li ionic conductor. *Journal of Solid State Chemistry* **1979**, *29*, 379-392.

- [219] S. Ye, L. Wang, F. Liu, et al. g-C₃N₄ Derivative Artificial Organic/Inorganic Composite Solid Electrolyte Interphase Layer for Stable Lithium Metal Anode. *Advanced Energy Materials* **2020**, *10*, 2002647.
- [220] S. Liu, X. Ji, N. Piao, et al. Inorganic-rich Solid Electrolyte Interphase for Advanced Lithium Metal Batteries in Carbonate Electrolytes. *Angewandte Chemie International Edition* **2021**, *60*, 3661.
- [221] L. Pan, Z. Luo, Y. Zhang, et al. Seed-Free Selective Deposition of Lithium Metal into Tough Graphene Framework for Stable Lithium Metal Anode. *ACS Appl Mater Interfaces* **2019**, *11*, 44383-44389.
- [222] Y. Liu, D. Lin, Y. Li, et al. Solubility-mediated sustained release enabling nitrate additive in carbonate electrolytes for stable lithium metal anode. *Nat Commun* **2018**, *9*, 3656.
- [223] Y. Li, Z. Yang, Z. Wu, et al. The effects of lithium salt and solvent on lithium metal anode performance. *Solid State Ionics* **2018**, *324*, 144-149.
- [224] C. Fiedler, B. Luerssen, M. Rohnke, et al. XPS and SIMS Analysis of Solid Electrolyte Interphases on Lithium Formed by Ether-Based Electrolytes. *Journal of The Electrochemical Society* **2017**, *164*, A3742.
- [225] Q. Zhao, X. Liu, J. Zheng, et al. Designing electrolytes with polymerlike glass-forming properties and fast ion transport at low temperatures. *Proc Natl Acad Sci U S A* **2020**, *117*, 26053-26060.
- [226] R. May, K. J. Fritzsche, D. Livitz, et al. Rapid Interfacial Exchange of Li Ions Dictates High Coulombic Efficiency in Li Metal Anodes. *ACS Energy Letters* **2021**, 1162-1169.
- [227] J. Pu, J. Li, K. Zhang, et al. Conductivity and Lithiophilicity Gradients Guide Lithium Deposition to Mitigate Short Circuits. *Nature Communications* **2019**, *10*, 1896.
- [228] N. Dong, G. Yang, H. Luo, et al. A LiPO₂F₂/LiFSI dual-salt electrolyte enabled stable cycling of lithium metal batteries. *Journal of Power Sources* **2018**, *400*, 449-456.
- [229] J. M. Whiteley, S. Hafner, S. S. Han, et al. FeS₂-Imbedded Mixed Conducting Matrix as a Solid Battery Cathode. *Advanced Energy Materials* **2016**, *6*, 1600495.
- [230] Y. Hu, W. Chen, T. Lei, et al. Graphene quantum dots as the nucleation sites and interfacial regulator to suppress lithium dendrites for high-loading lithium-sulfur battery. *Nano Energy* **2020**, *68*, 104373.
- [231] Q. Cheng, L. Wei, Z. Liu, et al. Operando and three-dimensional visualization of anion depletion and lithium growth by stimulated Raman scattering microscopy. *Nature Communications* **2018**, *9*, 2942.
- [232] X. Fan, C. Wang. High-voltage liquid electrolytes for Li batteries: progress and perspectives. *Chem Soc Rev* **2021**, *50*, 10486-10566.
- [233] R. Dedryvère, S. Leroy, H. Martinez, et al. XPS Valence Characterization of Lithium Salts as a Tool to Study Electrode/Electrolyte Interfaces of Li-Ion Batteries. *The Journal of Physical Chemistry B* **2006**, *110*, 12986-12992.
- [234] Q. Guo, W. Deng, S. Xia, et al. Nano-Channel-Based Physical and Chemical Synergic Regulation for Dendrite-Free Lithium Plating. *Nano Research* **2021**, *14*, 3585-3597.

- [235] J. I. Lee, G. Song, S. Cho, et al. Lithium Metal Interface Modification for High-Energy Batteries: Approaches and Characterization. *Batteries & Supercaps* **2020**, *3*, 828-859.
- [236] S. Zhang, W. Deng, X. Zhou, et al. Controlled Lithium Plating in Three-Dimensional Hosts through Nucleation Overpotential Regulation Toward High-Areal-Capacity Lithium Metal Anode. *Materials Today Energy* **2021**, *21*, 100770.
- [237] A. Hu, W. Chen, X. Du, et al. An artificial hybrid interphase for an ultrahigh-rate and practical lithium metal anode. *Energy & Environmental Science* **2021**, *14*, 4115-4124.
- [238] X. Ren, S. Chen, H. Lee, et al. Localized High-Concentration Sulfone Electrolytes for High-Efficiency Lithium-Metal Batteries. *Chem* **2018**, *4*, 1877-1892.
- [239] Q. Pang, L. Zhou, L. F. Nazar. Elastic and Li-ion-percolating hybrid membrane stabilizes Li metal plating. *Proc Natl Acad Sci U S A* **2018**, *115*, 12389-12394.
- [240] W. Wang, X. Yue, J. Meng, et al. Lithium phosphorus oxynitride as an efficient protective layer on lithium metal anodes for advanced lithium-sulfur batteries. *Energy Storage Materials* **2019**, *18*, 414-422.
- [241] Y. Feng, C. Zhang, B. Li, et al. Low-volume-change, dendrite-free lithium metal anodes enabled by lithophilic 3D matrix with LiF-enriched surface. *Journal of Materials Chemistry A* **2019**, *7*, 6090-6098.
- [242] G. He, Q. Li, Y. Shen, et al. Flexible Amalgam Film Enables Stable Lithium Metal Anodes with High Capacities. *Angewandte Chemie International Edition* **2019**, *58*, 18466-18470.
- [243] J. Tan, J. Matz, P. Dong, et al. A Growing Appreciation for the Role of LiF in the Solid Electrolyte Interphase. *Advanced Energy Materials* **2021**, *11*, 2100046.
- [244] J. Lang, Y. Long, J. Qu, et al. One-Pot Solution Coating of High Quality LiF Layer to Stabilize Li Metal Anode. *Energy Storage Materials* **2019**, *16*, 85-90.
- [245] R. Sliz, J. Valikangas, H. Silva Santos, et al. Suitable Cathode NMP Replacement for Efficient Sustainable Printed Li-Ion Batteries. *ACS Appl Energy Mater* **2022**, *5*, 4047-4058.
- [246] X. Zhang, T. Liu, S. Zhang, et al. Synergistic Coupling between $\text{Li}_{6.75}\text{La}_3\text{Zr}_{1.75}\text{Ta}_{0.25}\text{O}_{12}$ and Poly(vinylidene fluoride) Induces High Ionic Conductivity, Mechanical Strength, and Thermal Stability of Solid Composite Electrolytes. *Journal of the American Chemical Society* **2017**, *139*, 13779-13785.
- [247] Y. Wang, Y. Tian, D. Estevez, et al. Complementary hybrid design of solvated electrolyte membranes enabled by porous carbon reinforcement for high-performance lithium batteries. *Journal of Power Sources* **2021**, *506*, 230127.
- [248] C. Niu, D. Liu, J. A. Lochala, et al. Balancing interfacial reactions to achieve long cycle life in high-energy lithium metal batteries. *Nature Energy* **2021**, *6*, 723-732.
- [249] Z. Xie, Z. Wu, X. An, et al. Anode-Free Rechargeable Lithium Metal Batteries: Progress and Prospects. *Energy Storage Materials* **2020**, *32*, 386-401.
- [250] L. Lin, K. Qin, Q. Zhang, et al. Li-Rich $\text{Li}_2[\text{Ni}_{0.8}\text{Co}_{0.1}\text{Mn}_{0.1}]\text{O}_2$ for Anode-Free Lithium Metal Batteries. *Angewandte Chemie International Edition* **2021**, *60*, 8289-8296.

- [251] W. Chen, R. V. Salvatierra, M. Ren, et al. Laser-Induced Silicon Oxide for Anode-Free Lithium Metal Batteries. *Advanced Materials* **2020**, *32*, 2002850.
- [252] P. Bai, J. Guo, M. Wang, et al. Interactions between Lithium Growths and Nanoporous Ceramic Separators. *Joule* **2018**, *2*, 2434-2449.
- [253] P. Zou, Y. Sui, H. Zhan, et al. Polymorph Evolution Mechanisms and Regulation Strategies of Lithium Metal Anode under Multiphysical Fields. *Chemical Reviews* **2021**, *121*, 5986-6056.
- [254] X. Wang, W. Zeng, L. Hong, et al. Stress-Driven Lithium Dendrite Growth Mechanism and Dendrite Mitigation by Electroplating on Soft Substrates. *Nature Energy* **2018**, *3*, 227-235.
- [255] S. S. Zhang, X. Fan, C. Wang. A Tin-Plated Copper Substrate for Efficient Cycling of Lithium Metal in an Anode-Free Rechargeable Lithium Battery. *Electrochimica Acta* **2017**, *258*, 1201-1207.
- [256] V. Pande, V. Viswanathan. Computational Screening of Current Collectors for Enabling Anode-Free Lithium Metal Batteries. *ACS Energy Letters* **2019**, *4*, 2952-2959.
- [257] H. Kwon, J.-H. Lee, Y. Roh, et al. An Electron-Deficient Carbon Current Collector for Anode-Free Li-metal Batteries. *Nature Communications* **2021**, *12*, 5537.
- [258] L. Lin, L. Suo, Y. s. Hu, et al. Epitaxial Induced Plating Current-Collector Lasting Lifespan of Anode-Free Lithium Metal Battery. *Advanced Energy Materials* **2021**, *11*, 2003709.
- [259] Z.-J. Zheng, Q. Su, Q. Zhang, et al. Low Volume Change Composite Lithium Metal Anodes. *Nano Energy* **2019**, *64*, 103910.
- [260] C.-Y. Wang, Z.-J. Zheng, Y.-Q. Feng, et al. Topological Design of Ultrastrong MXene Paper Hosted Li Enables Ultrathin and Fully Flexible Lithium Metal Batteries. *Nano Energy* **2020**, *74*, 104817.
- [261] A. A. Assegie, J.-H. Cheng, L.-M. Kuo, et al. Polyethylene Oxide Film Coating Enhances Lithium Cycling Efficiency of an Anode-Free Lithium-Metal Battery. *Nanoscale* **2018**, *10*, 6125-6138.
- [262] Z. T. Wondimkun, T. T. Beyene, M. A. Weret, et al. Binder-Free Ultra-Thin Graphene Oxide as an Artificial Solid Electrolyte Interphase for Anode-Free Rechargeable Lithium Metal Batteries. *Journal of Power Sources* **2020**, *450*, 227589.
- [263] R. M. Gao, H. Yang, C. Y. Wang, et al. Fatigue-Resistant Interfacial Layer for Safe Lithium Metal Batteries. *Angewandte Chemie International Edition* **2021**, *60*, 25508-25513.
- [264] J. Qian, B. D. Adams, J. Zheng, et al. Anode-Free Rechargeable Lithium Metal Batteries. *Advanced Functional Materials* **2016**, *26*, 7094-7102.
- [265] H. Wang, Z. Yu, X. Kong, et al. Dual-Solvent Li-Ion Solvation Enables High-Performance Li-Metal Batteries. *Advanced Materials* **2021**, *33*, 2008619.
- [266] S. Menkin, C. A. O'Keefe, A. B. Gunnarsdóttir, et al. Toward an Understanding of SEI Formation and Lithium Plating on Copper in Anode-Free Batteries. *Journal of Physical Chemistry C* **2021**, *125*, 16719-16732.
- [267] H. Gan, R. Wang, J. Wu, et al. Coupling a 3D Lithophilic Skeleton with a Fluorine-Enriched Interface to Enable Stable Lithium Metal Anode. *ACS Applied*

Materials & Interfaces **2021**, *13*, 37162-37171.

- [268] S. Xia, X. Zhang, L. Luo, et al. Highly Stable and Ultrahigh-Rate Li Metal Anode Enabled by Fluorinated Carbon Fibers. *Small* **2021**, *17*, 2006002.
- [269] F. Liu, R. Xu, Z. Hu, et al. Regulating Lithium Nucleation via CNTs Modifying Carbon Cloth Film for Stable Li Metal Anode. *Small* **2018**, *15*, 1803734.
- [270] Z. Y. Wang, Z. X. Lu, W. Guo, et al. A Dendrite-Free Lithium/Carbon Nanotube Hybrid for Lithium-Metal Batteries. *Advanced Materials* **2021**, *33*, 2006702.
- [271] N. Shu, J. Xie, X. Wang, et al. Rolling Press of Lithium with Carbon for High-Performance Anodes. *Energy Storage Materials* **2020**, *24*, 689-693.
- [272] C. Sun, T. Wu, J. Wang, et al. Favorable Lithium Deposition Behaviors on Flexible Carbon Microtube Skeleton Enable a High-Performance Lithium Metal Anode. *Journal of Materials Chemistry A* **2018**, *6*, 19159-19166.
- [273] M. M. Islam, V. S. Bryantsev, A. C. T. van Duin. ReaxFF Reactive Force Field Simulations on the Influence of Teflon on Electrolyte Decomposition during Li/SWCNT Anode Discharge in Lithium-Sulfur Batteries. *Journal of The Electrochemical Society* **2014**, *161*, E3009-E3014.
- [274] S.-H. Wang, Y.-X. Yin, T.-T. Zuo, et al. Stable Li Metal Anodes via Regulating Lithium Plating/Stripping in Vertically Aligned Microchannels. *Advanced Materials* **2017**, *29*, 1703729.
- [275] A. Kolesnikov, M. Kolek, J. F. Dohmann, et al. Galvanic Corrosion of Lithium-Powder-Based Electrodes. *Advanced Energy Materials* **2020**, *10*, 2000017.
- [276] Y. Liu, X. Qin, F. Liu, et al. Basal Nanosuit of Graphite for High-Energy Hybrid Li Batteries. *ACS Nano* **2020**, *14*, 1837-1845.
- [277] W. Liu, Y. Xia, W. Wang, et al. Pristine or Highly Defective? Understanding the Role of Graphene Structure for Stable Lithium Metal Plating. *Advanced Energy Materials* **2019**, *9*, 1802918.
- [278] G. Wang, T. Liu, X. Fu, et al. Lithiophilic Amide-Functionalized Carbon Nanotube Skeleton for Dendrite-Free Lithium Metal Anodes. *Chemical Engineering Journal* **2021**, *414*, 128698.
- [279] T. S. Mathis, N. Kurra, X. Wang, et al. Energy Storage Data Reporting in Perspective—Guidelines for Interpreting the Performance of Electrochemical Energy Storage Systems. *Advanced Energy Materials* **2019**, *9*, 1902007.
- [280] H. Wang, X. Feng, Y. Chen, et al. Reversible Electrochemical Interface of Mg Metal and Conventional Electrolyte Enabled by Intermediate Adsorption. *ACS Energy Letters* **2019**, *5*, 200-206.
- [281] S. Sun, S. Myung, G. Kim, et al. Facile Ex Situ Formation of a LiF–Polymer Composite Layer as an Artificial SEI Layer on Li Metal by Simple Roll-Press Processing for Carbonate Electrolyte-Based Li Metal Batteries. *Journal of Materials Chemistry A* **2020**, *8*, 17229-17237.
- [282] A. B. Gunnarsdottir, C. V. Amanchukwu, S. Menkin, et al. Noninvasive In Situ NMR Study of "Dead Lithium" Formation and Lithium Corrosion in Full-Cell Lithium Metal Batteries. *Journal of the American Chemical Society* **2020**, *142*, 20814-20827.
- [283] A. Mashreghi, H. Zare. Investigation of Nucleation and Growth Mechanism

during Electrochemical Deposition of Nickel on Fluorine Doped Tin Oxide Substrate. *Current Applied Physics* **2016**, *16*, 599-604.

[284] N. Yao, X. Chen, X. Shen, et al. An Atomic Insight into the Chemical Origin and Variation of the Dielectric Constant in Liquid Electrolytes. *Angew Chem Int Ed Engl* **2021**, *60*, 21473-21478.

[285] G. Zhang, H. J. Peng, C. Z. Zhao, et al. The Radical Pathway Based on a Lithium-Metal-Compatible High-Dielectric Electrolyte for Lithium-Sulfur Batteries. *Angew Chem Int Ed Engl* **2018**, *57*, 16732-16736.

[286] K. S. Barros, J. A. S. Tenório, D. C. R. Espinosa In *Determination of Limiting Current Density of a Solution with Copper, Zinc and EDTA from the Effluent of Brass Electrodeposition*, Energy Technology 2018, Springer International Publishing: **2018**; pp 375-383.

[287] S.-S. Chi, Y. Liu, W.-L. Song, et al. Prestoring Lithium into Stable 3D Nickel Foam Host as Dendrite-Free Lithium Metal Anode. *Advanced Functional Materials* **2017**, *27*, 1700348.

[288] A. A. Assegie, C. C. Chung, M. C. Tsai, et al. Multilayer-graphene-stabilized lithium deposition for anode-free lithium-metal batteries. *Nanoscale* **2019**, *11*, 2710-2720.

[289] D. Lin, Y. Liu, Z. Liang, et al. Layered reduced graphene oxide with nanoscale interlayer gaps as a stable host for lithium metal anodes. *Nature Nanotechnology* **2016**, *11*, 626-632.

[290] J. Khan, S. A. Momin, M. Mariatti. A review on advanced carbon-based thermal interface materials for electronic devices. *Carbon* **2020**, *168*, 65-112.

[291] F. Joho, B. Rykart, A. Blome, et al. Relation between surface properties, pore structure and first-cycle charge loss of graphite as negative electrode in lithium-ion batteries. *Journal of Power Sources* **2001**, *97-98*, 78-82.

[292] F. J. Sonia, B. Ananthoju, M. K. Jangid, et al. Insight into the mechanical integrity of few-layers graphene upon lithiation/delithiation via in situ monitoring of stress development. *Carbon* **2015**, *88*, 206-214.

[293] D. J. Yoo, A. Elabd, S. Choi, et al. Highly Elastic Polyrotaxane Binders for Mechanically Stable Lithium Hosts in Lithium-Metal Batteries. *Advanced Materials* **2019**, *31*, 1901645.

[294] Q. Guo, Y. Yu, S. Xia, et al. CNT/PVDF Composite Coating Layer on Cu with a Synergy of Uniform Current Distribution and Stress Releasing for Improving Reversible Li Plating/Stripping. *ACS Applied Materials & Interfaces* **2022**, *14*, 46043-46055.

[295] H.-C. Chu, H.-Y. Tuan. High-performance lithium-ion batteries with 1.5 μm thin copper nanowire foil as a current collector. *Journal of Power Sources* **2017**, *346*, 40-48.

[296] D. G. Papageorgiou, I. A. Kinloch, R. J. Young. Mechanical properties of graphene and graphene-based nanocomposites. *Progress in Materials Science* **2017**, *90*, 75-127.

[297] Y.-X. Lin, Z. Liu, K. Leung, et al. Connecting the irreversible capacity loss in

Li-ion batteries with the electronic insulating properties of solid electrolyte interphase (SEI) components. *Journal of Power Sources* **2016**, *309*, 221-230.

[298] L. Wang, G. Luo. Atomistic Mechanism and Long-Term Stability of Using Chlorinated Graphdiyne Film to Reduce Lithium Dendrites in Rechargeable Lithium Metal Batteries. *Nano Letters* **2021**, *21*, 7284-7290.

[299] S. Grimme, J. Antony, S. Ehrlich, et al. A consistent and accurate ab initio parametrization of density functional dispersion correction (DFT-D) for the 94 elements H-Pu. *Journal of Chemical Physics* **2010**, *132*, 154104.

[300] J. J. Kim, G.-C. Wang, T.-M. Lu, et al. Contact potential induced carrier localization in nanometer-thin Cu/Ru, Cu/Co, and Cu/Mo superlattices. *Journal of Vacuum Science & Technology A* **2020**, *38*, 033208.

[301] X. Ren, L. Zou, X. Cao, et al. Enabling High-Voltage Lithium-Metal Batteries under Practical Conditions. *Joule* **2019**, *3*, 1662-1676.

[302] N. Gao, A. W. Abboud, G. S. Mattei, et al. Fast Diagnosis of Failure Mechanisms and Lifetime Prediction of Li Metal Batteries. *Small Methods* **2021**, *5*, 2000807.

[303] L. Xia, H. Miao, C. Zhang, et al. Review—recent advances in non-aqueous liquid electrolytes containing fluorinated compounds for high energy density lithium-ion batteries. *Energy Storage Materials* **2021**, *38*, 542-570.

Biography

Paper:

1. **Q. Guo**, W. Deng, S. Xia, Z. Zhang, F. Zhao, B. Hu, S. Zhang, X. Zhou, G. Chen, Z. Liu, Nano-channel-based physical and chemical synergic regulation for dendrite-free lithium plating. *Nano Research* **2021**, 14 (10), 3585-3597.
2. **Q. Guo**, Y. Yu, S. Xia, C. Shen, D. Hu, W. Deng, D. Dong, X. Zhou, G. Chen, Z. Liu, CNT/PVDF Composite Coating Layer on Cu with a Synergy of Uniform Current Distribution and Stress Releasing for Improving Reversible Li Plating/Stripping. *ACS Applied Materials & Interfaces* **2022**, 14 (40), 46043-46055.
3. **Q. Guo**, S. Wang, Y. Li, J. Wang, Y. Wu, Y. Yu, S. Xia, D. Hu, B. Hu, Z. Ye, X. Zhou, G. Chen, Z. Liu, Free-standing and Low-Density Composite of Graphene and PVDF as Promoting Current Collector for Reversible Lithium Deposition. *Advanced Functional Materials*. **2023**. (submitted to the journal)
4. S. Xia[#], **Q. Guo**[#], Y. Yu, Y. Li, S. Wang, D. Dong, Z. Liu, H. Zhou, X. Zhou, Z. Liu, Surface Modification of Carbon Fiber Cloth with Graphene Oxide Through an Electrophoresis Method for Lithium Metal Anode. *Carbon*. **2023**, 203, 743-752. (#: Co-first author)
5. D. Dong, F. Zhao, S. Xia, Z. Liu, S. Wang, **Q. Guo**, X. Zhou, Z. Liu, Ag Nanoparticle-Decorated Mesocarbon Microbeads for Homogeneous Lithium Deposition toward Stable Hybrid Anodes. *ACS Applied Nano Materials* **2022**, 5 (6), 7908-7916.
6. S. Zhang, W. Deng, X. Zhou, B. He, J. Liang, F. Zhao, **Q. Guo**, Z. Liu, Controlled Lithium Plating in Three-Dimensional Hosts through Nucleation Overpotential Regulation Toward High-Areal-Capacity Lithium Metal Anode. *Materials Today Energy* **2021**, 21, 100770.

Patent:

1. **郭强**, 周旭峰, 刘兆平, 一种用于锂金属电池的复合负极材料。(Application number: 202110620655.9)
2. **郭强**, 周旭峰, 刘兆平, 一种自支撑碳基集流体、其制备方法及应用。(Application number: 202210846180.X)

Conference:

Q. Guo, P. Fan, L. Guan, A. Croft, G. Chen, The critical capacity of Li deposition on Cu foam electrodes in ionic liquids. Molten Salts and Ionic Liquids Discussion Group Christmas Research Meeting, London **2022**. (Oral presentation)